Novel Magnetic Architectures for Next Generation Electric Vehicles

By

Oliver Joe Found

University of Sheffield

Materials Science and Engineering

A thesis submitted for the degree of Doctor of Philosophy

September 2023

Abstract

Magnetic materials are an important component in many modern electric motors, utilising NdFeB hard magnetic materials as a source of high magnetic flux density. Current methods to improve magnetic performance involve the addition of other rare-earth materials, such as Dy, to improve coercivity. Minimising the use of rare-earth materials and preventing the additional use of more should be the aim in order to achieve these more sustainable goals and reduce the social and economic cost associated with these materials. Increasing the performance of magnetic materials without the use of rare-earth materials is the motivation for this research.

This thesis will explore the potential of achieving an increased stability using magnetic films and a graded magnetisation region in 1D, 3D and simulated different permanent magnet architectures within an electric motor. Both methods are found to reduce the demagnetisation field of the bulk magnetic material to different degrees, but the reduction of bulk material results in the inevitable loss of external field. Optimising this trade-off is the balancing act to consider when designing a magnet for a final application. A magnetic film produced positive results, but the use of a multilayer film with variable magnetisation led onto the use of a graded magnetisation which significantly reduced the demagnetisation field to a higher degree than the reduction of external field. This new magnetic architecture has theoretical larger coercivity and would therefore result in an increased performance.

Acknowledgements

Firstly, I would like to express my gratitude towards all my supervisors for their continued support and guidance throughout my Ph.D. especially during the COVID-19 lockdown era and after as things slowly got back to normal. Professor Dan Allwood for giving me the confidence to conduct this research in a new field of magnetics, and who's assistance at the start of my research has been essential. Dr Julian Dean who has supported the modelling has been vital in all the research conducted and discussions of how the work can be improved, or most of the time fixed.

Secondly, I would like to thank my colleagues at the University of Sheffield for the discussions of my work and all their questions leading towards finding answers into the research completed. I would also like to thank everyone over at VW Group Innovation, who have helped guide me and helped massively with their expertise in electric motor simulations.

I would like to thank all my friends around Sheffield and elsewhere, who's very welcome distractions at times got me through some of the tougher times of my Ph.D. especially all the zoom quizzes during lockdown. And not to forget the impromptu late nights at the pub.

Finally, I would like to express my deepest condolences to my brother who will now have to also complete a Ph.D. to be seen as an equal in my parents' eyes. A huge thanks to my parents who supported me through everything I've decided to do in my life, and for not kicking me out of the house during lockdown, even though I'm sure they really wanted to. That extends to the rest of my family as well. Last but in no means least to my amazing girlfriend Rachael, who has supported me through everything, and after years of pestering, finally gave in and let us get the "Baddest of them all" puppy, Dougie. Her constant motivation has kept me going and to see it through to the end, and as with a lot of things, she claims her motivating me to complete things counts as her achievement. So, this is an immeasurable thanks to you, (Dr.) Rachael.

COVID impact statement

My Ph.D., like many others was affected by COVID-19 and the subsequent lockdowns that followed. I spent the initial 6 months of my Ph.D. under normal conditions, where I was undergoing training for the various pieces of equipment that I would be using throughout my experimental Ph.D. The nationwide lockdowns and restrictions in the department meant that I had to switch my initial approach to simulation-based work, and the experimental work I could undertake proved inadequate to use as a platform for the rest of my Ph.D. So, I spent over a year creating the 1D model that will be described later, and a few further months confirming as to whether the results obtained were sound and reliable before progressing onto more simulation work.

The results, opinions and conclusions expressed in this publication are not necessarily those of Volkswagen Aktiengesellschaft.

List of abbreviations

REM	Rare-earth magnets
CEM	Critical-earth-magnets
REE	Rare-earth elements
FEA	Finite element analysis
Φ	Magnetic flux
μ_0	Permeability of free space
p	Pole strength
H	Magnetic field strength
A	Area
Θ	Offset angle
m	Magnetic moment
E	Energy of dipole
B	Magnetic induction
M	Magnetisation
V	Volume / Activation volume
χ	Susceptibility
µ	Permeability
B_s	Magnetic induction saturation
M_s	Magnetisation saturation
B_r	Magnetic induction remanence
M_r	Magnetisation remanence
E_m	Magnetostatic energy
H_d	Demagnetisation field
N_d	Demagnetisation shape factor
E_a	Magnetocrystalline anisotropy energy
K_0, K_1 and K_2, K_u	Anisotropy constants
θ_m	Angle between magnetisation vector and easy axis
E_z	Zeeman energy
E_t	Gibbs free energy
E_e	Exchange energy
J_{ex}	Exchange integral
S_i and S_j	Spin quantum of two electrons
θ_s	Angle between the spins S_i and S_j
A_{ex}	Exchange stiffness constant

T_c	Curie temperature
δ_B	Free standing Bloch wall length
l_{ex}	Magnetocrystalline exchange length
BH_{max}	Energy density
H_A	Anisotropy field
H_c	Coercivity
I_c	Electrical current
τ	Torque
α	Angular acceleration
I_o	Moment of inertia
ε	Induced electromotive force
NCM	Nanocrystalline materials
$Mr_{//}/Mr_{\perp}$	Magnetic anisotropy parallel/perpendicular
τ	Average waiting time for switching
f_0	Attempt frequency
k_B	Boltzmann's constant
SW	Stoner-Wohlfarth
N_s	Shape anisotropy
$N_{\perp} and\ N_{\parallel}$	Demagnetisation factors for easy axis, perpendicular and parallel
GBD	Grain boundary diffusion
TEM	Transmission Electron Microscopy
FORC	First-order-reversal-curve
EPMA	Electron probe micro-analyser
XRD	X-ray diffraction
AC	Alternating current
DC	Direct current
PM	Permanent magnet
IM	Induction motor
SPM	Synchronous permanent magnet motor
PMBS	Permanent magnet brushless motor
PMHEM	Permanent magnet hybrid excitation motor
RM	Reluctance motor
SBM	Synchronous brushed motor
CM	Coreless machine
IWM	In-wheel motor
FEM	Finite element modelling

P	Pole strength
ΔM	Change in magnetisation
d	Cell length
r	Radius
d'	Hypotenuse cell length
H_e	External field
E_d	Demagnetisation energy density
ϕ	Length scaling factor (Lscale)
J	Current density
FoM	Figure of merit
I_A	Current equation for coil pair A
I_B	Current equation for coil pair B
I_C	Current equation for coil pair C
σ	Position of rotation
I_m	Maximum current
β	Number of pole pairs
$\emptyset$	Offset angle
ν	Revolutions per minutes
t	Rotational time

Contents

Abstract.....i

Acknowledgements.....ii

COVID impact statement.....iii

List of abbreviations.....v

1. Introduction.....1

1.1 Market demand.....1

1.2 Current issues.....1

1.3 Thesis outline.....3

2. Introduction.....5

2.1 Magnetism.....5

2.1.1 Magnetic flux.....5

2.1.2 Magnetic moment.....5

2.1.3 Magnetic dipole.....6

2.1.4 Magnetic induction and magnetisation.....6

2.1.5 Flux density.....7

2.1.6 Susceptibility and permeability.....7

2.1.7 Hysteresis.....7

2.2 Types of magnetic materials.....8

2.3 Energy terms.....10

2.4 Hard magnetic materials.....15

2.4.1 Energy density.....16

2.4.2 Brown's Paradox.....17

2.4.3 Coercivity theory.....17

2.4.4 Nucleation Field for Perfect Crystal.....19

2.5 Finite element analysis.....20

2.5.1 Mathematical background.....20

2.5.2 Finite element method 20
2.5.3 Element types 21
2.5.4 Meshing 21
2.5.5 Boundary conditions 22
2.5.6 Solvers 22
2.6 Permanent magnet electric motors 23
2.6.1 Electromagnetism and magnetic fields 23
2.6.2 Torque and rotation 24
2.6.3 Key principles and laws 25
3. Literature Review 26
3.1 History of permanent magnets 26
3.2 Processing of Nd-Fe-B permanent magnets 27
3.2.1 Nanocrystalline materials 28
3.3 Magnetisation reversal mechanism in permanent magnets 30
3.3.1 Nucleation of domain walls 30
3.3.2 Temperature dependence 32
3.4 Approaches to improve Nd-Fe-B permanent magnets 33
3.4.1 Grain size 34
3.4.2 Grain boundary diffusion 34
3.4.3 Alternatives to Dy 39
3.4.4 Thin films 45
3.5 Permanent magnet electric motors 52
3.5.1 History of electric motors 52
3.5.2 Motor topologies 53
3.5.3 Advancements of permanent magnets for electric motors 59
3.6 Summary 66
4. Methodology 68

4.1 Simulation 68
4.1.1 1D model 68
4.1.2 3D model 70
4.1.3 Motor Simulations 71
4.1.4 Graded magnetisation 73
4.1.5 COMSOL Multiphysics equations 74
5. 1D Model 77
5.1 Introduction 77
5.1.1 Explanation of terms 77
5.1.2 Figure of Merit 77
5.2 Creating a working model 78
5.3 Uniform magnetisation film 80
5.4 Grading magnetisation film 90
5.4.1 Initial graded magnetisation 91
5.4.2 Optimisation 92
5.5 Non-zero surface magnetisation 96
5.6 Single-ended graded magnetisation 98
5.7 Summary 102
6. 3D Model 103
6.1 Introduction 103
6.2 Creating a working model 103
6.3 Comparison to 1D model 105
6.3.1 Single film cylinders 105
6.3.2 Z-axis graded magnetisation 109
6.4 Cubic 3D models 112
6.4.1 Single film 113
6.4.2 Single axis magnetisation grading 115

6.4.3 Multi-axis magnetisation grading 122
6.5 Summary 131
7. Motor simulations 133
7.1 Introduction to motor model 133
7.1.1 Motor magnets 138
7.2 Reducing magnetisation 141
7.3 Volume fraction of magnetic film 145
7.3.1 X-axis volume fraction 145
7.3.2 Y-axis volume fraction 151
7.4 Ellipsoidal core-based magnets 156
7.4.1 Bulk and semi-circle core 161
7.5 Graded magnetisation 166
7.6 Summary 172
8. Summary and Future Recommendations 173
8.1 Summary 173
8.2 Future Recommendations 175
9. References 176
10. Appendix A 192

1. Introduction

1.1 Market demand

There has been an increase of 19% in the use of rare-earth magnets (REM's) in motor/generators in Japan from 2000-2007 [1], with an increase of 260% in the world-wide output of Nd-Fe-B magnets between the years 2000-2007 [2]. In 2013 20% of all car sales were from hybrid vehicles in Japan, and 6% in the USA [3]. Nd-Fe-B magnets have various applications such as iPods, children toys, magnetic separation units, sensors, braking systems and battery-operated applications [4]. Nd-Fe-B has versatile uses due to its relative size to magnetisation (energy density) when compared to other magnets [5], which makes Nd-Fe-B ideal for small-size applications.

1.2 Current issues

The main issues with REM's, is the cost of the rare-earth elements (REE's) used to create the magnets. This stems from the fact that one country (China) dominates production of REE's producing 105,000 tonnes in 2016 which was 83% of the market, shown in Figure 1. 1[6].

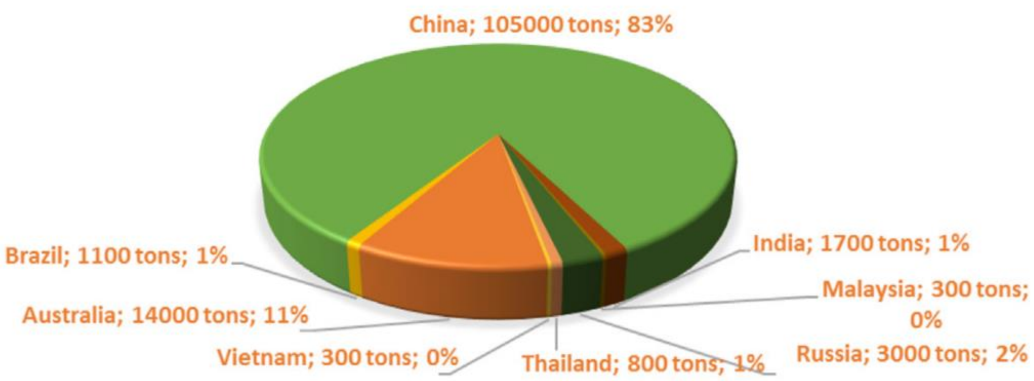

Figure 1. 1 Global mine production of REE's 2016 [6].

This monopoly in the REE market is due to the vast production by China, thanks to its relaxed or even unenforced environmental regulations [3], [7]. As China only exports 1/3 of its production quota [8] and is responsible for 1/3 of the world's natural reserves of REE's [9], the global need for these elements is at the mercy of China with regards to export quantity and price. Many countries have an import tax on REE's e.g. 25% in the USA on REE's from China [10] which only further increases the cost of manufacturing for companies and this price is eventually passed onto the cost of the final applications. Mining of REE's also comes with huge environmental impacts to the ecology of the local area, with the process of extracting the elements creating a lot of toxic and radioactive waste, as well as heavy elements such as cadmium and lead being emitted into ground water [3]. A mine in California was reported to have 600,000 gallons of wastewater leaked onto a desert floor and resulted in the mining company having to pay more than $1.4 million in fines and settlements after being sued by the San Bernardino County district in 1998 [7].

There is a world demand for a suitable replacement of REM's, but such a discovery has yet to be found. In the meantime, the focus is needed on optimising the use of REE's in magnets to reduce the environmental impact of mining and the eventual cost of the magnet, whilst maintaining or even improving on its magnetic properties. With the UK setting a target of the year 2040 for all vehicles to be "effectively zero emissions" [11], [12] the technology and advancements in the efficiency of electric vehicles must be improved to meet this target. With the increased demand for magnetic materials and only a finite supply, it is predicted that the price of the magnets will only increase (Table 1. 1) [13].

Table 1. 1 Comparison of motor magnet price and Energy density in 2016 and 2022 (estimated). Adapted from [13].

	Energy density (MGOe)		Price ($/kg)		Price/mass/Energy density $/kg/kG/kOe	
	2016	2022	2016	2022	2016	2022
Nd-Fe-B-Dy (NH42SH)	40-42	42	60	120	0.23	0.46
Sm-Co (SC-3215)	31-32	34	128	210	0.78	1.17
Al-Ni-Co-9	9	11	71	80	4.83	3.81
Ferrite (Sr-8B)	3.8	3.8	4	4	0.33	0.33

With the projected increase in price per kg of the magnets and with the already known demand set to increase, a real need for efficiency or cost reduction of the magnets without the lack of performance is needed to achieve the goals set by the world's governments.

Four of the five most common designs of electric motors utilise permanent magnets. The current situation of the electric vehicle market is largely a battle between Tesla and

Chinese car manufacturers, with greater market share of REE’s benefiting the Chinese companies. The annual production of electric cars for 2021 was 4 million globally with China producing over 2 million independently [14]. China is also on track to produce more than 8 million cars themselves by 2028 as they are heavily investing in new factories [14]. As current state of raw materials geographically and politically benefiting China, the outcome of a global electrification of transport seems unlikely to be reached for the rest of the world. A change is required to either design future electric motors, so they do not need to rely on permanent magnets, or where there is no alternative to use them only where absolutely necessary for performance.

1.3 Thesis outline

The main aims of this thesis are lined out as follows:

1. Create a working 1D model that can calculate the external and demagnetisation field of magnetic cylinders, then modelling the effect of different magnetisation magnetic films will have to these terms, to evaluate the performance of the magnet.
2. Develop a 3D model using COMSOL Multiphysics to validate the results obtained from the 1D model and then further investigate the effects, using the added benefit of extra dimensions. Transition into cubic magnets to more realistic represent the possible effects on real-world magnets.
3. Create a simulation model of an electric motor, applying the results from the previous 3D isolated magnet models into the motor to investigate what a change in magnetic architecture has the overall performance of the motor, mainly focusing on torque.

The following thesis consists of eight chapters, this current chapter being Chapter 1. Chapter 2 introduces the concepts and theories behind magnetism, magnetic materials and electric motors. Chapter 3 consists of a literature review of recent topics and papers of permanent magnets which will discuss current methods to improve certain properties of permanent magnets as well as a section reviewing electric motors and their performance. Chapter 4 will introduce the modelling methodology used within Chapters 5, 6 and 7.

Chapter 5 describes a mathematical approach to simulating magnetic fields of magnetic cylinders in 1D. This chapter will consist of establishing a standard magnet, and then changing the magnetic architecture to decrease the demagnetisation field in certain regions. Chapter 6 consists of replicating the 1D simulations in 3D, using the established COMSOL Multiphysics software, comparisons will be drawn between the results obtained in 1D and 3D to test the validity of the 1D models. Further expansion of simulations involves investigating different axis (dimensions) and finally moving onto cubic magnet models. Chapter 7 transitions from isolated magnets into a working electric motor simulation, where using knowledge obtained in chapter 5 and 6, different magnetic architectures are used to investigate their effect on motor performance. Chapter 8 will draw together the main outcomes and conclusions of the thesis and look towards the direction of potential future work.

2. Introduction

Magnetism is at the centre of many applications, even more so with the drive towards renewable energy and a more sustainable future. Within this chapter, the relevant background and principles of magnetism will be explained. Detailing how magnetism is characterised for permanent/hard magnetic materials and their use in the application of an electric motor. There will be a section discussing finite element analysis (FEA) as an important tool in simulation. The focus is on introducing relevant theories and phenomena to give context to later chapters of this work.

2.1 Magnetism

2.1.1 Magnetic flux

An important concept to consider is called magnetic flux (Φ). The term "flux" applied in this context is used to describe the field of a magnetic pole that is conveyed to a distant place. The flux is defined as the surface integral of the normal component of the magnetic field. So, the amount of flux passing through a unit area perpendicular field is equal to the field strength. Therefore, the field strength is equal to the amount of flux per unit area, and the flux is the field strength (*H*) multiplied by the area (*A*), shown in SI units below, where μ_0 is the permeability of free space (Equation 2.1)[15]:

$$\Phi = \mu_0 \boldsymbol{H} A \qquad \textit{(Equation 2. 1)}$$

2.1.2 Magnetic moment

A magnetic moment is an objects tendency to align with an externally applied magnetic field, where the moment can interact with the applied field. For context, imagine a bar magnet is at an offset angle θ to a magnetic field *H*. Using the force on each pole the torque acting on the magnet can be found using the force times the perpendicular distance from the centre of mass, shown below [15]:

$$p\boldsymbol{H}\, sin\theta\,\frac{1}{2} + p\boldsymbol{H}\sin\theta\,\frac{1}{2} = p\boldsymbol{H}l\sin\theta = m\boldsymbol{H}\sin\theta \qquad \textit{(Equation 2. 2)}$$

Where m=pl, the magnetic moment being the product of the pole strength and length of the magnet and in SI has the unit Am^2.

2.1.3 Magnetic dipole

In the relevant case, a magnetic dipole is defined as the magnetic moment (m) of a bar magnet, with the limit of a small length but has a finite moment. The energy of a magnetic moment can be defined as zero when the dipole is perpendicular to a magnetic field, the work done by turning through an angle $d\theta$ against the field is [15]:

$$d\,E = 2(p\,\boldsymbol{H}\,sin\theta)\frac{1}{2}d\theta$$

$$= m\boldsymbol{H}\,sin\theta\,d\theta \qquad \textit{(Equation 2. 3)}$$

The energy of a dipole at an angle θ to a magnetic field is:

$$E = \int_{\pi/2}^{\theta} m\,\boldsymbol{H}\,sin\theta\,d\theta$$

$$= -m\boldsymbol{H}\,cos\theta$$

$$= -m \cdot \boldsymbol{H}$$

In SI the equation is [15]:

$$E = -\mu_0 m \cdot \boldsymbol{H} \qquad \textit{(Equation 2. 4)}$$

2.1.4 Magnetic induction and magnetisation

When interacting with an externally applied magnetic field, the response of the material is called magnetic induction (B). The relationship between B and H is defined by a material property. It is the case that for some materials, and in free space, that B is a linear function of H, such as Fe, Ni, Co and their alloys, but this relationship is generally more complicated. The equation to relate B (Tesla) and H (A/m) in SI units is [15]:

$$\boldsymbol{B} = \mu_0(\boldsymbol{H} + \boldsymbol{M}) \qquad \textit{(Equation 2. 5)}$$

Where M is the magnetisation (SI units A/m) of the medium/material and depends on two factors. The individual magnetic moments of its constituent ions, atoms, or molecules, and how these dipole moments interact with each other and is defined as the magnetic moment per unit volume [15].

$$\boldsymbol{M} = \frac{m}{V} \qquad \textit{(Equation 2. 6)}$$

2.1.5 Flux density

The magnetic induction ($\boldsymbol{B}$), is the same as the density of magnetic flux (Φ) but for inside the material/medium. Within a material $\boldsymbol{B} = \phi/A$ and within free space $\boldsymbol{H} = \phi/A$. The flux density inside a material is generally different to the outside, this difference has become a way of classifying magnetic materials. Based on this difference, the material can be classed as diamagnetic, paramagnetic, antiferromagnetic, ferromagnetic and ferrimagnetic. These will be discussed in more detail later in Section 2.2.

2.1.6 Susceptibility and permeability

Other than magnetisation and induction, there are other ways to define the properties of a magnetic material. How these properties change in response to an externally applied magnetic field. The ratio of magnetisation (*M*) to its magnetic field (*H*) is called the susceptibility of the material and indicates how responsive a material is to an externally applied field [15]:

$$\chi = \frac{\boldsymbol{M}}{\boldsymbol{H}} \qquad \textit{(Equation 2. 7)}$$

The ratio of magnetic induction (*B*) and magnetic field (*H*) is called the material's permeability (μ) [15]:

$$\mu = \frac{\boldsymbol{B}}{\boldsymbol{H}} \qquad \textit{(Equation 2. 8)}$$

A material which has high concentration of flux density within its interior has a high permeability. Using the relationship in equation 2.9, the relationship between permeability (Henry/m) and susceptibility (dimensionless) in SI units is [15]:

$$\frac{\mu}{\mu_0} = 1 + \chi \qquad \textit{(Equation 2. 9)}$$

2.1.7 Hysteresis

Graphs that plot *B* or *M* against *H* are referred to as hysteresis loops, shown in Figure 2. 1.

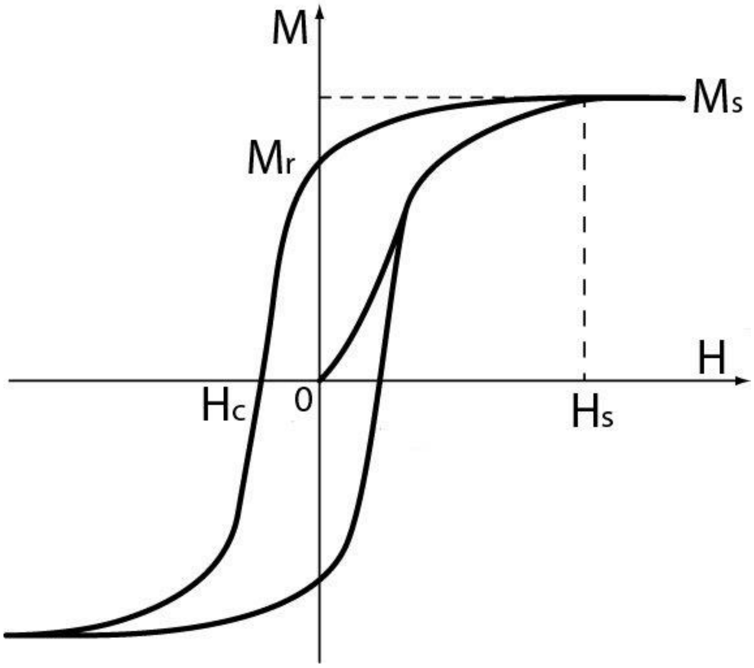

Figure 2. 1 Showing magnetic M-H hysteresis loop of a ferromagnetic material [16].

Ferro/ferrimagnetic materials retain magnetisation upon removing an externally applied field and then magnetisation will reverse the plot with an external field applied in the opposite direction to previous. For a virgin magnetic material, B or M will start of at zero when there is no external field applied, as the field H is increased as does B or M up until the point of a materials saturation B_s or M_s. The plot for B against H is square rather than curved, and B_s can be assumed when the gradient of the plot does not change. When H is reduced back to zero, the measured value of B/M is known as the remanence B_r or M_r. When the field H is introduced in the opposite direction, the point at which B or M is equal to zero is known as the coercivity (H_c) of the material. Depending on if the material is a hard or soft magnetic material, very different values for coercivity are observed and are suited to very different applications. This will be discussed further in Section 2.4. When H is increased further the negative B_s or M_s will be observed, this should represent an inversion of symmetry about the origin.

2.2 Types of magnetic materials

Magnetic materials can be classed by the ordering of their magnetic dipoles; paramagnetic, antiferromagnetic, ferromagnetic and ferrimagnetic. All these describe ways in the magnetic dipoles can align. The first to be discussed will be paramagnetic and antiferromagnetic, where they both have zero magnetisation when there is no applied field and do not retain any magnetisation when the presence of an applied field is removed. A paramagnetic alignment can be considered to have the magnetic dipoles in a random orientation and therefore zero total magnetisation. Antiferromagnetic alignment has the magnetic dipoles pointing in some sort of order (up and down) but like paramagnetic, results in a net zero magnetisation. A ferromagnetic ordering can be described as the magnetic moments having a preferred orientation of alignment, which results in a magnetisation in the absence of an applied magnetic field. When a field is applied to a ferromagnetic material, a phenomenon called hysteresis can be observed, where an applied field parallel to the magnetic moments will saturate the material, and when the field is applied in the opposite direction it is reduced to zero, then the material will retain magnetisation and continuing the applied field will fully saturate the material in the opposite direction. This full field profile is known as a hysteresis loop. Ferrimagnetic is a combination of both ferromagnetic and antiferromagnetic, where there is a preferred orientation but some of the magnetic dipoles will arrange in the opposite direction. The different orderings can be seen in Figure 2. 2:

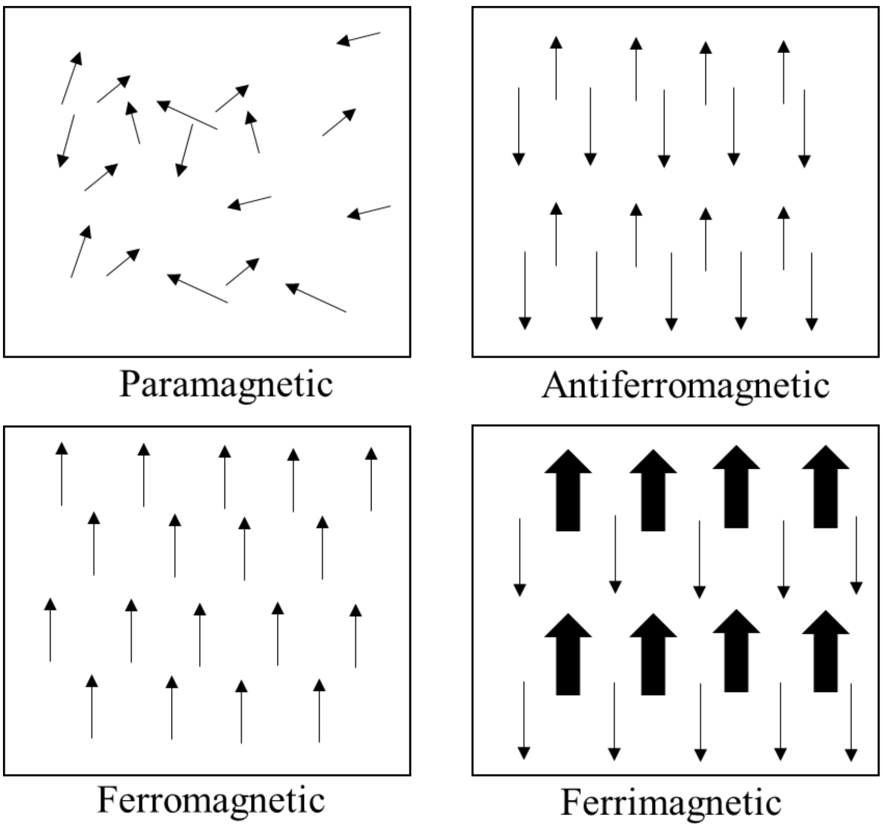

Figure 2. 2 Showing the ordering of the magnetic dipoles in magnetic materials.

2.3 Energy terms

To fully understand the properties of ferromagnetic materials it is helpful to describe it as four energy terms known **MAZE.** These are as follows:

M stands for magnetostatic energy, which describes when a ferromagnetic material is magnetised it will create its own magnetic field in the opposite direction to the material. This field represents the materials tendency to demagnetise its own magnetic field and is hence called the demagnetisation field (H_d) and has a contribution to magnetostatic energy (E_m) in equation 2.10 [15], [17], [18].

$$E_m = \frac{1}{2}\,\mu_0\,H_d\,M \qquad \textit{(Equation 2. 10)}$$

Where, H_d can be calculated for ellipsoidal shaped magnets from equation 2.11:

$$H_d = -N_d\,M \qquad \textit{(Equation 2. 11)}$$

N_d is the demagnetisation factor which can have a value between 0-1 [15], [17]. Shape anisotropy also has a contribution the magnetostatic energy which is related to the materials dimensions and shape, shown in Figure 2. 3.

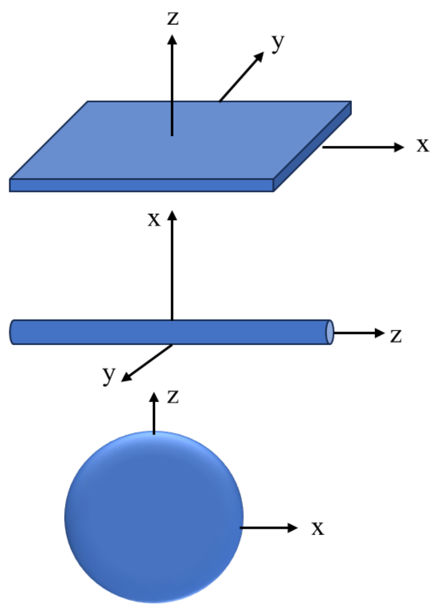

Shape	N_x	N_y	N_z
Thin disk or plate	0	0	1
Thin rod	1/2	1/2	0
Sphere	1/3	1/3	1/3

Figure 2. 3 Showing some simple shapes which have constant demagnetisation factor, adapted from [19].

This is key for understanding the origin of the demagnetisation field and where the energy is largest with respect to the different shapes of magnets. For a cubic shape, the demagnetisation field is largest at either ends of the magnet, where the poles are located. This feature is important for later literature review topics and the work discussed in chapter 5-7.

A stands for magnetocrystalline anisotropy energy, which is described as a material's tendency to be magnetised along a known crystallographic direction, also known as the 'easy axis' [15], [17]. Magnetising a material along this easy axis requires a lower magnetic field when compared to another axis. While the atomic magnetic moments arise from the spin and orbital motion the electrons the spin magnetic moments of electrons also interact with the magnetic field of their orbital motion leading to what is known as 'spin-orbit coupling'. Due to this, another energy is needed to rotate the spins of atoms. For this reason, magnetocrystalline anisotropy energy is derived from spin orbital coupling [15], [17]. The effect of spin orbital coupling is weak in most materials such as Fe or Co, and therefore have a low magnetocrystalline anisotropy energy. With larger atoms that have more electrons, they exhibit stronger spin orbital coupling which results in a larger value of magnetocrystalline anisotropy energy. The term for uniaxial magnetocrystalline anisotropy energy (E_a) can be calculated from equation 2.12:

$$E_a = K_0 + K_1 sin^2\theta_m + K_2 sin^4\theta_m + \cdots \qquad \textit{(Equation 2. 12)}$$

Where K_0, K_1 and K_2 are the anisotropy constants and θ_m is the angle between the magnetisation vector and the easy axis [15], [17].

Z stands for Zeeman energy, which arises from the interaction between the magnetic moment of a material and the applied field. This energy represents the external magnetic field contribution to the total magnetic energy of the system. Zeeman energy (E_z) can be calculated from equation 2.13:

$$E_z = -\mu_0\, M\, H\, cos\theta \qquad \textit{(Equation 2. 13)}$$

Where θ is the angle between the applied field and the sample's magnetization. There are also other energy contributions to the total energy of the system which come from magnetostrictive energy.

E stands for exchange energy (E_e), which is the result of the long-range ordering force that creates a tendency for magnetic moments to align parallel to each other, even in the absence of an applied magnetic field [15], [17]. The origin of this exchange energy found in ferromagnets is related to the electron spin moments that are explained by the Pauli Exclusion Principle and Hund's first rule [15]. The energy of exchange depends on the relative spin alignments of electrons, equation 2.14:

$$E_e = -2J_{ex}S_iS_j = -2J_{ex}S^2 cos\theta_s \quad \textit{(Equation 2. 14)}$$

Where J_{ex} is the exchange integral, S_i and S_j are the spin quantum of two electrons and θ_s is the angle between the spins [15]. The equation that defines E_e, indicates that it is energetically favourable for spins to align parallel to each other if $J_{ex}>0$, which is the case for ferromagnetic materials. On the other hand, it is energetically favourable for spins to align antiparallel if $J_{ex}<0$, which is true for antiferromagnetic materials [1]. The strength of the exchange energy in any magnetic material is expressed by a quantity known as the exchange stiffness constant (A_{ex}), which is dependent on the electronic structure of the atoms [15], [17]. Temperature can also influence the value for A_{ex}, due to an increased misalignment between magnetic moments, which leads to a reduced magnetisation [15]. The reason for this effect is due to the increased thermal energy resulting from higher temperatures which reduces the ordering of the molecular field, which disrupts the alignment between exchange magnetic moments [15], [17]. The material may have a magnetisation of zero at a certain temperature, due to the magnetic moments being randomly aligned. This is known as the Curie temperature (T_c) [15], [17], shown in Figure 2. 4.

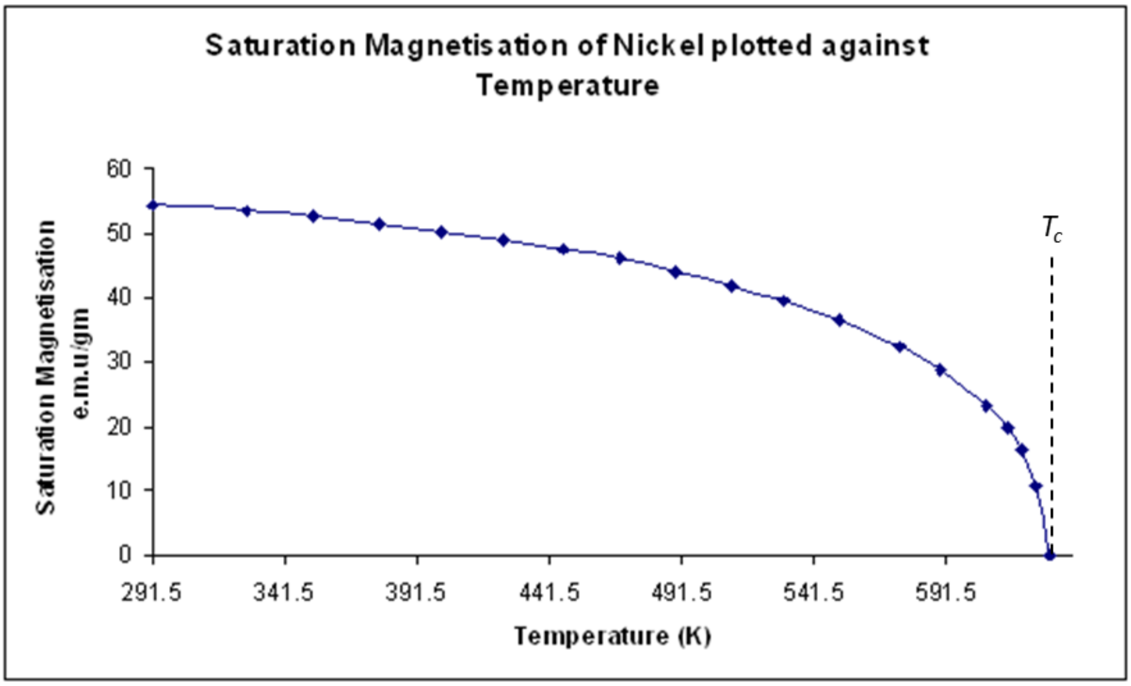

Figure 2. 4 Showing the magnetisation saturation with temperature for Nickel, adapted from [20].

The total energy of the system is known as the Gibbs free energy (E_t), which can be calculated from equation 2.15:

$$E_t = E_e + E_a + E_m + E_z \qquad \textit{(Equation 2. 15)}$$

A major problem with permanent magnets is demagnetisation which occurs by the nucleation and expansion of reverse domains. Where magnetic domains are regions within a material which has magnetic moments that are aligned in a common direction, this results in an overall magnetic polarisation. The domains are formed due to neighbouring magnetic interaction of the atoms or ions in a material. Figure 2. 5 displays the local demagnetisation field of a magnet, and shows the magnet is most susceptible to demagnetisation at the edges by the intensity of the arrows.

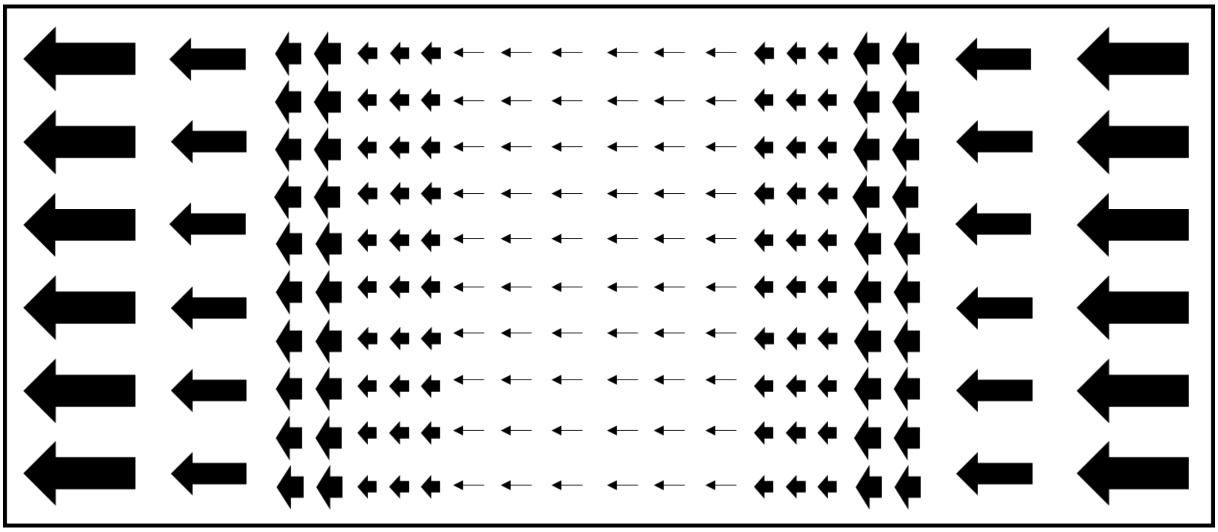

Figure 2. 5 Representation of internal demagnetisation field of a permanent magnet. Where the arrows give direction and intensity of demagnetisation field.

A reversed magnetic domain will lead to a sequence of reversal events, moving through the magnet grain by grain until the whole magnet is reversed. Potentially, adding a layer of a different magnetic material onto the surface of the bulk magnet could change the local magnetostatic energy, and combined with increased magnetocrystalline anisotropy, stabilise the surface against magnetisation reversal. Ideally a suitable material would have lower magnetisation to reduce the magnetostatic energy; this opens the prospect of also having a surface with increased magnetocrystalline anisotropy to provide an anchoring site to prevent this switching.

For hard magnetic materials with a dominant magnetocrystalline anisotropy, the typical domain wall is a Bloch wall. This is a result of the anisotropy energy attempting to collapse the wall and the exchange energy which tries to expand the wall [21]. A free-standing Bloch wall is found to have a length:

$$\delta_B = \pi \sqrt{A/K_u} \qquad \textit{(Equation 2. 16)}$$

Where A is the exchange stiffness constant and K_u is the anisotropy constant. The exchange length may vary on external factors such as geometry and applied fields, it is therefore safe to define the magnetocrystalline exchange length as equation 2.17:

$$l_{ex} = \sqrt{A/K_u} \qquad \textit{(Equation 2. 17)}$$

Using values for A ($1.25\text{x}10^{-11}$ J/m) and K_u ($4.5\text{x}10^6$ J/m^3) [22] the l_{ex} was calculated to be 1.66 nm for $Nd_2Fe_{14}B_2$. A short exchange length between grains ensures a strong exchange interaction between neighbouring magnetic moments within these grains, this leads to enhanced magnetic behaviour such as higher saturation magnetisation and improved coercivity. These short exchange lengths also mean that there is a more uniform magnetisation distribution within the grains and therefore demagnetisation can be minimised.

2.4 Hard magnetic materials

Ferromagnetic materials can be classed as being either soft or hard magnetically and are usually defined by their coercive field. Where soft magnetic materials such as Fe are known for a high magnetic moment but a low coercivity, meaning that they deliver a strong external field, but magnetisation reversal will happen under a weaker applied field. Hard magnetic materials such as Nd-Fe-B or Sm-Co are known for their strong coercivity, which makes them an important material within the electric motors and drives sector. The difference in soft and hard magnetic materials is best observed through their hysteresis loops, where a soft magnetic material will have a small and narrow coercive force, meaning that the field required to cause the magnetisation to reverse will be weak, unlike that of the wide coercive force of a hard magnetic material. The area of the curve can also be described as how much energy is stored within the material, shown in Figure 2. 6.

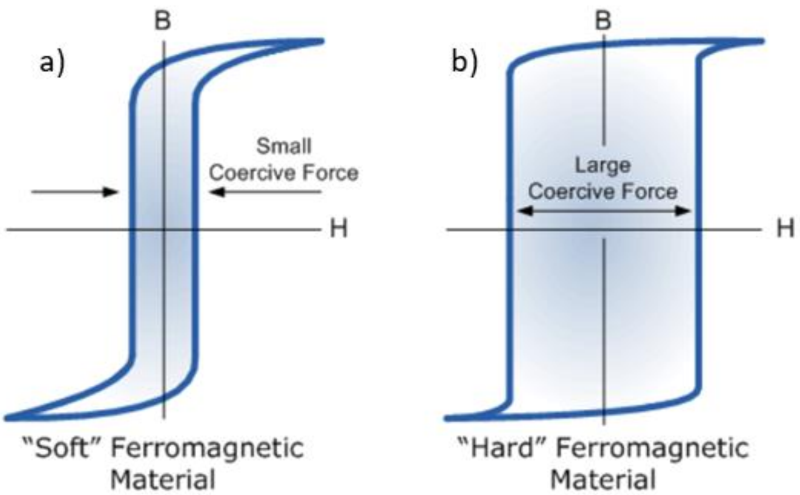

Figure 2. 6 Showing a general example of the hysteresis loops for a) soft and b) hard ferromagnetic materials [23].

2.4.1 Energy density

One of the main properties that engineers look at when using magnetic materials is its energy density, or energy product (BH_{max}). This term having a "density" refers to the maximum energy that the magnetic material can hold before a full magnetic reversal occurs. In theory, BH_{max} is interpreted from the ideal square loop of the second quadrant of a *B-H* hysteresis loop, shown in Figure 2. 7. For a perfectly optimised magnet, BH_{max} can be calculated through:

$$BH_{max} = \mu_0 M_s^2 / 4 \qquad \textit{(Equation 2. 18)}$$

As there are a range of commercially available hard magnetic materials, each with its own range of BH_{max} values achievable. Examples of popular high energy density magnets are the Nd-Fe-B and Sm-Co derivatives, where they are sought after for motor, generator and high-performance machines. Weaker BH_{max} hard magnets are available and regularly used such as the ferrites, steels and Al-Ni-Co. Equation 2.18 can be found by the second quadrant of the hysteresis loop in Figure 2.7, where the BH_{max} is a quarter of the total area of the square in the quadrant.

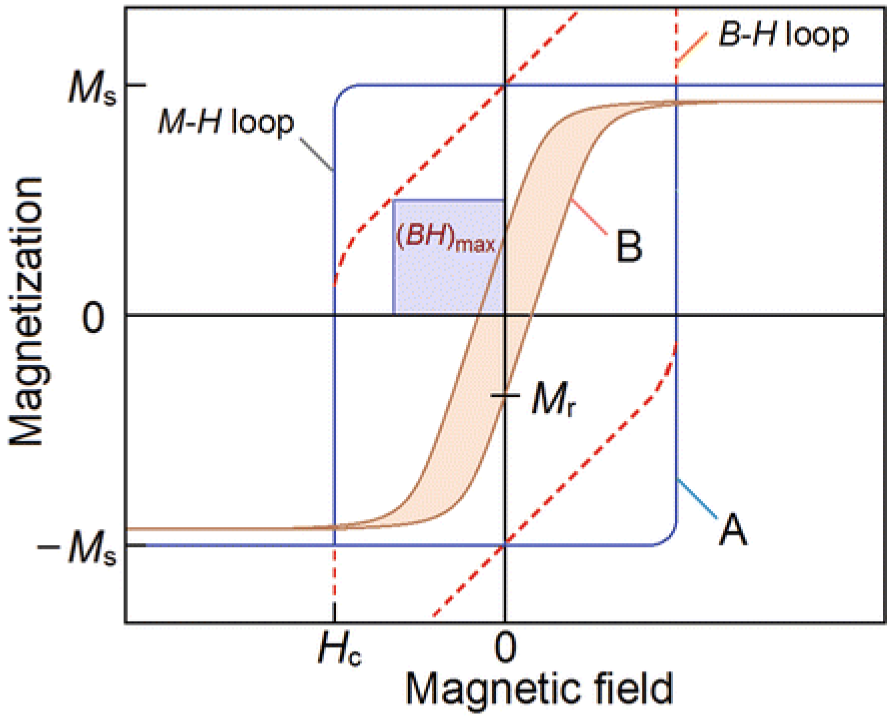

Figure 2. 7 Showing a M-H and B-H hysteresis loop with the BH_{max} region in the second quadrant identified [24].

2.4.2 Brown's Paradox

The Stoner-Wolfharth model first introduced the model of coherent rotation of magnetisation in ferromagnetic materials [15], [25], [26]. It describes a mechanism of magnetisation rotation for a single domain particle to the opposite direction. In this model, the field which is required to rotate the magnetisation of a single domain particle coherently into a demagnetised state is referred to as the anisotropy field (H_A), calculated from:

$$H_A = {}^{2K_1}/_{M_s} \qquad \textit{(Equation 2. 19)}$$

Where, K_1 is the magnetocrystalline anisotropy constant. According to this model, the coercivity of hard ferromagnetic materials should be equal to the anisotropy field, H_c=H_A. However, experimentally the coercivity of Nd-Fe-B magnets is only 20-30% of their anisotropy field values. This difference of experimental and theoretical coercivity values is known as 'Brown's paradox' and is attributed to the effect of microstructural features of the magnet's microstructure. Brown's paradox represents a need to increase understanding of the link between a magnet's microstructure and the magnetic performance, to reduce the discrepancy and potentially improve the coercivity of real-world hard magnets.

2.4.3 Coercivity theory

Coercivity has a technical definition (the reverse magnetic field required to bring a material's magnetisation to zero) but can also be regarded as a measure of a magnetic material's resistance to changes in its magnetisation. A good permanent magnet should have a high coercivity (typically 800 – 2000 kA/m) so that it can remain stable to an externally applied magnetic fields to prevent magnetisation reversal, as well as high remanence to deliver a strong magnetic field [15], [17]. However, the mechanism of coercivity is still a topic of research with varying equations from different models [27]. The Stoner-Wohlfarth (SW) [26] model is the model most often used. The SW model assumes coherent rotation of magnetic moments of the single-domain grains with respect to their easy axis and gives the equation for coercivity for a bulk material with an easy-axis parallel to the externally applied field direction as:

$$H_c = H_A \qquad \textit{(Equation 2. 20)}$$

From equation 2.20, H_A is defined as the anisotropy field which is the theoretical field that would be able to align the magnetisation perpendicular to the c-axis. The model assumes that the corresponding remanence, M_r, is equal to M_s in equation 2.19. Using this assumption, the remanence given by the SW model is still within an acceptable range to that of the experimental values [28]–[31]. However, the experimental and theoretical values for coercivity can vary, with models typically overestimating coercivity by about 20-40% [27]. This large discrepancy is assumed to be due to crystal defects and inter-grain interactions that are not included in the SW model. Despite this flaw in the model, the SW model is still used within magnetism modelling thanks to its simple and clear coercivity mechanism, as well as having a link from coercivity to anisotropy field.

Other models include additional phenomena, an example is the inclusion of domain wall motion [28], [29], [32], proposed by Kersten and Néel in the 1940's [27]. In this model, the coercivity is due to the hinderance of domain wall motion by stress or impurities. This model gives smaller coercivity values than that of the SW model, and it has been agreed that the mechanism of coercivity for multi-domain grains occurs through wall motion compared to rotation for a single-domain [27]. This presents problems of its own, for example, domain walls exist in magnets composed of multi-domain grains in a demagnetised state, but when a large enough external field is applied it means no domain walls exist in the saturation state, and the grains are composed of single domains. If the demagnetisation field is now applied, the domain wall must first be nucleated before it moves. Before nucleation, a demagnetising process with a material that consists of multi-domain grains in the demagnetised state should be the same as single-domain grains. Therefore, the dominant mechanism is the nucleation for domain walls in some materials rather than the pinning mechanism. On the other hand, domain wall motion and pinning are part of the main mechanism for initial magnetisation curves where nucleation is not necessary. It can therefore be assumed that the reversal mechanisms for magnetisation and demagnetisation to be different [27]. Nucleation was first considered by Brown [32] and Frei *et al.* in the 1940's [33] and then later by Aharoni *et al.* [29] in the 1960's, and suggested that nucleation originates at crystal defects as well as surface edges and corners of a material.

Another approach to describe the formation of domain walls within the demagnetisation process is the nucleus expansion model proposed by Givord *et al.* [30] in the 1980s. This model represents the first nucleus formed by a reversed magnetisation, as expansion occurs towards the critical volume of the nucleus and domain wall rotation occurs when: $H_a^{nucleus} \ll H_a$ [30]. Both models have been applied successufully under certain conditons, even though each have different philosophies. The nucleation model used as a micromagnetic approach can show the reversal mechanisms, but cannot be used as a global approach.

Various other mechanisms have been debated recently, with both the nucleation and pinning models having experimental support but ultimately have failed to explain some experimental phenomena [27]. Within the community, a compromise has been reached that there are actually two types of permanent magnets, defined by their coercivity mechanisms: nucleation and pinning types [28], [29], [34]. For example, it is believed that the mechanism of Sm_2Co_{17} is mainly pinning whilst the Nd-Fe-B material is nucleation dominant [27].

In recent decades, technology and computing power has vastly increased, which allows for complex and detailed micromagnetic simulation to investigate coercivity mechanisms. With simulations improving and developing rapidly, the fabrication methods have had to keep up in order to replicate the conditions that are used within the simulations. Improved fabrication methods are allowing for the creation of nanostructured permanent magnets with greater control of microstructures and grain sizes so that the experiments can be closer compared to the simulation results and reveal the underlying coercivity mechanism [27].

2.4.4 Nucleation Field for Perfect Crystal

Within the SW model there are the assumptions that the magnetic behaviour of a grain that responds to an external applied field is a coherent rotation and only two energy terms are considered. However, this assumption is not always correct. Brown [32] later considered a more rigorous approach, known as the micromagnetic method. He considered a ferromagnetic material with a body of any shape, where the magnetisation is any function of the space and the total energy of the particular (*m(r)*) is made up of the anisotropy energy, Zeeman energy, exchange energy and magnetostatic energy. Brown considered there was a small variation of the magnetisation vector *m(r)* and its value to be *m(0)*. This state physically corresponds to the saturation state and if a variation of this state occurs, this implies that at some point in the process the state of saturation along the original direction of the applied field no longer becomes stable. Some change will take place to cause the sample to be saturated in the other direction. This field at which the original saturation becomes unstable, and any change in the configuration of the magnetisation can start is called the nucleation field [27]. There is a later definition of the nucleation field: where the field at which the dominant magnetic reversal occurs or at which the nucleus completes its expansion [27].

Based on this new method, Brown arrived at a micromagnetic equation for the nucleation field, which describes the applied field at which coherent rotation can occur in a material is decreased to:

$$H = -\frac{2K}{\mu_0 M_s} + N_s M_s \qquad \textit{(Equation 2. 21)}$$

The first term originates from the crystalline anisotropy and the second term corresponds to the shape anisotropy. $N_a = N_\perp - N_\parallel$, where $N_\perp$and $N_\parallel$ are the demagnetisation factors for the easy axis. For spherical grains the shape anisotropy equals zero ($N_\perp = N_\parallel$), and the equation reduces to the SW model. Therefore, the SW model can be regarded as one way the nucleation process occurs (uniform rotation) [27].

2.5 Finite element analysis

Finite element analysis (FEA) is a key tool in research and development, there is a cost and time saving benefit but it also allows us to link the magnetic materials microstructure to its performance. The numerical method of FEA involves the use of smaller mathematical models to simulate behaviour of a larger complex system. This sub-chapter will give an overview of FEA as a method of simulation.

2.5.1 Mathematical background

FEA is based on mathematical principles such as calculus, linear algebra, numerical methods, continuum mechanics and materials science. This sub-section will give brief overview of these principles and how they are used within FEA simulations [35].

First a representation of the system is required. This is typically drawn in CAD as a series of lines, surfaces and volumes, where each can be assigned its own material property. This is then broken down in elements through a process called discretisation. This divides the problem of a continuous domain into a finite number of discrete elements or subdomains. The process involves approximating the solution of the governing differential equations of the main problem within each element, and then a solution for the entire problem is obtained by assembling the solutions for each element into a global system of equations [36].

2.5.2 Finite element method

Finite element method (FEM) is a numerical method of solving partial differential equations by discretising the problem, and then the equations are assembled into a global system of equations that can be solved using matrix methods. Once the problem is discretised, the governing equations for each element are derived by applying the principle of “virtual work”. Virtual work states that the work done by internal and external forces on a system must be equal. The element equations typically involve interpolation functions that approximate the governing equations applied within the element. The equations for each element are then assembled into a global system of equations which represent the entire problem domain. This involves defining the degrees of freedom for each node, and the relationship between them. The solution of the system or problem is then obtained using numerical methods which terminate as direct or iterative solvers. The solution provides values of the nodal degrees of freedom which can be used to obtain the solution for the entire problem domain. The solution can then be developed in post processing to visually represent information using, plots, graphs and animation with the use of colour [37].

2.5.3 Element types

The choice of element types is dependent on the geometry and material properties observed within the problem, as well as the desired level of accuracy. Common types of elements are Beam, Shell, Plate and Hexahedral. Relevant elements are discussed below [38]:

- Solid elements are used to model objects in three dimensions. This means that they can resist forces in three planes and allows for solutions and post processing to in depth and varied. A common use for this element is machine parts.
- Tetrahedral elements are used to model complex geometries using various sizes of tetrahedral to give more refinement to certain areas. This element type can resist forces in three dimensions.

2.5.4 Meshing

Meshing is the process of dividing the problem domain into a finite number of smaller elements. The quality of the mesh can have an impact on the accuracy and reliability of the simulation results. There are different types of meshing techniques which each have advantages and disadvantages, they are selected by the specific problem being analysed. They are discussed below [39]:

- Structured meshing divides the problem domain into a grid of regularly spaced uniform elements. This is useful as it relatively simples and provides efficiency for computation but is not appropriate for complex geometries or irregular domains.

- Unstructured meshing divides the problems into a collection of irregular shaped elements. This provides more flexibility compared to structures meshing but comes with the cost of requiring more computational effort to generate.
- Adaptive meshing involves refining the mesh in regions where the solution varies rapidly, which coarsening the mesh in regions where the solution varies gradually. This technique can improve the accuracy and efficiency by reducing the number of elements required to represent the problem domain. However, it requires more computational resources to implement and more complex to generate.

2.5.5 Boundary conditions

Boundary conditions are constraints which are imposed on a system to simulate its behaviour. In FEA, boundary conditions are used to ensure that the problem is set up well to obtain meaningful results. Different types of boundary conditions are as follows [40], [41]:

- Dirichlet boundary conditions, also known as essential boundary conditions, specify the values of a solution at certain points or surfaces. An example would be in an applied current to the stator coils of a motor.
- Neumann boundary conditions, also known as natural boundary conditions, specify the values of the normal derivative of the solution variables at certain points or surfaces in the problem domain. An example is magnetic insulation, where beyond the insulation boundary a magnetic value of zero will be specified.
- Mixed boundary conditions are a combination of Dirichlet and Neumann. An example can be given for fluid flow analysis, where a mixed boundary condition can be used to specify velocity at a certain point or surface.
- Symmetry boundary conditions are used to simulate a symmetrical problem domain, where any symmetrical object can be divided amongst a plane to study displacement, where a segment of a motor can be simulated, and antisymmetric boundary conditions can be assigned to complete an entire motor.
- Periodic boundary conditions are used to simulate a system with repeating patterns. For example, a motor with alternating segments of magnetisation direction can be made up of two sections, which is repeated five times to complete the motor.

2.5.6 Solvers

FEA consists of a system of governing equations that describe the behaviour of a physical system and is usually very large and complex. This could be as simple as $V = IR$ for Ohm's law to the more complicated solution of Maxwell's equations. To obtain solutions to the equations, numerical methods such as solvers are employed. Solvers can be described as algorithms that solve the system by performing matrix operations on the equations. The two main types of solvers used in FEA are direct and iterative [42].

Direct solvers are algorithms that solve the system of equations by performing a finite number of steps that can be set beforehand. This method works well for small to medium-sized problems but can become computationally expensive for large problems.

On the other hand, iterative solvers solve the equations through an iterative process in the aim of a convergence towards a solution. These methods are generally more efficient than direct solvers for large or more complex problems as they can solve the problem in smaller pieces at a time.

2.6 Permanent magnet electric motors

Electric motors are a crucial piece of technology, they play a major role in many modern-day applications, with a specific focus on renewable energy such as electric cars, wind-turbines etc. This sub-chapter will discuss the theory of how an electric motor works, stating the principles of magnetism and torque, which are applied and derived in an electric motor. This will give context to later work, where examples of electric motors will be discussed in the literature review and chapter 7.

2.6.1 Electromagnetism and magnetic fields

Electromagnetism is a fundamental concept in the understanding of how an electric motor works. It refers to the relationship between electrical currents and magnetic fields and works when an electric current is passed through a conductor to generate a magnetic field around the conductor. The strength and direction of the magnetic field is dependent on the current amps and the direction the current is applied [43], [44].

The strength of a magnetic field can be defined by its magnetic flux density, typically measured in units of Tesla (T) or Gauss (G). The relationship between magnetic field strength and the electric current is given by Ampere's law, which describes a magnetic field at a point in space is proportional to the electric current flowing through the conductor, expressed by:

$$\int B \cdot dl = \mu_0 I \qquad \textit{(Equation 2. 22)}$$

Where B is the magnetic flux density, I_c is the electrical current and μ_0 is the permeability of free space. The integral on the left of the equation represents the line integral of the magnetic flux density around a closed loop, shown in Figure 2. 8.

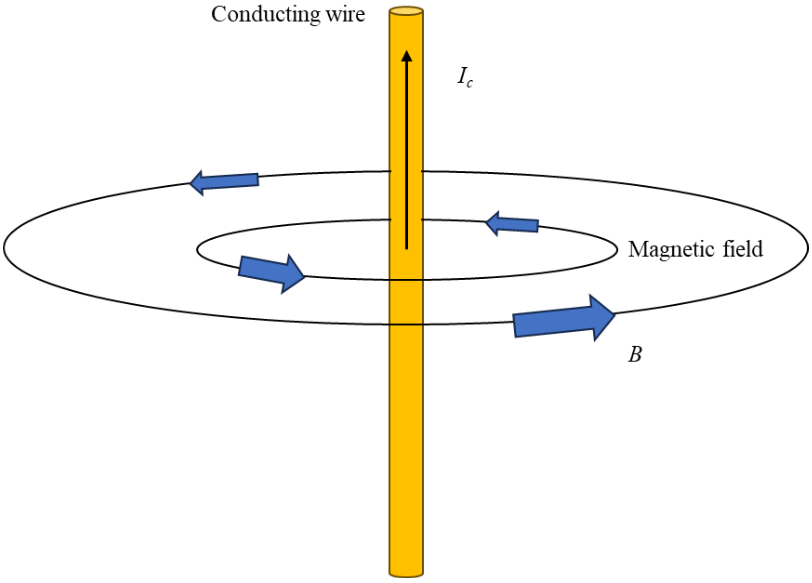

Figure 2. 8 Showing the direction of current in the conducting wire and the direction of the magnetic field produced by the wire.

An important interaction to consider is the effective force magnetic fields can have on each other, in terms of how they attract and repel each other depending on their magnetic field strength. This depends on the orientation of the magnetic fields, and with this interaction of attraction and repulsion, magnetically induced rotation can occur [43], [44].

2.6.2 Torque and rotation

Torque is an essential concept in the understanding of how an electric motor operates and how performance is measured. Torque measurement of the rotation force applied to an object, notated by the symbol τ and measured in Newton-meters (N*m). In the context of a motor, torque is the force that causes the rotor portion of the motor to rotate [45], [46].

The magnitude of torque of the magnet depends on a few factors, such as strength of the magnetic field, the amount of current flowing through the motor and physical architecture of the motor (stator/rotor). A relationship between torque and rotation can be described with the equation:

$$\tau = I_o \alpha \qquad \textit{(Equation 2. 23)}$$

Where the torque is equal to the moment of inertia of the rotating object (I_o) interacting with the angular acceleration of the object (α). In an electric motor, the moment of inertia is proportional to the radius of rotation and the mass of the rotor. The angular acceleration is the rate of change for the angular velocity of the motor [45], [46].

The practical application of a motor works by the torque being generated through the interaction of the magnetic field and the electric current flowing through the motor. In the motor example to be discussed later, the magnetic field is present from the permanent magnets in the rotor and the electric field flowing through the coils in the stator generates an attractive/repulsive magnetic field.

2.6.3 Key principles and laws

There are key principles and laws that govern the operation of electric motors. These include Faraday's law of electromagnetic induction, Lenz's law and the conservation of energy.

Faraday's law of electromagnetic induction states that a changing magnetic field induces an electric current in a nearby conductor, and can be expressed as [47]:

$$\varepsilon = -d\phi/dt \qquad \textit{(Equation 2. 24)}$$

Where the electromotive force induced in the conductor (ε) is proportionate to the magnetic flux (ϕ) over time and the negative sign indicates that the induced currents flow in a direction that opposes the change in the magnetic field.

Lenz's law is a consequence of Faraday's law and states that the direction of the induced current is in such that it opposes the change in the magnetic field that produced it. Lenz's law manifests due to the conversation of energy principle which states that energy cannot be created or destroyed, but only transform from one form to another. This principle is what results in the operation of a motor, where the motor converts electrical energy into mechanical energy through the interaction of magnetic fields produced by the magnets and input electrical current. The system conserves energy with this conversion and some energy is lost through heat dissipation of the system. Understanding these laws and principles are essential when it comes to design and optimisation of electric motors to minimise inefficiencies and losses of energy [47]. How an electric motor works will be discussed later in Section 3.5.

3. Literature Review

3.1 History of permanent magnets

Magnets have been used and developed over decades for their highly sort after properties. The use of magnets started in the 1910's with Kichizaemon Sumitomo (KS) steel, which then progressed onto Mishima Kizumi Magnetic (MKM) steel [1]. These steels showed very poor energy density, therefore were not suited to the applications they were used for. However, the discovery of the critical-earth magnet (CEM) Al-Ni-Co in the 1940's changed this [1]. Al-Ni-Co had an unrivalled energy density when compared to other CEM/REM's available at the time. This resulted in an interest into these sorts of magnets for different purposes and applications. The magnets were investigated and developed further for practical applications where a high energy density would be desirable, leading to the discovery of Sm-Co magnets. $SmCo_5$ was developed in the 1960's, with nearly four times the energy density of Al-Ni-Co, this compound became the first rare-earth high-performance magnet [48], [49]. Over the next few decades $SmCo_5$ continued to be developed and dominate the market for uses of magnets in commercial applications until the discovery of $Nd_2Fe_{14}B$ in the 1980's. By the 1990's the energy density of $Nd_2Fe_{14}B$ had nearly doubled that of the highest reported $SmCo_5$, hence replacing it as the main product on the market for magnetic purposes [2]. Now with an increased energy density, the more suited the magnets became towards high performance generators and small-scale functions. Explained by the increased use of these magnets in motor/generator applications [1].

The properties of Nd-Fe-B permanent magnets come from the combination of the 4f (Nd) and 3d (Fe) sublattice, where the 4f provides high magnetic anisotropy and the 3d gives high Curie temperature and magnetisation to the magnetic material [50]. High anisotropy implies most of the magnetic spins are preferred to be orientated in the same direction, when the spins are pointing in the same direction this gives a ferromagnetic arrangement. This high anisotropy results in a high anisotropic field; which is the field that would be required to align the magnetic spins perpendicular to the easy axis [51]. Nd-Fe-B magnets are widely used for their specific properties such as a high coercivity, remanence and energy density, based on the application, (equation 2.5).

Energy density of the magnet is a result of the area created by coercivity and remanence on a hysteresis loop [52], [53], as discussed in Figure 2. 7. Table 3. 1 shows expected values for magnetic properties.

Table 3. 1 Showing values for key magnetic properties of sintered Nd-Fe-B magnets. Adapted from [54].

Energy density (BH_{max})		Coercivity (H_c)		Remanence (B_r)		Curie temperature (T_c)	
MGOe	kJ/m^3	kOe	kA/m	kGs	mT	^{o}C	K
34.0	270.6	36.3	2888.6	11.7	1170	342	615

These three factors that determine the strength of the magnet can be changed by inducing changes to the microstructure with manufacture technique or the ratio of elements used. The microstructure of Nd-Fe-B magnets consists of a bulk grain of $Nd_2Fe_{14}B$ surrounded by an Nd-rich grain boundary surrounding each grain and Nd/Nd-oxide filling the space in-between grains [55]–[57]. Investigations into the microstructure found a correlation between the grain size and coercivity, where small changes in the microstructure, created by the sintering process, can have a drastic reduction on coercivity [55].

3.2 Processing of Nd-Fe-B permanent magnets

Nd-Fe-B magnets are processed in various ways with each way resulting in different physical and magnetic properties such as anisotropy, grain size, energy density and coercivity [55], [58], [59]. Sintered Nd-Fe-B magnets made up 80% of the manufactured magnets in 2007, due to the larger energy density of sintered magnets, and having higher anisotropy when compared to melt-spun magnets. The main route of production for sintered Nd-Fe-B magnets are found to be step-wise as follows [58]: powder production, compaction of powder into a mould, sintering of the powder to form a bulk at ~1100°C, machining into the desired shape, adding a coating to prevent oxidation and then finally magnetisation of the finished bulk magnet, shown below (Figure 3. 1).

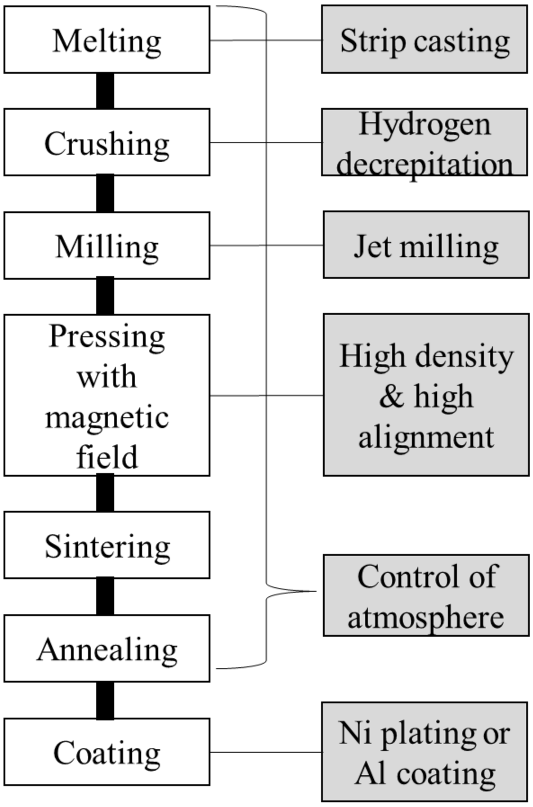

Figure 3. 1 Basic manufacturing process of sintered Nd-Fe-B magnets. Adapted from [1].

The process has been optimised over the recent years by controlling the oxygen content in the sintering process to prevent the formation of oxides within the magnet microstructure witch eventually result in irreversible degradation of the magnet [50].

3.2.1 Nanocrystalline materials

Nanocrystalline materials (NCM's) are single or multiphase crystals that have distinct characteristics and typically have grain sizes ranging a few (1-10) nm. They have a high density of defect cores, where 50% or more of the atoms are situated around these cores [60]–[63]. These materials are of interests for a few reasons 1) they have an atomic structure that differs from the two known solid-state structures; crystalline state (long range order) and glassy state (short range order), with the atoms situated in a grain or interphase boundary with a random atomic arrangement. 2) NCM's properties differ when compared to crystalline/glassy state with the same composition. 3) NCM's seem to allow for the alloying of components which are immiscible in the solid or molten state [61]. NCM's contain two different atoms; crystal and boundary, these two atoms form different components which are characterised by their nearest-neighbour configuration. The crystal atoms form the crystalline component, a froth like component is formed by the boundary atoms [61]. An example of

NCM's research is materials that have targeted defects, for example, in the grain boundaries where different structured nanocrystalline materials can be generated. However, as they differ in structure, they all have a common microstructural feature, which is a large volume fraction of defect cores surrounded by strained crystal lattice regions [60]. Another type of NCM can be magnetic, these magnetic NCM's can also have different features based on their properties (hard, soft and exchange spring etc.).

A recent study by Li *et al*. [64] researched new bulk $SmCo_3$ nanocrystalline magnets and their magnetic anisotropy, in which they addressed the challenge of fabricating nanocrystalline materials with grain sizes between 10-20 nm and a strong crystallographic texture [65]–[67]. Using amorphous precursors and a high-pressure thermal compressor, they fabricated anisotropic bulk nanocrystalline $SmCo_3$ with a strong (001) texture and the desired grain size of 10-20 nm. These magnets had a magnetic anisotropy $Mr_{//}/Mr_{\perp} = 1.53$ and $BH_{max} = 33.8$ kJ/m^3, which compared to the isotropic magnets fabricated with the same precursors having magnetic anisotropy $Mr_{//}/Mr_{\perp} = 1.01$ and $BH_{max} = 15.1$ kJ/m^3 [64]. Figure 3. 2 shows the temperature performance $SmCo_3$:

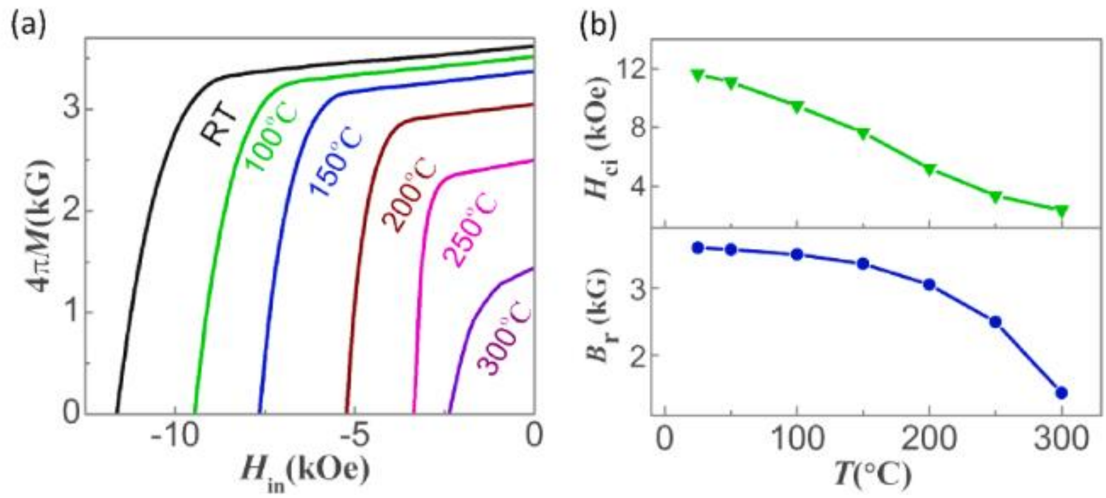

Figure 3. 2 Characterization of high temperature magnetic properties of the fabricated $SmCo_3$ magnet. (a) The demagnetization curves at 25–300 °C. (b) Dependence of coercivity H_{ci} and remanence B_r, on the measurement temperatures [64].

The authors explained the small grain sizes are arising from the high-pressure thermal compression and suggested that the small strain-energy anisotropy was the reason for the (001) texture formation [64]. They concluded that these results show $SmCo_3$ materials to have potential for high temperature applications. However, the temperature for the BH_{max}

measurement of 33.8 kJ/m^3 was not stated. If this is assumed to be at 298K, then a comparison with reported BH_{max} values for commercially available Sm_2Co_{17} (254.6 kJ/m^3) and $SmCo_5$ (159.1 kJ/m^3) [13], suggests that the potential for the nanocrystalline $SmCo_3$ magnets to be a replacement seems ambitious. Li *et al*. did not report the BH_{max} values above room temperature. They did however state that after annealing between 700-850°C it led to an increased remanence, decreased coercivity and overall increased BH_{max}. This was the result of the average grain size increasing from ~12.3 to 52.4 nm, but they did not report the increased BH_{max} values [64]. Bulk $SmCo_3$ permanent magnets have been reported before, but only stated a coercivity of 2626 kA/m (33 kOe) has been given [68]. The method of reducing the grain size (without showing thermal instability) shows real promise and addresses a real issue, but the lack of like-for-like comparison between the new anisotropic bulk $SmCo_3$ magnets and magnets already in use and the values reported suggests that $SmCo_3$ might not be a suitable replacement.

3.3 Magnetisation reversal mechanism in permanent magnets

The demagnetisation mechanism is an important factor to consider when using permanent magnets to fully understand the difference in between theoretical and experimental values of magnetic properties (Brown’s paradox, Section 2.4.2) [69], [70]. The following subsection will discuss the mechanism of magnetisation reversal and its importance for performance of REM’s.

3.3.1 Nucleation of domain walls

Nucleation first occurs at weak spots that are most susceptible such as the corners/edges where the demagnetisation field is highest (Figure 3. 3) [71], [72].

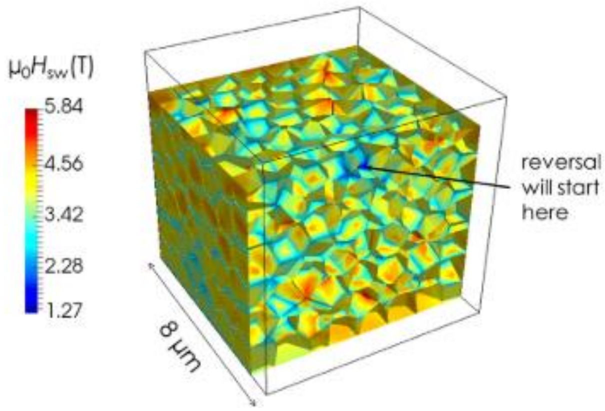

Figure 3. 3 Map of the local switching field for a large grained $Nd_2Fe_{14}B$ magnet for h =0. The colour map gives the local switching field computed by the embedded Stoner-Wohlfarth model. Magnetisation reversal will start where the local switching field has its lowest value [71].

When nucleation occurs, the grain becomes demagnetised, which then affects the next grain and so on. Without any features to prevent the spread of this effect the entire magnet could be compromised. Figure 3. 4 shows the effect of nucleation from a surface grain at the edge of an Nd-Fe-B magnet.

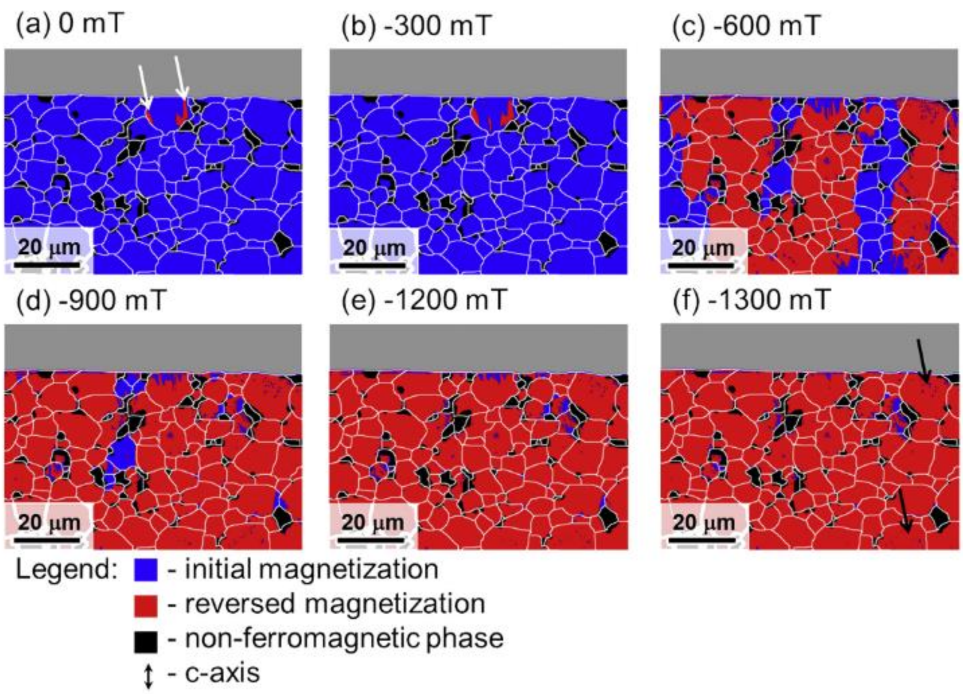

Figure 3. 4 Showing domain nucleation and propagation in the demagnetisation process for the edge of Nd-Fe-B magnet under the presence of a reverse applied field a) 0 mT b) -300 mT c) -600 mT d) -900 mT e) -1200 mT f) -1300 mT [72].

Work has been done to address the issue of demagnetisation within the magnet and will be discussed in Section 3.4. But in the literature discussed there was not an investigation into preventing nucleation at the edges of magnets.

3.3.2 Temperature dependence

Magnetisation of a material is dependent upon temperature [73]–[75]. When temperature is increased, the values for coercivity and remanence decrease due to the loss of magnetisation at the Curie temperature of the material. This is a problem for magnets that are used in applications that operate in high temperature environments, such as some motors or generators, which can have an operating temperature between 160-200℃ [52]. At these temperatures, Nd-Fe-B magnets experience a decreased BH_{max} from 358 to 88 kJ/m^3 for 300K and 475K respectfully [13]. This trend is commonly observed for permanent magnets investigated e.g. (Al-Ni-Co, $Nd_2Fe_{14}B$, $SmCo_5$, Sm_2Co_{17}) but as they are different materials, they all have different T_c. Research by Cui *et al*. [13] also confirmed that the grain boundary diffusion of Dy into Nd-Fe-B increased BH_{max} to 159 kJ/m^3 at 475K, which makes a Dy diffused magnet more suitable to use in motors compares to non Dy diffused magnets as first suggested by Li *et al*. [13]. Cui *et al*. also found that the highest BH_{max} at 475K belonged to Sm_2Co_{17} (219 kJ/m^3). These magnets outperform other materials and are more suited to high temperature applications such as locamotive traction motors and heavy industrual generators. They retain their BH_{max} (263 kJ/m^3 at 300K) better at operating temperature when compared to the Nd-Fe-B. However, the high price of raw elements Sm (11.14 £/kg) and Co (46.19 £/kg) compared to Fe (0.06 £/kg), Nd (48.04 £/kg) and B (1,910 £/kg) means that Sm-Co is far more expensive that Nd-Fe-B, considering B is used in such small quantities [76]. A 10 pack of 10x10x5 mm cubes of Nd-Fe-B retails for £10.81, where Sm-Co retails for £14.21 [77]. A cheaper option of magnetic materials would be the ferrites, such as $SrFe_{12}O_{19}$ which has much cheaper elements O (0.5 £/kg) and Sr (4.19 £/kg) but they have much lower BH_{max} with 31 kJ/m^3 at 300K. Ferrites are a cheap alternative and are more suited to large scale production such as cheap products like fridge magnets etc. [13]. These results suggest there is a choice to be made for which magnet to be used in different applications, if the temperature remains close to 300K then Nd-Fe-B magnets are likely to be most suitable due to their high BH_{max}, but if the temperature exceeds 400K then the Sm_2Co_{17} magnet becomes be more suitable despite the increased price.

Magnets at non-zero temperatures also have a finite probability of undergoing thermally-excited magnetisation reversal. The mean time between switching events is given by the Arrhenius-Néel equation:

$$\frac{1}{\tau} = f_0\, exp\left(-\frac{K_u V}{k_B T}\right) \qquad \textit{(Equation 3. 1)}$$

where τ is the average waiting time for switching, f_0 is the attempt frequency, k_B is Boltzmann's constant, K_u is magnetocrystalline anisotropy and V is the 'activation volume' of a reversed magnetic domain. In practice, K_u can be temperature-dependent and applied reverse magnetic field further reduce the waiting time for reversal. Equation 3.1 emphasises the need for materials with a high value of K_u in order to maintain their magnetisation.

3.4 Approaches to improve Nd-Fe-B permanent magnets

The most common approach to improve performance of Nd-Fe-B magnets involves the addition of Dy, by adding it into the pre-sintered magnet at the expense of remanence to have an increased coercivity due to Dy coupling antiferromagnetically within the grains (Figure 3. 5) [78]. The addition of Dy in this case, resulted in an increased Curie temperature and therefore an increased temperature performance having double the BH_{max} (159 kJ/m^3) of Dy-free Nd-Fe-B at 475K [13].

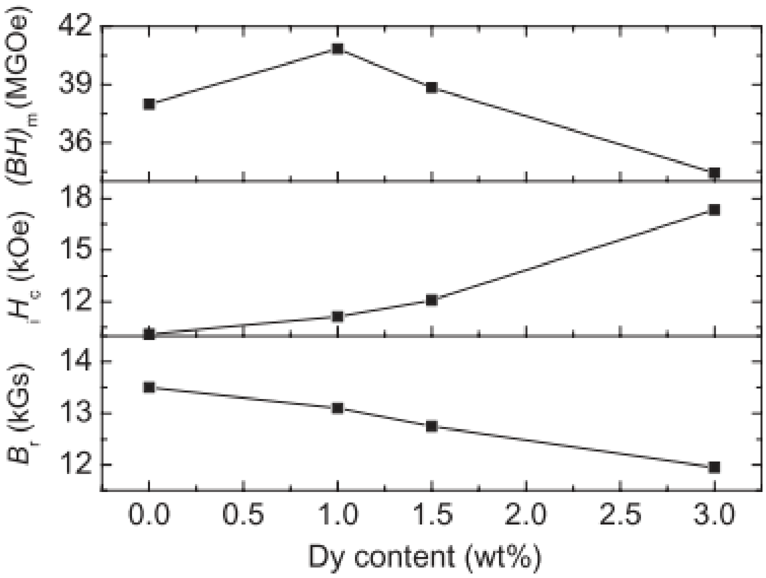

Figure 3. 5 Showing the magnetic properties of sintered Nd-Fe-B with varying wt% of doped Dy [78].

Attempting to increase the coercivity of Nd-Fe-B magnets has been achieved in a few different ways [55], [56], [79], [80], as discussed below.

3.4.1 Grain size

The correlation between grain size and coercivity has previously been investigated by Liu *et al*. [81] where the Nd-Fe-B magnets were processed at different temperatures, which yielded different grain sizes. Through initial simulations it was suggested that a reduction in grain size decreased the demagnetising field, hence leading to an increase in coercivity as well as an improvement of the temperature dependent factor of coercivity. Practical experiments also proved this to be the case and showed that grain size can affect coercivity. However, there is a limit, as reducing the grain size to 0.5 µm requires powders of size ~0.3 µm which comes with handling issues, as the ultrafine powders would prove challenging when scaled up to mass production due to their explosive nature [81]. Li *et al.* [82] investigated sub 0.3 µm grain sized magnets but found a degradation in coercivity due to oxidation of the Nd-rich phase at grain boundaries. As this is a problem in the processing of the material, reducing the grain size shows some limitations. If this impurity could be overcome, then coercivity could potentially be improved.

3.4.2 Grain boundary diffusion

Another way of increasing the coercivity was by the doping of Dy into the magnet. Dy diffused into the grain boundary under heating above 700°C, forming a Dy-rich shell around and Dy-poor core within each of the grains [83]. During magnetisation reversal, nucleation occurs at the surface of the grains or sharp corners and edges of bulk magnets [84], due to defects, and the effect works through to the core of the magnet. The addition of Dy-rich shell around and a Dy-poor core reduced this effect [83], reflected in a study by Li *et al.* [79] where the magnetic properties of Nd-Fe-B magnets doped with Dy was investigated. The process involved sputtering a DyZn film onto sintered Nd-Fe-B before using a heat treatment at 700-900°C for 5 hours to allow the Dy to diffuse into the bulk magnet. This process was then followed by an annealing treatment at 500°C for 1-3 hours (Figure 3. 6).

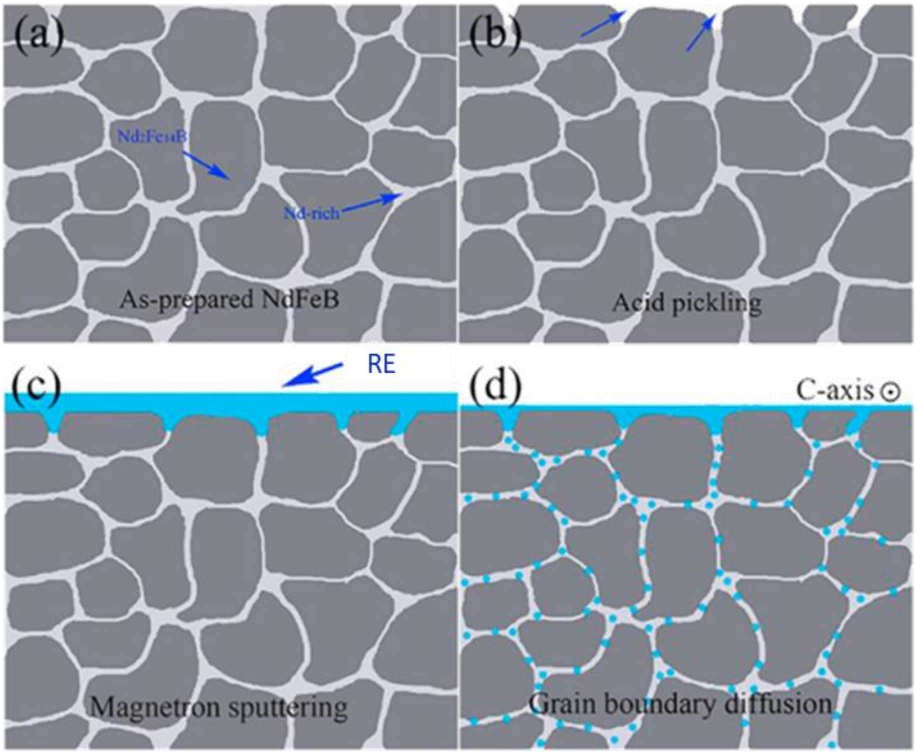

Figure 3. 6 Showing the process of grain boundary diffusion a) initial Nd-Fe-B material b) after acid picking c) sputtering of rare-earth element d) grain boundary diffusion of the rare-earth element [57].

Li *et al.* [79] compared Dy-diffused and Dy-free magnets at different operating temperatures 20-180°C. At the lower temperature the Dy-free magnet had lower H_c = 1174 kA/m but a larger B_r = 1.20 T and BH_{max} = 281 kJ/m^3 when compared to the Dy-diffused magnet H_c = 1711 kA/m, B_r = 1.19 T and BH_{max} = 274 kJ/m^3. As the temperature increased towards 180°C, the Dy-free BH_{max} dropped to 128 kJ/m^3 whereas the Dy-diffused BH_{max} only dropped to 178 kJ/m^3 [79]. Both types of magnet experienced drastic decreases in their values for H_c and BH_{max}, due to the affect an increased temperature has on coercivity [52]. As Dy diffuses into the grain boundary in-between the Nd-Fe-B and substitutes for Nd in this phase, this caused a reduction in B_r as Dy has antiferromagnetic coupling with Fe [85]. However, this prevents the nucleation of reverse domains within Nd-Fe-B, hence increasing H_c [79]. Li *et al.'s* findings are consistent with other research into the grain boundary diffusion (GBD) of Dy [73], [80], [86]. With the high mean price of $405 per kg of dysprosium oxide [87], only small percentages of Dy (0.6-11 wt.%) [88] are used to keep the magnet cost effective due to China's export policies [8]. Perhaps strategic targeting of the Dy on places more susceptible to nucleation of reverse domains rather than coating the entire magnet, and using GBD could reduce the cost even further whilst still maintaining a similar level of performance.

Dy is commonly used to improve the coercivity of Nd-Fe-B magnets through GBD and increasing the anti-ferromagnetic coupling between the 2:14:1 grain (matrix phase). To enhance the coercivity without using more Dy, which has associated cost issues. Song *et al.* [89] investigated the effect of Dy diffusion on Nd-Tb-Fe-B magnets. Sintered Nd-Fe-B magnets with compositions $(Pr,Nd)_{29.8-x}Tb_x(Cu, Co, Ga, Ti)_{1.2}Fe_{bal}B_{0.95}$ (x = 0, 0.5, 0.8, 1.4 in wt.%) prepared by powder metallurgical process, strip-casting, hydrogen decrepitation, jet milling, pressing, magnetic alignment and sintering. Samples were held in a Dy-vapour at 900°C for 8 hours for Dy GBD followed by an anneal at 480°C for 3 hours.

Figure 3. 7 shows some of the magnetic results from this study. Every increase of 1wt.% of Tb led to an increase of 0.37 T in coercivity and the GBD of Dy was not affected by the alloying of Tb and increased the coercivity as expected. This study shows that a combination of alloying and GBD different REE's can be used to improve the coercivity of Nd-Fe-B magnets. As a note, there is no mention of how much Dy was used in the GBD to allow for a direct comparison to other studies. However, as Tb is plagued by the same issues as Dy, although to a lesser degree, this process perhaps would not be viable in industry moving away from the use of REE's.

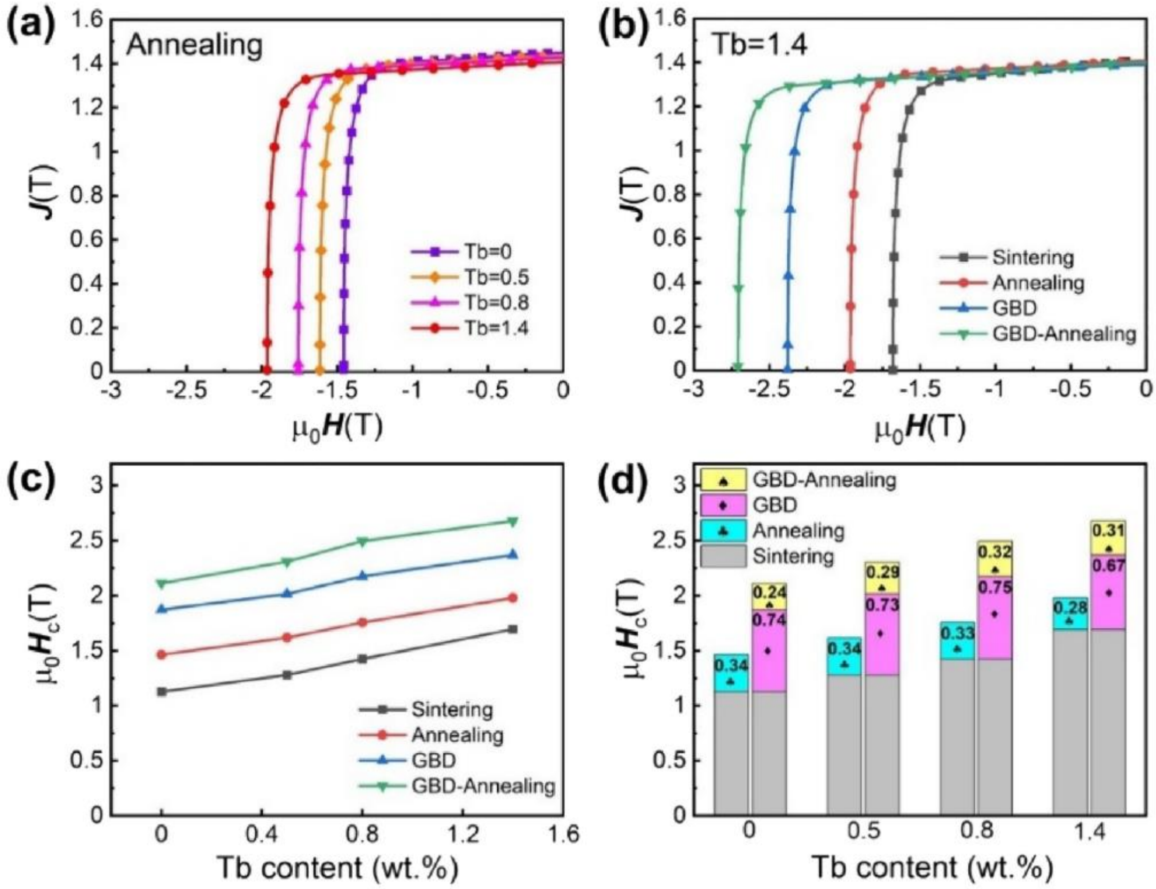

Figure 3. 7 A) Room temperature demagnetisation curves for different Tb wt.%. B) Room temperature demagnetisation curves for 1.4wt.% Tb magnets after different treatments. C) Coercivity with Tb wt.% after different treatments. D) Coercivity increment after each treatment for different Tb wt.% [89].

Recently Jin *et al*. [90] investigated the effect of co-doping (Nd,Pr)H_x and Cu on Nd-Ce-Fe-B magnets. Ce replaced 30wt.% of the Nd in and increased the corrosion resistance but also reduced the coercivity from 970.8 to 740.1 kA/m [91]. This reduction occurs due to the coercivity of Nd-Fe-B being highly dependent on the formation of a continuous non-ferromagnetic grain boundary phase that isolated neighbouring grains from each other [55]. Current materials used for diffusion rely heavily on rare-earth additives. These result in increased coercivity but due to the antiferromagnetic coupling, there is a reduction in the remanence and often the energy product [90]. To recover the loss of coercivity from the Ce being introduced to Nd-Fe-B, and attempt to mitigate the reduction of remanence and energy product, various ratios of $(Nd_{80}Pr_{20})H_x$ and Cu powders were diffused into the material. Various Ce magnetic powders $[(Nd_{80}Pr_{20})_{75}Ce_{25}]_{30.5}Fe_{bal}M_1B_1$ (M = Al, Ga, Zr in wt.%) were prepared by induction melting, strip casting, hydrogen decrepitation and jet milling.

$(Nd_{80}Pr_{20})H_x$ powders were prepared by hydrogenating the Nd-Pr alloy for 2 hours at 673K followed by coarse crushing. $(Nd_{80}Pr_{20})H_x$ and commercially available Cu powders were blended together with the Ce-25 powders in nitrogen atmosphere. The mass ratio of the $(Nd_{80}Pr_{20})H_x$ and Cu powders varied in 10:0, 9:1, 8:2, 7:3 to 5:5. The mixed powders were aligned in a 1.8 T magnetic field followed by isostatic pressing under 200MPa, the compacts then underwent a two-step annealing at 1163K and 768K in a vacuum furnace below $1x10^{-3}$Pa [90]. From analysis of the experiments Jin *et al*. [90] suggested that the co-doping of $(Nd_{80}Pr_{20})H_x$ and Cu created positive microstructural changes: 1) as a result of the doping, Fe was partially substituted by Cu in the $REFe_2$ intergranular phase, as well as Ce for Nd/Pr proven by TEM and EPMA. This causes extra Fe and Ce to be released into the intergranular regions during the annealing/sintering phase. 2) a mechanism driven by concentration gradients caused dehydrogenated Nd/Pr originating from $(Nd_{80}Pr_{20})H_x$ diffused into the 2:14:1 grains and caused a substitution and expulsion of Ce into the intergranular regions, supported by the higher Curie temperature present in the 8:2 and 10:0 magnets. 3) both effects results in extra Ce and Fe atoms within the intergranular region to form additional $REFe_2$ phase upon annealing/sintering. Shown in Figure 3. 8 are the demagnetisation curves for the different ratios used.

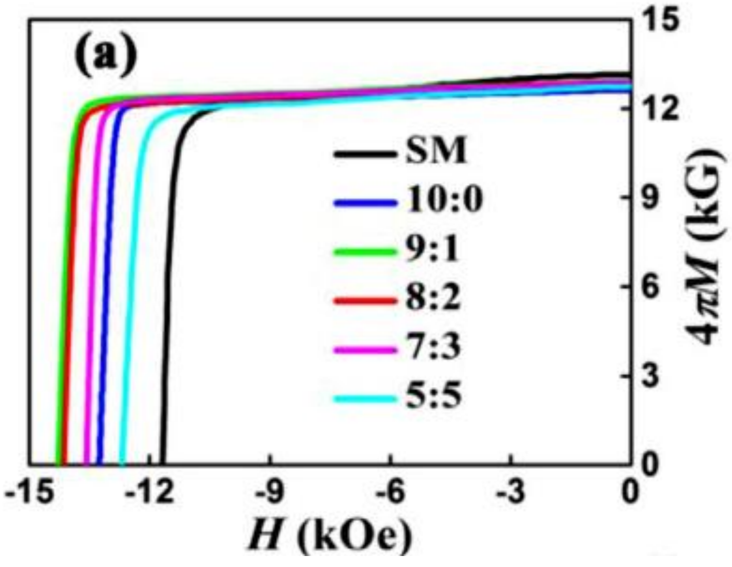

Figure 3. 8 Showing the demagnetisation curves for the $(Nd_{80}Pr_{20})H_x$ and Cu doped Nd-Ce-Fe-B sintered magnets (SM=starting magnet) [90].

Jin *et al*. [90] concluded that the improved coercivity was due to the release of Ce and Fe into the intergranular phase which then promotes to the $REFe_2$ phase under annealing/sintering. This increase along with the raised Cu concentration gave a better continuity of the non-ferromagnetic grain-boundary, and improved stability of the intergranular region to enhance corrosion resistance [90]. The energy product is increased for the 9:1 ratio, from 314.3 kJ/m^3 for the SM to 316.7 kJ/m^3 for the 9:1 doped magnet. The study also showed that having Cu as a co-dopant resulted in a higher energy product than having none, shown by a comparison between the 5:5 and 10:0.

This study shows real promise as the coercivity and corrosion resistance are improved and, importantly, the remanence loss is mitigated with the co-doping of $(Nd_{80}Pr_{20})H_x$ and Cu for the reasons discussed previously. The study finds an optimal ratio and experiments for the effect of temperature as well as uses cheaper materials compared to other REE dopants. This study provides a good basis, but a future study could be carried out on other co-dopants. Cu is used to improve the performance at higher temperatures, but perhaps an element with lower melting point such as Al or Mg, which has being used in different studies, could help the diffusion depth of the dopants to potentially improve the magnetic properties to allow for a deeper diffusion of $(Nd_{80}Pr_{20})H_x$.

3.4.3 Alternatives to Dy

Other 4f elements have also been diffused into Nd-Fe-B magnets such as La and Ce [92]. Like Dy, La and Ce diffuse into grain boundaries and substitute for Nd in ratios of $Nd_{2-x}Y_xFe_{14}B$. Of all the combinations the highest BH_{max} reported for Ce was 170 kJ/m^3 at x = 0.3 and for La BH_{max} = 107 kJ/m^3 at x = 0.2 [92]. These BH_{max} results are lower than that of the Dy-diffused magnet, but that is to be expected as La and Ce do not couple antiferromagnetically like Dy, but instead affect the microstructure to create the observed changes. Ce substitution caused grain coarsening and hence magnetic properties were reduced with an increased ratio, but the optimum ratio of x = 0.3 led only to mild deterioration of the magnetic properties. La at x = 0.2 led to a pronounced grain refinement, enhanced remanence, and maintained a high Curie temperature due to its effect of anisotropic lattice expansion [92]. A combination of La and Ce could help reduce the amount of Dy required to achieve the previous Dy-diffused magnets by increasing the Curie temperature and changing the microstructure to be more favourable. It can also be noted that La (£5.60/kg) and Ce (£5.60/kg) are much cheaper than Dy (£280/kg) [76] and held in much higher quantities due to the lack of applications. Tb has also been used as a replacement for the diffusion of Dy, but the problems that plague the use of Dy are arguably worse in the use of Tb with the element being even more rare and more expensive than Dy [93].

Loewe *et al*. [94] also investigated a similar principle as discussed above. Where they looked at the surface-bulk coercivity after GBD of different REE's (Dy, Tb, Ce and Gd) in two different types of commercially available Nd-Fe-B magnets: Dy-lean and Dy-rich. They also implemented software simulations to predict the coercivity values and compared them to the experimental results obtained.

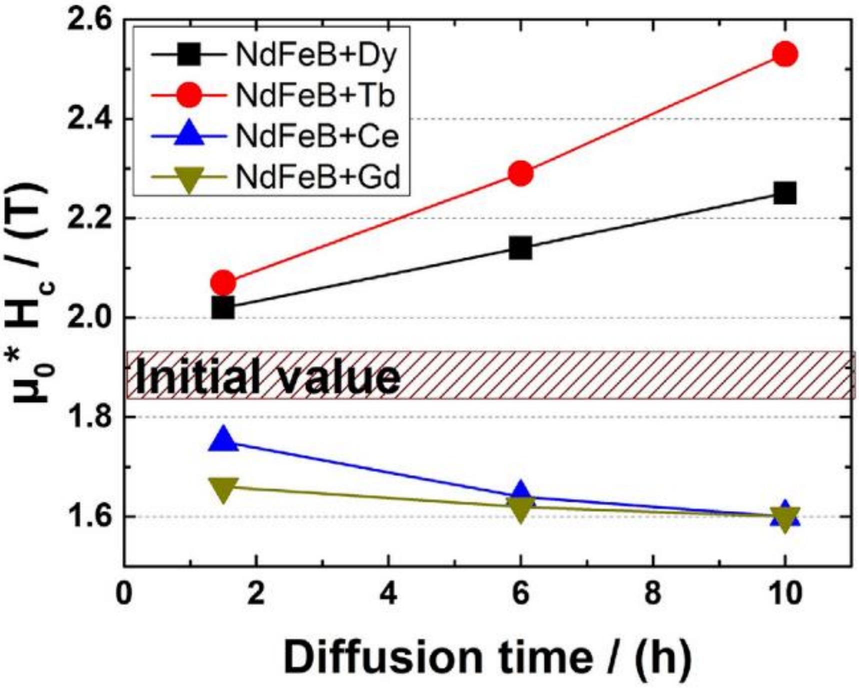

Figure 3. 9 Coercivity value against diffusion time for GBD of different REE's [94].

As shown in Figure 3. 9, the GBD of Ce and Gd had a negative effect on the coercivity over time. The BH_{max} results of Ce shown here are similar to the BH_{max} previously discussed [92], where the GBD of Ce reduces the coercivity. Perhaps following up on the work by Poenaru *et al.* [92] could in the future investigate the effect of diffusion time would have on Ce, as they have already found the optimum ratio, this could further increase the BH_{max} of the magnet.

Table 3. 2 The experimental and theoretical values for GBD of different REE's in selected gradient magnets. Adapted from [94].

REE and diffusion time in hours	Coercivity (T)	
	Measured	Simulated
Dy 1.5h	2.02	2.06
Dy 10h	2.25	2.25
Tb 1.5h	2.07	2.17
Tb 10h	2.53	2.58
Ce 1.5h	1.32	1.60
Ce 10h	1.56	1.56

Table 3. 2 shows there is a slight deviation in the theoretical and experimental values for coercivity. This was suggested to be because it is difficult to precisely determine the surface coercivity of the magnet and as in the simulations the model was used for perfectly aligned grains, which in practice is not the case. Through their simulations they did also find that an over-proportional value for coercivity is exhibited in the surface layer to a few 100 μm thickness, which has positive implications for the application of GBD. It is therefore not necessary to create a homogenous coercivity distribution throughout the magnet and targeted GBD can be used to focus on certain areas of the magnet [94].

More recently, Zhong *et al*. [95] investigated reducing the amount of Dy used by co-depositing Mg. They compared an original Nd-Fe-B, a Dy-diffused and a DyMg-diffused magnet. Through the process of co-deposited sputtering of DyMg, as opposed to individual deposition, they found the consumption of the Dy element to be reduced by 39% and gave an enhanced coercivity when compared to the Dy-diffused magnet (Figure 3. 10) [95].

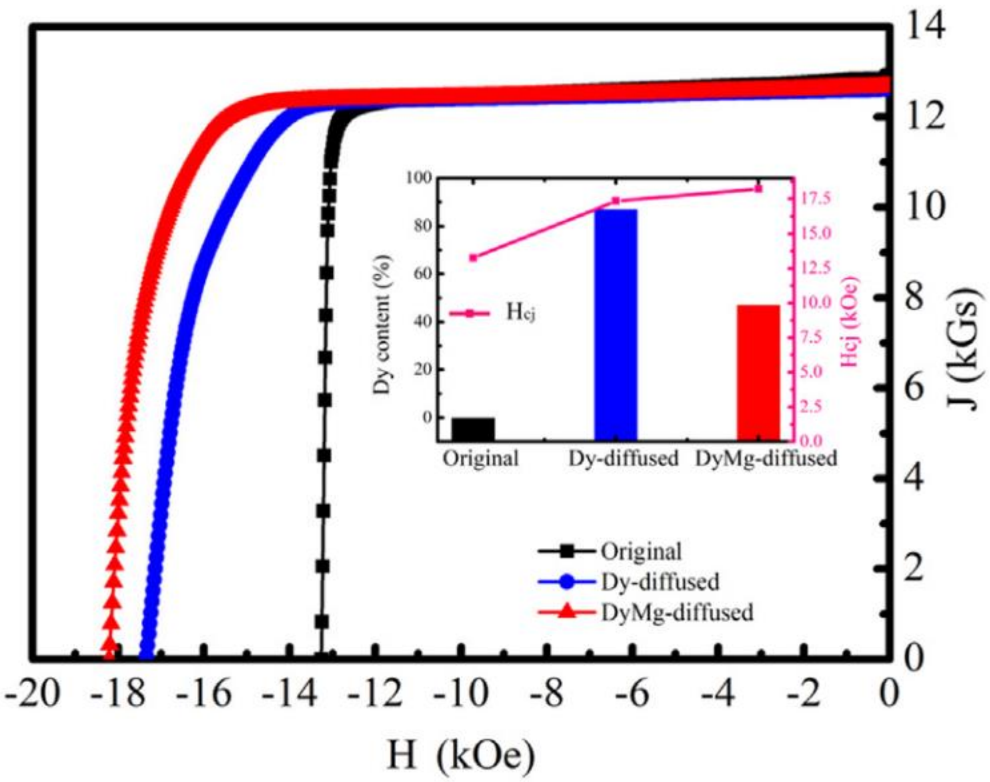

Figure 3. 10 Demagnetisation curves of the original, Dy-and DyMg-diffused magnets. The inset shows the amount of the Dy element deposited into the magnets and corresponding H_{cj} [95].

The results reported show that there is a decrease in the BH_{max} from 39.75 MGOe (316 kJ/m^3) to 39.09 MGOe (311 kJ/m^3) when comparing the original to the DyMg-diffused magnet, which is consistent trend as reported by others for the introduction of Dy into the magnet. But the Dy-diffused magnet reported results for BH_{max} 38.92 MGOe (309 kJ/m^3), which is expected as an increased quantity of Dy will further reduce BH_{max}. It can also be seen in the correlation that an increased coercivity is resulted from the introduction of Dy. However, it is predicted that the increased Dy content would result in a higher coercivity, but this is not the case for the DyMg-diffused magnet. As it is reported to have higher coercivity values across all measured temperatures 300-380K than the Dy only [95]. This suggests potentially some other reason for this rather than the trend being the more Dy the higher the coercivity. Zhong *et al*. investigated the GBD and microstructure of the phases, they found issues with the diffusion in the Dy-diffused magnet to be due to a few factors. 1) grain boundary continuity 2) melting point of the Nd-rich phase 3) formation of Dy agglomerates on the surface [95]. The diffusion of Dy is slow and shallow, the melting point of the Nd-rich phase (1,016°C) does not favour the diffusion of Dy, hence resulting in agglomerates forming on the surface on the magnet. This means there is poor grain boundary continuity through the magnet. With the addition of Mg, this created an alloy with a lower melting point than Dy (1,412°C) (slightly higher than Mg 650°C), this allowed the Dy to diffuse along the grain boundaries more easily, and gave a more uniform distribution of diffusion as well as deeper diffusion depth (Figure 3. 11) [95].

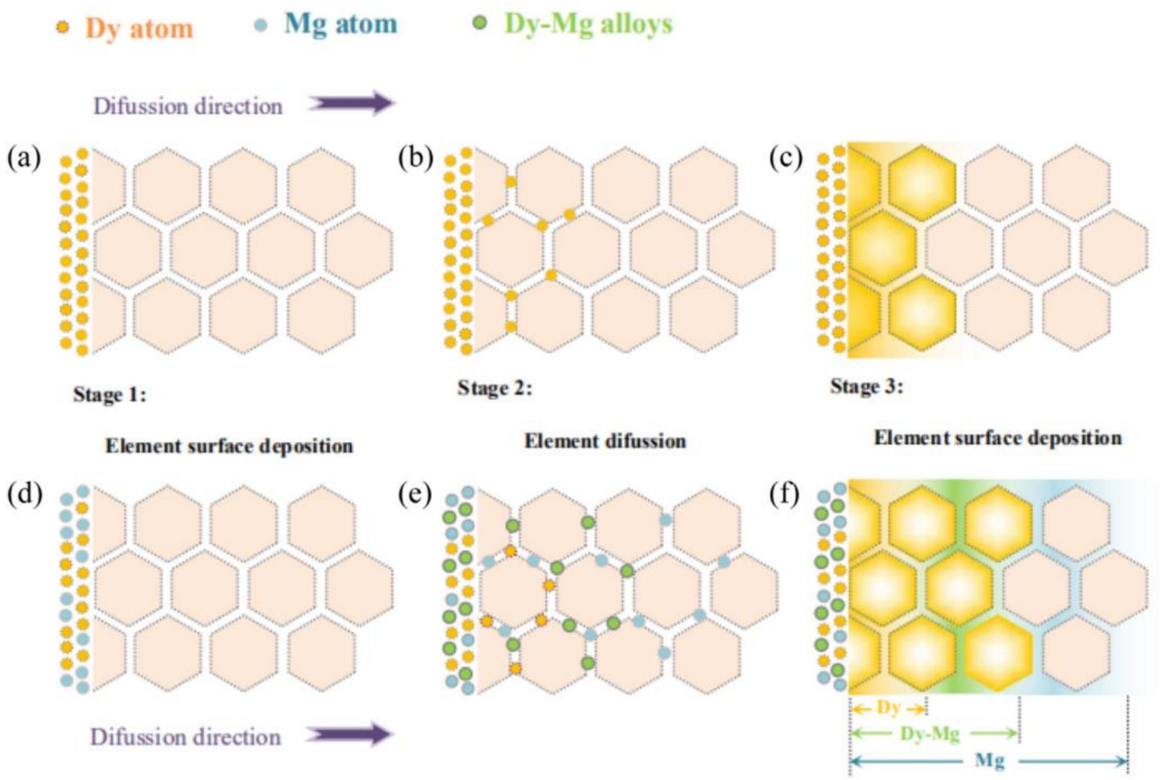

Figure 3. 11 Schematic diagram demonstrating the diffusion mechanism and microstructure evolution a) surface deposition of Dy b) GBD of Dy c) grain lattice diffusion of Dy d) surface deposition of DyMg e) GBD of DyMg f) grain lattice diffusion of DyMg [95].

The grain boundary itself was also investigated, through TEM they found that the grain boundary had reduced in size from ~17 nm to ~8 nm for Dy-diffused and DyMg-diffused respectfully. This presence of a thin grain boundary in the DyMg-diffused magnets leads to weak demagnetisation coupling and an enhanced coercivity [95]. Additionally, the introduction of Mg induced the formation of the Nd-O-Fe-Mg phase during the heat treatment process which increased the O content which made the grain boundary of the magnet more stable [95]–[97].

Where previously discussed work looked at replacing the Dy element with other REE's [92]–[94], this work by Zhong *et al*. [95] provides a different approach of simply creating a lighter alloy with the use of Dy. This has shown to give even better results for coercivity then a Dy-diffused magnet whilst reducing the amount of the elements used which in return makes the overall magnet cheaper. This solution to the problem of REE's in permanent magnets shows promise, potentially a further study could be carried out with alternative elements to Mg which could potentially increase coercivity or BH_{max}, and could potentially be combined with the previously discussed research to attempt to multi-deposit different elements, and study the diffusion time and how that could optimise the magnetic properties.

As previously discussed, different permanent magnets have different magnetic properties, and each is more suited to certain applications because of their coercivity enhancement from single-domain size and the remanence from coupling effects of magnetic grains [98]. However, each nanostructure of permanent magnets varies and therefore has its own advantages and disadvantages, it would be ideal to have a magnet with the BH_{max} of Nd-Fe-B with the thermal stability of Sm-Co [99]. A hybrid magnet is made from two or more permanently magnetic materials that are combined to improve specific aspects of a magnet such as coercivity, BH_{max} or corrosion resistance. Previous attempts to make hybrid magnets have had a limited success due to two main difficulties: 1) the different thermal processes for manufacturing the separate phases; and 2) interdiffusion of atoms between the two phases present at elevated temperatures during processing [100]. Wang *et al.*[101] investigated exchange-coupled nanoscale Sm-Co/Nd-Fe-B magnets, and found that the magnetic properties of the hybrid system is very sensitive to the ratio of the two phases used. They found that as the wt.% of $Nd_2Fe_{14}B$ is increased to 0.4 wt.% the BH_{max} increased to 111 kJ/m^3 but reduced at 0.5 wt.% to 95 kJ/m^3. This was attributed to increasing $Nd_2Fe_{14}B$, resulting in the creation of a large $SmCo_2$ phase grain, which dramatically reduced the coercivity and lead to a deterioration of the energy product [101]. At 0.4 wt.% of $Nd_2Fe_{14}B$ in $SmCo_5$ the peak value of BH_{max} 111 kJ/m^3 is 20% larger than that of single phase $SmCo_5$ with improved thermal stability [101].

A more recent study by Pan *et al.* [102] investigated magnetisation reversal in the same hybrid system of Sm-Co/Nd-Fe-B nanocomposite alloys, where an $SmCo_5$ magnet was produced with varying wt.% of $Nd_2Fe_{14}B$ added. They found through x-ray diffraction (XRD) that with the introduction of Nd-Fe-B there was no effect on the single grain of Sm-Co and through first-order-reversal-curve (FORC) analysis found that 20 wt.% Nd-Fe-B provided the highest BH_{max} of 23.5 kJ/m^3 and showed a higher exchange coupling strength. This research shows it is possible to increase the magnetic properties of a magnet on the nanoscale by creating a hybrid magnet. Perhaps it would be therefore possible to start off with an $Nd_2Fe_{14}B$ magnet and add in other magnetic based materials to increase the temperature performance or coercivity. It might also be a possibility to use a much cheaper bulk material, such as iron, to create the core of the magnet and then create an outer shell of $Nd_2Fe_{14}B$.

3.4.4 Thin films

The magnetic properties of thin films based on Fe or Co have been widely investigated to understand the origins and dependencies of the properties in order to attempt to control them to improve key magnetic properties such as H_c, BH_{max} and M_s [103]–[106].

3.4.4.1 Buffer layers

A study by Jiang and O'Shea studied the dependence of magnetic properties of Nd-Fe-B thin films upon buffer layers made up from different elements (Table 3. 3) [107].

*Table 3. 3 Magnetic properties for buffer elements with different thickness (d) and different annealing temperature T_a measured at 300K. * indicates that some constriction was observed in the hysteresis loop for this sample. Adapted from* [107].

Buffer	*d* nm	T_a (°C)	H_{ci} (kOe)	H_{ci} (kA/m)	$\lvert dH_{ci}(\%)/dT \rvert (\%/°C)$	M_r/M_s	BH_{max} (MGOe)	BH_{max} (kJ/m^3)
Cr	540*	575	3.9	310.4	0.85	0.54	1.2	9.5
	180	575	6.7	533.2	0.70	0.59	6.8	54.1
	90*	575	4.7	374.0	0.85	0.53	2.3	18.3
	54	600	2.7	214.9				
Mo	540	550	12	954.9	0.61	0.66	9.9	78.8
	180	550	17	1352.8	0.62	0.64	10.3	82.0
Nb	540	600	10.5	835.6	0.63	0.67	7.7	61.3
	180*	650	20	1591.5	0.34	0.54	1.5	12.0
	90	600	0.2	15.9				
	54	625	0.4	31.8				
Ta	540*	650	10	795.8	0.33	0.53	3.2	25.5
	180	600	0.4	31.8				
	90	600	0.3	23.9				
	54	600	0.2	15.9				
Ti	540	575	15	1193.7	0.56	0.79	9.3	74.0
	180*	575	11	875.3	0.29	0.64	0.59	4.7
	90*	575	11	875.3	-	0.56	0.9	7.2
	54	650	2.0	159.2				
V	540	575	2.4	191.0			2.1	16.7

They investigated the magnetic properties of sandwiching Nd-Fe-B 20 nm between buffer layers of elements Cr, Mo, Nb, Ta, Ti and V of various thicknesses and at various annealing temperatures. Through this research they found that no single buffer material greatly improved the properties, with the highest H_c resulting from Nb while the highest BH_{max} changed with the use of Mo. The study also showed that samples with the largest coercivity had $Nd_2Fe_{14}B$ grain sizes in the range of 25-35 nm which were found to be the optimal size for this study. This small grain size was due to rapid 30 seconds anneal from temperatures ranging from 550-650°C, depending on the buffer material used [107]. The same authors then later investigated the effect of annealing temperature.

Recently Xu *et al*. [108] showed promise of an increased coercivity in Co films by modulating the films with a Ta/Bi buffer layer on top of the Co. Two samples were made by magnetron sputtering elements (Ru, Co, Ta, Bi) onto thermally oxidised Si substrates at room temperature, followed by annealing between 250-450°C under vacuum (5x10^{-5} Pa). The difference in the samples was the use of either Ta(5 nm) buffer layer or a Ta(5 nm)/Bi(5 nm) dual buffer layer on top of the Co(8 nm), with Ru(3 nm) acting as a capping layer. Hysteresis loops are shown in Figure 3. 12.

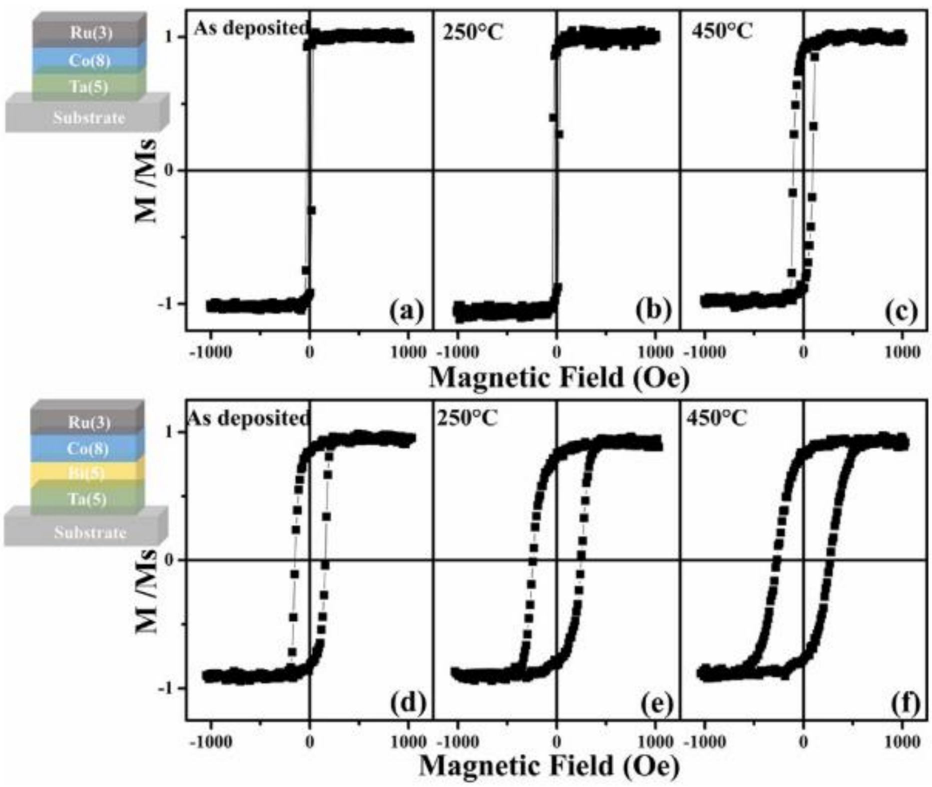

Figure 3. 12 In-plane M-H hysteresis loops of Ta(5)/Co(8)/Ru(3) (in nm) (a) as-deposited and annealed at (b) 250 ℃ and (c) 450 ℃; In-plane M-H hysteresis loops of Ta(5)/Bi(5)/Co(8)/Ru(3) (in nm) (d) as-deposited and annealed at (e) 250 ℃ and (f) 450 ℃. The upper left illustrations of (a) and (d) are schematic diagrams of the corresponding sample structures [108].

Xu *et al.* [108] reported the coercivity of the Ta buffer layer sample to be 27 Oe (2.15 A/m) and 163 Oe (12.97 A/m) with the Ta/Bi dual layer which is a factor of 6 increase [108]. It was stated the diffusion of Bi atoms affects the bulk defect density in the film and increases the pinning strength on the domain walls, which could be a reason for the larger coercivity value. In addition, Bi atom diffusion modified the microstructure of the Co layer (which can be inferred from the change in hysteresis loop shape above), to increase the in-plane magnetic anisotropy this process can be tuned by controlling the annealing temperature.

Xu *et al*. [108] showed promising results to increase coercivity by using the Ta/Bi buffer layer. Future work could be done to combine the two studies and potentially investigate different combinations of buffer layers with different magnetic materials (Fe, Co, Sm-Co, Nd-Fe-B etc.). Nd-Fe-B could be coated with a similar layer or a combination of layers to provide additional pinning barriers which would help to prevent the formation of reversed nucleation domains.

3.4.4.2 Annealing effects of multilayer films

A different study by Jiang and O'Shea investigated the effect annealing has on the magnetic properties of $Nd_2Fe_{14}B$/α-Fe thin films [106]. Films were deposited onto a silicon (100) substrate *via* sputtering, with a 20 nm thick Nb layer added as a buffer layer and a top layer to protect a Nd-Fe-B layer. The temperature range (600-750°C) and speed of annealing from 30 seconds or 20 minutes were varied and the exchange-spring behaviour of $Nd_2Fe_{14}B$/α-Fe evaluated (Table 3. 4).

Table 3. 4 The coercivity and BH_{max} values for samples annealed at different temperatures and speeds. Samples 1-4 under a 20 minute anneal and sample 5 under 30 seconds anneal. Adapted from [106].

Sample No.	Fe/Nd ratio	Annealing Temp (°C)	BH_{max} (MGOe)	BH_{max} (kJ/m^3)	H_{ci} (kOe)	H_{ci} (kA/m)	M_r/M_s
1	6.0	600	7.7	61.3	10.5	0.84	0.67
2	7.7	600	10.1	80.4	4.8	0.38	0.64
3	9.4	625	7.3	58.1	4.5	0.36	0.62
4	11.1	600	3.9	31.0	2.1	0.17	0.57
5	9.4	750	12.6	100.3	10.8	0.86	0.64

Annealing was shown to affect the magnetic properties of Fe sputtered onto Nd-Fe-B in a range from 600-750°C [106]. The films annealed for 30 seconds had a higher energy product compared to the 20-minute annealed films, which was suggested to be due to the creation of more uniform grain sizes. This was later proven with TEM by Yang *et al*. [109]

where they compared a 15 minute anneal at 750°C to an electron-beam heating technique at an accelerating voltage of 10 kV and a current of 1.8 mA for 0.1 seconds. The research by Jiang and O'Shea also looked at varying the Fe/Nd ratio, and how that affected magnetic properties; magnetisation was observed to increase with the concentration of Fe due to Fe having a larger moment than Nd. However, as the ratio of Fe/Nd increased, the normalised remanence M_r/M_s reduced. Coercivity was also observed to decrease with an increased Fe content. An increased Fe content lowered anisotropy and the maximum energy density; therefore, it can be determined that energy density is a function of the Fe content [106]. However, the study did not report results for a 20 minute anneal at 750°C so a comparison to the 30 second anneal can't be made. This would have given a more comparable value to see if the increase in BH_{max} was due to the change in annealing temperature or the annealing duration. Additional understanding could be obtained by investigating the effect of different annealing times at a constant Fe/Nd ratio to be able to draw results by comparison.

Annealing temperature was also investigated by Xu *et al.* [108] in the previously discussed study on Co films with Ta/Bi buffer layers. Although, they focused more on the effects of the buffer layer and how annealing changed the magnetic properties of the films. They reported an increase in coercivity from 97 Oe (7.7 A/m) with a Ta buffer layer (450°C anneal) to 262 Oe (20.9 A/m) with Ta/Bi (450°C anneal); this was found to arise from the diffusion of Bi through the Co layer towards the edge of the film. This diffusion caused the orientation of the Co layer to align, and resulted in the easy magnetisation axis closer to the film plane which caused an increase of the in plane magnetic anisotropy. Therefore, the magnetic domain wall energy increased resulting in an increased energy barrier to the nucleation of a reverse domain, and an increased coercive field [108].

3.4.4.3 Exchange coupling

Ao *et al.* [110] investigated exchange coupling and remanence enhancement in nanocomposite Nd-Fe-B/FeCo multilayer films. Here, 1-50 nm thick FeCo was sandwiched between a 20 nm and 3 nm thick Nd-Fe-B layers [110]. Increased thickness of the FeCo resulted in overall increased remanence but with this the coercivity decreased. This was first reported by Coehoorn *et al.* [111]. Through making a thinner film the opposite trends in remanence and coercivity resulted in a maximum BH_{max} of 215 kJ/m^3 at 5 nm FeCo; this was an increase from 95 kJ/m^3 for Nd-Fe-B all at room temperature. The Nd-Fe-B/FeCo multilayer films were all found to have characteristic magnetic properties that are expected for nanocomposite magnets (high BH_{max} and remanence), with the presence of both hard and soft phases, which proved that the FeCo and Nd-Fe-B are well exchange coupled within the multilayer films [110].

Cui *et al*. [112] investigated the anisotropic behaviour of exchange coupling in Nd-Fe-B/α-Fe multilayer films. The films were synthesised by sputtering layers of Mo(50 nm)/$Nd_{16}Fe_{71}B_{13}$(800 nm)/Fe(11 nm)/$Nd_{16}Fe_{71}B_{13}$(800 nm)/Mo(50 nm) on a Si heated substrate. A coercivity of 620.7 kA/m and BH_{max} 142.4 kJ/m^3 was reported for this multilayer film but it was increased to 198.9 kJ/m^3 when the thickness of the Fe layer was increased to 36 nm [112], which is to be expected when adding more soft magnetic material with high magnetisation. Exchange coupling was investigated by measuring the hysteresis loops of the films at 180K, the first film (Fe 11 nm) showed an improvement in coercivity to 1152.0 kA/m which is due to the enhancement of anisotropy at lower temperatures [112]. However, they did find that there was a kink within the hysteresis loop in the direction parallel to the film plane, which suggests there is exchange decoupling between the hard and soft magnetic layers, this was not observed in the perpendicular direction. The thickness of the α-Fe was changed so that its effect on exchange coupling between the hard and soft layers could be investigated, and due to the use of the Mo spacer layer an effective critical correlation length L_{ex}^{eff} was proposed [112]. This term is the thickness of α-Fe at which the kink in the hysteresis loop occurs and the values are listed in the Table 3. 5:

Table 3. 5 Effective critical correlation length L_{ex}^{eff} for textured Nd-Fe-B/ α-Fe multilayer films. Adapted from [112].

	295 K	180 K
L_{ex}^{eff} perpendicular direction (nm)	38	26
L_{ex}^{eff} parallel direction (nm)	18	10

Through investigating films without the presence of α-Fe they found that the kinks in the hysteresis loops are due to the presence of α-Fe within the multilayer film, but kinks did not occur if the thickness of the α-Fe was below the effective critical correlation length. This suggests that exchange decoupling is strongly related to the soft phase, but through further experimentation they found that the effective critical correlation length was due to the shape anisotropy from the textured structure in the hard phase [112]. They do seem to have stated how the results were obtained, and important with the future of larger energy product materials coming out of further research into this area. However, they do not clearly state a protocol for how they managed to control growth of the hard layer as to increase the anisotropy.

Alternatively, Neu *et al.* [113] researched the texture, layer thickness and magnetic properties of exchanged coupled $[SmCo_5/Fe]_n/SmCo_5$ multilayers with the number of layers ranging from n=1 to 5 whilst keeping the thickness of each material layer constant (Fe 25 nm) (Sm-Co 50 nm). All the samples were created by pulsed layer deposition onto a Cr-buffered MgO (110) substrate at 500°C. They found that through increasing the layers the theoretical and experimental values for BH_{max} increased but showed a decrease after n = 2 (Figure 3. 13).

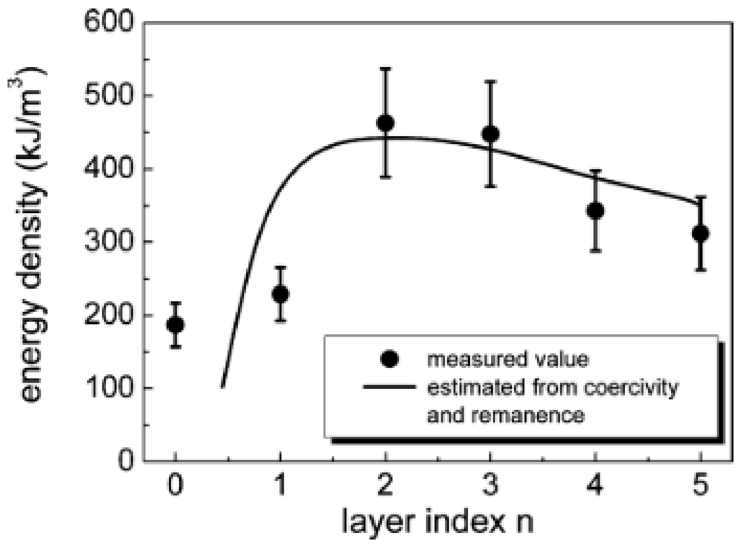

Figure 3. 13 BH_{max} as a function of layer index n together with an estimation based on the interpolated data of remanence and coercivity, error is caused by thin film thickness [113].

Within the same layers there was a trend of decreased coercivity and increased remanence which is to be expected with the increase of Fe, and it was suggested that the Co was also diffusing into the Fe layer creating a high saturation polarisation Fe-Co alloy [113]. However, they did suggest that coercivity could be improved by reducing the thickness of the hard layer from 25nm to 6nm due to its sensitivity to thickness of the soft layer.

3.4.4.4 Bilayer films

Fullerton *et al.* [114] investigated bilayer films for SmCo/Fe and SmCo/Co, to study exchange-spring effects through the use of the coupled hard/soft magnetic layers. When investigating the SmCo/Co system, Fullerton *et al.* stated the BH_{max} to be 87.5 kJ/m^3 for a

450 Å thick Sm_2Co_7 layer at room temperature. With the introduction of Co layers which ranged from 0-400 Å the BH_{max} increased to ~111.4 kJ/m^3 at 100 Å, and then sharply decreased as the thickness of the Co layer increased. This decreased BH_{max} stemmed from the Co layer introducing more soft magnetic properties, the coercivity of the bilayer decreased even though the total M_s increased, the softening of the overall magnetic properties degraded the BH_{max} [114]. Use of 25-200 Å thick layers of Fe instead of Co resulted in an immediate drop in coercivity for example reducing from 3.4 T for pure Sm-Co, to ~1.7 T with only 25 Å Fe [114]. This reduction of 50% of the coercivity is quite dramatic, the experimental BH_{max} was not reported. A similar trend to that of the SmCo/Co bilayer where BH_{max} increased, as a result of increasing the ratio of soft high magnetisation material cannot be assumed as the coupling of the Co could occur differently in reality.

Through simulations of varying thickness of both the Sm-Co and Fe layer, Fullerton *et al.* [115] suggested that the theoretical BH_{max} is greater when the thickness of Sm-Co was small as there is a larger ratio of the soft layer. Their more recent research has confirmed this theory, as when H increased, a Bloch wall within the Fe layer became compressed against the Sm-Co layer. This then caused the interfacial spins in Sm-Co to become increasingly rotated [114]. At the field where the energy density of the domain wall in the soft layer became greater than if in the hard layer, the domain wall found in the soft layer moved and switched into the hard layer via domain wall motion [114]. The use of the coupling soft magnet has proved to be promising at increasing the overall BH_{max} in thin film bilayers. They did not investigate the use of thin films on bulk materials. However, this could be an avenue for future research as to how the use of specific thin films in different locations, and thicknesses could affect the magnetic properties of the bulk material.

3.5 Permanent magnet electric motors

This section will discuss the history of the electric motor and review the development into different magnetic architectures to improve performance, as well as a discussion of recent developments of magnetic materials for use in the application of electric motors.

3.5.1 History of electric motors

In 1834 Faraday published his work on the discovery of electromagnetic induction, with the idea that moving a magnet near a wire can produce an electric current within the wire. This works due to the magnetic field of the magnet creating a force on the electrons within the wire, causing them to move. This movement of electrons is what generates an electric current in the wire. Faraday’s discovery was a ground-breaking development in electricity and has become the foundation for many applications such as generators and motors [116]. Thomas Davenport built the first electric motor in a small model car in 1834, demonstrating the electric motor could do useful work. In 1873 Nikola Tesla invented the AC motor which is more efficient and powerful than DC and is the dominant type of motor used today. Development of such motors over the 20th century have seen changes to design and materials used to improve efficiency and reliability. These developments have led to electric motors becoming common place in many applications, from household appliances to electric machines and drives. Throughout the development of electric motors, over 100 different topologies can be found throughout modern vehicles [117], [118]. General designs of these motors will be covered in the following section.

3.5.2 Motor topologies

One of the distinguishing differences in motor topologies is the position of the magnets, where they can be surface or internally mounted depending on the design. The motors themselves also vary in principle and design, with DC, induction (IM), permanent magnets based: synchronous (SPM), brushless (PMBS) and hybrid excitation (PMHEM), reluctance (RM) and synchronous brushed (SBM) [118]. Each will be discussed with their respective rotor characteristics as well as different stators commonly used.

3.5.2.1 Rotor

DC motors consist of a stator with a stationary field and a rotor with a brush commutation system. The field created by the stator is usually induced by coils but can be created by permanent magnets for small machines. The field windings may be in series or shunt connected with the rotor depending on the required characteristics of the motor, shown in Figure 3. 14.

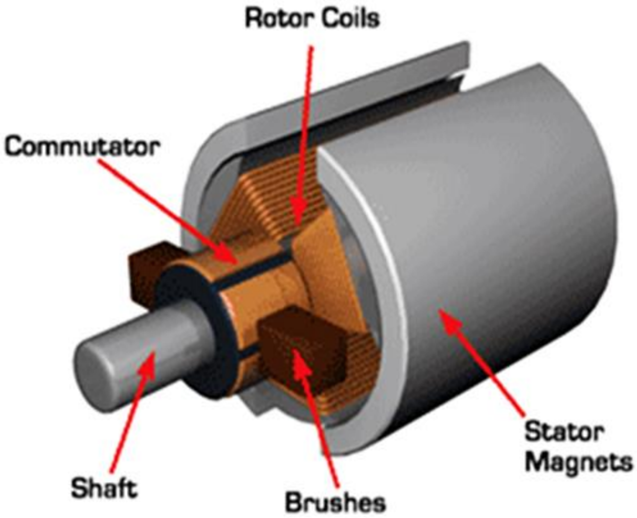

Figure 3. 14 Showing the design of a brushed DC motor [119].

The commutator is made up of a set of copper segments which induce more friction than slip rings and consequently produces dust. Advantages of this type of motor are that the technology is well established and therefore has good reliability and is relatively inexpensive with simple design and allows for hardy control. This made DC motors the preferred option of motor design for variable speed applications before the advancement into power electronics. The main disadvantages of a DC motor are its low power density, costly maintenance, and low efficiencies (85%) [120]. Despite this DC motors still have a range of applications focused on the lower and middle power range vehicles [118], [121].

Induction motors (IM) main advantage is its simplicity of construction. Where the stator and rotor consist of a stack of laminated steel surrounded by a squirrel cage like shape of short-circuited aluminium or copper bars, shown in Figure 3. 15.

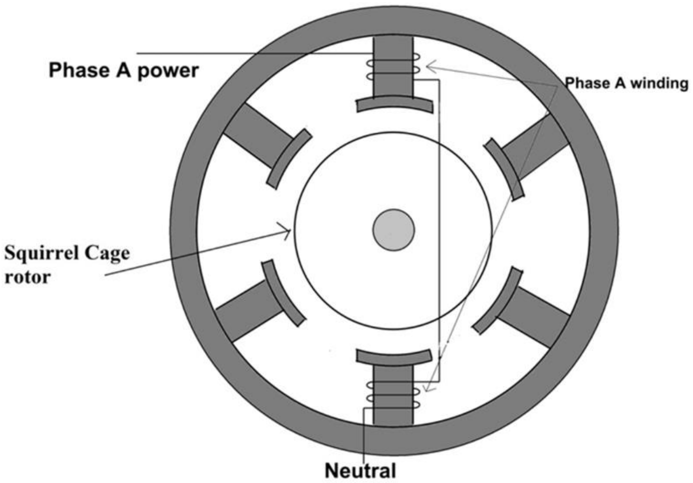

Figure 3. 15 Showing the design of an induction motor [122].

The magnetic field of the stator will rotate at a slightly higher speed than that of the rotor, this difference or “slip” between the rotor and the stator frequencies induces rotor currents which will produce the motor torque [118]. Induction motors are relatively inexpensive, robust, reliable and require very little maintenance, they can achieve efficiency of over 95% for static applications but to obtain better performance over a wider speed range the efficiency is reduced to around 75% for a variable speed motor. However, IM’s control circuit is complex and has a relatively low efficiency and power density compared to PM’s leading it to a lower global market share. [118], [121].

Permanent magnet DC motors (PMDC) are characterised by their constant rotor magnetisation. Here the PM’s within the rotor induce magnetic field in the air gap without the need for excitation currents, leading to a high power density, shown in Figure 3. 16.

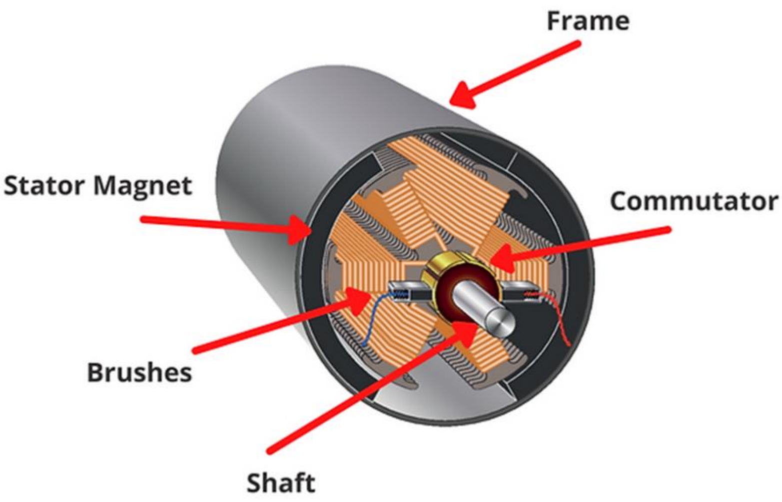

Figure 3. 16 Showing the design of a permanent magnet DC motor [123].

This lack of excitation current does require less cooling and increases efficiency, but a more complex control of the excitation field is required to regulate the field [121], [124]. Coinciding with the development of high coercivity permanent Nd-Fe-B magnets in the 1980's, permanent magnet motors are increasingly being used for automotive applications. These new PM's are brittle and very temperature sensitive meaning that insufficient cooling may lead to a reduction in performance and demagnetisation [118], [121]. The PMDC motors require more maintenance and exhibit more torque fluctuation due to the commutator and brush system. A permanent magnet synchronous motor has a stator with a three-phase winding similar to IM and RM motors. As the PM's can be positioned in many orientations within the rotor, there is a large variety of possible arrangements and orientations. In terms of the flux path, radial and axial flux are the most common, radial-flux machines can have the magnets mounted either on the surface or internally, but axial-flux machines usually have surface mounted magnets. Synchronous permanent magnet motors allow for more flexibility in design and due to their compact design, they are often used to fit in places of limited space such as electric rear wheel drive vehicles [118], [125]. Well-designed internally mounted PMS motors have a high reluctance torque, efficiency, compact and with low noise have led this to become one of the dominant motor designs in traction motor applications [121]. A brushless PMDC motor is a structurally theoretically specialised synchronous motor where instead of a sinusoidal current waveshape it is trapezoidal, the commutator-brush system is not required. However, torque ripple and noise do appear during electrical commutation and with this design it is difficult to achieve a maximum torque that is beyond twice the value of the base speed [121]. Adding excitation windings to a PMSM will create a hybrid motor with the combination of PM, the motor has minimum flux leakage and possesses a high flux density in the air gap, high power density and relatively good torque and speed characteristics. As there is an extra excitation, the control and topology are complex [121].

Reluctance motors have attracted a lot of attention due to the concern of price increase and shortage of magnetic materials which is predicted to occur when electric vehicles enter large scale mass production [126]. The stator and rotor are composed of Si steel laminates, there are no windings, slip rings or permanent magnets on the rotor and a simple use of concentrated windings are installed on the stator [121], shown in Figure 3. 17.

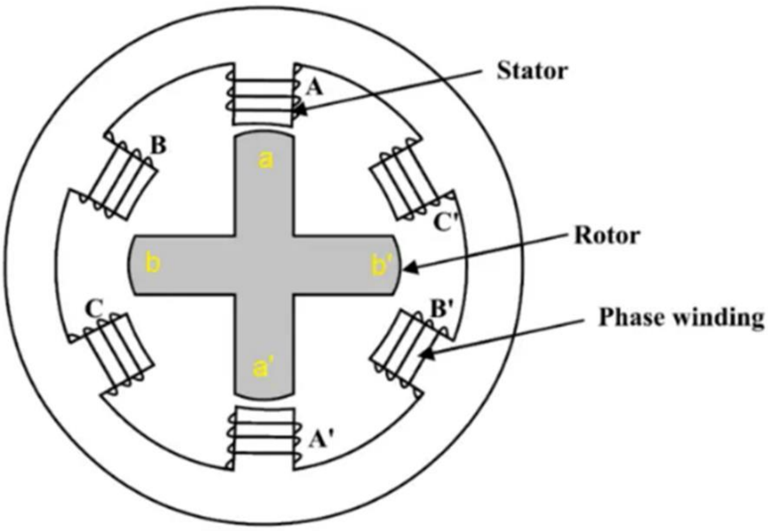

Figure 3. 17 Showing the design of a reluctance motor [127].

The main characteristic of RM's is their use of rotor salient poles, where the torque is produced by the direct axis and quadrature axis synchronous reactance as the rotor lacks excitation. A RM is relatively cheap to produce and not temperature sensitive and has a peak efficiency comparable to that of the IM motor over variable speeds. A drawback of this type of motor is the high ripple torque resulting in higher noise and vibrations resulting in this motor design being very uncommon for electric vehicle use [118], [121].

Synchronous brushed motors have a coil in the rotor connected to a source of stationary voltage through a slip ring, shown in Figure 3. 18.

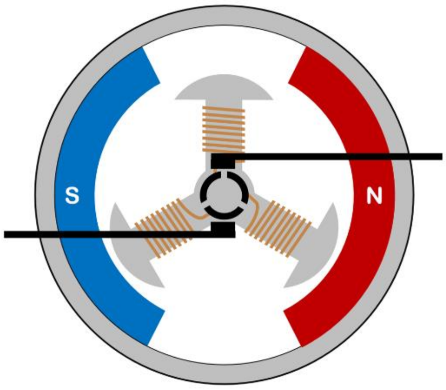

Figure 3. 18 Showing the design of a synchronous brushed motor [128].

This motor is robust and operational temperature is limited by the insulation of the conductor [129], [130]. A main advantage of this motor design is the possibility of regulating the magnetic flux linkage, a reduction of this allows for high-speed operation at a constant power without the field weakening operation that is present in permanent magnet machines. The efficiency can be improved by running the motor at a partial operational load of the iron which reduces the excitation losses. As the field is generated by excitation currents in the stator, this motor’s full load operational efficiency is lower than comparable machines without current in the stator due to Joule losses in the magnetising current [118].

3.5.2.2 Stator

A stator can be a coreless machine (CM), where the windings are placed in a stator made of a non-magnetic material [131], [132]. As this means the stator cannot be made of iron there are no associated iron losses, the lack of iron in the teeth increases the reluctance of the magnetic circuit but the lack of iron also results in more active material is required for a given power rating to compensate for the larger air gap. The absence of iron does reduce the weight of the stator and with no associated losses, this compensates for the increase of the expensive active material required. CM motors are most commonly used in high performance applications where weight and efficiency outweigh the overall cost [118], [133].

The stator can contain multiple phases, the standard three phase is the minimum number of phases required to deliver constant power over each cycle. Increasing the number of phases increases the complexity of the system and hence is only used when special performance is required. Associated advantages of three phases are a reduction of harmonic content, low acoustic noise and an increase of torque density and efficiency. However, the fault tolerance and lower power rating of each phase is associated as the main factor for the market position. This fault tolerance is the key reason for the role in fulfilling the safety requirements for aircraft [134], [135]. The lower power rating for each phase allows the use of robust but less expensive power electronic devices. Occasionally multiple phase systems consist of duplicate three phase systems with an angle shift, but in principle a phase number above four is possible. Motors that contain more than three phases are less common for road vehicles but due to their high torque capabilities they are more suited for the propulsion for ships and planes [118], [136], [137].

In-wheel motors (IWM's) have a confined outer diameter determined by the space available inside the wheel. These motors can be directly driven, and some designs also include planetary gear and even the brake disks [138]. All topologies are suitable for this type of motor but PM motors that have outer rotors or an axial flux configuration give a better power density and utilise the available volume more efficiently. There are examples of IWMs that have a reluctance motor configuration, but this is less common [118], [139], [140].

3.5.3 Advancements of permanent magnets for electric motors

Most research into improving the performance of the RE magnets focuses on the coercivity, remanence and BH_{max} of the magnets, as discussed in Section 3.4. There is also the possibility of replacing REE based magnets with the more abundant ferrite-based magnets, with their low cost, thermal stability and reasonable magnetic properties [141] they could be used to partially replace the RE magnets in a cost against performance compromise. The following review will cover changes to the magnets such that they effect the performance of an electric motor.

A comparative study by Oti *et al*. [142], investigated the affect different magnetic materials have on the electromagnetic output of a permanent magnet machine. Using ANSYS-MAXWELL the motor is set up as in Figure 3. 19.

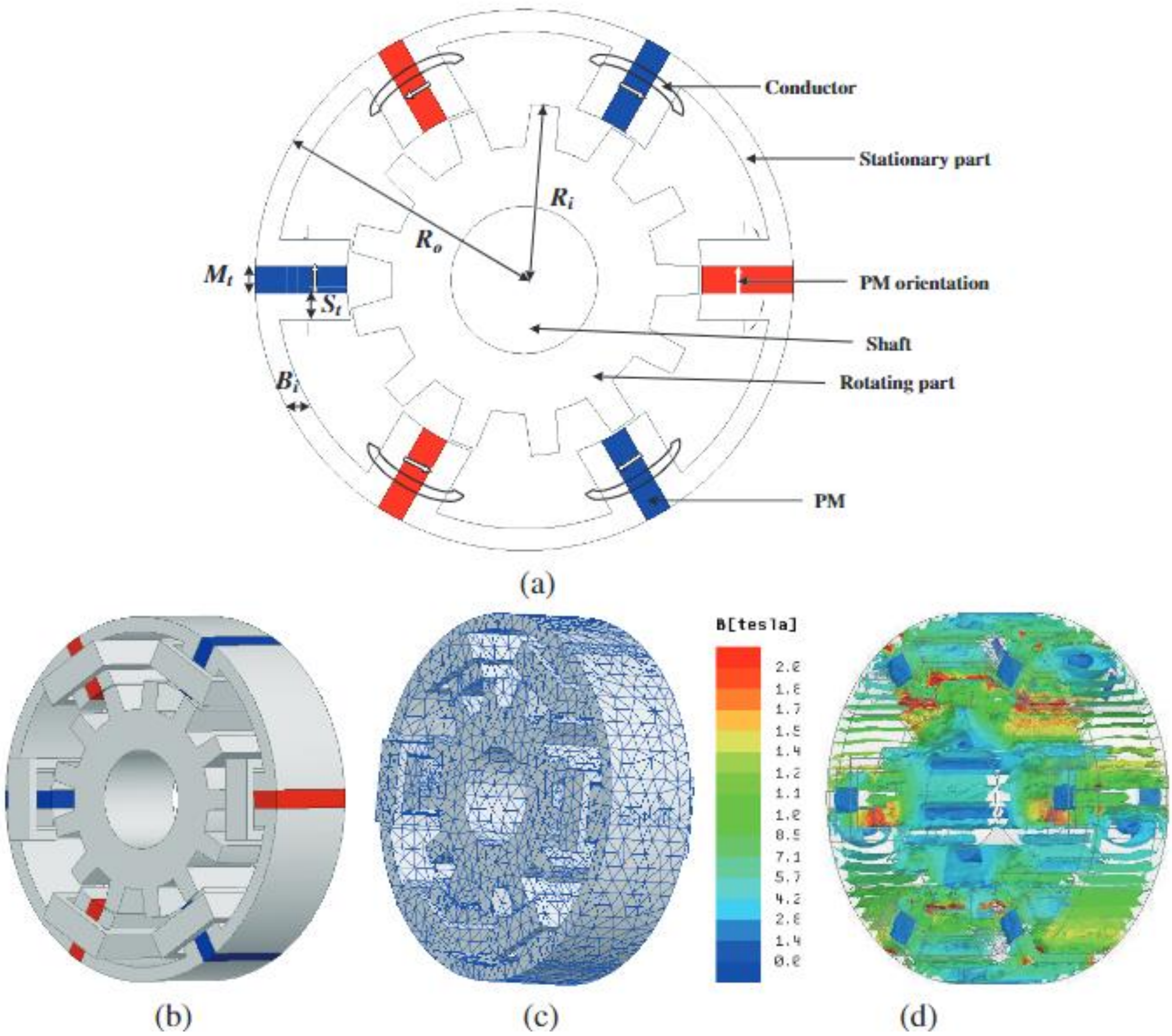

Figure 3. 19 Showing the schematic of the investigated machine model. a) 2D FEA mode b) 3D FEA model c) 3D FEA mesh d) 3D FEA flux density [142].

The four magnetic materials chosen in the study are: AlNiCo, ferrite, Nd-Fe-B and Sm-Co. With the motor having constant dimensions and properties the variables come from the properties of the individual magnetic shown in Table 3. 6.

Table 3. 6 Showing the parameters of the different magnets used within the motor. Adapted from [142].

Magnetic Material	AlNiCo	Ferrite	NdFeB	SmCo
Remanence, B_r (T)	1.16	0.4	1.47	1.05
Coercivity, H (kA/m)	230.75	303.15	1063.4	795.77
Electromagnetic power at base speed (W)	206.57	186.57	449.67	396.40
Efficiency at rated speed (%)	79.83	75.76	87.22	86.58
Energy product, BH_{max} (MGOe)	4.4	3.7	53	25.8
Cost (£/lb)	20	2	35	70

Property values given for the magnetic materials in table suggest that the RE based magnets of NdFeB and SmCo should produce the highest power and efficiency machine at room temperature but at the highest cost. And as expected Oti *et al*. found through simulation that the machines equipped with the RE magnets provided a higher torque, a greater fault-tolerance ability and improved power and efficiency compared to the non-RE magnets. This demonstrates that in a direct comparison of magnetic materials there is no real suitable substitute for RE magnets within an electric motor when maximum performance and efficiency is the goal.

To reduce and optimise the quantity of RE material, Chen *et al.* [143] investigated the use of a hybrid magnet configuration, by utilising the cheaper and crucially RE-free magnetic material ferrite permanent magnet in combination with NdFeB and changing the magnet topology. The reference motor is shown in Figure 3. 20.

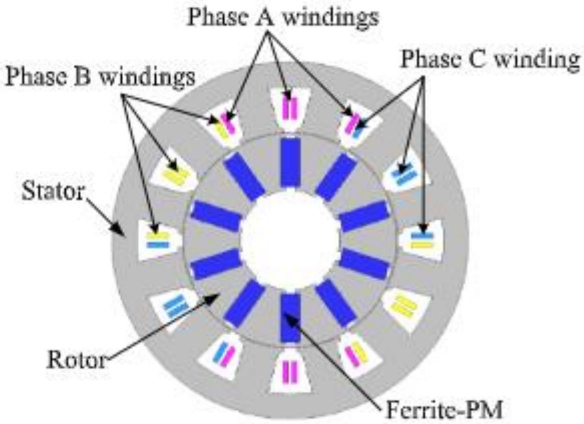

Figure 3. 20 The structure of the reference motor with a non-rare-earth ferrite-PM [143].

The reference motor consists of 12-slots and 10-poles in a three-phase excitation current system. The reference motor magnets are the ferrite-PM and the study simulates the addition of NdFeB in a series, parallel or mixed pattern into the motor shown in Figure 3. 20.

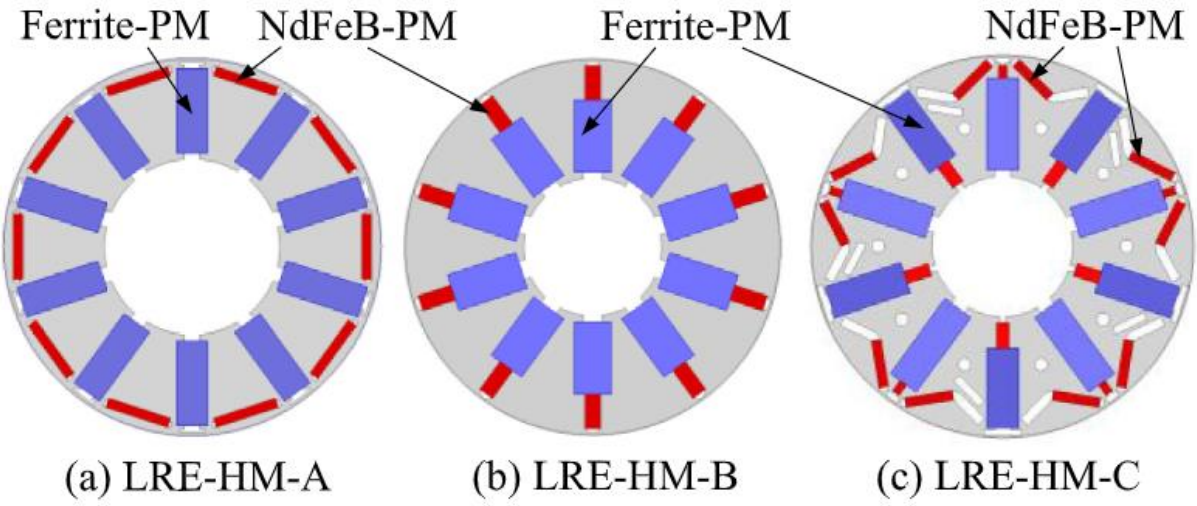

Figure 3. 21 Showing the different rotor topologies of less-rare-earth hybrid-magnet motors (LRE-HM) in a) A-series, b) B-parallel, c) C-mixed [143].

The study describes a changing volume of ferrite-PM and NdFeB in which it was observed the central diameter of the rotor is changing but the total diameter remains constant. The specific changes are listed in Table 3. 7.

Table 3. 7 Stating the specification and performance of the three hybrid-magnet motor designs, adapted from [143].

Specification	Reference	A-Series	B-parallel	C-mixed
NdFeB volume (cm^3)	0	42.16	35.70	34.00
Ferrite volume (cm^3)	183.6	179.5	183.6	183.6
Axle diameter (mm)	56	56	44	44
Torque ripple (AC RMS/Mean)	3.348	3.126	2.495	2.928
Efficiency (%)	83.96	87.76	90.14	88.08
Core loss (W)	45.74	36.31	42.1	41.5

Evaluated from data in Table 3.7 the introduction of NdFeB has varying results depending on the topology of the magnets which is being utilised. The introduction of NdFeB into the series configuration reduced the torque ripple, and core losses and increased the efficiency of the motor. Which is to be expected with the introduction of a hard magnetic material, but the change from a series to a parallel configuration gave the same trend again except for an increase in the core loss of 5.79 W when comparing series to parallel. This increase is likely due to the increased volume of iron as the volume of NdFeB is reduced. The efficiency increases by 2.38%, as the volume of NdFeB decreased and the volume of ferrite increased, this increase of efficacy is down to the change in topology. By aligning the magnets end-to-end and assuming the magnetisation direction is along the radius of the rotor, this would confine the magnetic flux towards the same direction and the introduction of the NdFeB would mean that an anchorage and boost to performance of the ferrite is occurring. However, Chen *et al*. also tried to optimise the design further by creating a mixed design with anti-symmetry of the magnets, this mixed topology reduced the volume of NdFeB but resulted in a lower efficiency. This demonstrates that there are different aspects to consider when designing a motor for efficiency. An increase of NdFeB does not necessarily result in an increase of efficiency and a suitable change of topology can achieve this. Although this study does show the benefit of an optimal design and the performance gain from using RE magnets, it lacks suitable comparison to itself and other studies. As the changes by Chen *et* *al*. are not singular with each step, for example the change of series to parallel topology of the NdFeB also has the change of axial diameter, so there is no certainty that the performance gain is coming solely from the magnet topology change. There is also a change of NdFeB volume, although this comes along with the change in topology it seems flawed to assume that the performance gain is due to this. The study could be improved and have a better comparison if the reference motor was designed in such a way that it did not require a dimension change and had initial space to create all the desired changes in topology. This would mean that there would be a constant volume of the NdFeB, and a true indication to the performance of the motor can be seen when changing the topology. Perhaps a different approach entirely could be taken within the study, as it is well established that a large reason for the high efficiency of these magnets is due to the use of RE magnets. And as any introduction of these materials will increase efficiency, it could be more representative of current motors to have a reference motor with only NdFeB magnets and then attempt to reduce the volume of the RE by replacing it with the ferrite and investigate the effect this will have on performance and efficiency.

A later study by Chen *et al*.[144], optimised the mixed topology of series and parallel into a more accurate representation of the mixed topology shown in Figure 3. 22.

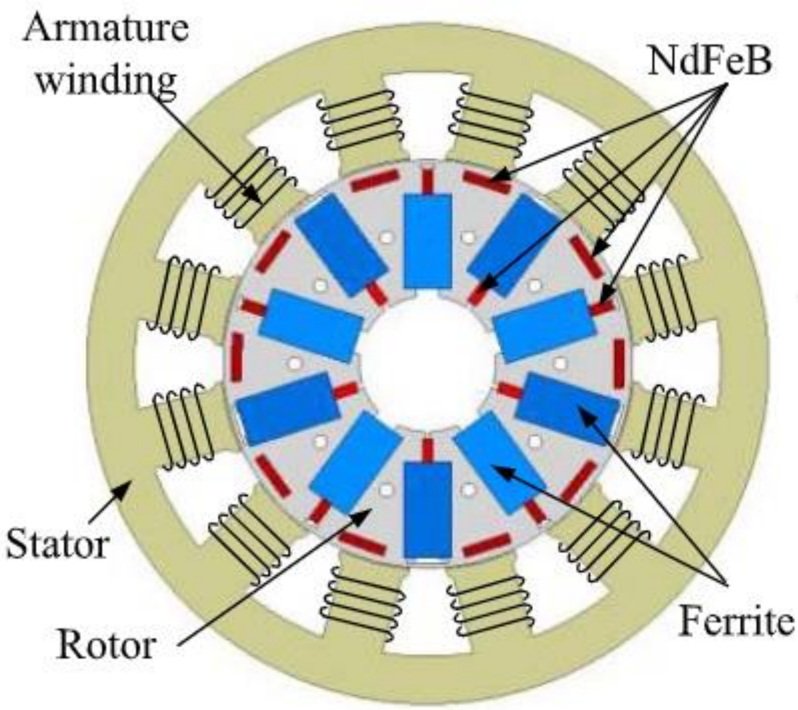

Figure 3. 22 Showing the optimised mixed series/parallel topology of hybrid magnets [144].

Through simulation and experimental verification the proposed optimisation was found to improve the torque by 8% and torque ripple decreased by 11% [144]. This only demonstrates the principles of the first study where a change in motor design can improve the performance but still no real comparison can be made to a motor consisting mainly of RE magnets [142].

A recent study compared two motors with similar design, but the standard motor consisted of only Nd-Fe-B, and the second motor introduced ferrite magnets (Figure 3. 23) [145]. Which is the opposite to what Chen *et al.* proposed [143], [144].

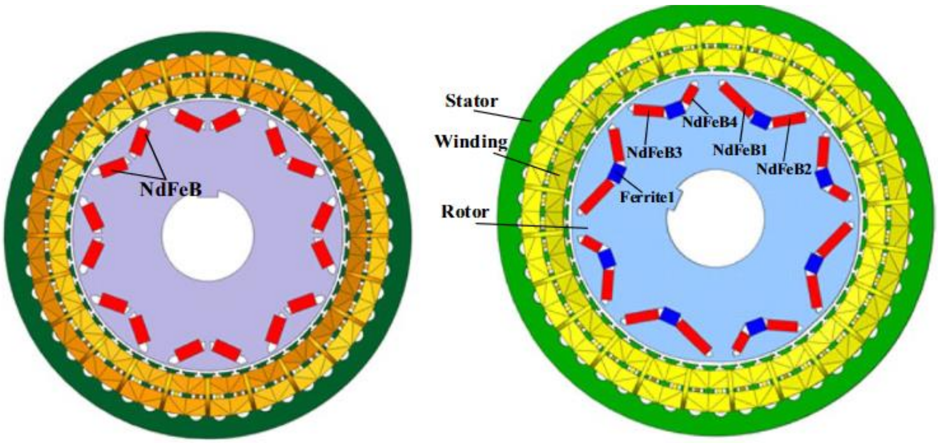

Figure 3. 23 Showing the two topologies of motor with traditional permanent magnet motor (TPMM) (left) and asymmetric hybrid permanent magnet motor (AHPMM) (right) [145].

Through theoretical analysis and verification with experimental methods and an optimisation method that with the introduction of Ferrite into the motor, the quantity of RE materials is reduced by 18.5% without any decrease in the output torque. As slightly mentioned in other studies but more prevalent by Liu *et al.*[145], an important aspect is the magnetic flux circuit shown in Figure 3. 24.

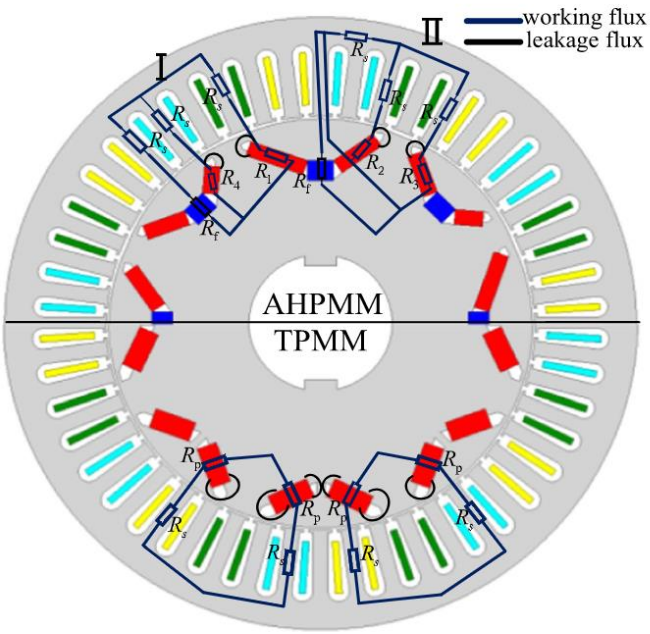

Figure 3. 24 Showing a simplified magnetic circuit comparison diagram of the AHPMM and TPMM [145].

The introduction of the ferrite, with a small change in the NdFeB size and position angles, changes the route of the magnetic circuit. This change confines the magnetic flux and with the combination of series and parallel magnets the total reluctance in the magnetic circuit is reduced whilst increasing the total permeability with a saving of the quantity of RE material used.

This study demonstrates a more realistic method of optimising a permanent magnet electric motor with a hybrid-magnet system. The reduction of RE material will lower the cost and ensure that the material is only used where it is necessary, and the cheaper ferrite can be used to try and bridge the performance gap. This approach seems the logical direction to pursue until more sustainable RE-free magnetic materials with good properties are established through a reliable mass manufacture path.

3.6 Summary

Nd-Fe-B permanent magnets have emerged as one of the leading magnetic materials for a diverse range of applications due to its high BH_{max} and coercivity. Through a relatively unchanged manufacture route, and being an Fe based material it is used more often than the Sm-Co materials which do show better performance at higher temperatures. Approaches in improving the coercivity of Nd-Fe-B have mainly been by the introduction of a non-magnetic or anti-ferromagnetic material, such as Dy or Tb. Initially by addition to alloy and the later by GBD process to reduce the quantity of RE material used. PM based electric motors are one of the most common found within modern electric cars due to their high energy density, and simple control and design. PM’s used within these motors have the issue of a loss of magnetic performance at higher or operational temperature of the motor, which leads to an overall loss of performance of the motor, and the REE content increases the price of the materials. The end goal would be to produce a hard magnetic material with suitable properties that contains no REE’s, but in the meantime a shift towards a reduction in the use of REE’s must be the route towards that goal in order to meet climate change goals, and a sustainable energy future. As the total removal of RE-magnets from applications will significantly reduce the performance of the motor, the RE-magnets must be used optimally, and alternative more abundant magnetic materials must be utilised to bridge the gap of cost against performance.

4. Methodology

This research included simulation work of 1D, 3D and *in-situ* measurements of an electric motor using finite element modelling (FEM). Experimental characterisation of magnetic properties was also obtained. Detailed in this chapter are the processes involved in creating a working model, the experimental sample preparation procedure and characterisation techniques used.

4.1 Simulation

The aims of the simulations were to identify suitable models, first in 1D, then investigate how this translates and compares to 3D using FEM, models that showed promise were implemented within an electric motor simulation.

4.1.1 1D model

The reasoning behind creating a 1D model was to quickly and easily create a model that can accurately calculate the demagnetisation field at the internal edge of a magnet. Creation of such a model allowed for much more control of magnetisation and gave an insight to locally measured values anywhere inside the magnet. The model is based on magnetic pole theory, where pole strength (P) is calculated from a change in magnetisation (ΔM) and an area (A), adapted from [146]:

$$P = \Delta M \times A \qquad \textit{(Equation 4. 1)}$$

Imagine a cylindrical magnet, which has a length (L_t) and radius (r), a single cylindrical magnet's pole strength can be calculated from the change of magnetisation (ΔM) found at the pole surface from the "air" to the magnet. Rather than having one large cylindrical magnet, the cylinder is divided into many cylindrical "slices" (cells) which gives the same overall magnetic values as the large magnet but gives a more detailed view of local fields inside the magnet, shown in Figure 4. 1.

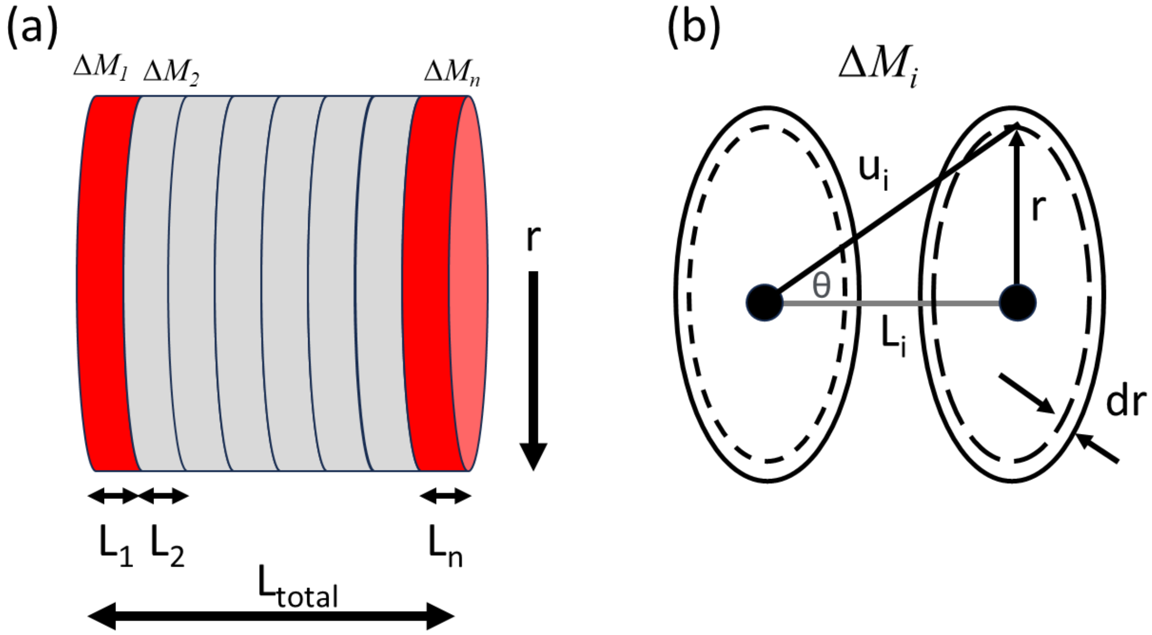

Figure 4. 1 The 3D representation of the 1D mathematical model. Here the magnet is of total length L_{total} with radius r. (a) schematic of the magnet broken into 8 elements, each of length d. The red elements indicate a region of different magnetization. The change in magnetization ΔM *can then be found across each element. (b) a single element highlighting the relationship between u, radius r, and element size L_i.*

To recreate pole theory into a 1D model the following is applied. Firstly, the area is defined as:

$$A = 2\pi \, r \, dr \qquad \textit{(Equation 4. 2)}$$

Where a theoretical/potential small difference in radius (*dr*) can be used to calculate area.

$$u^2 = L^2 + r^2 \qquad \textit{(Equation 4. 3)}$$

As with Pythagorean theorem, the hypotenuse distance (*d'*) is calculated from the radius and distance of the cell. Now equation 4.4 can be satisfied, adapted from [147] .

$$H = \frac{P}{4\pi u^2} \, cos\theta = \frac{\Delta M \times A}{4\pi u^2} \, cos\theta \qquad \textit{(Equation 4. 4)}$$

Where,

$$cos\theta = \frac{L}{u} = \frac{L}{\sqrt{(L^2 + r^2)}} \qquad \textit{(Equation 4. 5)}$$

Equation 4.2, 4.3 and Equation 4.5 can be substituted into Equation 4.4 to give the following Equation 4.6:

$$dH = \frac{2\pi\, \Delta M\, r\, dr}{4\pi(L^2 + r^2)^1} \frac{L}{(L^2 + r^2)^{1/2}} = \frac{2\, \Delta M\, L\, r\, dr}{4\,(L^2 + r^2)^{3/2}} \qquad \textit{(Equation 4. 6)}$$

$$H = \left[-\frac{2\, \Delta M\, L}{4(u)^{1/2}} \right]_{u=L^2}^{u=L^2+r^2} \qquad \textit{(Equation 4. 7)}$$

Introducing the new limits and cancellations gives the final equation:

$$H = \frac{\Delta M}{2} - \frac{\Delta M\, L}{2(L^2+r^2)^{1/2}} \qquad \textit{(Equation 4. 8)}$$

The final Equation 4.8 is therefore dependent on a change in magnetisation, the length and radius of the cell. The many cells can be used to find local fields which make up the larger full scale cylindrical magnet.

The source of the field is derived from where there is a change in magnetisation. The example in Figure 4.1 shows a uniformly magnetised bulk magnet (blue) with a uniformly magnetised film (red) which is of a different magnetisation to that of the bulk material. For this case, there are four changes of magnetisation, from this change there is a source of field at the interface between cells, which is then calculated as an effective field in every cell. So, the further away from the source, the weaker the effective field will be. Within this model, external field values can be calculated by stating a distance for the external field, achieved by changing the cell size and then setting the magnetisation to zero, to replicate that of the air. A field will be generated in the air region from the change in magnetisation at the magnet surface.

An equation for coercivity used to in later chapters is defined as:

$$H_c = -\frac{2K}{\mu_0 M_s} + H_d \qquad \textit{(Equation 4.15)}$$

4.1.2 3D model

To test the validity of the 1D model, using pre-established FEM software is crucial. The 1D model was replicated within COMSOL Multiphysics [148] with a coordinate system relevant to the applied to make the addition of films and changing the magnet dimensions later easier. The initial comparison involves the magnetic cylinders discussed in Section 4.1.1 and involves the exact dimensions of a length 3 cm, and radius 0.5 cm. The model transitions to cubic cylinders the more accurately represent the geometry of magnets used in the final application, shown later in Section 6.4.

4.1.3 Motor Simulations

Our industrial partner VW GI, provided a motor geometry that they can still use information gained from the model in comparison with their models. The geometry provided in Figure 4. 2 will first be set up in ANSYS Maxwell with the correct applied and working physics. This will serve as a benchmark during the transition of the model into COMSOL. The way rotating machines are modelling varies between COMSOL and ANSYS, so it is vital that the models set up in both software produce the same results under a standard condition. Comparable results are vital to achieve reliable results when introducing different magnetic architectures into the simulation.

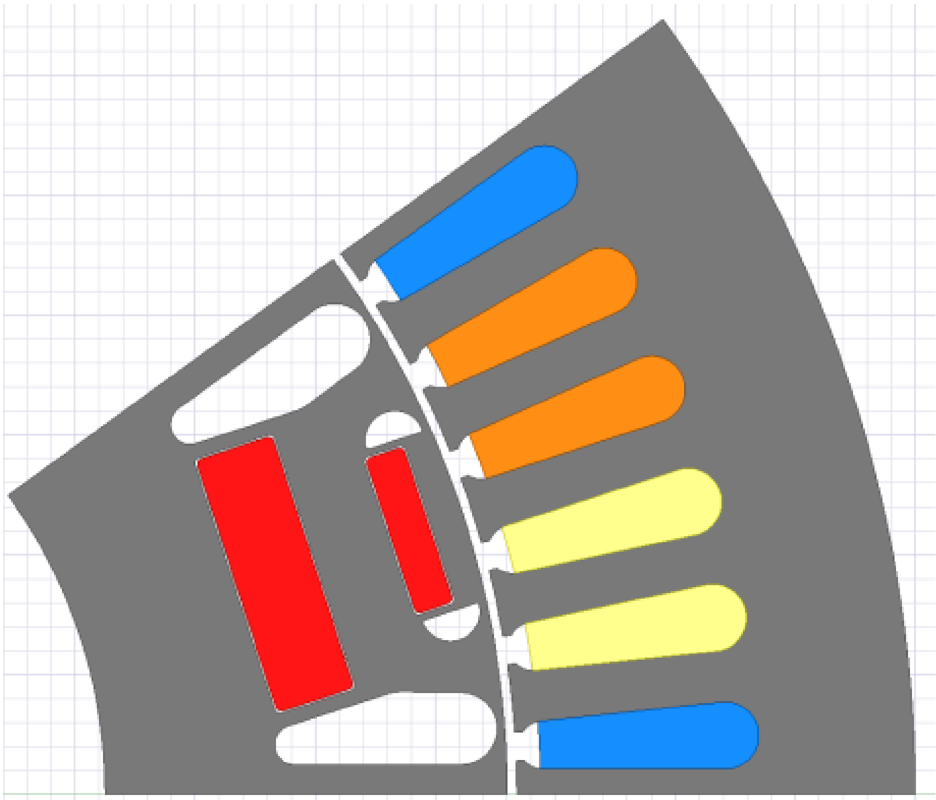

Figure 4. 2 Showing the motor geometry, with the rotor and stator Iron (grey), the magnets (red) and the phased windings (blue, orange, yellow).

The phases work as follows, orange:Phase A, yellow:Phase B, blue:phase C, where both coils in phase A are considered positive, both coils in phase B will be negative and the top coil of phase C will be negative and the bottom one will be positive. The properties for the magnet are provided at operational temperature, as well as BH-curve data for the iron stator and rotor to be used in the magnetic modelling physics.

4.1.3.1 Motor parameters

To create the working motor, certain parameters have initially been set in regard to material properties and definitions for the coils; the main parameters to have a basic model are described below in Table 4. 1.

Table 4. 1 Describing the parameters required and used within COMSOL to create a working model.

Name	Expression	Description
Rpm	1000[rpm]	Revolutions per minute
Nturn	N/A	Number of turns in coils
Imax	600[A]	Max current amps
PolePair	N/A	Number of different working magnet pairs
Sectors	10	Number of sectors to create entire architecture
Offset	30[deg]	Optimal initial angle of offset
T_tot	12[ms]	Working simulation time
Ms	1.18[T]	Magnetisation saturation @ 361.15K
Modellength	N/A	Depth (Z-axis model length)

Some of the parameters are used in the definitions of the variables which as the name suggests will change over time and rotation. Listed in Table 4. 2.

Table 4. 2 Describing the variables required and used within COMSOL to create a working model.

Name	Expression	Description
I_A	$I_m \sin((\sigma\,\beta) - (\emptyset\,\beta))$	I_m= Maximum Current [A] σ = Position of rotation β = Number of pole pairs $\emptyset$ = Offset angle [Deg]
I_B	$I_m \sin((\sigma\,\beta) - (\emptyset\,\beta - 120))$	I_m= Maximum Current [A] σ = Position of rotation β = Number of pole pairs $\emptyset$ = Offset angle [Deg]
I_C	$I_m \sin((\sigma\,\beta) - (\emptyset\,\beta - 240))$	I_m= Maximum Current [A] σ = Position of rotation β = Number of pole pairs $\emptyset$ = Offset angle [Deg]
σ	$2\,\pi\,\nu\,t$	ν = Revolutions per minute [s^{-1}] t = Rotational time [s]

4.1.4 Graded magnetisation

For the use of controlling the magnetisation profile in simulations. The radius of an ellipsoid is used at the template for the magnetisation profile, shown in Figure 4. 3.

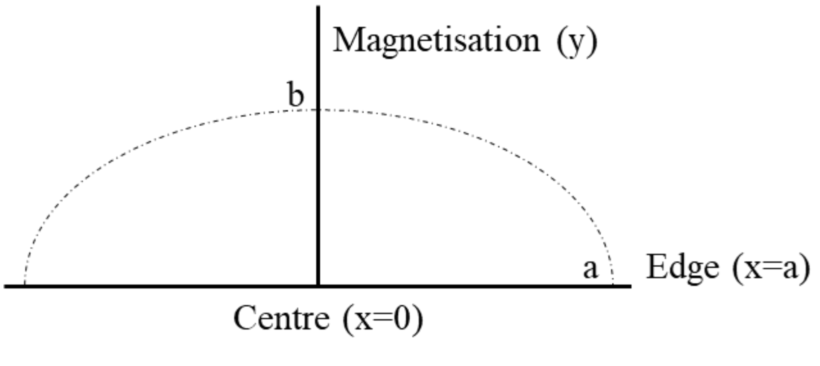

Figure 4. 3 Showing the magnetisation profile as the profile as an ellipsoid.

Consider the 1D model as the x-axis, instead of having a uniform magnetisation from edge to edge, scaling the magnetisation as a function of the ellipsoidal radius equation below.

$$1 = \frac{x^2}{a^2} + \frac{y^2}{b^2} \qquad \textit{(Equation 4. 9)}$$

$$y = b\sqrt{(1 - \frac{x^2}{a^2})} \qquad \textit{(Equation 4. 10)}$$

Equation 4.9 has been rearranged to find *y* which when mapped onto Figure 4. 3 is the calculated magnetisation. With b being the peak magnetisation at *x*=0, where *x* is the position along the magnet and a is max length from the centre to the edge. Manipulation of equation 4.9 allows for changing graded magnetisation profile. As the equation previously consisted of two dimensions and one of them has now being replaced by the magnetisation profile. When introducing this property into 2D and 3D models, certain considerations and alterations to the equation will need to be made to incorporate the extra dimensions needed in the equation.

$$\Delta = d\sqrt{\left(1 - \frac{x^2}{2\phi a^2} - \frac{y^2}{2\phi b^2}\right)} \qquad \textit{(Equation 4. 11)}$$

$$\Delta = d\sqrt{\left(1 - \frac{x^2}{3\phi a^2} - \frac{y^2}{3\phi b^2} - \frac{z^2}{3\phi c^2}\right)} \qquad \textit{(Equation 4. 12)}$$

The calculated magnetisation Δ can now be calculated as a function of the peak magnetisation and either ½ or 1/3 of the x,y,z axis variables with a term ϕ (Lscale) used as a scaling factor to give greater control of the magnetisation profile by forcing the mathematics to extend or reduce the length of the graded region of magnetisation.

4.1.5 COMSOL Multiphysics equations

For results of the simulations to be obtained, FEA follows the method discussed in Section 2.2 where the problem is broken down into smaller basic equations and then solved for the larger problem. A description of the simulation physics problems is broken down below:

<u>Isolated magnets in a stationary model</u>

A magnetic material has a remanent flux density, which is radiated as external field through magnetic flux conversion. The magnet is suspended inside an air region which has a relative permeability and a magnetic insulation, there is also a magnetic flux conservation for the air region. Table 4.3 below describes the equations used within COMSOL to solve and Table 4.4 displays the material properties used within the solution.

Table 4.3 Displaying the COMSOL solution equations to solve for a stationary model for isolated magnets.

Physics	Equations	Comments
Magnetic Flux Conversion	$\nabla \cdot \boldsymbol{B} = 0$	
Magnetic Flux Conversion	$\boldsymbol{B} = \mu_0 \mu_r \boldsymbol{H}$	Where, $\mu_r$refers to a materials permeability
Magnetic Flux Conversion	$\boldsymbol{H} = -\nabla V_m$	
Magnetic Insulation	$n \cdot \boldsymbol{B} = 0$	Boundary of non-permeable magnetic field
Remanent Flux Density	$\boldsymbol{B} = \mu_0 \mu_{rec} \boldsymbol{H} + \boldsymbol{B_r}$	Where, μ_{rec} is the recoil permeability and B_r is the remanent flux density norm of the material.

Table 4.4 Displaying the relevant material properties and their values to satisfy the relevant equations and solutions.

Material	Property	Value
Nd-Fe-B	Remanent flux density (**B**)	1.31 T
Nd-Fe-B	Relative permeability (μ_r)	1.05
Air	Remanent flux density (**B**)	0 T
Air	Relative permeability (μ_r)	0

Electric motor stationary model

A stationary model of the electric motor is required to calculate all initial values at a time of 0s. All the regions; air, magnets, stator and rotor require Ampere's law, with the magnetisation model for the magnets being remanent flux density and the rotor and stator Iron having a B-H curve relationship with the curve data provided by VW GI. Table 4.5 below describes the equations used within COMSOL to solve and Table 4.6 displays the material properties used within the solution.

Table 4.5 Displaying the COMSOL solution equations to solve for a stationary model of an electric motor model.

Physics	Equations	Comments
Amperes Law	$\nabla \times \boldsymbol{H} = \boldsymbol{J}$	Where, *J* is the electrical current
Amperes Law	$\boldsymbol{B} = \nabla \times \boldsymbol{A}$	
Amperes Law	$\boldsymbol{J} = \sigma \boldsymbol{E}$	
Amperes Law	$\boldsymbol{B} = f(\lVert\boldsymbol{H}\rVert)\frac{\boldsymbol{H}}{\lVert\boldsymbol{H}\rVert}$	B-H relationship for soft Iron.
Coil	$\boldsymbol{J_e} = \frac{N\, I_{coil}}{\boldsymbol{A}}\boldsymbol{e_{coil}}$	

Table 4.6 Displaying the relevant material properties and their values to satisfy the relevant equations and solutions.

Material	Property	Value
Soft-Fe	BH-Curve	Data provided by VW GI
Copper	Electrical Conductivity	Data provided by VW GI

<u>Electric motor, time dependent model</u>

All applied physics remained the same for the time dependent model, with the addition of Ampere's law for the coils which would be active over the time scale. Table 4.7 below describes the equations used within COMSOL to solve.

Table 4.7 Displaying the COMSOL solution equations to solve for a stationary model of an electric motor model.

Physics	Equations	Comments
Force - Torque	$\boldsymbol{F} = \int_{\partial\Omega} d\,\boldsymbol{n}\,T\,dS$	
Force - Torque	$\boldsymbol{\tau} = \int_{\partial\Omega} d(\boldsymbol{r} - \boldsymbol{r_0}) \times (\,\boldsymbol{n}T)\,dS$	
Force - Torque	$\tau_{ax} = \frac{\boldsymbol{r}_{ax}}{\lvert\boldsymbol{r}_{ax}\rvert} \cdot \boldsymbol{\tau}$	

5. 1D Model

5.1 Introduction

Modelling is an important step for many research areas to provide detailed analysis of criteria in a relatively short time, compared to replicating the conditions experimentally and then completing analysis. The 1D model developed in this chapter is to investigate the effect thin films have when acting as a capping material. These will be placed onto the poles (easy-axis) of a bulk magnetic material, focusing the investigation on the film and interface regions. Creating a mathematical model allowed for much greater control over the chosen length scale of the magnet and having the benefit of the model instantly updating to any changes made.

5.1.1 Explanation of terms

Discussed in this chapter will be the methods and reasoning behind the chosen approach. But to understand the results, a few terms will be explained and defined for context.

The first term and probably the most important due to it being the main aim of research is the **demagnetisation field**. The demagnetisation field is a local field calculated for each internal cell and gives an indication of how likely magnetisation reversal is or the stability of the internal field. Demagnetisation field for a uniformly magnetised material is negative, where a higher negative value implies the region is more likely to reverse its magnetisation at that point.

The second term, and one of the most associated with bulk magnetic materials, is the **external field**. External fields in literature are often called a few different things but to avoid discrepancies between terms that will later be discussed, the field measured externally that is delivered by the magnetic model will be called external field. External fields here are positive values and will increase with the proximity of the magnet surface and reduce with distance.

5.1.2 Figure of Merit

As the modelling can become complicated with the different iterations, a figure of merit (FoM) was used to have one number to suggest if the changes to the model have a positive or negative effect on the performance. The FoM looks at the changes of both the demagnetisation and external field, where it is ideal to have a larger reduction in the demagnetisation field than the inevitable and unavoidable reduction to the external field. This can be shown in equation 5.1.

$$Figure\ of\ Merit = \frac{\%\ reduction\ of\ external\ field}{\%\ reduction\ of\ demagnetisation\ field} \qquad \textit{(Equation 5. 1)}$$

5.2 Creating a working model

After verifying the mathematics was correctly calculating local magnetic fields. The process began to create a working model that simulated magnetic cylinders that gave results comparable to the literature. The initial concept of the model was to have larger cell sizes for the uniform bulk material and then reduce the cell size towards the edges in the aim of providing a more detailed look at the more important region. This assumption was made on the theory of the largest demagnetisation field being at the edge of the magnet, therefore simulation of the centre of the magnet is not as key to see a change It is noted that the magnetisation value and radius remained constant throughout the following models, only the cell size is altered to optimise the model to look at the desired edge regions. The first line scan is shown in Appendix Figure A1.

Initially demagnetisation energy was the first term investigated and was later changed to demagnetisation field. Although the values between the two will be different, the plots remain the same as the demagnetisation energy is calculated from the demagnetisation field but there is an inverse of the sign in the values and will be shown as an example later. From observing Figure A3, it appears to show that the highest demagnetisation energy resides in the middle region and that the lowest demagnetisation energy is at the edges, which is counter to theory. Further iterations were required to tune the model to get the desired outcome.

The transition from Figure A1 to A5 can be described as a desire to produce a line scan with a continuous flowing curve and contains no sudden increases of gradient. This involved modifying the call size length (L_i) in order to have more detail and refinement of the edge region. However, this did not provide the expected result and required a uniform cell length to be required to provide a characteristic smooth curve. The following work discusses the model iterations of a uniform cell length and comparisons of the terms; demagnetisation field and external field.

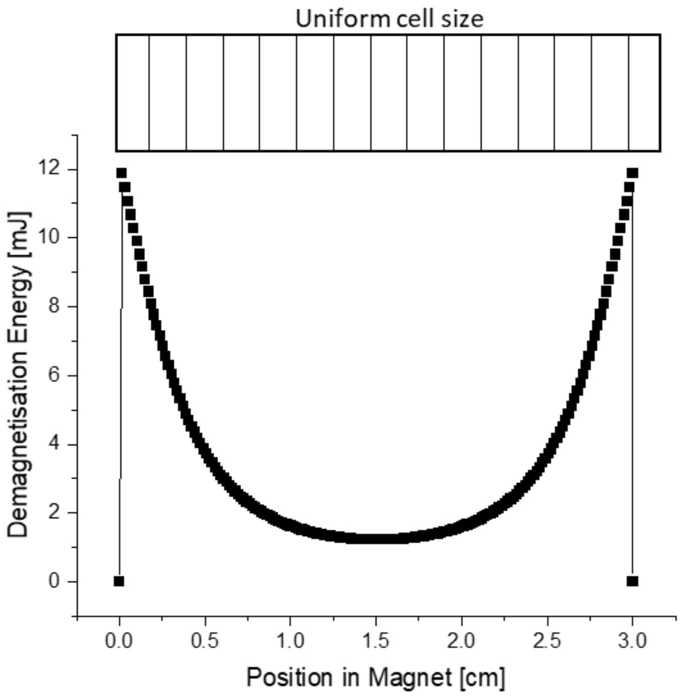

Figure 5. 1 Showing a line scan of demagnetisation energy with a uniform cell size.

Creating a model with a uniform cell size appears to have solved both issues previously mentioned, the sharp gradients in the line scan and the calculated values for demagnetisation energy suggested that the middle region was the highest. Figure 5. 1 shows a very smooth curve that shows the edges of the magnet having the highest demagnetisation energy, which is to be expected. At this point in creating the model line scans included an air region with the same cell size but with zero magnetisation. This is required to allow the model to work as it relies on changes in magnetisation, the points that are now only visible as outliers where there is zero demagnetisation energy at the edges are this air region and are removed from later models.

Now that the has been verified to work correctly, the number of cells used in the model are increased to allow for a reduced cell size and give a more accurate picture of the line scan data. This is shown in Figure 5. 2.

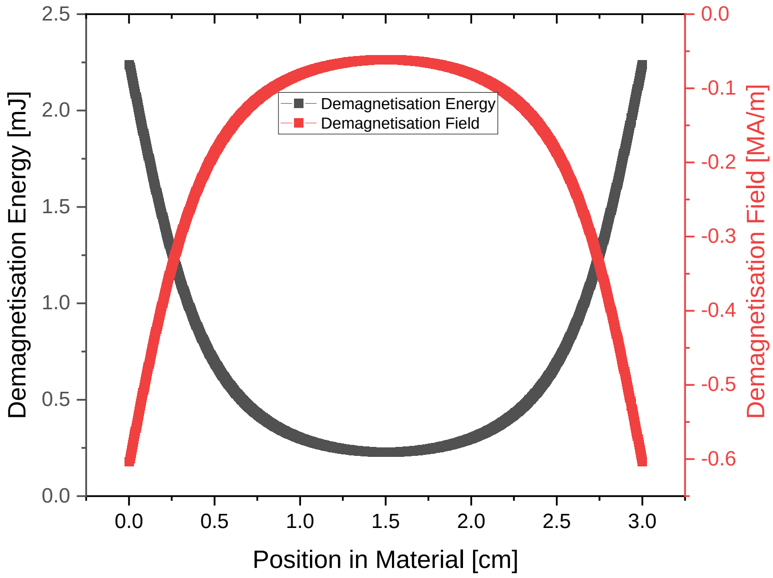

Figure 5. 2 Showing the line scans of demagnetisation energy and field for the new model with an increased number of cells and a decrease in uniform cell size.

Now a working model has been presented we use it now to produce line scans which is the accumulation of approximately one thousand cells each solved for their local fields and energies. The model simulated is a magnetic cylinder with the magnetisation direction in the plain of the line scan from pole to pole. Producing the line scan in Figure 5. 2, where demagnetisation energy and field are at their highest magnitude at the very edge of the magnet and having a region of stability at the centre. This agrees well with the theory; hence, it can be concluded that the 1D model is correctly calculating the demagnetisation field.

5.3 Uniform magnetisation film

Once a working model had been created, the use of magnetic thin films as a capping layer was investigated. The initial premise was to look at what existing magnetic materials are available and that can be used for this purpose, with the aim of reproducing experimentally later. The investigation initially looked at the use of Fe and MnAl, where Fe is readily available in multiple mediums and MnAl, although not made in a bulk material yet, did appear to show desirable properties when looking amongst the Novamag database [149]. Shown in Figure 5. 3 are the line scans for an example of both cases.

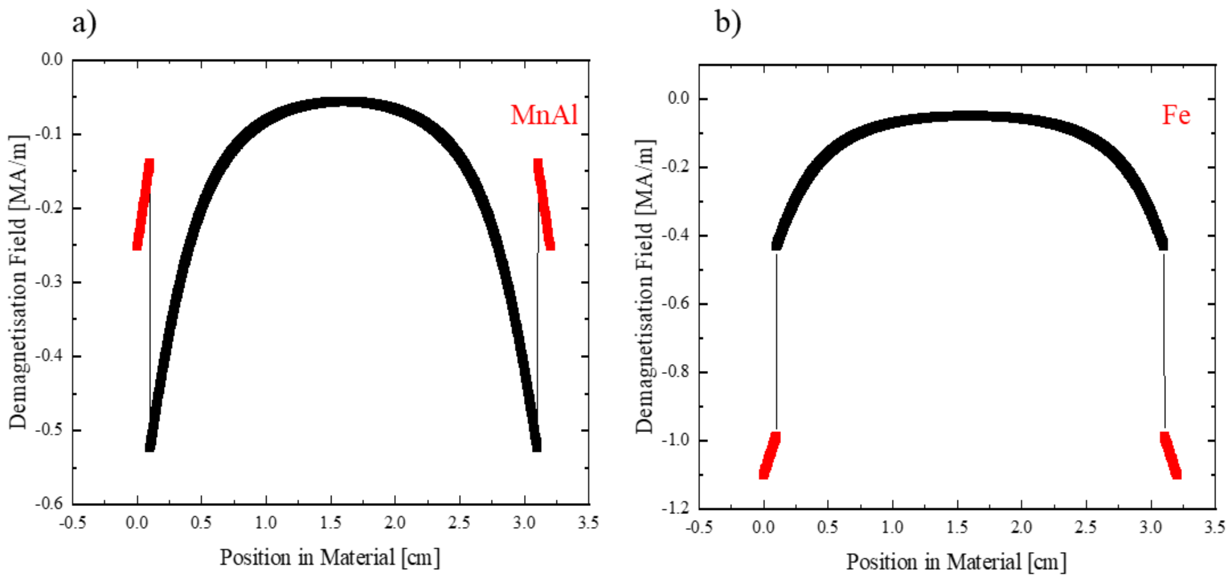

Figure 5. 3 Showing line scans of demagnetisation field for uniform 3cm Nd-Fe-B with 1mm of capping material a) MnAl and b) Fe, the film region (red) and the bulk region (black).

In Figure 5. 3, the results are shown for a magnetic bulk material NdFeB (black) (1.2 MA/m), capped with two different materials (red) that have magnetisation either higher or lower than that of NdFeB.

MnAl having a magnetisation of M=0.8 MA/m, therefore lower than the bulk, clearly shows a reduction in the demagnetisation at the edge. Reducing from H_d=-0.6 MA/m for the uniform case to around H_d =-0.53 MA/m when 1 mm MnAl film is applied. The reduction can be explained by referring to equation 2.11 where the demagnetisation field magnitude is related to the magnitude of the magnetisation. The MnAl film acting independently will have a lower demagnetisation field than that of NdFeB due to it simply having a lower magnetisation, this can be observed in Figure 5. 3, this region acting as a sort of anchor and stabilising region of low demagnetisation field reduces the demagnetisation of the adjacent bulk region. This highlights the main idea, where the use of a film affects the demagnetisation field of the bulk material.

Although MnAl showed promise at reducing the demagnetisation field, Fe was modelled as a simple proof of principle and a material that can easily be used experimentally. Fe was not a real candidate for a suitable material to achieve the reduction of demagnetisation field but as a proof of concept, using an Fe film should increase the demagnetisation field and compromise the stability of the magnet. This prediction is observed to be correct in Figure 5.

3, for the same principle that MnAl produces a smaller demagnetisation field than the bulk material. Fe (M=1.7 MA/m) produces a larger demagnetisation field which becomes a much larger region of instability, which when exposed to any load fields would be more likely for demagnetisation to occur. This highlights that Fe would certainly not be a suitable material for any application but does confirm the principle.

While the reduction of the demagnetisation field in the magnet is the main aim, the method of applying thin films to do so will also have an effect on the external field delivered by the magnet (Figure 5. 4).

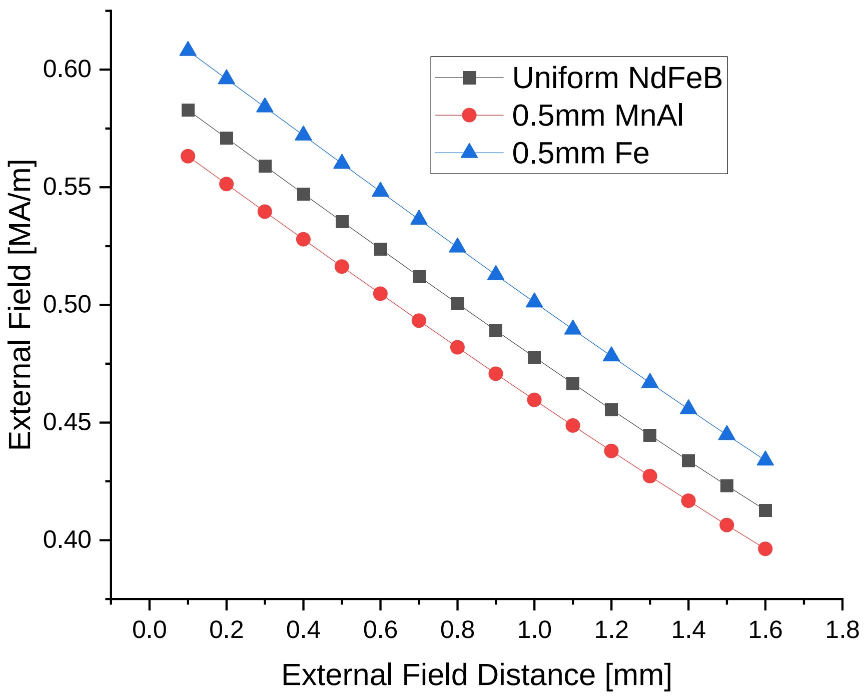

Figure 5. 4 Showing the external field delivered by a uniform magnet, a cap of 0.5mm film of MnAl and Fe.

Influencing the internal demagnetisation field has an unintentional, and in most cases, an undesirable effect on the external field. As seen in Figure 5. 4, using a film of Fe increased the external field delivered by the magnet even over larger distances as there was an introduction of material with a larger magnetisation into the system, this increase is to be expected. As is the reduction of the external field seen in the use of a lower magnetisation material in MnAl. This is where it is first observed that there is a trade-off between two types of fields associated with the magnet. This poses the question: can the demagnetisation field be reduced further than the associated reduction in the external field.

A few more investigations were carried out to confirm the basis of the model and give more faith in what results future simulations will give and if they can be comparable.

The model of the system has previously been a 3cm bulk material with the film placed on each size to make the model > 3 cm in length. To allow for future results to be comparable it was decided that the total length of the magnet would equal 3cm. Meaning that however thick the film was, this would end up replacing a portion of the bulk material to keep a constant 3cm simulation length (Figure 5. 5).

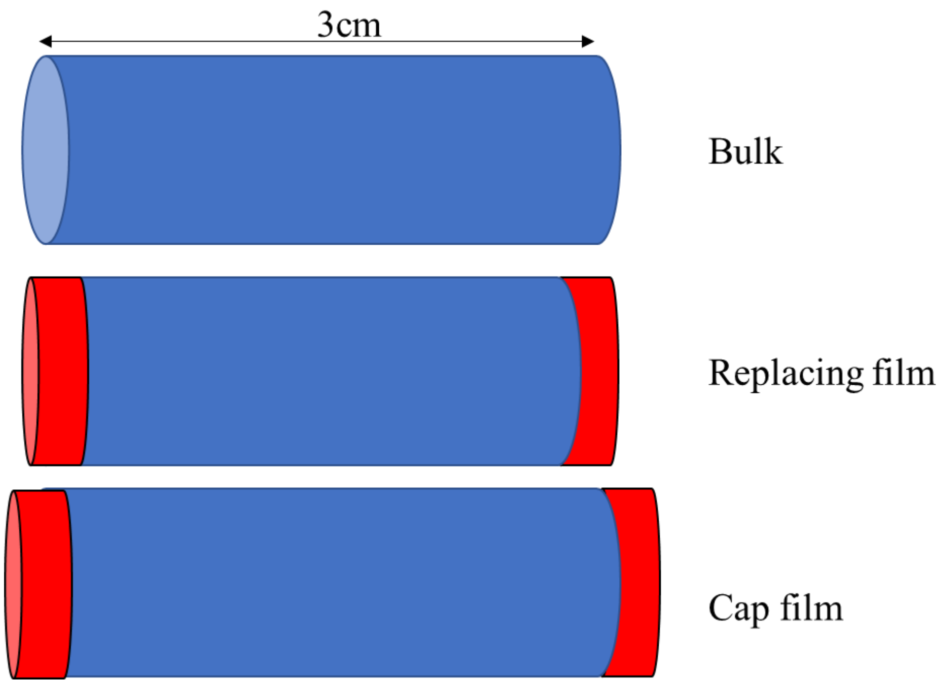

Figure 5. 5 Showing a visualisation of the difference in a replacing and capping film compared to the standard bulk example to maintain a constant uniform 3cm magnet length.

This is also thought to be helpful for experimental applications as the physical magnets supplied by VW were most likely the sizes they are for a reason. An investigation into the difference between the two methods of films as either a cap or a replacing film has on the calculated external field (Figure 5. 6).

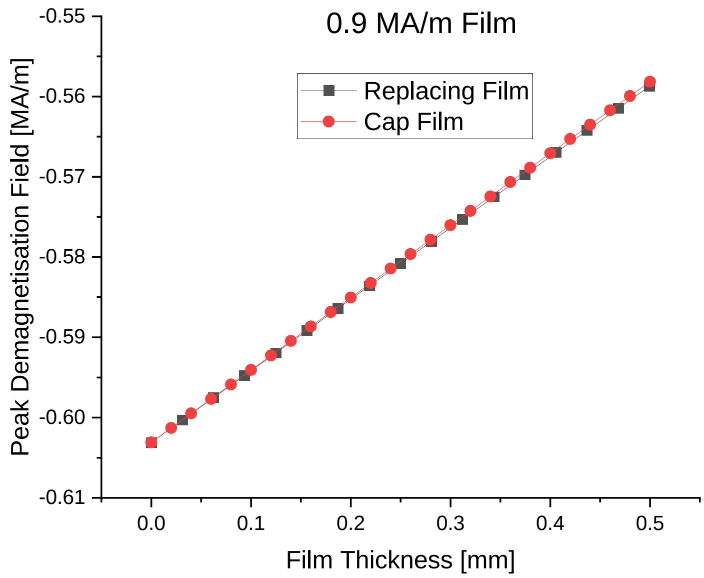

Figure 5. 6 Showing the external field for the different film application systems, of either a cap (>3 cm length) or a replacing film (=3 cm length) using a film magnetisation of 0.9 MA/m.

The different systems for film application appears to have a very small difference, with the use of a replacing film reducing the peak demagnetisation field more as the films become thicker. The difference in the two systems starts of at 0% for no film and then increases to 0.1% for a 0.5 mm film, this slight difference in the two systems could be down to the total length of the model and the total amount of magnetic material or due the replacing film removing some of the bulk material, hence making the demagnetisation field in the bulk lower. As the replacing film method reduced the peak 0.1% demagnetisation field more this is the method that will be followed going forward.

As previously shown in Figure 5. 4, the external field delivered by the magnet reduces over distance but is the distance at which the field is calculated important to the obtained results for such things as a varying film thickness (Figure 5. 7).

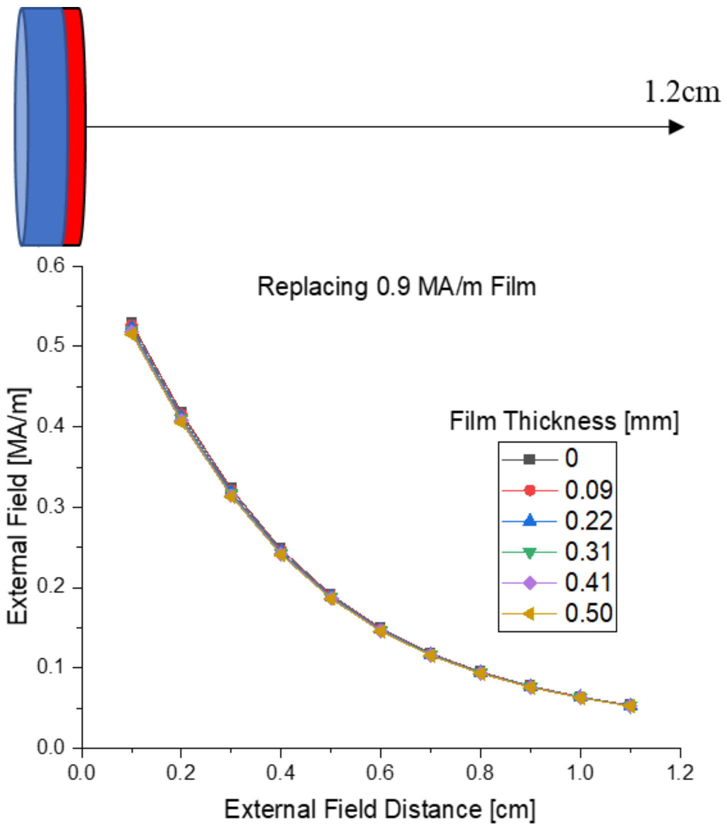

Figure 5. 7 Showing external field values for varying replacing film thickness with a magnetisation of 0.9 MA/m.

The external field values appear to converge over a greater distance, this highlights that the chosen distance to measure is important. If a distance closer to the magnets surface is chosen, then there is a larger variability between the measured values. For example, there is a 3% difference when comparing the magnet with no film to a 0.5 mm film at a distance of 0.1 cm from the pole. Whereas there is a 2.2% difference 1.1 cm from the pole surface. This is also an important concept to understand when thinking about actual applications. As within a motor for example, the distance of the magnets to the stator coils needs to be considered to not have varied performance and to try and find an optimal distance.

Considering that the external field converges over greater distances, a realistic application distance is considered to look at if this influences how the FoM is perceived. Figure 5. 8 shows the FoM for a varying film thickness.

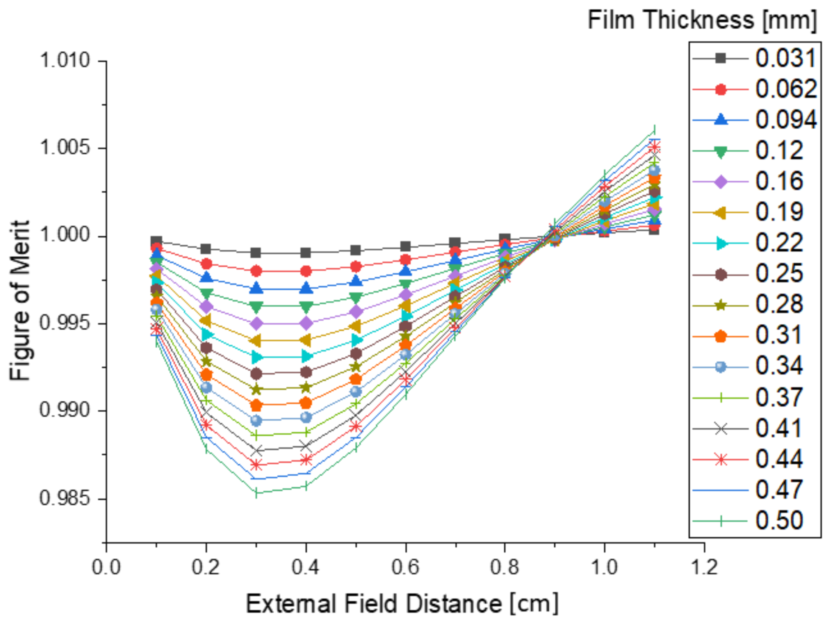

Figure 5. 8 Showing the figure of merit for varying film thickness of 0.9 MA/m over external field distances.

Using a film magnetisation of 0.9 MA/m, Figure 5. 8 was constructed by varying the film thickness and studying the effect varying the chosen external field distance has on the FoM. The FoM for the chosen magnetisation of 0.9 MA/m only becomes greater than 1 when measured at around 0.9 mm from the magnet surface. Beyond this point, all models show a FoM greater than 1, with the thickest film having the largest FoM beyond this distance, peaking at a 0.5% increase. This again shows that it is important to consider which external field distance will be chosen to be included in a final FoM.

To compensate for the reduction of the external field delivered by the magnet which occurs by affecting the edge of the magnet. The centre of the magnet can be affected in the opposite way to give a boost to the external field without compromising the integrity of the magnet with the increase to demagnetisation field in the centre. Theory suggests the centre region is the most stable as it has the lowest demagnetisation field. This implies that an increase to the magnetisation in the centre would contribute to an increase of external field, and not affect the demagnetisation field at the edges of the magnet (Figure 5. 9).

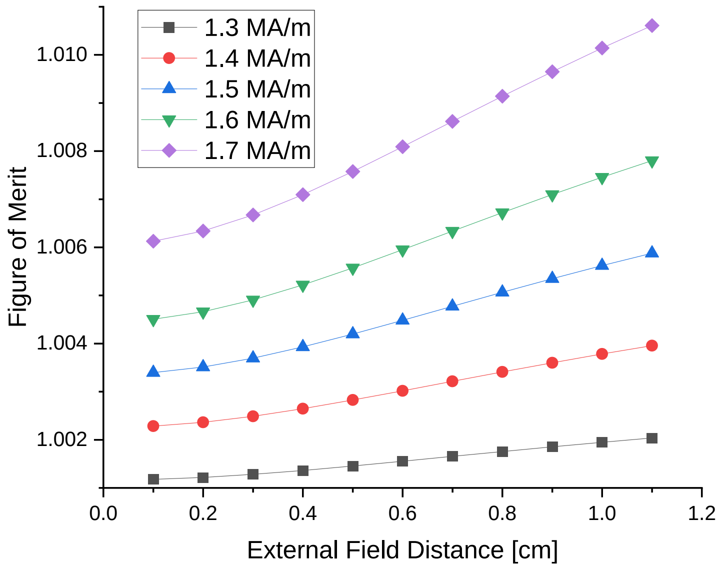

Figure 5. 9 Showing the external field of the magnet when the centre 1.1mm of the bulk material is replaced with a higher magnetisation value.

Replacing some of the centre region of the magnet seems impractical and maybe a little difficult to create physically, especially the case of using a 1.7 MA/m which is that of Fe, which would prove impractical. However, this does prove the principle that increasing the centre magnetisation does provide benefits to the external field. This could be achieved by doping Fe to create an Fe-rich region at the centre, rather like how literature describes Dy-rich regions at the edge to improve coercivity.

Rather than focusing on what existing magnetic materials are fit for purpose, as this does not provide a diverse range of materials to investigate and simulate. Instead, the best film magnetisation will be chosen based on their simulation results irrespective of whether a material exists with those properties (Figure 5. 10).

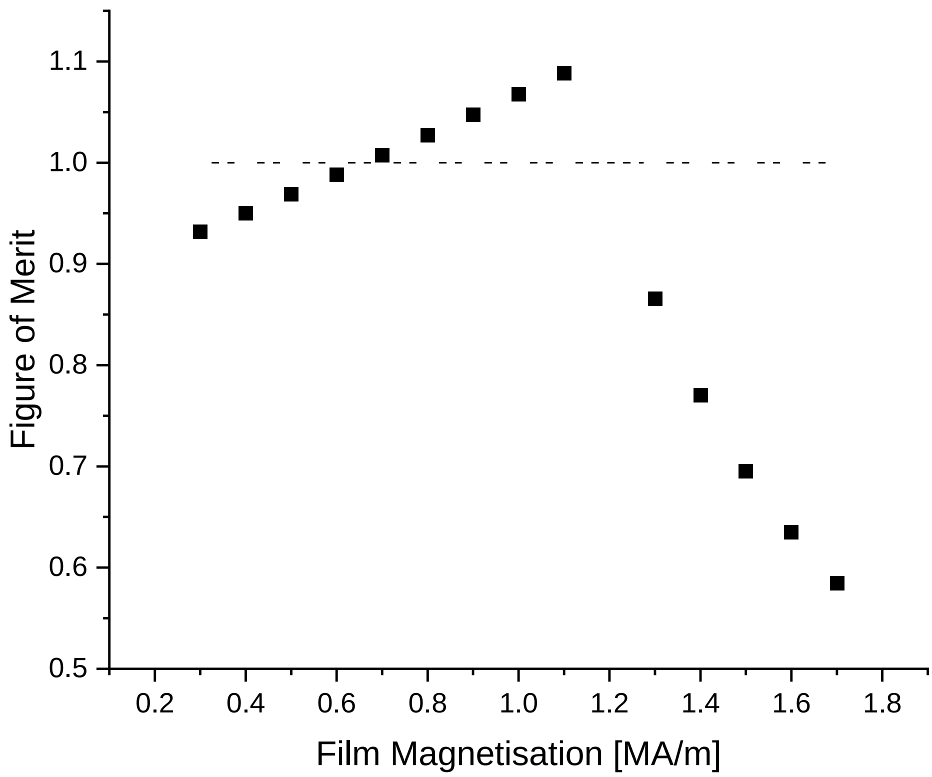

Figure 5. 10 Showing the figure of merit for a 2.9cm NdFeB magnet with 0.5mm film on either side, external field value 1.1cm from pole surface.

Shown in Figure 5. 10 the highest FoM is from the film with a magnetisation of 1.1 MA/m, closest to that of the bulk material (1.2 MA/m). It is also observed that any film magnetisation above that of the bulk material does not result in a FoM >1, this is due to the increased external field not outweighing the increased demagnetisation field. Similar can be said for any film below 0.7 MA/m, interestingly, there is a minimum magnetisation that the film must have to give a FoM >1. This is due to the reduced demagnetisation field not being greater than the reduced external field. What can also be interpreted from Figure 5. 10 is that the best FoM arises from the 1.1 MA/m film and provides an anchor for the bulk material. This material could also be supported with another, which could be achieved using multilayer films. These multilayer films could gradually reduce to a certain magnetisation, as shown in Figure 5. 11.

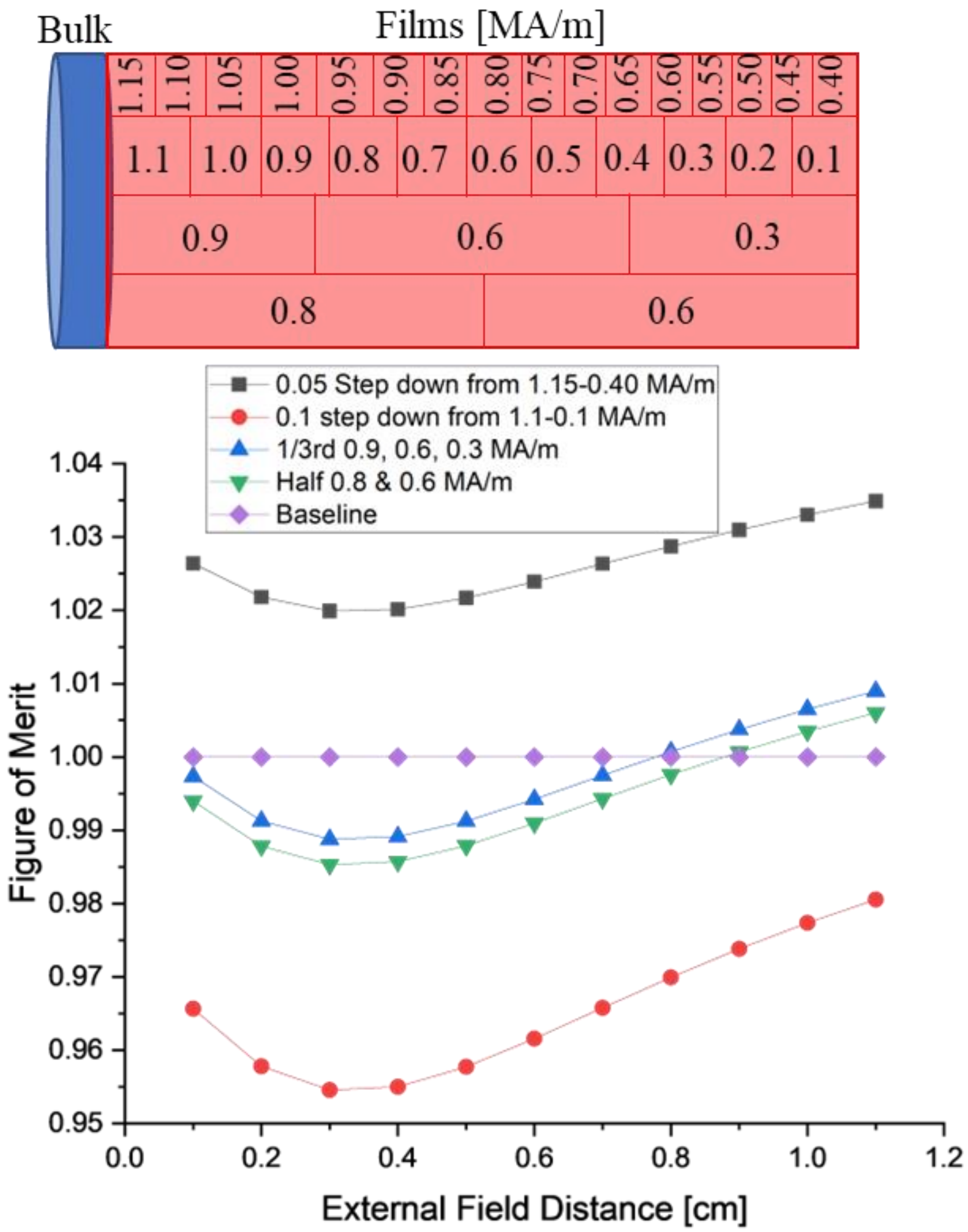

Figure 5. 11 Showing the figure of merit for different 0.5mm multilayer films, with a visualisation of the multilayer films magnetisation, with the same total length.

Two different approaches were taken when modelling the films, either the multilayer films were created in blocks, shown as the green and blue plots in Figure 5. 11. These blocks resemble multilayers of a declining magnetisation block to block. The second approach was to create a constant reduction/graded magnetisation reducing in different increments. As the FoM changes with distance, it appears that the two block approaches only become beneficial above 0.8 cm but the large difference in the two different graded films is surprising. The difference could originate from either the rate of decline being too large and is not having the desired effect on the demagnetisation field, or the edge magnetisation being 0.1 MA/m which is reducing the external field produced like what was shown in Figure 5. 10. The black plot shows the largest improvement to the FoM yet seen, this is due to the more gradual decline of the film magnetisation from the bulk material and stopping the film magnetisation at 0.4 MA/m to not hinder the external field too much.

5.4 Grading magnetisation film

When previously discussed multilayer films, an approach to create a graded magnetisation in the aim of a reduced magnetisation field could produce a greater FoM. There is a known property associated with ellipsoidal magnets, where they have a uniform demagnetisation field, which is to say that as any point on the magnet the demagnetisation field is the same. This could be a useful property for bulk permanent magnets, as rather than there being weak points from the high demagnetisation field, there becomes a constant stability and rather than nucleation occurring gradually it will happen all at once but will hopefully require a larger field.

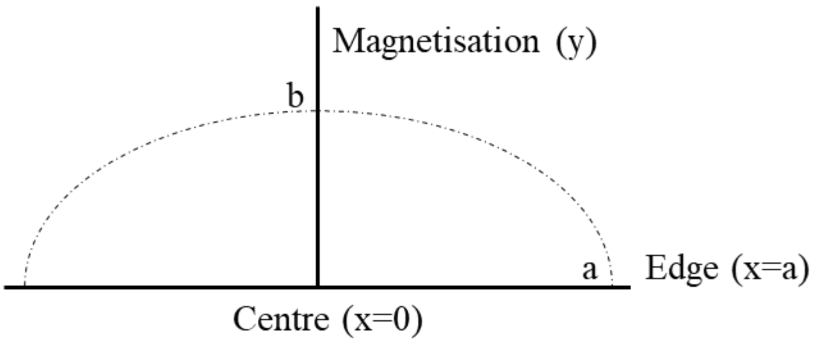

Figure 5. 12 Showing how the magnetisation can be mapped onto any shape of magnet following the radius of an ellipse.

Using the translation of ellipsoid to magnetisation profile shown in Figure 5. 12 this should result in the desired demagnetisation field following the equation:

$$1 = \frac{x^2}{a^2} + \frac{y^2}{b^2} \qquad \textit{(Equation 5. 2)}$$

$$y = b\sqrt{1 - \frac{x^2}{a^2}} \qquad \textit{(Equation 5. 3)}$$

Where a is the max distance from the centre to the edge of the magnet, in this case being 1.5cm. The relating term x, is the variable distance from x =0 to $x = a$. The calculated magnetisation y is function of the peak magnetisation value b over the length scale of x.

5.4.1 Initial graded magnetisation

Using equation 5.3 within the 1D model with a total length of 3 cm and a peak magnetisation of 1.2 MA/m gives the demagnetisation field in Figure 5. 13.

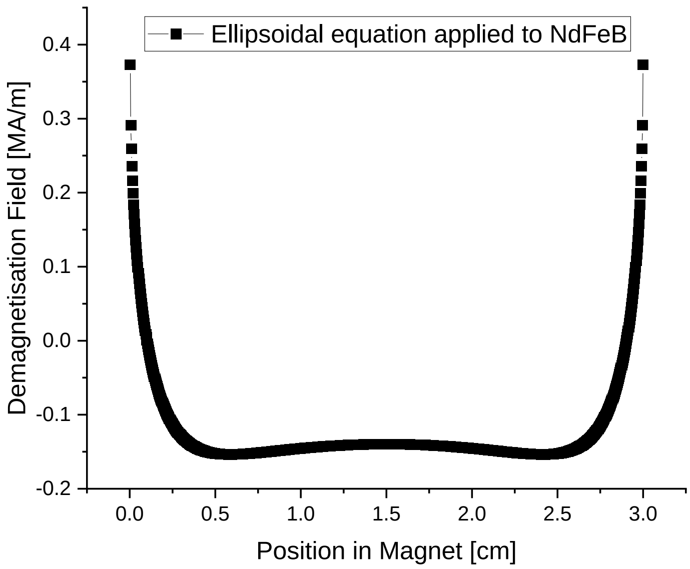

Figure 5. 13 Showing a line scan of the demagnetisation field when the ellipsoidal grading equation is used to calculate magnetisation.

While initial thoughts were that creating a graded magnetisation in this way would result in a flat demagnetisation field to remove any peaks of demagnetisation field and nucleation being less likely. It is interesting to note that this has not occurred and appears to have inverted the demagnetisation field so that now the edges are no longer a region of high demagnetisation and have transitioned into a region of stability for the magnet. The centre of the magnet appears to have a very similar value to that of the uniform magnet and between 1-2 cm on the line scan there is still the visible hump which can be compared to the uniform case. This dramatic increase in stability occurs at the 0.5 mm from the centre. Looking at the rest of the magnet's response, there is not much variation and could be considered a "flat" line which was the idea of using the grading system.

At the edge region of 0.5mm where the greater region of stability is being calculated, the cell size is uniform, and the magnetisation is getting smaller and smaller towards the edge. This means the change of magnetisation also gets smaller and smaller. This creates a very small magnetic field for each of the cells in this region, and when the field's effects are accumulated this results in a positive demagnetisation field or region of stability.

This has shown an even better principle and idea than was originally considered. It will be said and shown later that the external field produced by this graded magnet is dramatically reduced, which is not ideal for any real-world application. However, the magnet does have a very desirable coercivity profile which creates a FoM greater than two due to this huge decrease in the peak demagnetisation field.

5.4.2 Optimisation

As a method for optimisation for potential real-world applications, the external field delivered by the magnet would ideally be higher than the fully graded model. This can be achieved by incorporating concepts as seen in Figure 5. 8, where the increase of the centre magnetisation creates an increase of the external field. An example is shown below and compared to previous iterations of the model in Figure 5. 14.

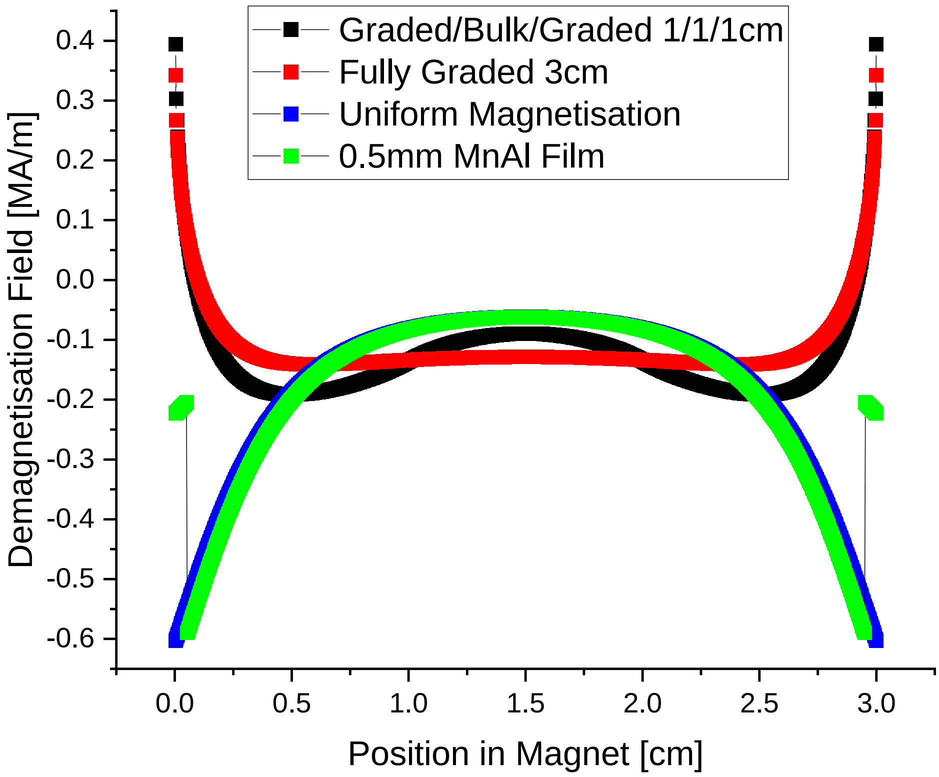

Figure 5. 14 Showing a line scan of the demagnetisation field for previous model iterations and the newly combined graded/uniform/graded model.

In the graded/bulk/graded model, the total length of the magnet is 3 cm, the centre 1cm has a uniform magnetisation of the bulk material (1.2 MA/m) and the two 1 cm sections either side of the uniform region consists of a graded magnetisation from 1.2-0 MA/m to increase the external field, shown in Figure 5. 15.

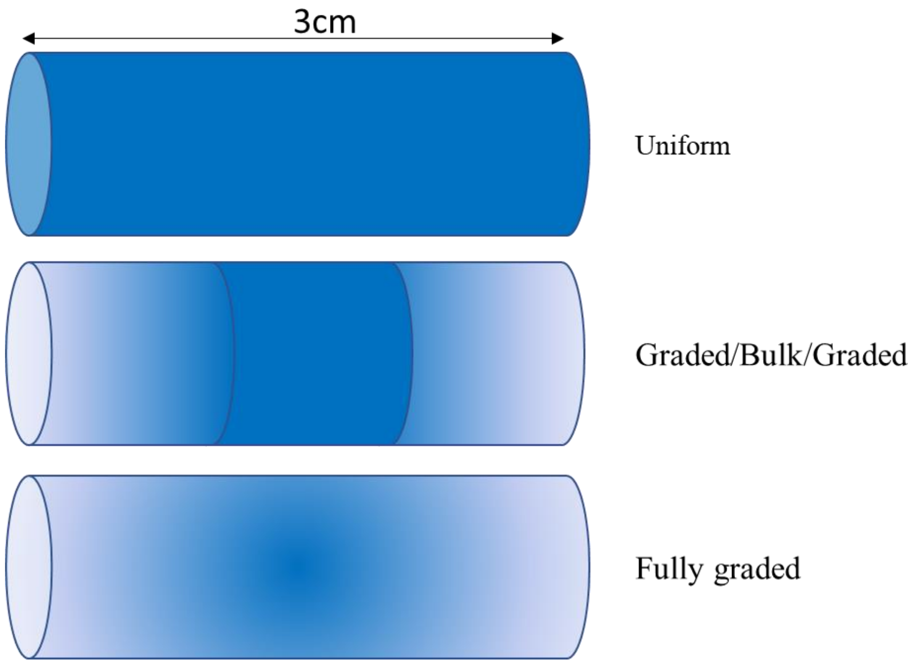

Figure 5. 15 Showing a visual representation of the different graded magnetisation models, where the intensity of blue indicates magnetisation strength. Darker blue = higher magnetisation.

Firstly, as the demagnetisation field was the intended topic of investigation, this was looked at to see if the increased size of the uniform region. It appears in Figure 5. 14 that there is a small effect on the edge demagnetisation field in comparison to fully graded (0.342 MA/m) graded/bulk/graded (0.395 MA/m). But there is an increase of 0.5 MA/m to the demagnetisation field at the centre of the magnet. This should not pose an issue as it was fully expected that this would be the case but as in applications this region is rather insignificant when it comes to the nucleation of magnetisation reversal. As such, the centre can be manipulated to create an increase to the external field whilst the edge region can be changed to increase stability and coercivity.

Table 5. 1 Showing the demagnetisation and external field data for the discussed model iterations with figure of merit and minimum and maximum coercivity.

Magnet Type	Peak Demagnetisation Field (MA/m)	External Field at 1.6 mm (MA/m)	Figure of Merit	Minimum Coercivity (MA/m)	Maximum Coercivity (MA/m)
Uniform	-0.604	0.413	N/A	4.99 Edge	5.54 Centre
0.5mm film MnAl	-0.589 (-2.5%)	0.407 (-1.5%)	1.02	5.04 (+1.0%) Centre	8.12 (+46.6%) Edge
Fully Graded	-0.141 (-76%)	0.233 (-44%)	2.42	5.47 (+9.6%) Centre	87.1 (+1472%) Edge
Graded/bulk/graded	-0.191 (-68%)	0.269 (-35%)	2.06	5.46 (+9.42%) Centre	71.1 (1324%) Edge

The results are summarised in Table 5. 1 highlighting the key values associated with the modelling. As expected, having more uniform bulk material increased the external field by 9% compared to the fully graded case but still reduced the demagnetisation field by 68% compared to the uniform magnetisation. The graded/bulk/graded case produced a FoM of 2.06 due to the reduction in the demagnetisation field but the FoM has reduced due to the larger demagnetisation when compared to the fully graded case with an FoM of 2.42. As such compromise had to be made. The external field could be increased by increasing the amount of uniform bulk material, but this would result in an increase to the demagnetisation field. As such this is application dependent but means there is a large range of what could be considered 'ideal properties'.

5.5 Non-zero surface magnetisation

A graded magnetisation that ranges from the centre and peak value down towards zero could also increase the external field. The external field could also be increased by creating a graded magnetisation profile that does not reduce all the way to zero at the edge region. The results from this are shown in Figure 6.21.

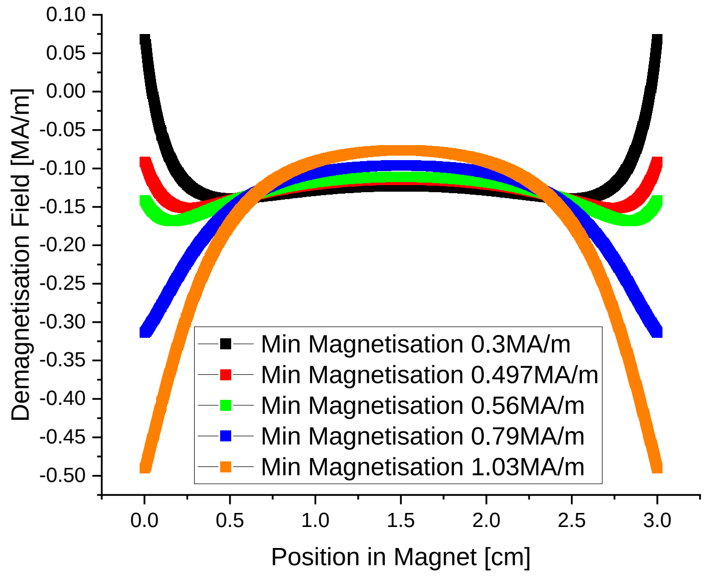

Figure 5. 16 Showing the demagnetisation field line scan for a fully graded magnetisation magnet with varying minimum magnetisation at the edge.

With the way in which the model works, minimum magnetisations are not "set", instead to achieve this the term a is increased to give a larger area of grading>3 cm but only calculating the x variable to 1.5 cm. Varying the minimum magnetisations in Figure 5.16 it is observed that for a minimum magnetisation around 0.56-0.49 MA/m that a near flat demagnetisation field is created when compared to the 1.0 MA/m. This resembles the uniform bulk magnet and the 0.3 MA/m which resembles the fully graded magnet shown in Figure 5.13. These results help in explaining why the original attempt at using a graded system did not produce a flat demagnetisation field (Section 5.4.1). Towards the edge of an ellipse, the increment of reduction in magnetisation becomes greater towards the edge (Figure 5. 12). This implies that there is an optimal magnetisation reduction increment to achieve a flat demagnetisation field profile. If it is too small the magnet appears to resemble that of the bulk and if made too large it will resemble a fully graded system.

Table 5. 2 Showing the figure of merits achieved by creating a minimum magnetisation.

Minimum Magnetisation [MA/m]	Figure of Merit at 1.6 mm
Fully Graded	2.42
Graded/Bulk/Graded 0	2.06
1.03	1.13
0.790	1.55
0.560	2.53
0.497	2.67
0.300	2.70

The FoM results of varying minimum magnetisation are summarised in Table 5. 2. A minimum magnetisation above 0 MA/m appears to produce a greater figure of merit, producing a greater coercivity when the minimum magnetisation is in the range of 0.560-0.790 MA/m. This can be explained by similar principles as previously discussed, in that with not enough of a decline in the peak demagnetisation field as such would resemble that of a bulk material. If the magnet possesses a minimum magnetisation of 0.3 MA/m, it will produce a larger FoM compared to a fully graded system. This is due to the increase in external field produced by the magnet being greater but with very little change in the demagnetisation field profile.

As there is a varying profile of demagnetisation field from this approach, this creates a variety in the coercivity values calculated as shown in Figure 5. 17.

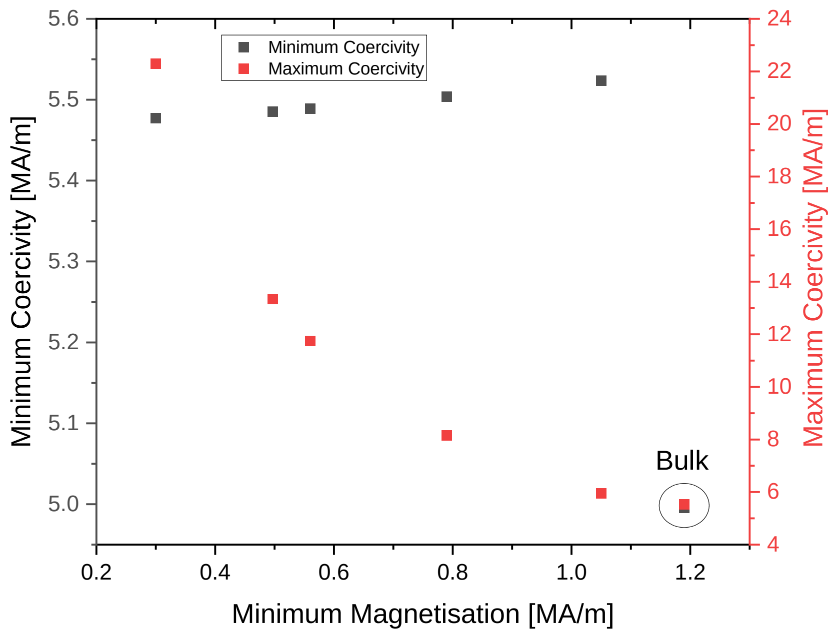

Figure 5. 17 Showing the minimum and maximum coercivity with different minimum magnetisations.

There is a difference in the minimum coercivity when varying the minimum magnetisation of 0.85% (0.047 MA/m) when excluding the bulk material. This is to be expected as the change to the profile is not significantly affecting the centre of the magnet, where the minimum coercivity is located. The increase in the calculated maximum coercivity can be explained by the reduced demagnetisation field and magnetisation at the edges of the magnet.

Although it is of benefit to ensure the largest coercivity as possible, reducing the magnetisation ever so slightly for the example of 1.03 MA/m could be more achievable and realistic in practice.

5.6 Single-ended graded magnetisation

To try and design the magnet more to an application, the concept of a single-ended graded magnetisation could be a good method of optimisation. Within a motor, only one face of the magnet will be facing the applied field from the stator coils, so it would stand to reason that the reduction of demagnetisation field at the cost of external field performance need only be required at the edge/face closest to the applied field origin, shown in Figure 5. 18.

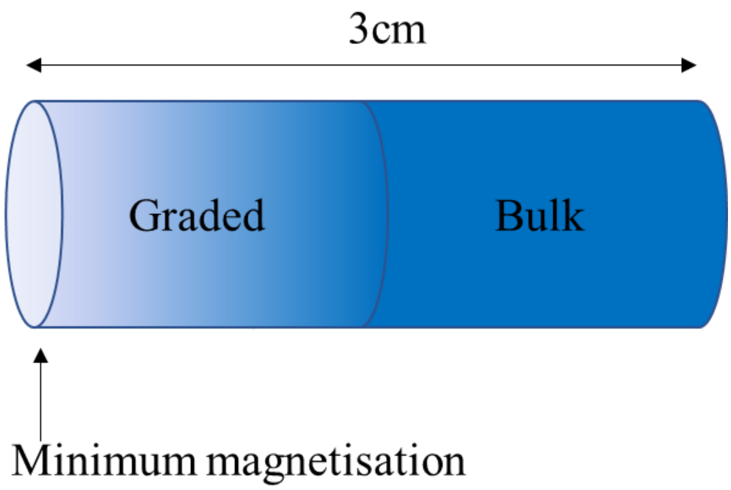

Figure 5. 18 Showing a visualisation of half of the magnet as bulk material and half as a graded region, with the potential to change the minimum magnetisation and the size of each region.

As found previously, a minimum magnetisation in the range of 0.56-0.49 MA/m produced a high FoM and a relatively flat demagnetisation field profile, when observing the line scan from left to the centre, compared to non-graded iterations, Figure 5. 19.

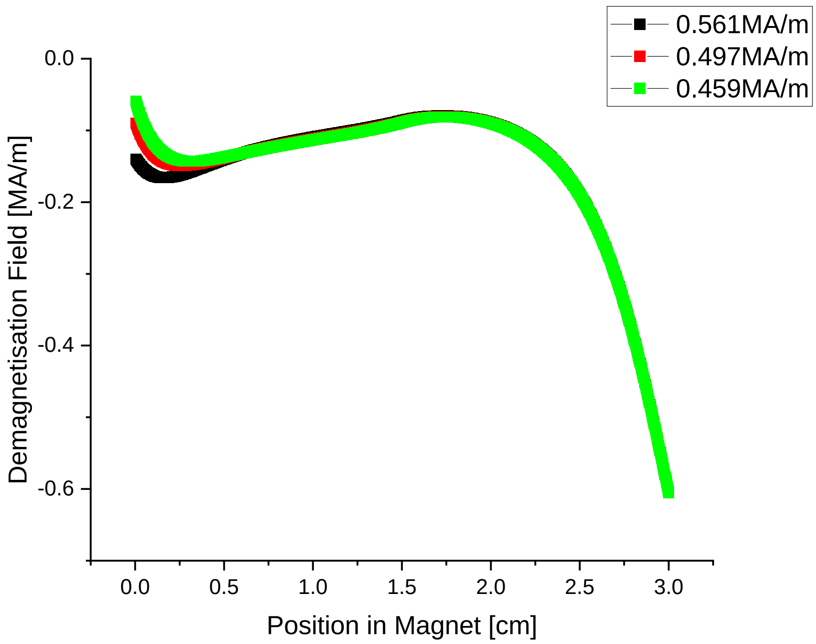

Figure 5. 19 Showing the demagnetisation field line scan for a single-sided graded magnetisation system with different minimum magnetisations.

Grading only half the magnetisation should give the best of both worlds in terms of a targeted reduction of demagnetisation field where it is required and the half of bulk uniform magnetic material giving the necessary external field. Varying the minimum magnetisations very slightly shows a near identical line scan profile with an edge demagnetisation having a difference of 0.081 MA/m, the greatest difference is found below 0.5 cm. Here it shows that a lower magnetisation gives a lower demagnetisation field by 98% when comparing the edge values, which agrees with the results shown previously.

Table 5. 3 Showing the figure of merits for either side of the single-sided graded magnetisation magnets.

Minimum Magnetisation [MA/m]	Figure of Merit at 1.6 mm Graded (left) side	Figure of Merit at 1.6 mm non-Graded (right) side
0.560	2.58	0.994
0.497	2.77	0.995
0.459	2.82	0.995

Table 5. 3 display the FoM data of both sides of the magnet when only one side has been graded. Grading one side produces a higher FoM. This is due to the increase in the length of the bulk uniform region providing greater external field than the fully graded systems. Combining this with the magnetisation minimum and graded system, gives the best of both worlds and could represent a good initial model for optimising the magnet for different applications.

Following on from this, Figure 5. 20 shows how the region of bulk material can be increased in size to provide more field now that the grading of the magnetisation is not set to zero.

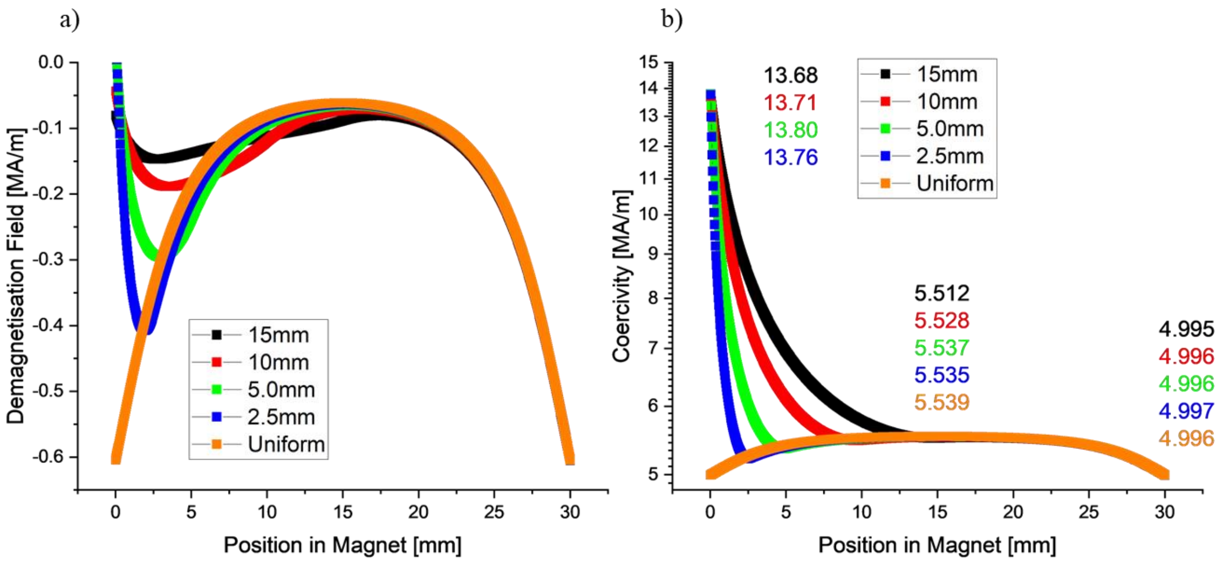

Figure 5. 20 Showing a) demagnetisation field and b) coercivity line scans for a single-sided graded magnetisation system with a 0.48 MA/m minimum magnetisation but graded over different lengths.

Changing the length of the graded region appears to have very little change on the calculated values at the edge for demagnetisation field with a range of 0.133 MA/m between the graded length of 15 mm and 2.5 mm. There is a difference of 0.08 MA/m in coercivity between the same plots. However, there is a visual difference in the line scan profiles as the gradient between the uniform region and the graded region. This is to be expected at the range of the grading is over a reduced range so therefore the change in the line scan would be quite sharp. In terms of stability, the 1.5 cm grading would be the most stable magnet as it has the flattest demagnetisation field, but this comes with the lowest external field. Again, it is down to a compromise between the demagnetisation field and external field in the FoM as summarised in Table 5. 4.

Table 5. 4 Showing the figure of merits scans for a single-sided graded magnetisation system with a similar minimum magnetisation but graded over different lengths.

Length of graded region [mm]	Figure of Merit at 1.6 mm Graded side	Figure of Merit at 1.6 mm non-Graded side
2.5	1.34	1.01
5.5	1.70	1.01
10	2.37	1.00
15	2.80	0.99

5.7 Summary

The use of thin films with bulk uniformly magnetised magnets has been shown to reduce the demagnetisation field of the bulk material and minimise the reduction the external field delivered. Using a film with magnetisation closest to that of the bulk material gave the best results for the use of single films with a FoM of 1.09, whereas the use of a graded magnetisation profile gave a significant improvement in the FoM (2.42) due to the reduction of the demagnetisation field creating a region of greater stability compared to the rest of the magnet. However, the original and basic method of grading the magnetisation may provide a much-improved demagnetisation field but the resulting reduction of the external field becomes an issue for any real-world application.

Optimisation of the model through an increased quantity of bulk material and setting a minimum magnetisation for the graded region provided the highest FoM of 2.82. This model was optimised for the intent of a real-world application where only one side of the magnet faces the load field of the stator coils and this is therefore the region of focus to reduce the demagnetisation field and result in an increased stability of this region, combined with a uniformly magnetised region starting from the centre of the magnet towards the far edge of the magnet to provide the necessary external field and being in a region that is less likely for magnetisation reversal to nucleate. The model can be changed in either of these ways to be optimised for a particular application.

6. 3D Model

6.1 Introduction

Limitations of the 1D model mean that there are no other considerations to magnetic field calculations other than a magnetisation and a cell size. The lack of contribution of other properties such as permeability are not considered in any calculation. Therefore, a 3D model was created using COMSOL Multiphysics for two reasons. Firstly, to validate the results obtained from the 1D model and secondly to expand the work to cubic magnets which are more representative of those found in real world applications. As COMSOL can give a 3D representation both visually and for calculations, it is an important tool for the following work, especially later when exploration into a graded magnetisation is used.

6.2 Creating a working model

To establish a magnet that can be compared to the 1D model presented in chapter 5, a cylindrical magnet of length 3 cm and radius of 0.5 cm in an air region of 2x2x3 cm was created to simulate a uniform magnet, Figure 6. 1.

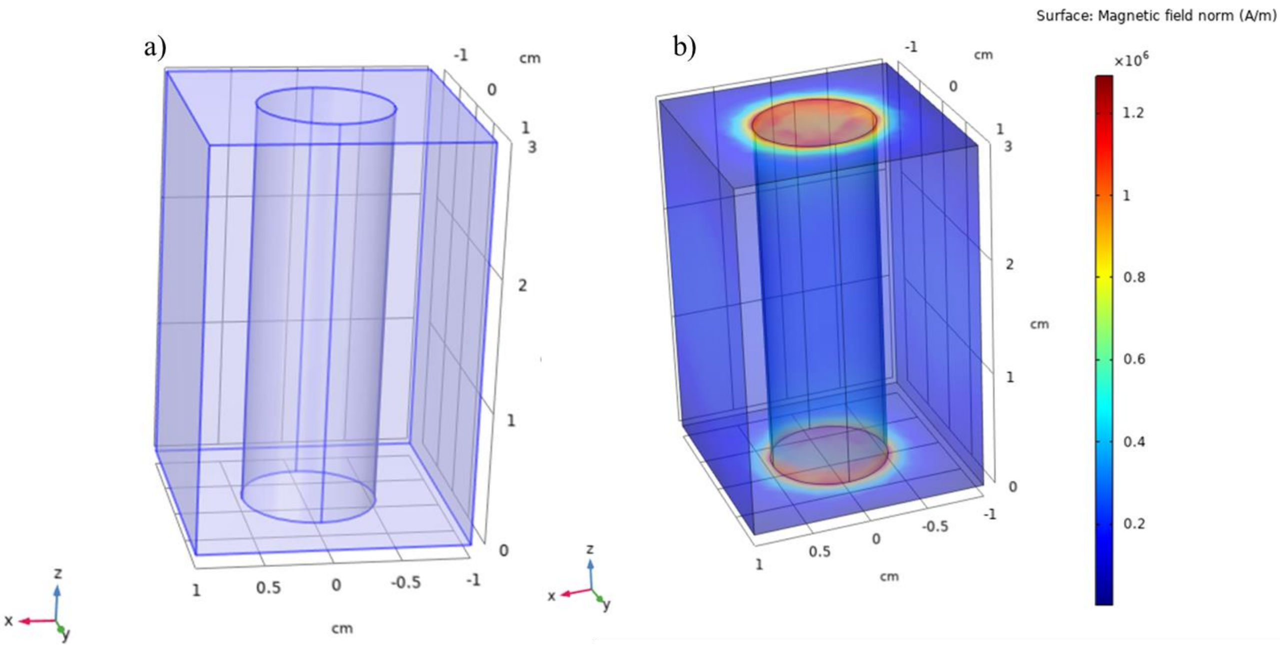

Figure 6. 1 Showing the first iteration of the 3D model of a cylindrical magnet within an air region with a) the different isolated objects and b) the magnetic field produced from the cylinder in an air region.

This model produced some issues, as the magnetic field observed was not consistent with what was to be expected. This was found to be due to the size of the air region, which was constraining and obstructing the external field, this also impacted the internal demagnetisation field. To address this a convergence study was conducted to investigate how varying the mesh and air size affected the result and computational time.

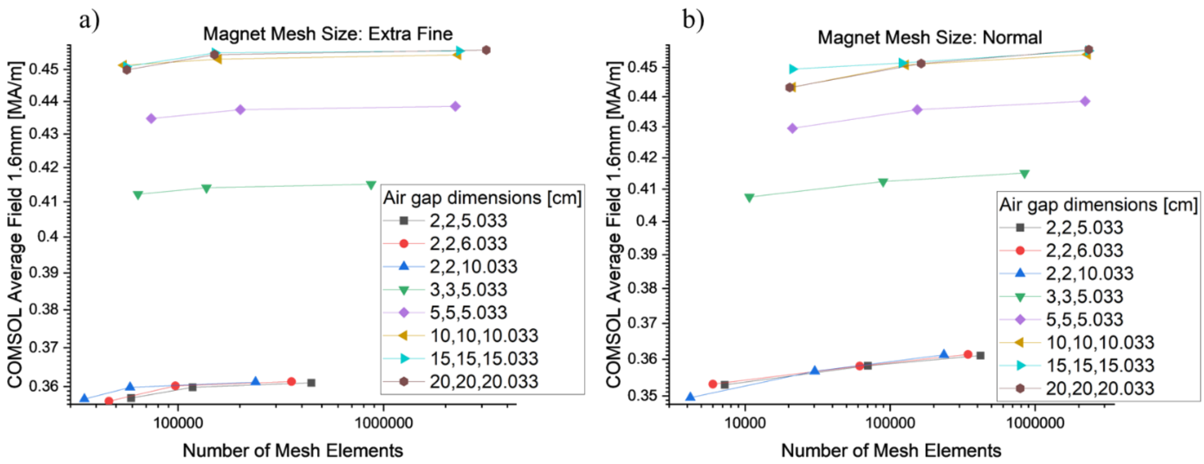

Figure 6. 2 Showing the average external field at 1.6mm calculated in COMSOL for varying the air and mesh size and the magnet mesh size with a) Extra fine magnet mesh b) Normal magnet mesh (x,y,z in cm).

In Figure 6. 2 the average external field is shown to vary by changing the size of the air region, confirming the confinement issue. The results show in Figure 6. 2 a) and b) with an air size of 10x10x10 cm or higher the results did not vary more than 1%. In COMSOL the mesh size can be changed through a pre-defined selection of sizing such as; Normal, Finer, Extra fine etc. which increases the number elements present within the model, a change of the model such that there is the highest number of elements increases computational time, though when the air region is a 10x10x10 cm the simulation on has 54k elements, whereas with more elements 2.3M the measured value for the average field has a 0.72% difference. This is an increase in the number of elements by a multiple of 42 for the 0.72% value difference, this investigation provides more confidence that using 54388 elements results in good convergence when simulation and isolated magnet in air, this is the minimum number and conditions for future simulations.

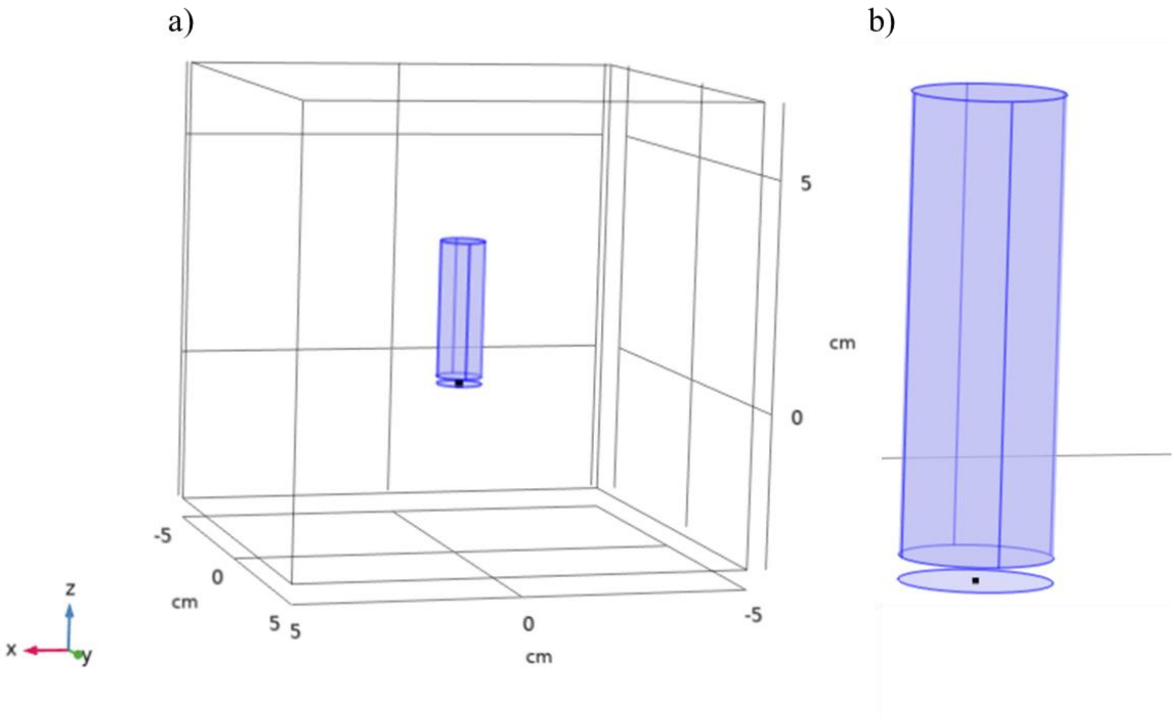

Figure 6. 3 Showing the updated model with the cylindrical magnet a) suspended in an air region and b) a magnified picture of the magnetic cylinder with a measurement area 1.6 mm from the pole surface.

Shown in Figure 6. 3 is the model with applied physics in an air region of 10x10x10 cm. This will be the standard model upon which further developments are made, starting with those that can be compared to the 1D model.

6.3 Comparison to 1D model

To confirm the validity of the results from the 1D model, the model was replicated from chapter 5 before moving onto grading magnetisation models.

6.3.1 Single film cylinders

The first examples of comparisons between the 1D and 3D model include the isolated bulk magnet and then the additional films with different magnetisations. Figure 6. 4 also shows the bulk magnet with different magnetic film domains.

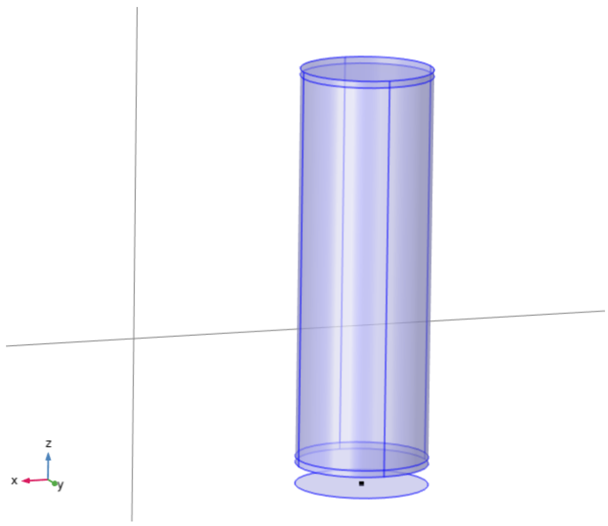

Figure 6. 4 Showing the cylindrical magnet architecture with a 0.5 mm film on each pole surface.

The first iteration of the model is described with a constant total length of 3 cm with two 0.5 mm films on each pole included. The magnetisation of the films is varied to calculate the effect of external and demagnetisation field and compared to the results obtained in the 1D model.

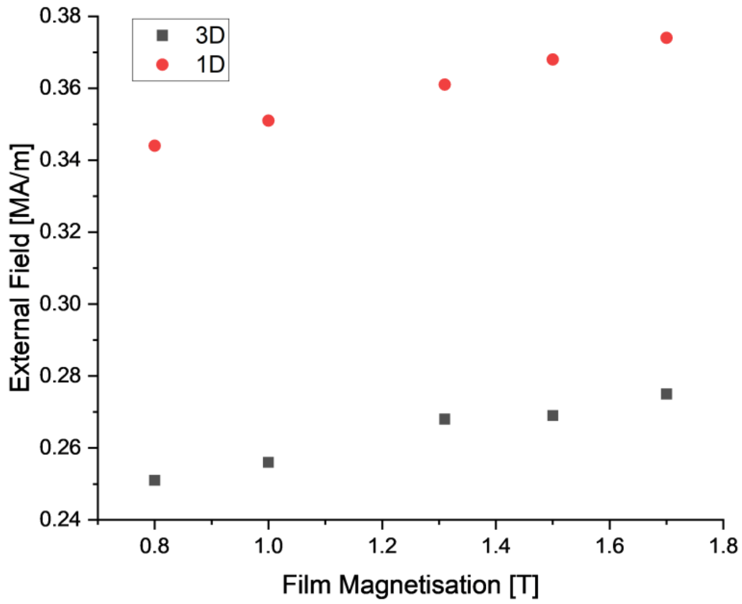

Figure 6. 5 Showing the calculated external field when changing the magnetisation of the film for the 3D and 1D models.

Evaluating the results of Figure 6. 5, the comparison of results for the external field data between the COMSOL 3D and the 1D model has a calculated 26% difference. Although this comparison may appear to be quite a large difference, the reason for this can be explained by the chosen method of COMSOL values for the external field. To have a comparison between the 1D, where all the magnetic fields are constrained to the volume of each cell, the external field in COMSOL will be unrestricted. To measure the external field in the 1D model, a flat 0.5 cm radius circle region was placed 1.6 mm from the surface and the average external magnetic field measured within this region was the value used for comparisons. This does mean that not all the external field will pass through this measured area and therefore it can be expected that the value calculated will be lower than that of the 1D model. When comparing the actual trend difference of the 3D and 1D model separately, the trends are very similar, and the percentage change of the measured fields are nearly identical which gives the confidence that the 1D model is working correctly, although the values may differ for the reason mentioned previously.

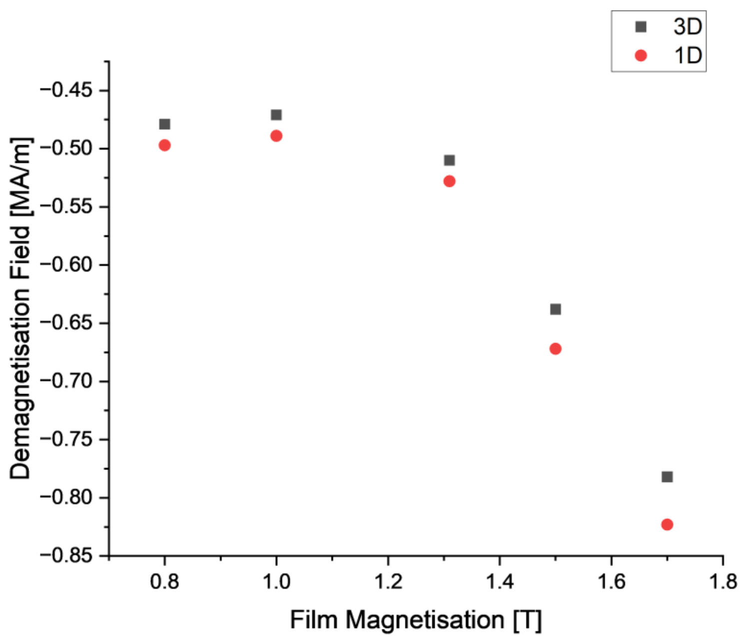

Figure 6. 6 Showing the calculated demagnetisation field when changing the magnetisation of the film for the 3D and 1D models.

Figure 6. 6 provides the demagnetisation field data for inside the magnet with the different magnetisation films. Unlike the external field data, the comparison of calculated values between 3D and 1D only vary from around 3-6%. This is a more acceptable tolerance

for comparison and provides confidence when considering the internal field (demagnetisation) results obtained from the 1D mode. This is also reiterated in the relative field change calculated when using different magnetisation films in the 1D and 3D model where they only vary by less than 3%. Using the data in Figure 6. 5 and Figure 6. 6 a FoM can be found, shown in Figure 6. 7.

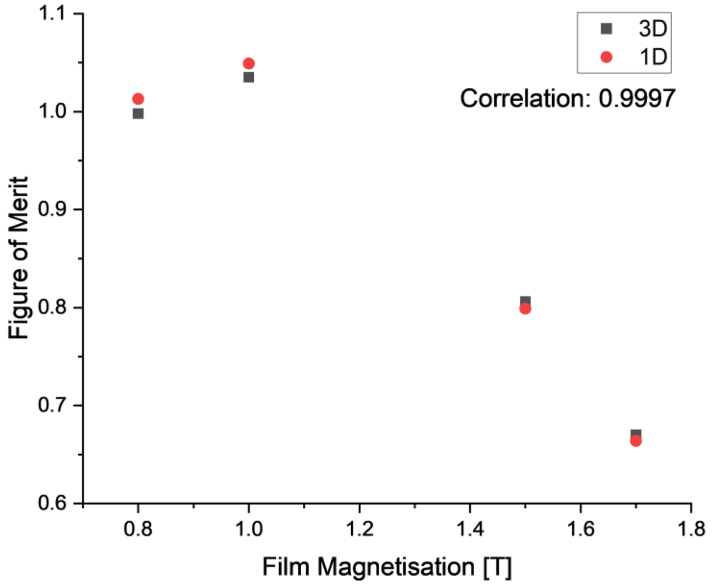

Figure 6. 7 Showing the calculated FoM when changing the magnetisation of the film for the 3D and 1D models.

Figure 6. 7 shows the final FoM for the iterations discussed previously. Again, the FoM describes the relationship between the desired change of demagnetisation field against the undesired change of external field. The relative FoM calculated for similar 3D and 1D configurations have a calculated correlation coefficient of 0.9997, calculated from the FoM dataset, this gives great confidence in the calculated data and means that moving forward onto more complex models can proceed with the knowledge that the results obtained from COMSOL give confirmation to the 1D model and can be trusted. However, it will be noted that upon closer inspection of the FoM values for the 0.5 mm 0.8 T model that there is a slight difference in the values but depends on which software is chosen the results obtained are either good or bad. This implies that there will be a value of magnetisation for a set thickness of film which will give a FoM either side of 1 depending on which model is used and will be something to bear in mind for in future simulations.

6.3.2 Z-axis graded magnetisation

The next step in developing the 3D model is through the introduction of graded properties. Here the magnetisation is set within the model with a peak at the centre and an arced gradient reduction of magnetisation towards zero at the edge using equation 5.3, shown in Figure 6. 8.

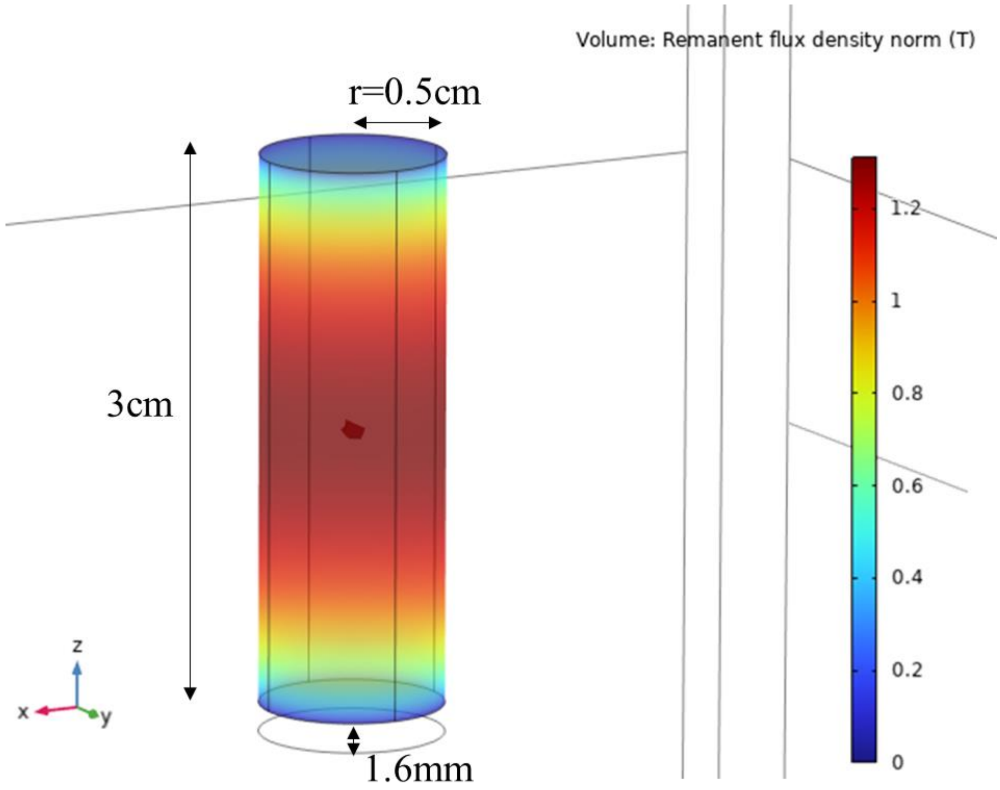

Figure 6. 8 Showing a visual for the COMSOL cylindrical model with the basic graded magnetisation applied.

Compared to the 1D model, COMSOL has the ability of visualising and post-analysing the data as a heat map. This is shown in Figure 6. 8, where the centre of the cylinder can be seen having the highest remanent flux density falling to zero at the edge. This provides a visual of how the remanent flux density does not reduce by the same increment and the gradient of the reduction gets larger towards the edge region, determined by the larger region of "red" in the heat map.

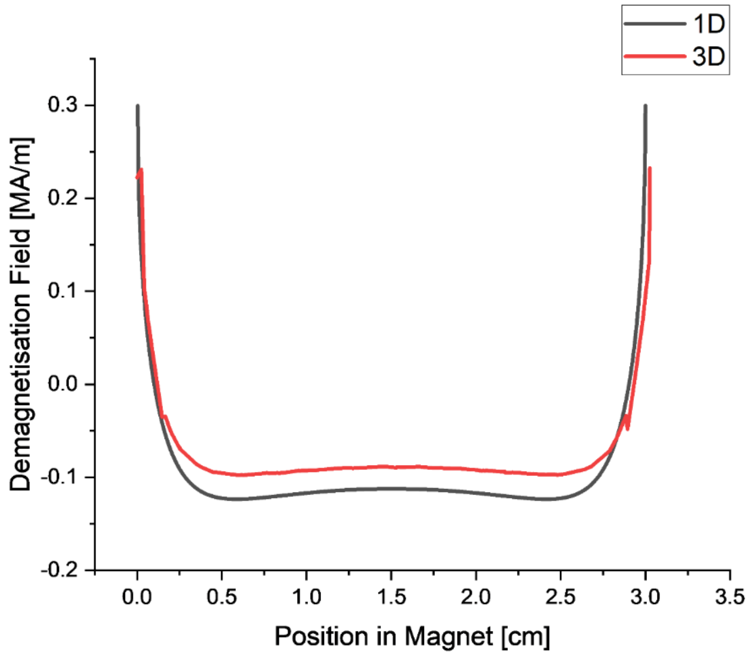

Figure 6. 9 Showing a comparative demagnetisation field line scan of the basic graded magnetisation equation applied to the 1D and COMSOL model.

The comparison of the demagnetisation field shown in Figure 6. 9 has a good correlation, especially at the edge region, although there is a difference in the centre and a slight difference in the edge region. The line scans do show the same trend/shape, it can therefore be interpreted that the applied equation is working the same way in both models but there is a difference of 21% for the central region. This difference especially in the region where there is a higher magnetisation could be due to the 1D model interpreting a volume whereas COMSOL can calculate the volume from the actual model. And where the magnetisation is lowest there is less variation, so there is better convergence.

Table 6. 1 Showing the average external field data at 1.6mm from the magnet surface for both COMSOL and Excel models with the application of a graded magnetisation in the Z-axis only.

	External Field at 1.6 mm				
Magnet type	COMSOL average (MA/m)	Excel (MA/m)	Comparison	COMSOL field change	Excel Field Change
Uniform (1.31T)	0.268	0.361	74.07%		
Graded 1.31 to 0T	0.121	0.204	59.31%	45.15%	56.51%

As discussed previously, the calculated value for the external field has a considerable difference between the 3D and 1D models and most likely down to the same reasons as a constrained field in the 1D model. The trend in the respective field change is within 12%, and this increase is down to the much lower external field observed within the 3D model, Table 6. 1.

Table 6. 2 Showing the peak demagnetisation field for both COMSOL and Excel models with the application of a graded magnetisation in the Z-axis only.

	Demagnetisation Field				
Magnet Type	COMSOL average (MA/m)	Excel (MA/m)	Comparison	COMSOL field change	Excel Field Change
Uniform (1.31T)	-0.510	-0.528	96.65%		
Graded 1.31 to 0T	-0.103	-0.123	83.45%	20.19%	23.38%

Like previous model iterations, there is a very close comparison of the demagnetisation field between 3D and 1D models, which vary by 13% but have respective calculated changes of 3%, shown in Table 6. 2. Even under the concept of a graded magnetisation which gives further confidence in the results obtained from the 1D Excel model, whilst still understanding why there is a difference in the external field between the different models.

Table 6. 3 Showing the FoM for both COMSOL and Excel with the application of a graded magnetisation in the Z-axis only.

Magnet Type	COMSOL FoM	Excel FoM
Graded 1.31 to 0T	2.236	2.418

Although the values for the external field are different, the respective changes seen are very similar along with the demagnetisation field results give a FoM in Table 6. 3. Which describes a large improvement in the potential magnet performance, due to the huge reduction of the demagnetisation field which results from the controlled reduction of the magnetisation. This is the highest FoM (2.236) achieved in COMSOL so far and shows real promise that the underlying theory and principles can be applied to achieve this.

6.4 Cubic 3D models

So far, we have focused on the modelling of cylindrical magnets, mainly to follow the 1D which was limited by the symmetry and shape it could solve. This provides a proof of principle and shown the transition to established modelling software, but for end application the magnets found within motors and generators are usually a cubic shape rather than cylindrical. As such, moving on with the 3D model provides greater flexibility and realism in what it can solve. To ensure confidence in the results are high, the external field is measured 1.6 mm from the pole of the magnet, with a change an area the same dimensions as the magnet pole face. This will be a constant dimension and any addition of film will result in a reduction of the bulk dimensions, shown in Figure 6. 10. Like the cylindrical models, cubic models allow for grading and magnetisation control in 3 dimensions. But as discussed in the literature, demagnetisation is more likely to occur at the edges and corners near the poles of a magnet, transitioning to modelling cubic systems gave a more realistic view of film effects and how graded properties have on a magnet.

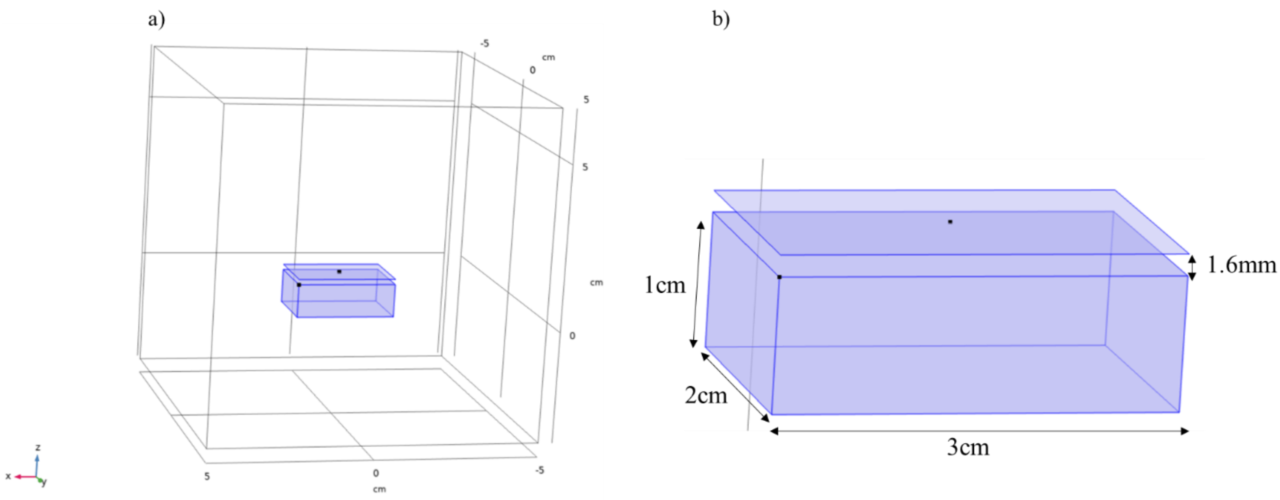

Figure 6. 10 Showing a) the visual layout for the cubic magnet in free space and b) the dimension and measurement points marked and the area for external field measurements.

6.4.1 Single film

Using knowledge gathered from the previous models, varying the thickness of the films and with magnetisations close to the bulk material gave an early indication that the principle transferred over to cubic models, shown Figure 6. 11.

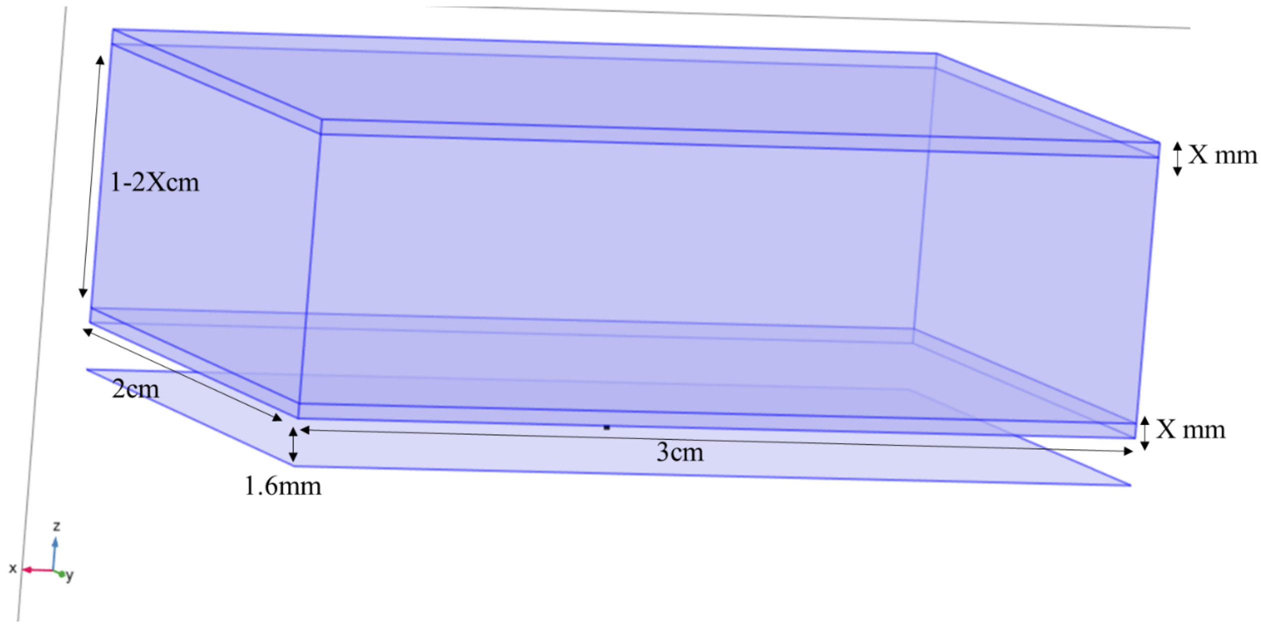

Figure 6. 11 Showing an example of the model set up for a single layered film on a cubic magnet.

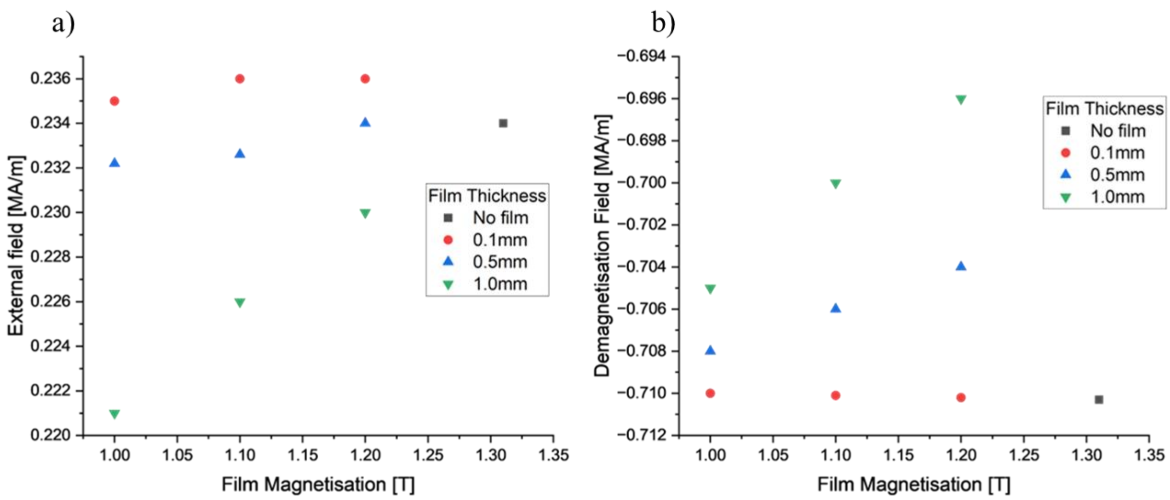

Figure 6. 12 Showing the external a) and demagnetisation b) for a varying thickness and magnetisation film.

Figure 6. 12 shows that a film magnetisation closest to the bulk material lowers the demagnetisation field more, 2% compared to 0.7% for the 1.0 mm film. It is apparent that there is something not right with the 0.1 mm film which appears to be the inverse and is also apparent in the increase in external field observed for this thickness of film.

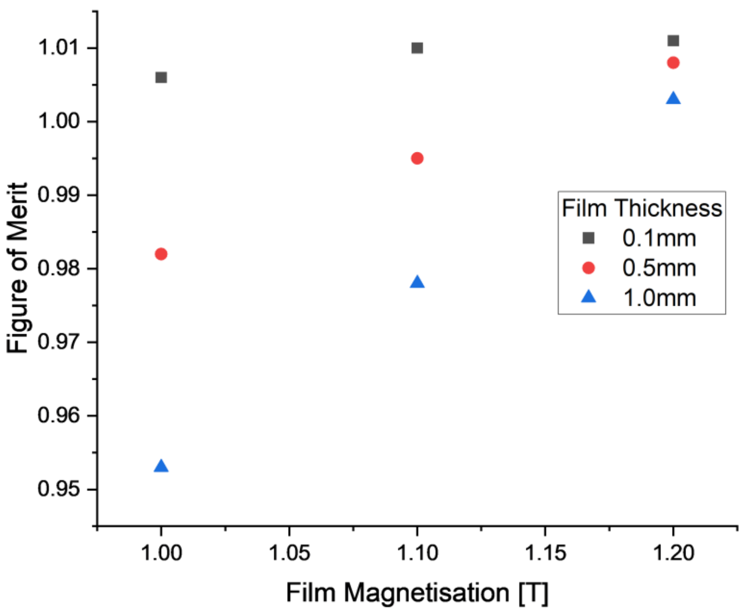

Figure 6. 13 Showing the FoM for a varying thickness and magnetisation film.

Deduced from previous results and that shown in Figure 6. 13, the thinnest film with magnetisation closest to the bulk material gave the highest FoM of 1.01. Also deduced from the table, there appears to be a sweet spot for each magnetisation and film thickness combination which was also discussed in the 1D model, this implies that grading the magnetisation in the way of the previous cylindrical models should translate into a cubic system.

6.4.2 Single axis magnetisation grading

Using a graded magnetisation with a cubic magnet system provided a more realistic insight into the effects of real-world magnets that can be used in practical applications. Also, one of the reasons behind a graded magnetisation is to reduce the demagnetisation field at the edges of the magnet. Grading magnetisation should have a much greater effect on a cubic shape with more corners and edges compared to a cylindrical magnet. Therefore, for the cubic magnet, to have a better representation of the effect on the demagnetisation field a FoM will be found in the previous way (Z-axis) as well as the corner of the magnet, where the FoM is predicted to be the highest due to the effect on the demagnetisation field. Grading through the pole to pole, or through the Z-axis, is shown visually in Figure 6. 14.

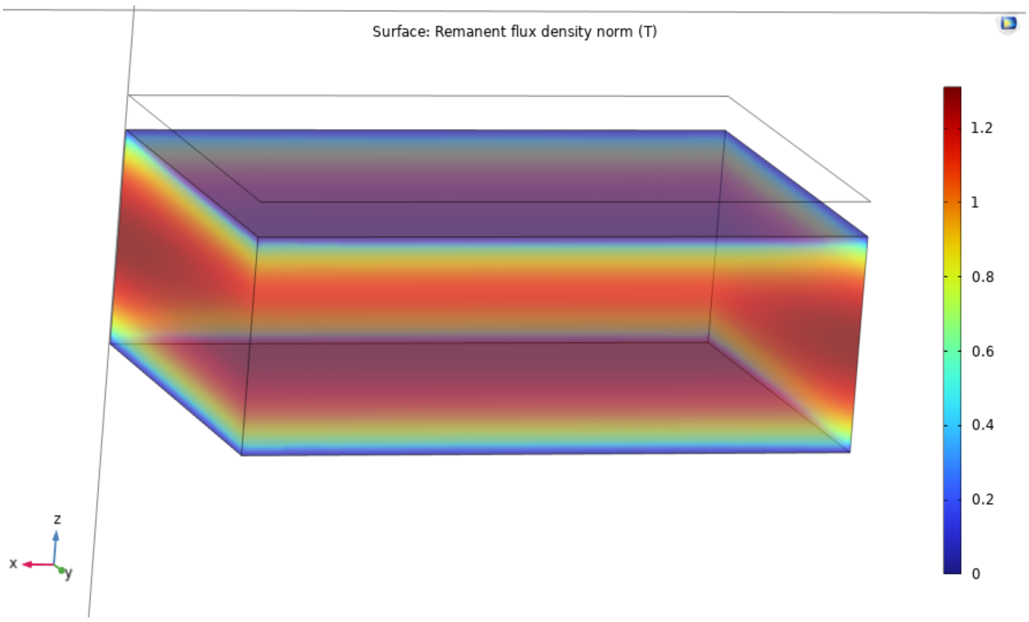

Figure 6. 14 Showing a visualisation of the Z-axis graded magnetisation in a cubic magnet.

The visual heatmap represents the same effect as Figure 6. 8 and the cylindrical magnet. Shown in later figures and with different axis grading the colour heatmap will show visual representation of what grading in different axis' does to the magnetisation over 2 and 3 dimensions.

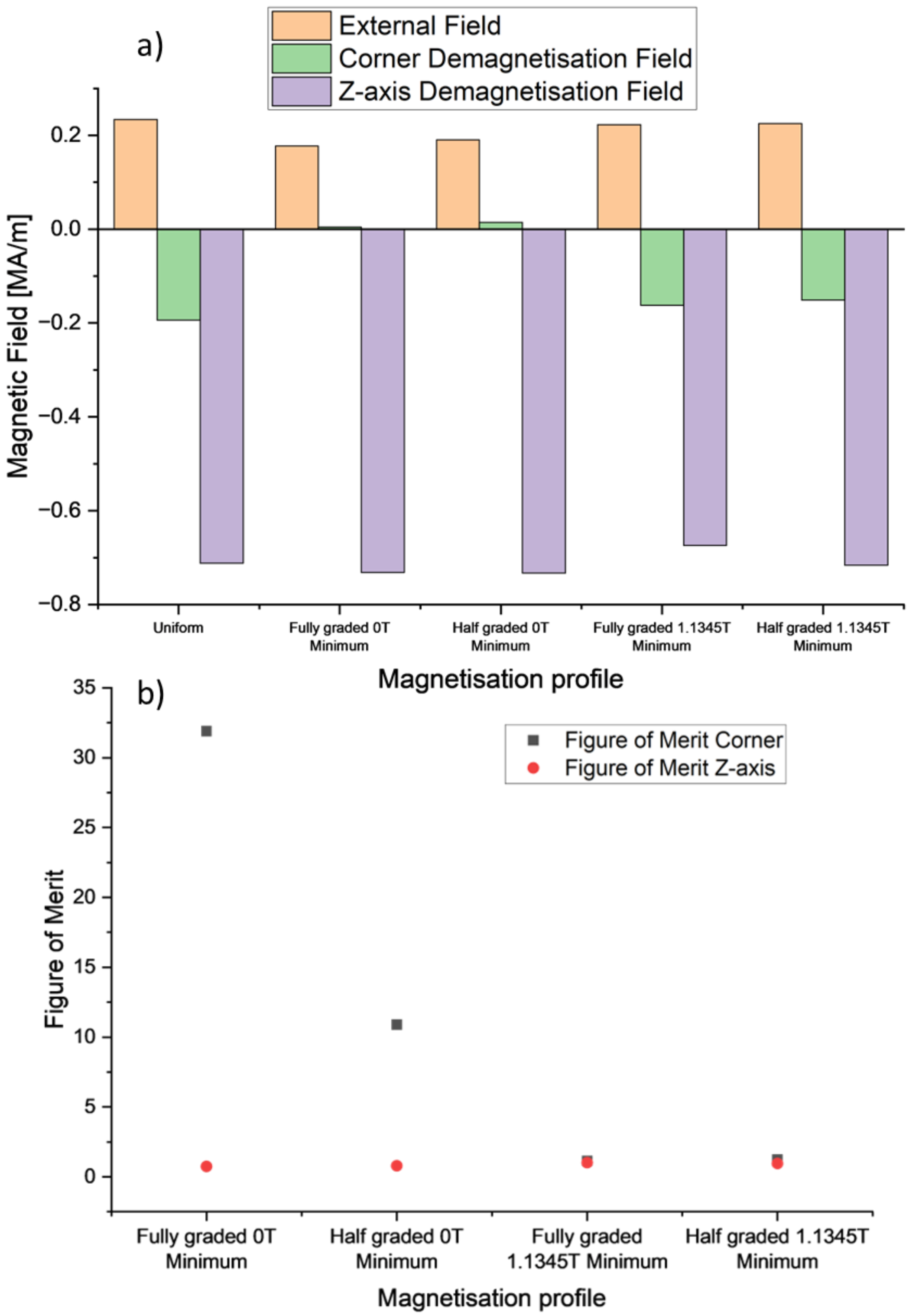

Figure 6. 15 Showing a) the external, corner demagnetisation, Z-axis demagnetisation and b) FoM when the magnetisation is graded in the Z-axis.

Shown in Figure 6. 15 above is the data for average external field 1.6 mm from the magnet pole surface and the demagnetisation field for the corner and the peak through the Z-axis, and compares the uniformly magnetised magnet to the different Z-axis grading. Where the Z-axis demagnetisation field is measured through the centre of the cube along the Z-axis, and the corner demagnetisation field is measured in the same corner which is facing the external field measurement surface. The definition of half graded is the same as discussed in Chapter 5. Where, the half graded magnet is only is refereeing the polar axis (Z-axis) and the half which is graded is the half which is facing the external field measurement area.

Comparing the FoM from the cylindrical model (Table 6. 1) to the cubic model data shown in Figure 6. 1, grading through the Z-axis (pole to pole) gave a FoM 2.2 for the cylindrical model but is not found for the cubic model where only one of the iterations gives a FoM of 1.008. All the FoM that resulted lower than 1, is due to the reduction in the external field produced by the magnet but also due to an increased demagnetisation field. This is the first time this has been observed for a graded system and is most likely due to the grading occurring over the short axis distance whilst also being between the two poles of the magnet. This compression is causing the magnetisation grading to be to sharp decline over such a distance and is therefore hindering the demagnetisation field. This can be confirmed by comparing the results when the minimum magnetisation is set to 1.1345 T. This produced the intended result of a lower demagnetisation field (5%) through the Z-axis and confirmed the suspicion that the grading of magnetisation can negatively affect the FoM if the grading is too steep over a ‘short’ distance, at least in the case of the Z-axis or pole to pole direction.

The FoM for the corner of the magnet are significantly improved compared to the centre Z-axis to 31. Although the percentage change calculated for demagnetisation field is negative due to the change of sign for the calculated value, this is due to the corner region now becoming an anchoring region of stability instead of the nucleating point of weakness. Ignoring the sign of the FoM there is an impossibly large value for the FoM with the iterations which have a corner magnetisation of 0T. This only highlights a theoretical potential as a magnetic material with no magnetic moment, therefore no magnetisation, and having a high magnetocrystalline anisotropy, this property is not available in current magnetic materials. However, iterations with the 1.1345 T minimum magnetisation at the corners demonstrates a more realistic representation of what could be possible, these iterations give a FoM in the range of 1.1-1.2, and as shown in the 1D model, the best FoM comes from having half of the material as the uniformly magnetised material and then grading the magnetisation towards a value in the region of that of the bulk material.

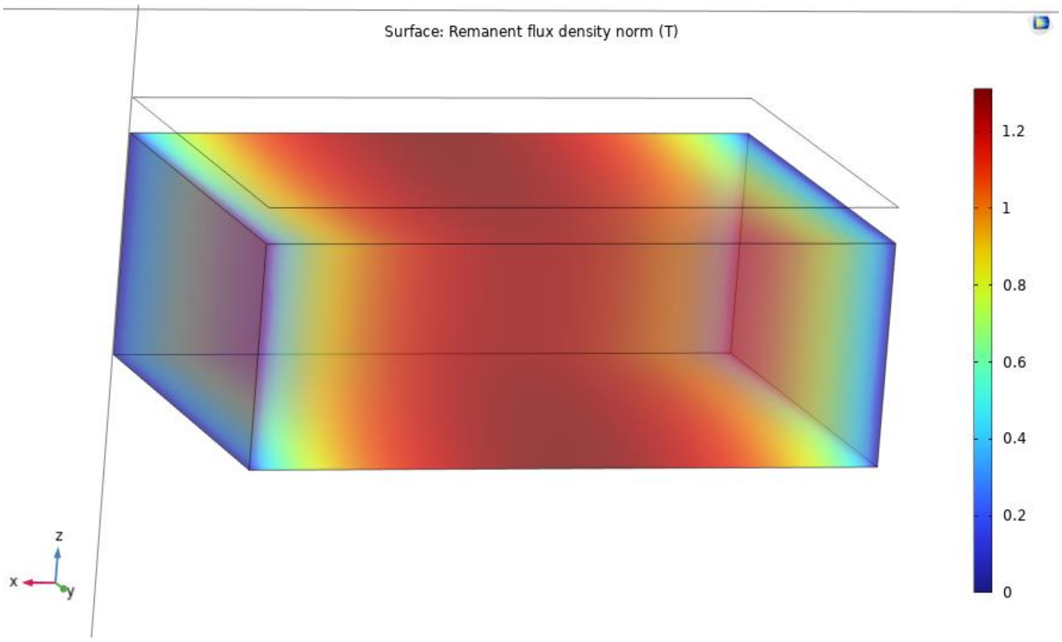

Figure 6. 16 Showing a visualisation of the X-axis graded magnetisation in a cubic magnet.

Figure 6. 16 above visualises a grading in the X-axis of the cubic magnet. The visual difference between grading in the X and Z axis is that through the Z-axis centre, there should be no change in magnetisation with the X-axis grading, but this still created a lower magnetisation in all eight corners of the magnet as intended. The results for such are shown below in Figure 6. 17.

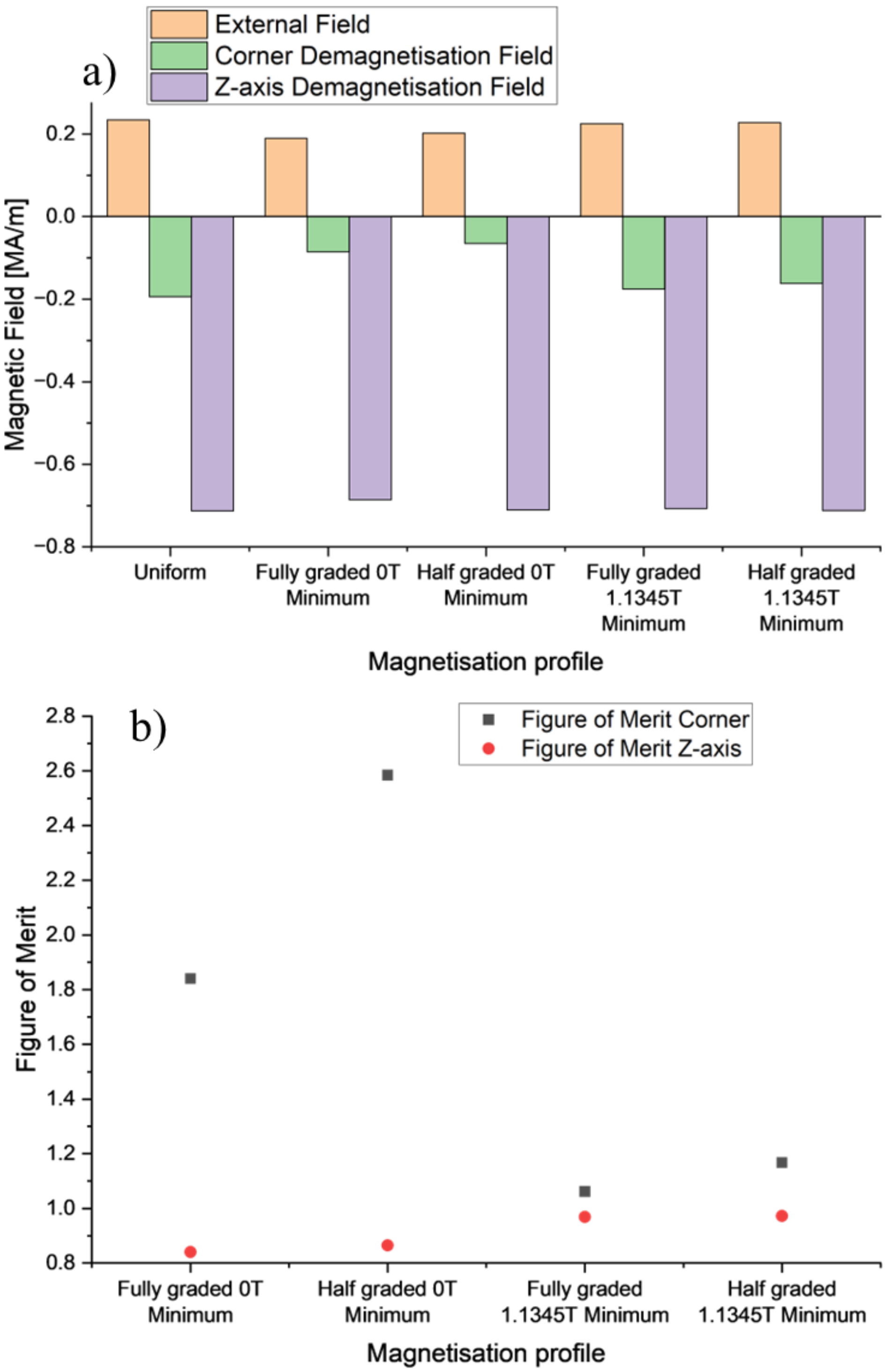

Figure 6. 17 Showing a) the external, corner demagnetisation, Z-axis demagnetisation and b) FoM when the magnetisation is graded in the X-axis.

Like the Z-axis grading, changing the magnetisation in the X-axis does not produce a FoM greater than 1 when looking at the demagnetisation field for the centre of the magnet, this confirms one the initial presumptions that creating a graded magnetisation in this way does not give a benefit to the magnet at the centre. But as the place where the nucleation of demagnetisation is less likely to occur then it can be afforded to have a loss in performance for higher performance increased at the corner region of the magnet. As an example, the graded X-axis model gave a FoM of 0.84 which is 16% lowering of performance in the Z-axis, but when compared to the corner which has a FoM of 1.841, which is an 84.1% increase in performance. Like the FoM itself being a comparison trade up between the desirable reduction of the demagnetisation field and the undesirable but inevitable reduction of external field, comparing the FoM's themselves for the centre and the corner would provide another interesting insight as to where the performance gain is and where it is also lost.

The trend for the two datasets so far is consistent with the FoM being the highest at the corners for the models which have 0T, as discussed this is not a realistic view for real world materials but does demonstrate the theoretical possibility. Grading to a magnetisation of 1.1345 T gives FoM>1 which is consistent with the data Figure 6. 15, although the values a lower for the X-axis grading, this shows that depending on the axis of the grading can give different external field and demagnetisation field values.

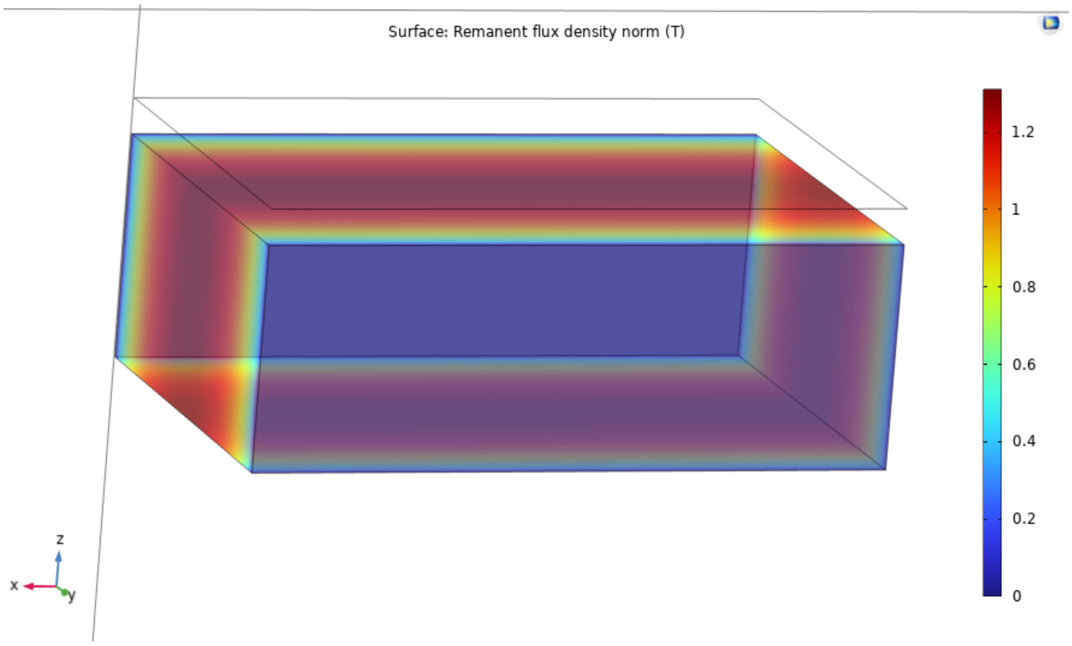

Figure 6. 18 Showing a visualisation of the Y-axis graded magnetisation in a cubic magnet.

Figure 6. 18 visualises a grading of magnetisation in the Y-axis, much like the Z and X-axis grading the corners remain a region of lower magnetisation. But the direction of the grading has obviously changed its axis. The field data is shown below in Figure 6. 19.

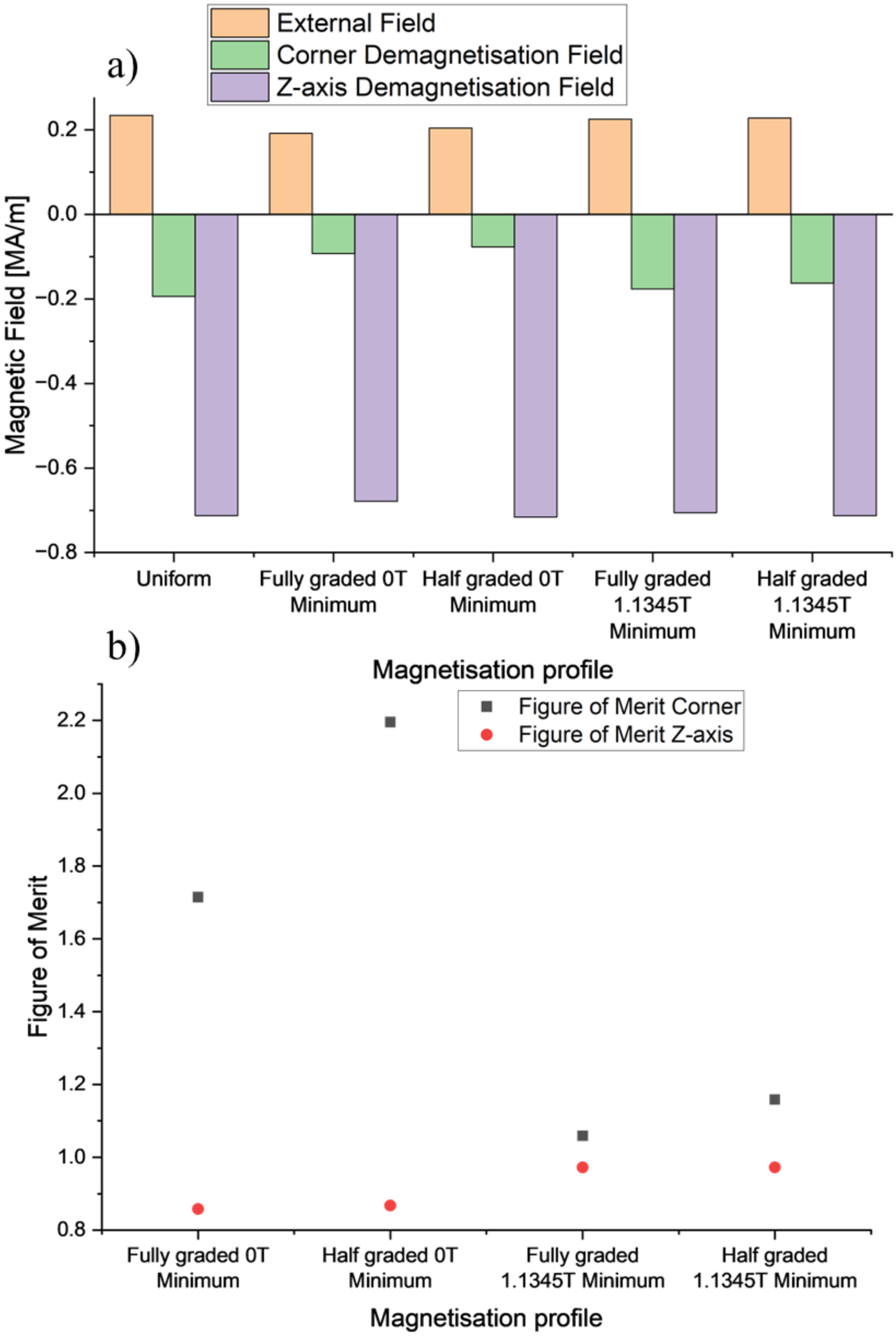

Figure 6. 19 Showing a) the external, corner demagnetisation, Z-axis demagnetisation and b) FoM when the magnetisation is graded in the Y-axis.

Much like the Z and X-axis grading and which is inferred from the 1D model and the 3D cylinder model. All single axis models of graded magnetisation provide a FoM less than 1 when looking through the centre Z-axis, and the FoM is greater than one when looking at the corner demagnetisation field of the magnet ranging from 1.05-2.2. With the highest FoM coming from the models with a corner magnetisation of 0 T and an improved FoM when half of the magnet is uniform material due to the increase in external field the uniform material delivers.

6.4.3 Multi-axis magnetisation grading

Grading in a multi-axis way should produce higher FoM than the single-axis method in the Z-axis due to the corners still being the target for a lower magnetisation and therefore lower demagnetisation field, but as shown for the different single-axis method, grading in the different axis gives different results for the demagnetisation and external field. By combining single-axis grading this allowed for different compensations or even a double down approach on a demagnetisation field. It will also be mentioned that by overlapping different single-axis gradings the magnetisations also overlap, therefore the maximum value will still be 1.31 T but the corner magnetisations no longer reduce to 0 T, with the magnetisation at the corners no longer being 0 T, it is expected that the FoM will reduce, but only a reduction from the unachievably high values towards something which can be more realistic. Figure 6. 20 below shows the first model of multi-axis grading.

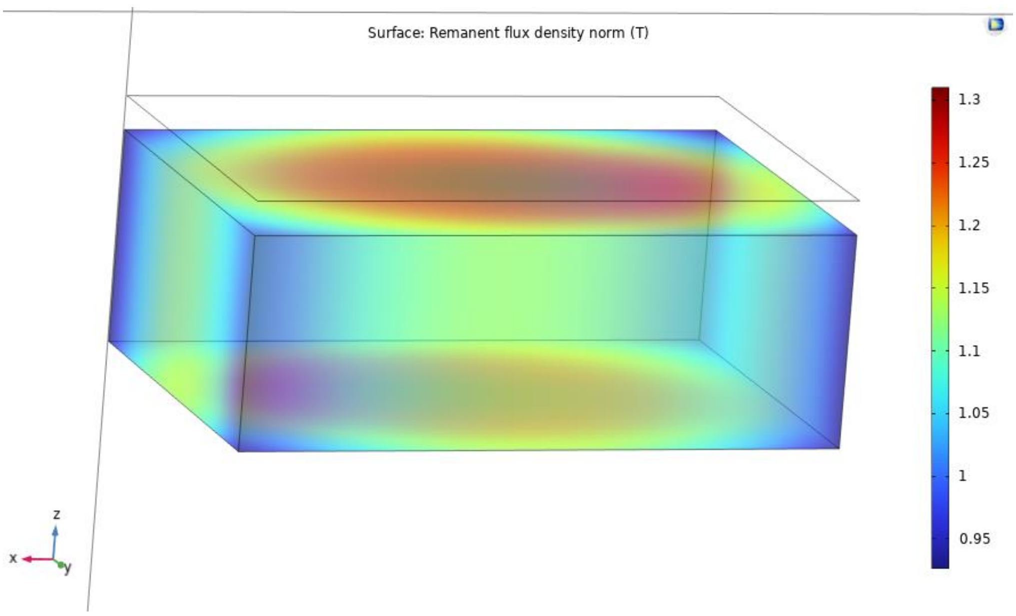

Figure 6. 20 Showing a visualisation of the XY-multi-axis graded magnetisation in a cubic magnet.

Shown in the heatmap of Figure 6.20, and as discussed previously the peak magnetisation is 1.31 T but the corner magnetisation is no longer 0 T. Visually there is an ellipsoid shape running through the Z-axis. This makes sense due to the grading only occurring in the XY-axes and the peak value will be running through the Z-axis and then grading out as defined by the equation. Figure 6. 21 shows calculated results for the different fields of the XY-multi-axis grading.

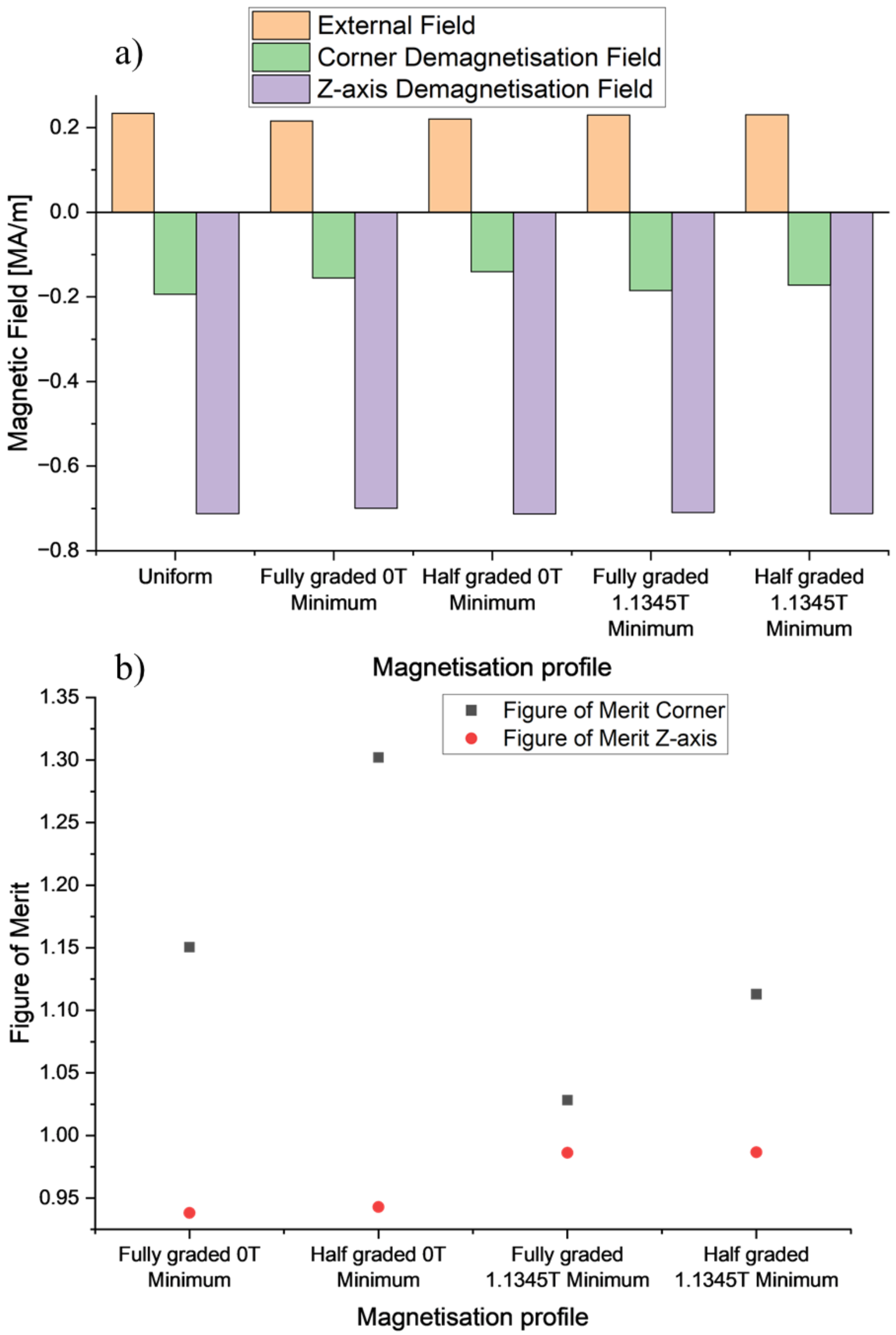

Figure 6. 21 Showing a) the external, corner demagnetisation, Z-axis demagnetisation and b) FoM when the magnetisation is graded in the XY-axis.

The FoM for the Z-axis is below 1 as seen in all the previous single-axis models, although not as low (0.998). This suggests that the creating of a multi-axis graded system is providing some compensation to the XY-axis and perhaps with a different combination the FoM of 1 or higher could be achieved. The trend for the corner FoM remains consistent with the previous single-axis models with an FoM ranging from 1.03-1.3. Although comparisons are lacking between 0 T models due to it not being achievable with how the graded magnetisation works. With the lower magnetisation at the corner producing a smaller demagnetisation field which leads to a higher FoM coupled with not as much loss of external field. The FoM (1.3) is also better for the model with half of the material as uniformly magnetised material.

The corners seem to be where the main benefit is, even after the creation of a multi-axis grading, but as mentioned, a different combination could hopefully produce some benefit to the Z-axis of the magnet. The figure below shows a different iteration of the multi-axis system.

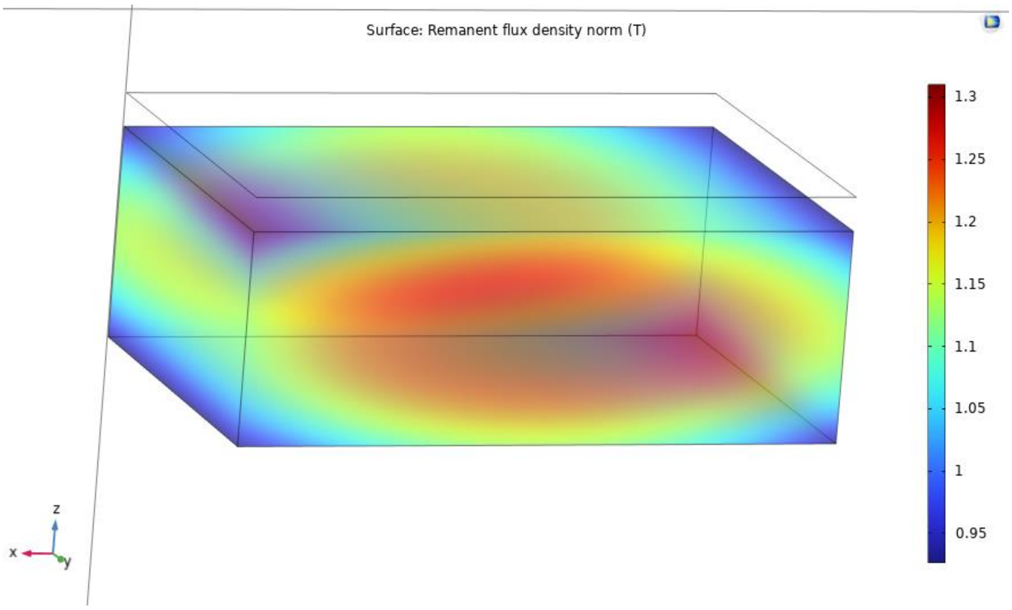

Figure 6. 22 Showing a visualisation of the XZ-multi-axis graded magnetisation in a cubic magnet.

Figure 6. 22 appears very much like Figure 6.11 just rotated, which makes is to be expected for a different combination to create the multi-axis. Figure 6. 22 shows the data for an XZ-multi-axis graded system.

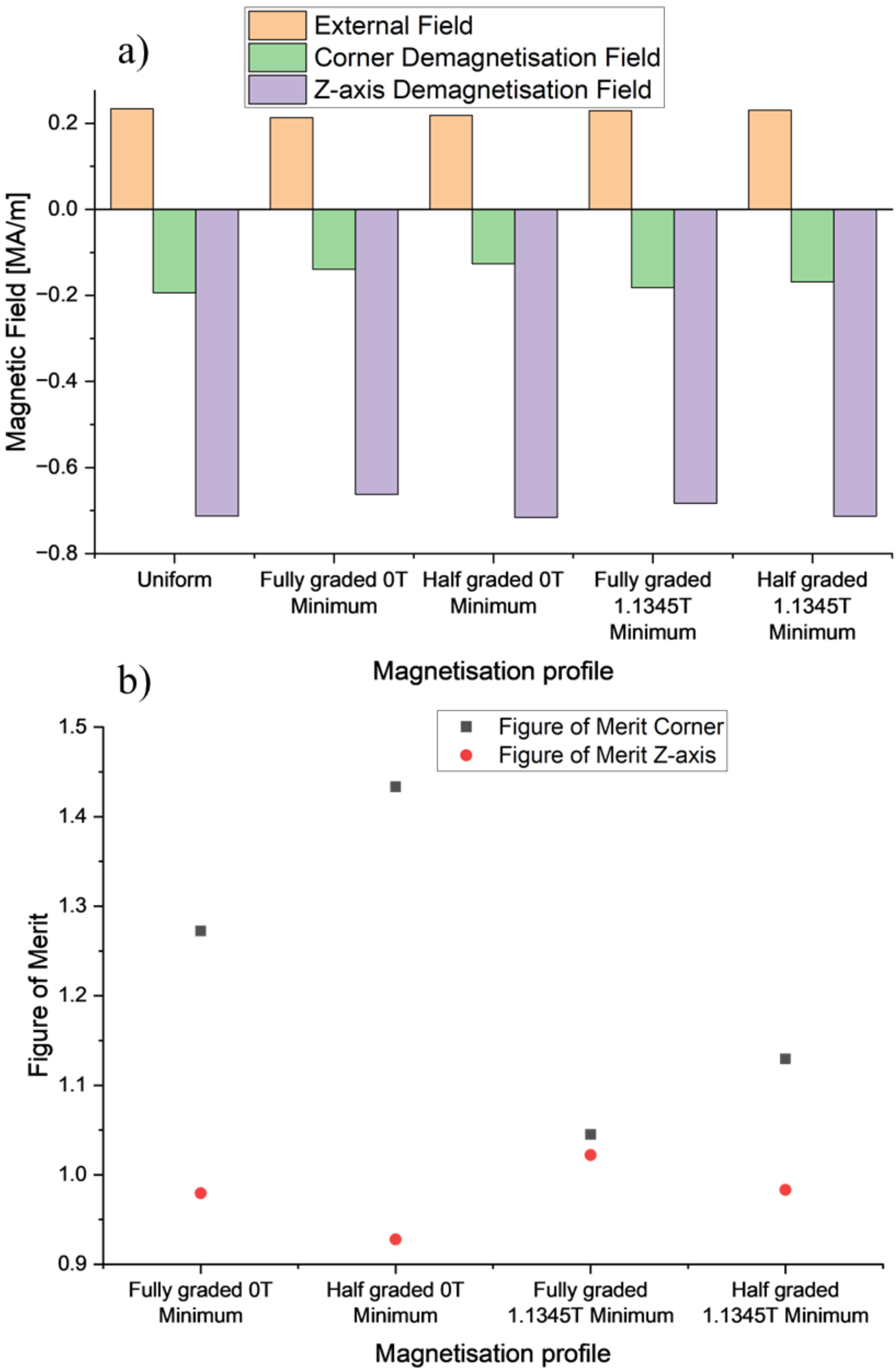

Figure 6. 23 Showing a) the external, corner demagnetisation, Z-axis demagnetisation and b) FoM when the magnetisation is graded in the XZ-axis.

First looking at the data for the Z-axis FoM, the iteration of a fully graded system with a higher corner magnetisation gives a FoM of 1.022. This is the first iteration where this has been calculated so far. This iteration also gives a corner FoM ranging from 1.05-1.4, this demonstrates that with the correct combination of grading axis it is possible. The rest of the FoM follow the same trend as all previous model iterations.

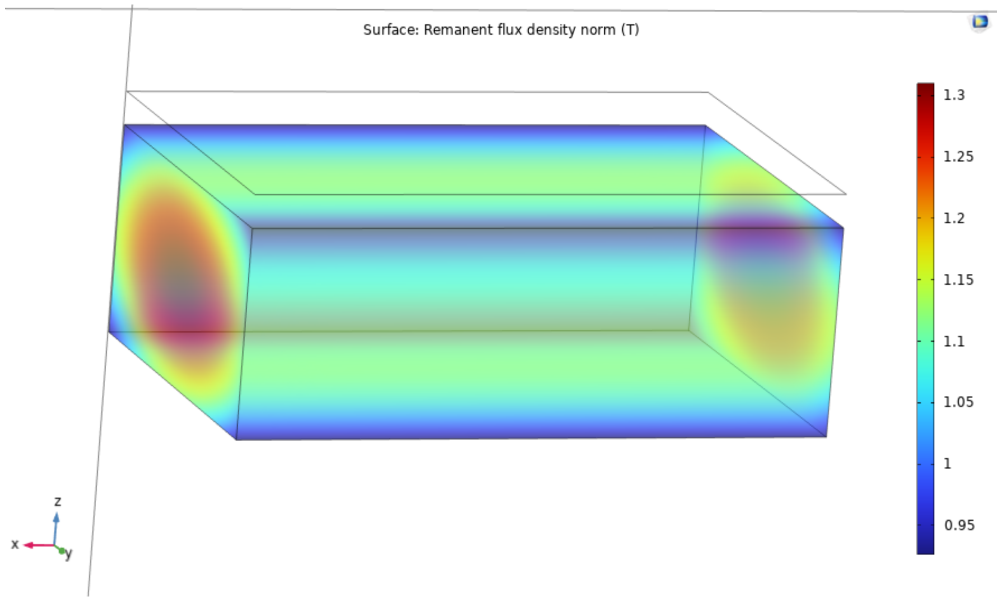

Figure 6. 24 Showing a visualisation of the YZ-multi-axis graded magnetisation in a cubic magnet.

As in the previous model, grading in the YZ-multi-axis produces a FoM above 1 for the model with the higher magnetisation at the corner from changing the degree of grading which minimised the reduction of external field produced, shown in Figure 6. 24. By combining a different set of single-axis this again produced a FoM of 1.023, deduced from this there is a preferable multi-axis grading which occurs in any axis involving the Z-axis. This is likely due to the measurement points for the demagnetisation field and the external field being in the Z-axis. For the corner demagnetisation field, the results for the FoM follow the same trend and range from 1.04-1.4, shown in Figure 6. 25.

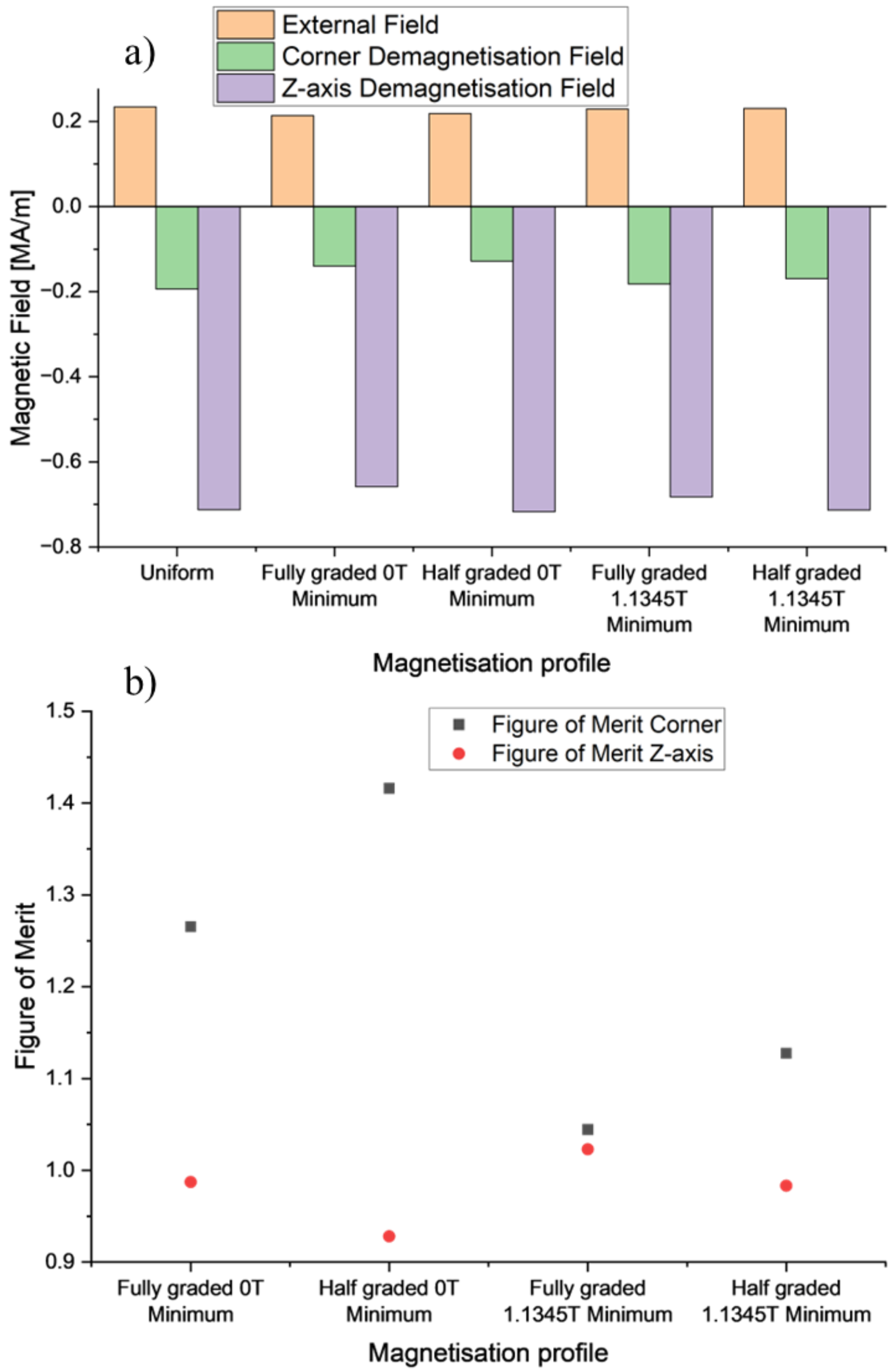

Figure 6. 25 Showing a) the external, corner demagnetisation, Z-axis demagnetisation and b) FoM when the magnetisation is graded in the YZ-axis.

Previous models showed that combining two single-axis can improve the FoM by compensating for the loss of magnetisation in a certain axis. Grading in all the axes should provide the best results so far, due to the overlapping grading providing a grading in the XYZ-multi-axis and having a lower magnetisation at the corners which maximises the region of higher magnetisation. Figure 6. 26 below shows the heatmap of magnetisation for an XYZ-multi-axis graded magnet.

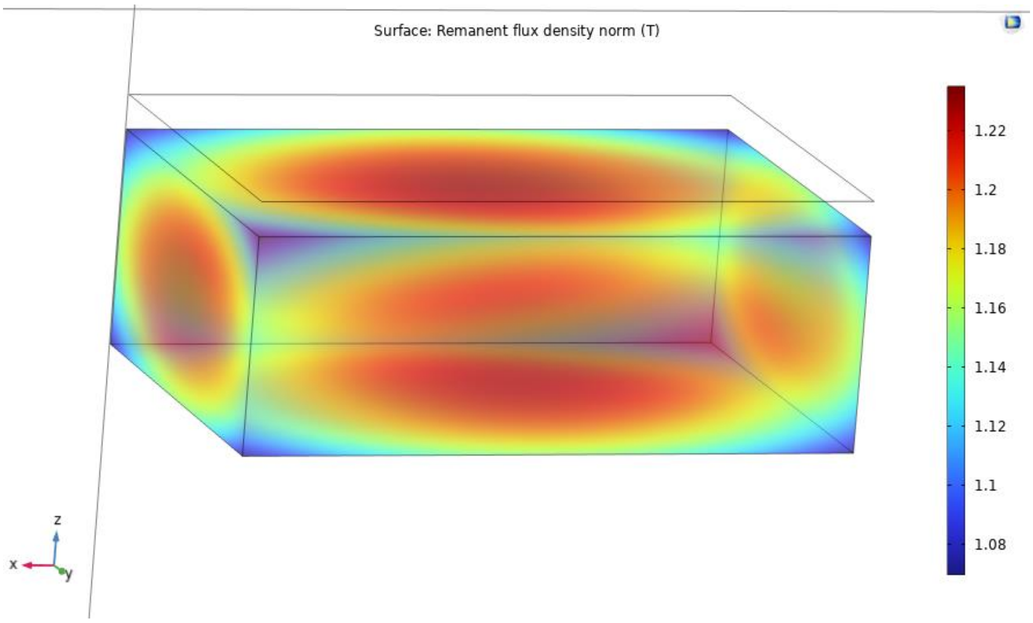

Figure 6. 26 Showing a visualisation of the XYZ-multi-axis graded magnetisation in a cubic magnet.

Due to the three different overlapping grading axis the corner magnetisation is higher than that of the previous models, but as found in previous models, the FoM is larger when the magnetisation at the corner is lower. This trend is also calculated in the XYZ graded model, as seen in Figure 6. 27. This model also gives a FoM of 1.023 for Z-axis magnetisation also when a lower magnetisation is used at the corners 1.007. This is the first time this has been calculated, and is likely down to the tri-axis grading reducing the demagnetisation field in the Z-axis whilst keeping the reduction of external field to a minimum. However, grading the magnetisation to a lower value at the corners would certainly improve the FoM for this region, as backed up by previous models, this will most certainly reduce the FoM through the Z-axis to below zero. Again, like all previous models the trend of the FoM at the corners ranges from 1.02-1.24.

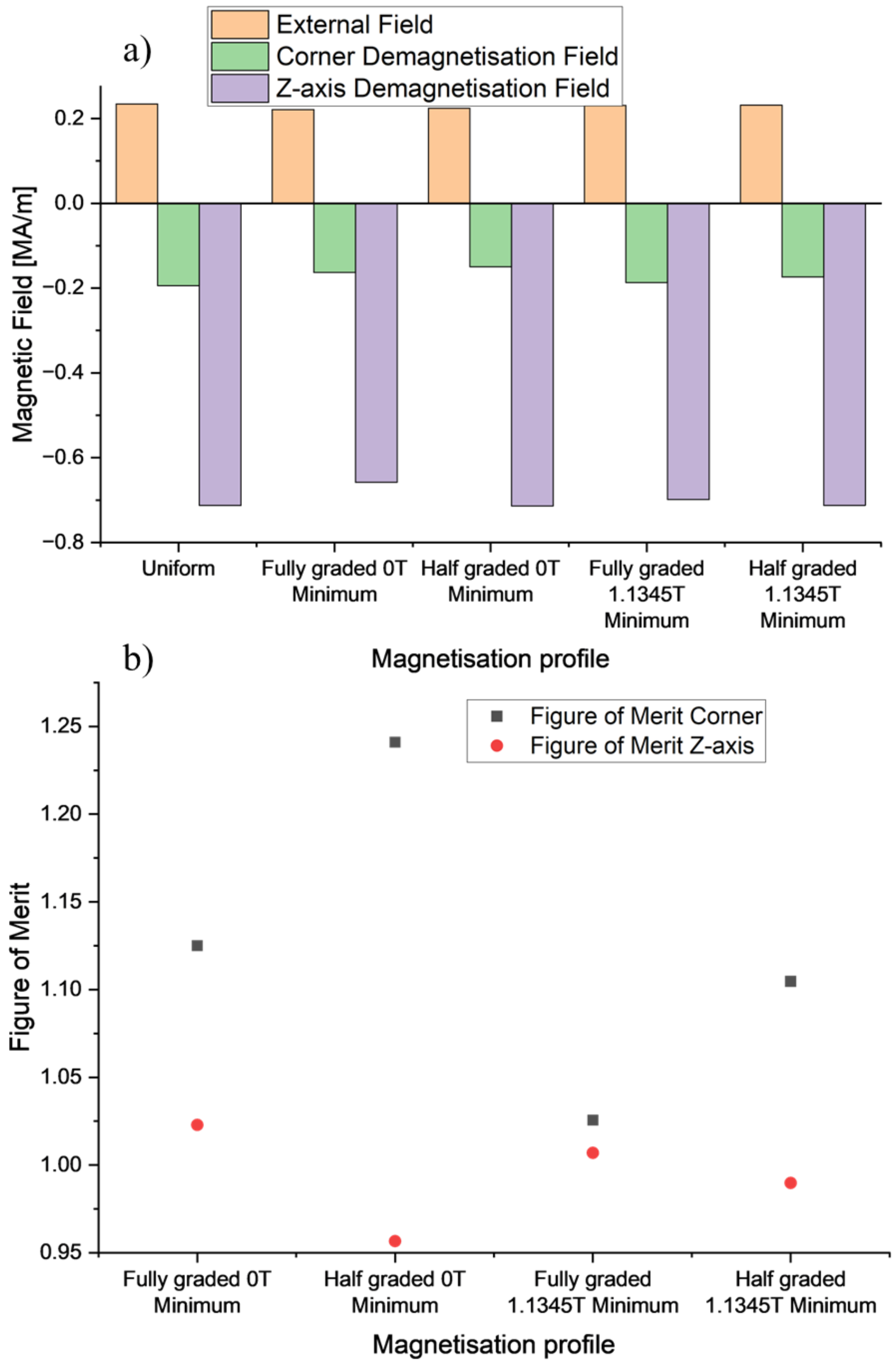

Figure 6. 27 Showing a) the external, corner demagnetisation, Z-axis demagnetisation and b) FoM when the magnetisation is graded in the XYZ-axis.

Interestingly, the XYZ-multi-axis graded magnet produced a “flat” demagnetisation field, observed in Figure 6. 28. Going back to the literature and what was discussed when a graded magnetisation was first discussed within the 1D model. The original idea was to achieve the property found in ellipsoidal shaped magnets where, because of their shape factor, they have a uniform demagnetisation field. Which means that the magnet should not have any weak points, or regions of higher demagnetisation field, and therefore have a higher coercivity. In which if the magnet was exposed to a strong applied field, it should be able to work against until such an applied field strength would be enough to cause a nucleation of magnetisation reversal which would happen to the entire magnet at once rather than a specific region.

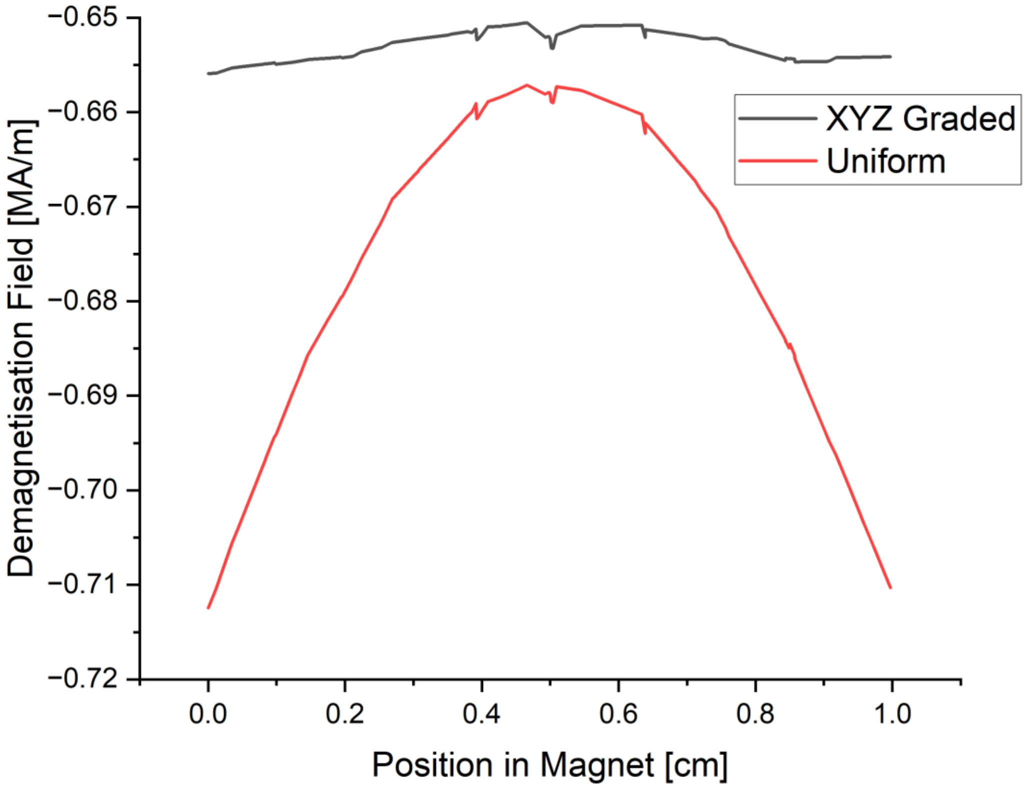

Figure 6. 28 Showing a comparison of the demagnetisation field through the Z-axis of the uniform cubic magnet and the XYZ-multi-axis graded magnet.

6.5 Summary

A 3D modelling approach was created to explore the reliability of the results obtained from the 1D Excel model. Investigating how the results calculated through a 1D mathematical pole theory approach compare to established simulation software for all models, mainly focusing on the use of a graded magnetisation. Initial studies looked at the effect the size of the air region has, and the mesh size required to obtain consistent results. Once the cylindrical magnets confirmed the results from the 1D model, the magnet model transitioned into a cubic model which represented real world magnets. Using a cubic model allowed for a multi-axis graded model to create new results but which trends can also be compared to the cylindrical model.

Simulations of the cylindrical model have proved a very strong correlation to the 1D models and gave a firm belief in the reliability of the results obtained from the 1D model. The results were of a high correlation for the internal demagnetisation field which is very promising. However, the results for the external field showed some difference, this is due to a discrepancy in how the external field was calculated for both, with the 1D model having its field confined to the cell region, whereas the 3D model is a surface average of a region 1.6mm from the pole surface, so not all the field will pass through this region hence the field calculated is likely to be smaller.

The use of films and a graded magnetisation follow the same trend of the FoM for the 1D and cylindrical model translates into the cubic model. The highest FoM are calculated in the cubic model for single-axis graded models, with the highest FoM coming in the half X-axis graded model of 2.58. The XYZ grading did produce a FoM of 1.125 at corners but also through the centre Z-axis, 1.023. A higher FoM was achieved for the corner of 1.25 but this resulted in a reduction to the Z-axis FoM of 0.957. This is important for potential different applications as being able to grade the magnetisation in different axes provided different benefits.

7. Motor simulations

To understand the impact changing the magnetic architecture of the magnets will have on the performance of an electric motor, a simulation of a motor was created in partnership with VW that will be important to see the potential application working whilst also allowing VW to use the data to draw comparisons to their motor designs.

7.1 Introduction to motor model

Firstly, in partnership with VW GI, a working motor design was provided by VW GI using ANSYS Maxwell, shown in Figure 7. 1.

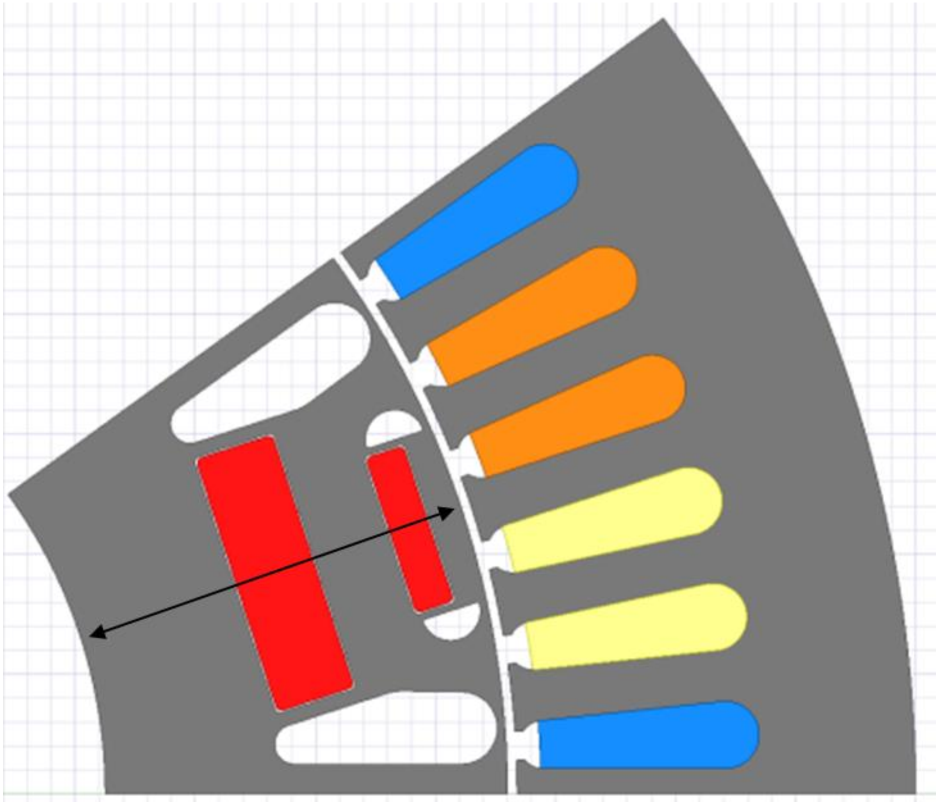

Figure 7. 1 Showing the motor layout with the stator and rotor irons, the magnets and different phases of coil pairs, with the magnetic field line scan path shown by the arrow.

The following work will discuss the translation of the ANSYS model into COMSOL Multiphysics and carrying out a set of three studies to investigate different magnetic architectures. The first is a study on weaking the entire magnet strength (lower magnetisation value) and therefore weakening the magnetic field to find the effect this has on torque. The second will involve adding a film in different axis to the magnets and then changing the area fraction of the magnet to the film and observing the torque. The third will be a continuation of the second study but instead creating an ellipsoidal core with a surrounding film to fill the magnet space and changing the area fraction. Each will be described visually later.

For the COMSOL model to be reliable, it must produce the same results as that of the established ANSYS model. One of the properties that is defined and should produce the same result, is the input current of the coils. Using the equations in Table 4.2 to define the current for the coil pairs, the current produced by each software appears identical, both shown in Figure 7. 2.

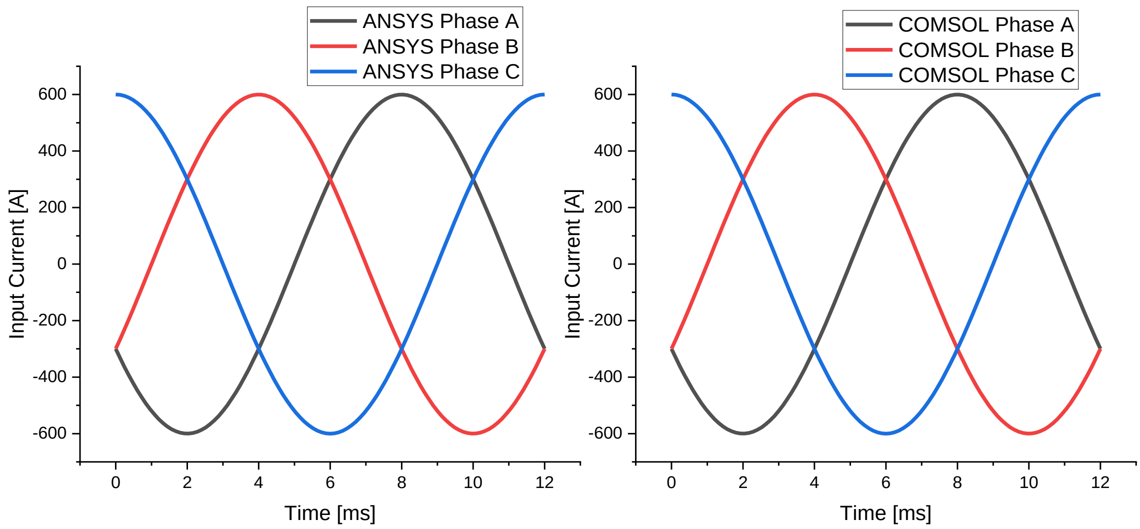

Figure 7. 2 Showing the input current over time for the ANSYS and COMSOL motor model.

A comparison of the phases shows that there is a very slight deviation of a 0.7-2.4 pA in phase C at the point where the wave crosses 0 A shown in Figure 7. 3. With this deviation it is can be confirmed that the coil currents are working in the same way.

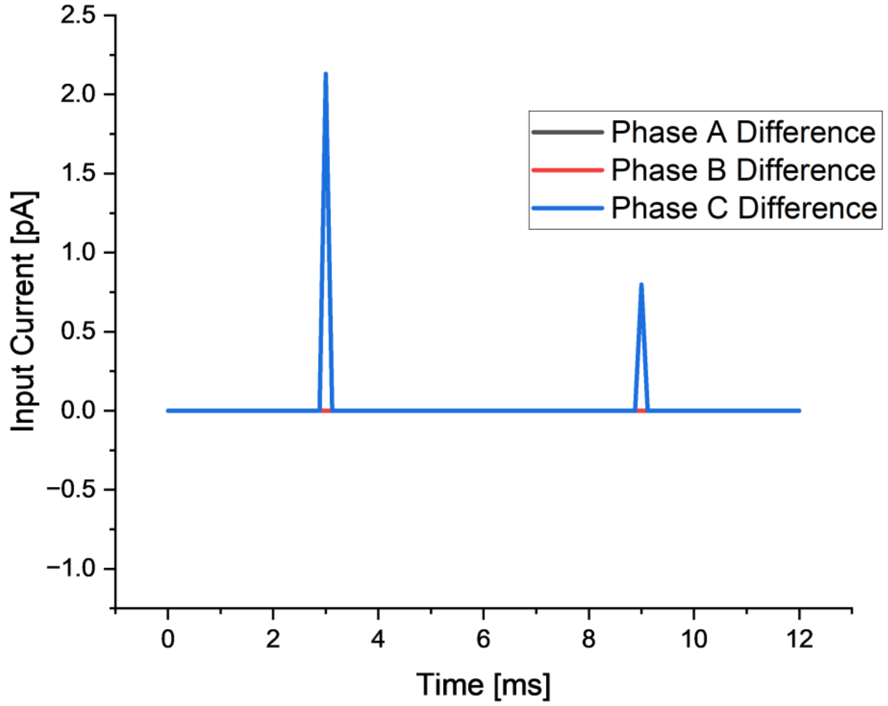

Figure 7. 3 Showing the deviation of the input current between the phases in ANSYS and COMSOL.

The next term which is deduced from the coil current and is also dependent on the model thickness.

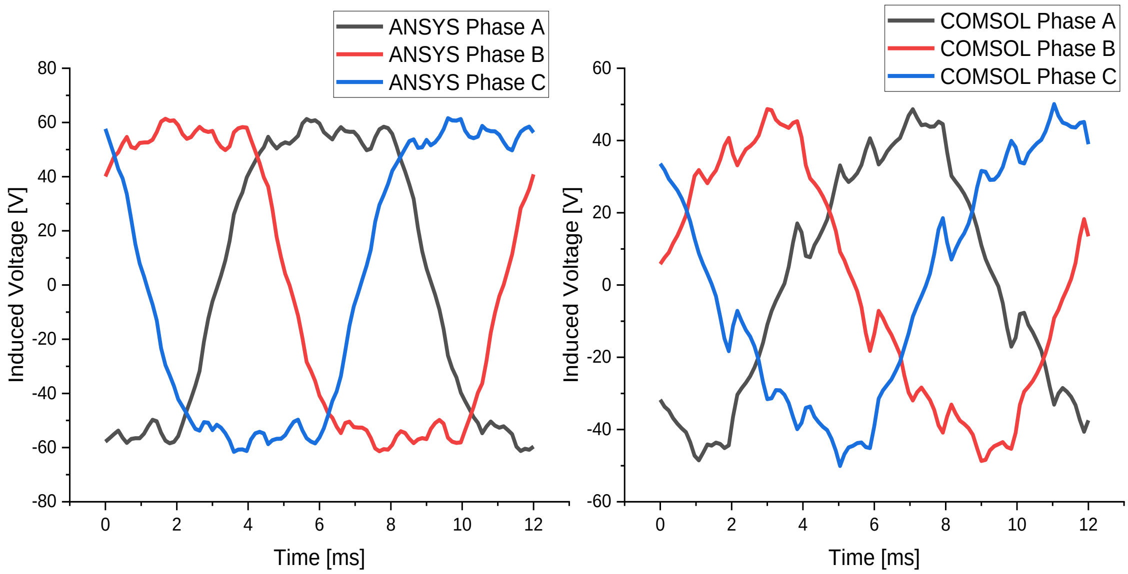

Figure 7. 4 Showing the induced voltage over time for the ANSYS and COMSOL motor model.

Figure 7. 4 shows that there is a deviation ~15 V in the induced voltage between the two models, however it is key to note that the different phase peaks line up. The difference varies the highest at the peaks and converges at the waveform returns to 0 V. This is assumed to be down to the discrepancies in the software's method of calculation and simulation. Peak values change depending on the thickness of the model but the plots themselves remain identical shown in Figure 7. 5. The waveform is identical for all three phases but instead of a peak of 50 V for the standard 17 cm model, the peaks increased to 300 V for a 1m thick motor and 150 V for a 0.5 m thick motor.

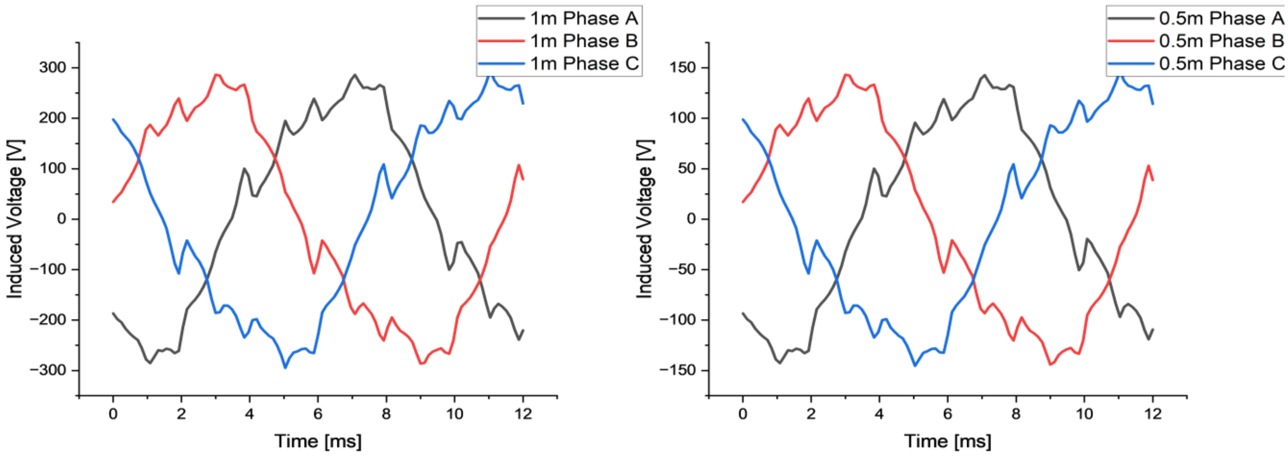

Figure 7. 5 Showing the induced voltage from the COMSOL model with differing model thickness, 1 m (left) and 0.5 m (right).

The resulting torque from the models with the same thickness (17 cm) differ, especially in the phases of the sin wave, shown in Figure 7. 6.

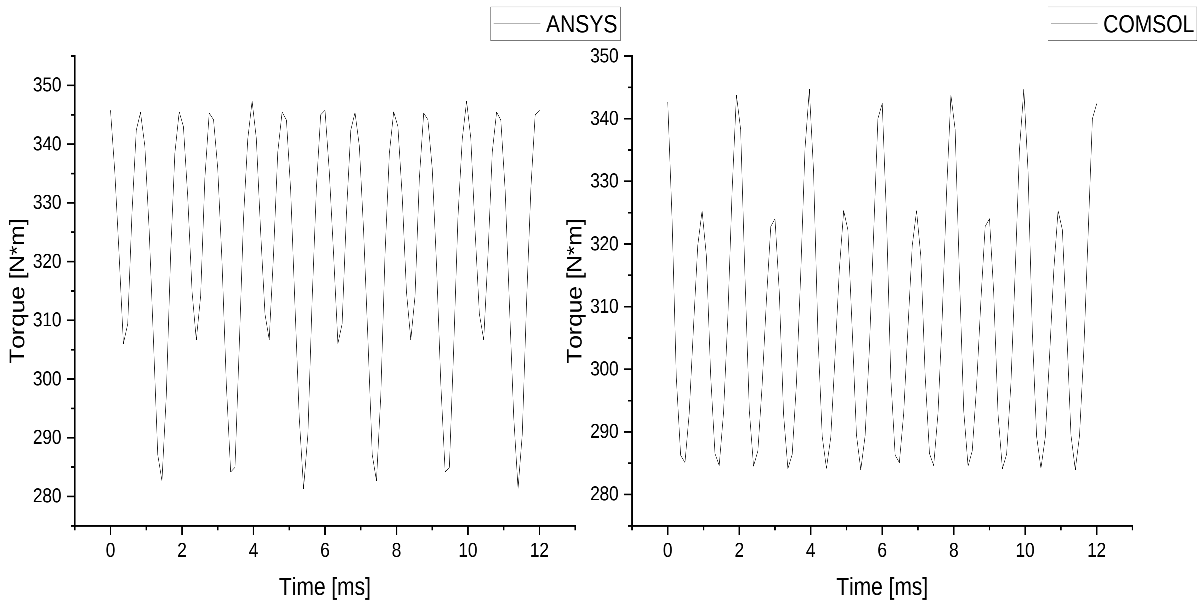

Figure 7. 6 Showing the torque over time for the ANSYS and COMSOL motor model.

Visually the two torque plots look very similar with regards to the minimum of 281 Nm and 283 Nm for ANSYS and COMSOL respectively. The maximum values are 347 Nm for ANSYS and 344 Nm for COMSOL however, the torque generated from the COMSOL model is the inverse to that of ANSYS. This is important to consider as all comparisons that follow will have to be drawn between the COMSOL plot. Although the minimum and maximum are quite close (2-3 Nm), the average values differ by 14 Nm due to this rotation causing the higher concentration of the waveform to be closer to the minimum than the maximum like in ANSYS, meaning COMSOL produces a lower average torque.

7.1.1 Motor magnets

The motor layout in Figure 7. 1 shows there are two magnets of different size within the rotor section. The magnet layout must be intentional to create a performance benefit. To understand this, when all other features of the motor are removed, the effects the magnets have on one another can be identified.

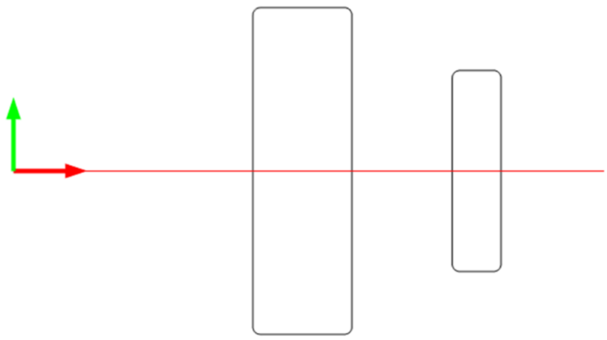

Figure 7. 7 Showing the isolated magnets as they appear in the motor with a line scan direction shown.

Measuring magnetic field through the arc length (line scan) labelled in Figure 7. 7, the external and demagnetisation field will be observed through the centre of the magnets to see the influence these magnets have on each other's performance.

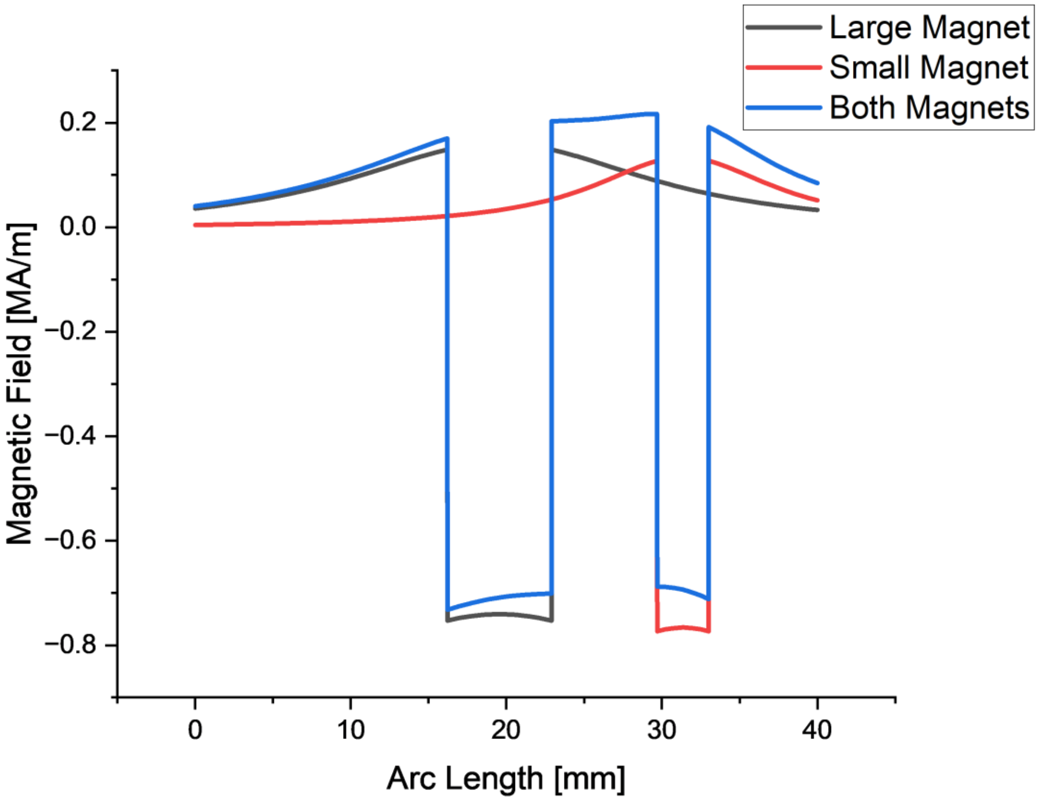

Figure 7. 8 Showing line scans of the isolated magnets in the motor system, of each magnet individually and together.

Evaluation of the line scans in Figure 7. 8, the external field is boosted by the presence of both magnets, where the large magnet produces 0.03 MA/m at the edge of the stator, the small produces 0.05 MA/m but when both magnets are together, they produce 0.08 MA/m. With both magnets being in the system the demagnetisation field of each magnets reduces compared to their isolated case respectfully, with the small magnet reducing the demagnetisation field by 8% and the large magnet having a 7% reduction. This boost in the external field to the right of the small magnet, which will be the external field acting against the load field created by the coils, is essential to an increase in performance. In Figure 7. 9 is the scalar potential of the two magnets in the system.

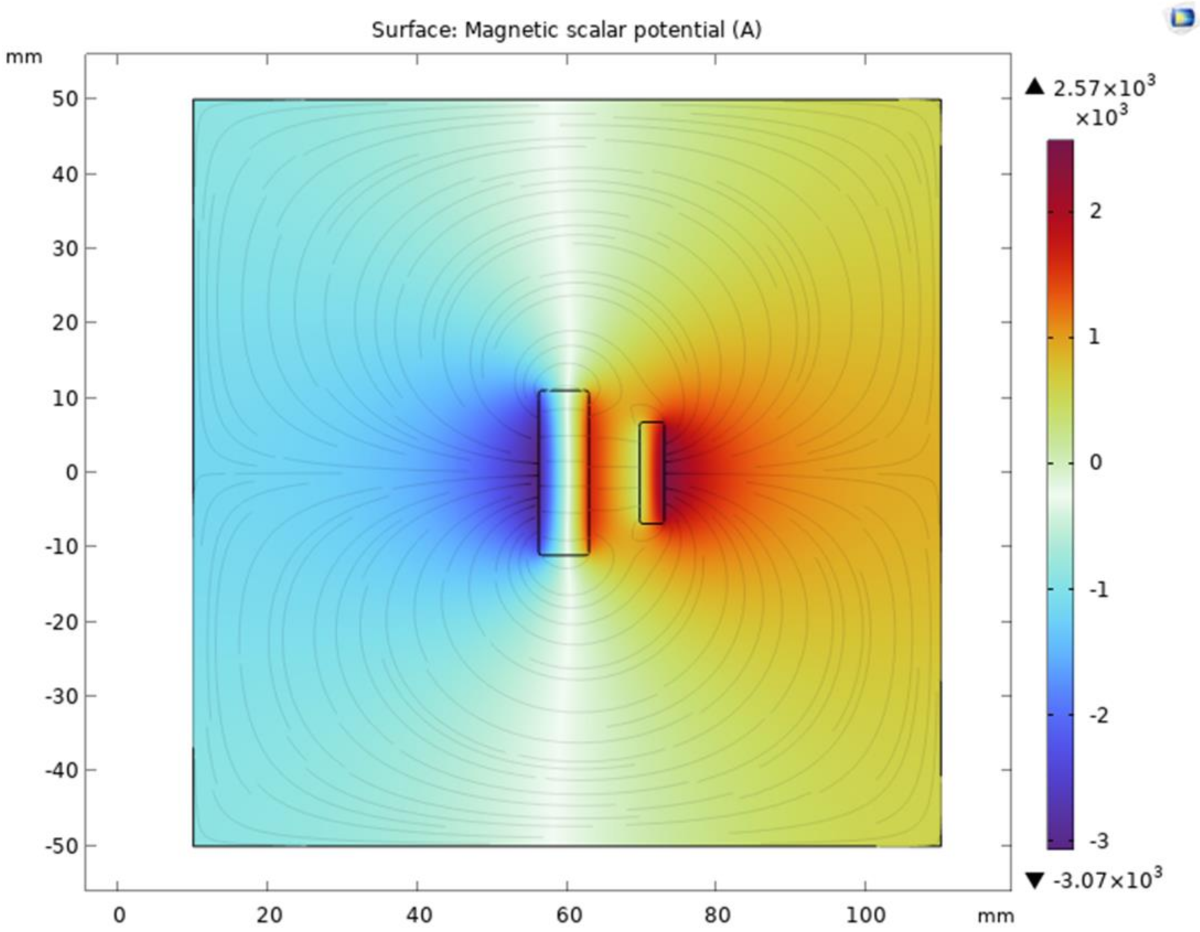

Figure 7. 9 Showing the magnetic scalar potential of the two magnets as a visual, highlighting in colour, the north and south poles of the magnet.

The large magnet appears to cause a strain on the smaller magnet, distorting the north pole of the small magnet and causing an increase in external field delivered by the magnet. Another factor to consider with the magnets in this orientation is the magnetic flux density, shown in Figure 7. 10.

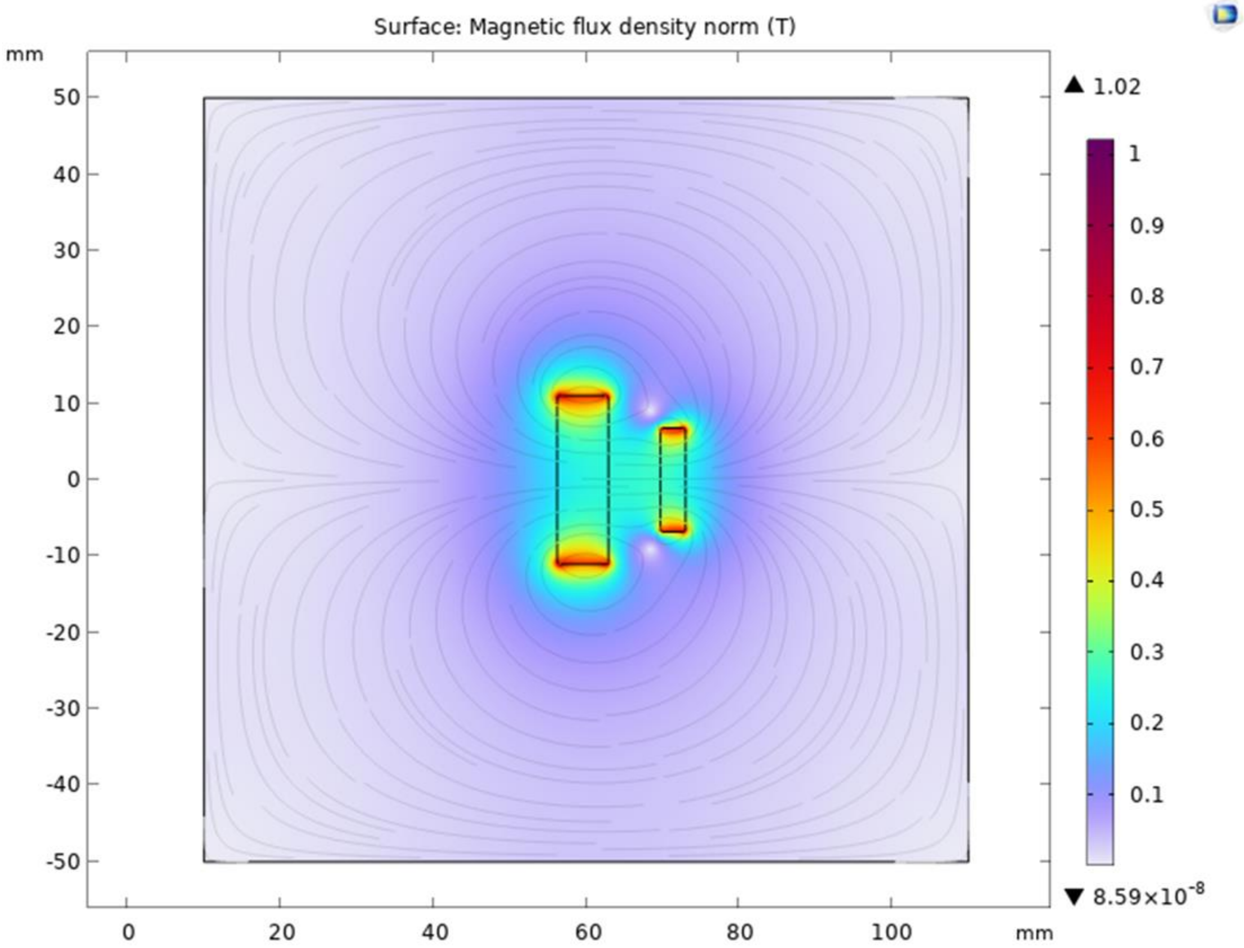

Figure 7. 10 Showing the magnetic flux density of the two isolated magnets within the motor system.

The magnetic flux density is shown to be highest at the corners and through the short axis length in the direction of magnetisation.

Now that a working COMSOL model has been established that creates similar results to that of the ANSYS model, with the differences understood we can continue to develop the model. The first study will focus on changing the magnets to see their effect on torque can be investigated whilst drawing comparison to the standard COMSOL model.

7.2 Reducing magnetisation

The first study investigated the effect of lowering the magnetisation of the magnets in the motor and investigated the effect this has on torque performance of the motor.

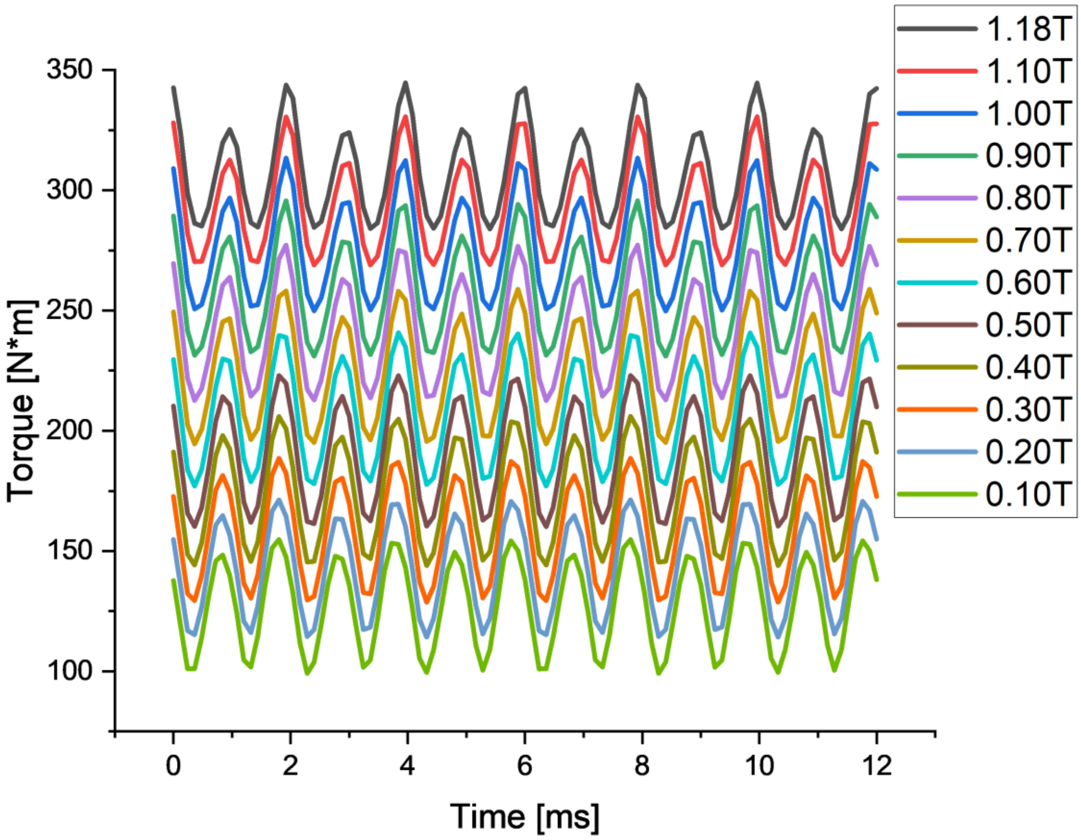

Figure 7. 11 Showing torque over time for the motor with different a magnetisation of the magnets.

Figure 7. 11 demonstrates the loss in performance of torque, which is to be expected, a weaker magnet produces a weaker external field which is not going to work as efficiently against the applied field from the coils. A more detailed analysis of the torque for the investigation is shown in Figure 7. 12.

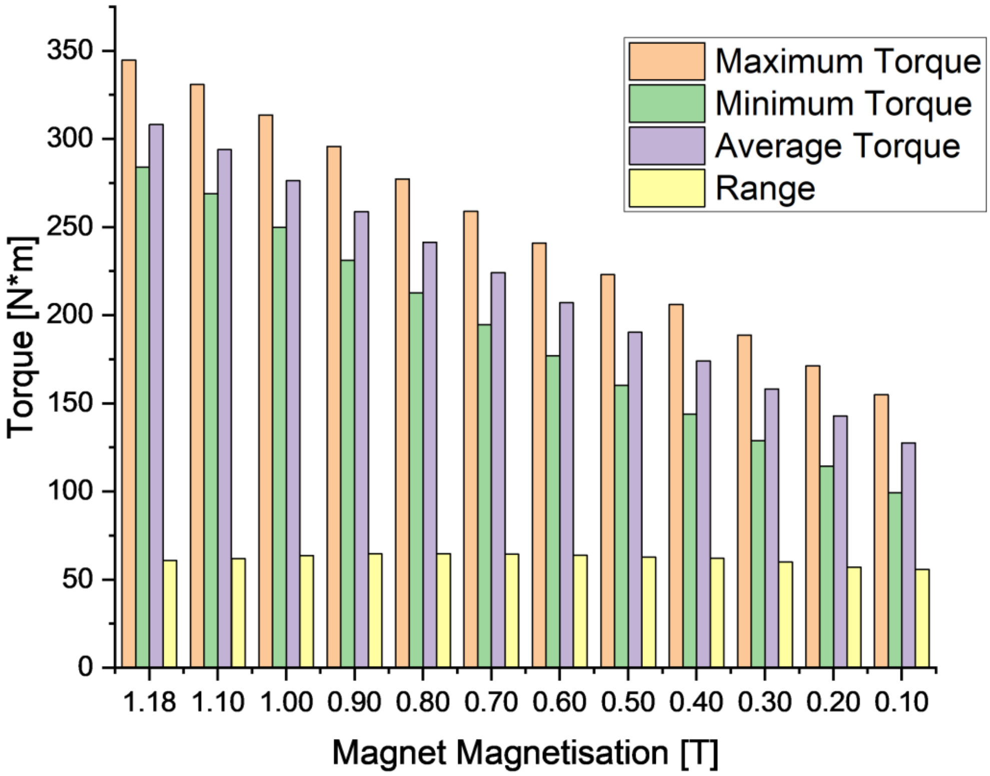

Figure 7. 12 Showing the changing maximum, minimum, average and range of torque for the motor with different magnetisation magnets.

The different terms extracted from the torque plots clearly highlight that the performance of the motor is reducing with a lower magnetisation of magnet. Interestingly the range of the minimum and maximum torque values does not seem to vary when changing the magnetisation, percentage change is shown in more detail in Figure 7. 13.

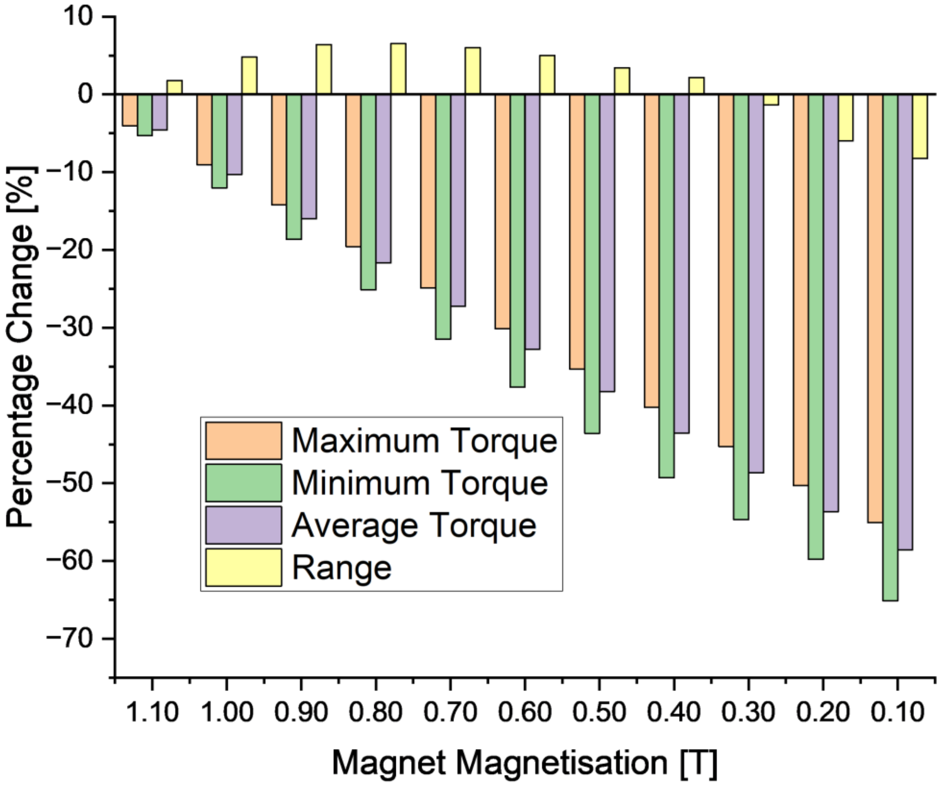

Figure 7. 13 Showing the percentage change of the maximum, minimum, average and range of torque compared to the standard 1.18 T model.

Figure 7. 13 gives a better visual of how the different torque values are changing with a reduced magnetisation, at some magnetisation values the range between the minimum and maximum increases by 6.5% for a magnetisation of 0.8 T and then reducing by 8.3% for a magnetisation of 0.1 T. There seems to be a magnetisation value where the range will be reduced the most before it starts to increase.

When considering the use of films, the magnetisation of the films will be 0.3 T, as this produced the smallest change in the range (-1.4%) and represented a definite change in magnetisation compared to the bulk material. This is also drawn from the work in Section 6.5 where a 1.2 MA/m bulk and a minimum magnetisation of 0.35 MA/m produced the best FoM.

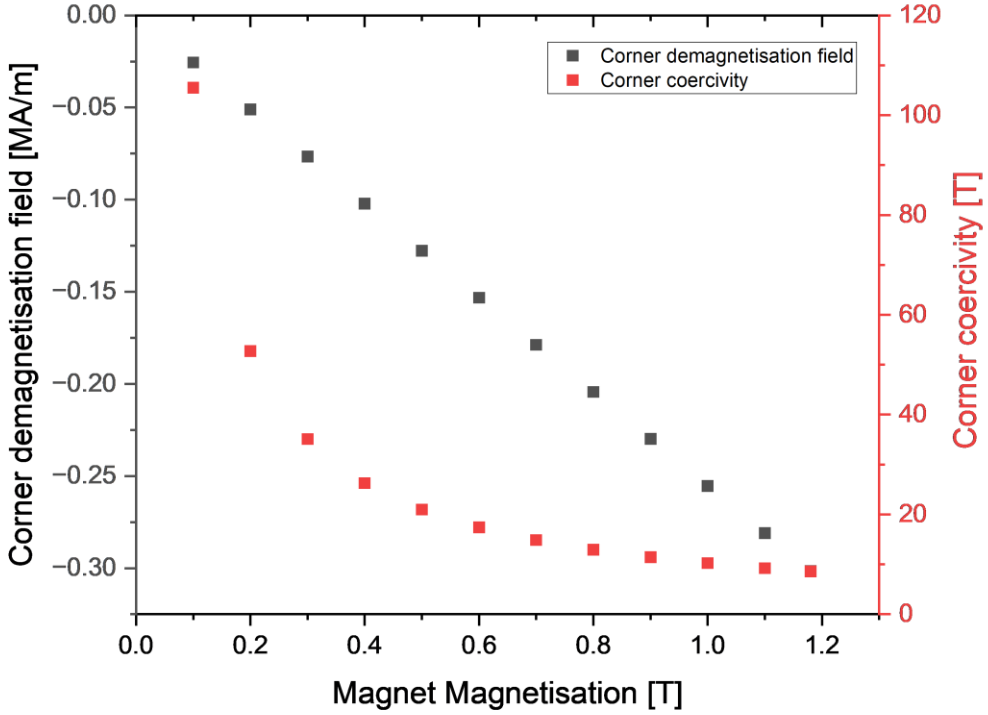

Figure 7. 14 Showing the corner demagnetisation field and coercivity of the magnets with varying magnetisations.

Figure 7. 14 shows that the demagnetisation field appears to have a linear decline as the magnetisation reduces from -0.301 MA/m to -0.00255 MA/m and the coercivity increases from 8.57 to 105.5 T. Like that discussed previously in the 1D model, these values seem unattainable for materials but can show the potential of what a film could add to a bulk material. Coercivity is calculated using equation 4.15, and assumes that as the magnetisation profile changes, the magnetocrystalline anisotropy of the material remains constant.

7.3 Volume fraction of magnetic film

7.3.1 X-axis volume fraction

The following study will investigate a varying volume fraction of bulk:film in order to minimise performance loss and maximise the amount of film present. The focus of the film will be on the corners of the magnet that are facing the field from the coils in order to reduce the demagnetisation field in the corners. The first attempt at this for the magnets is shown in Figure 7. 15.

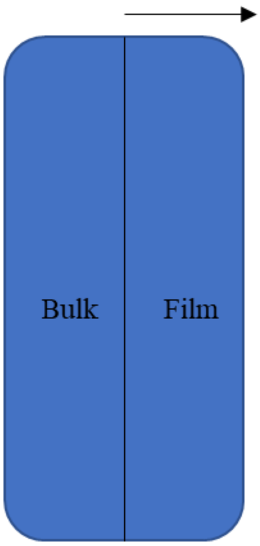

Figure 7. 15 Showing a 50:50 volume fraction in the x-axis of the bulk and film, with the direction of the volume fraction division will be moving is shown.

Varying the volume fraction in this way will create a film that is over the corners that will face the coils. Torque results for a bulk of 1.18 T and a film of 0.3 T with a varying volume fraction are shown in Figure 7. 16.

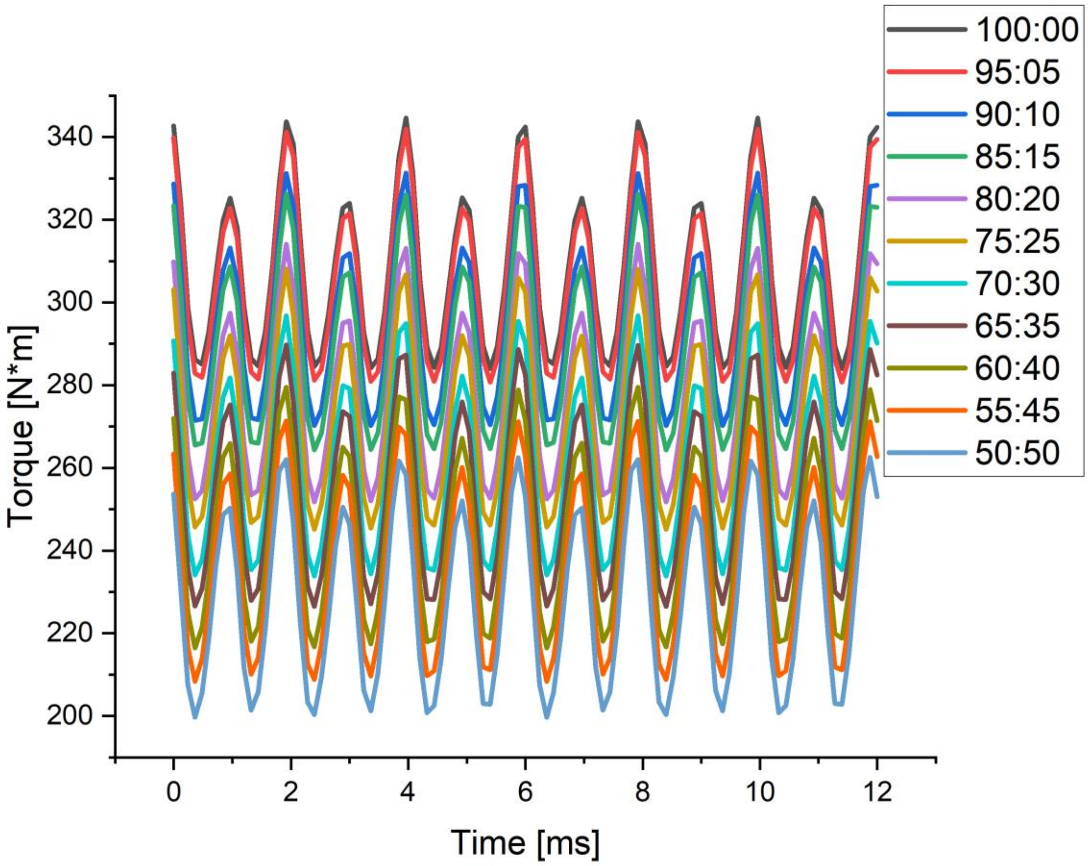

Figure 7. 16 Showing the torque plots for a varying volume fraction with the magnet being divided through the x-axis.

Reducing the volume of bulk material in turn reduces the torque of the motor, which can be understood as less bulk material, a weaker external field which acts less on the coils. The values obtained from the torque are described in more detail in Figure 7. 17.

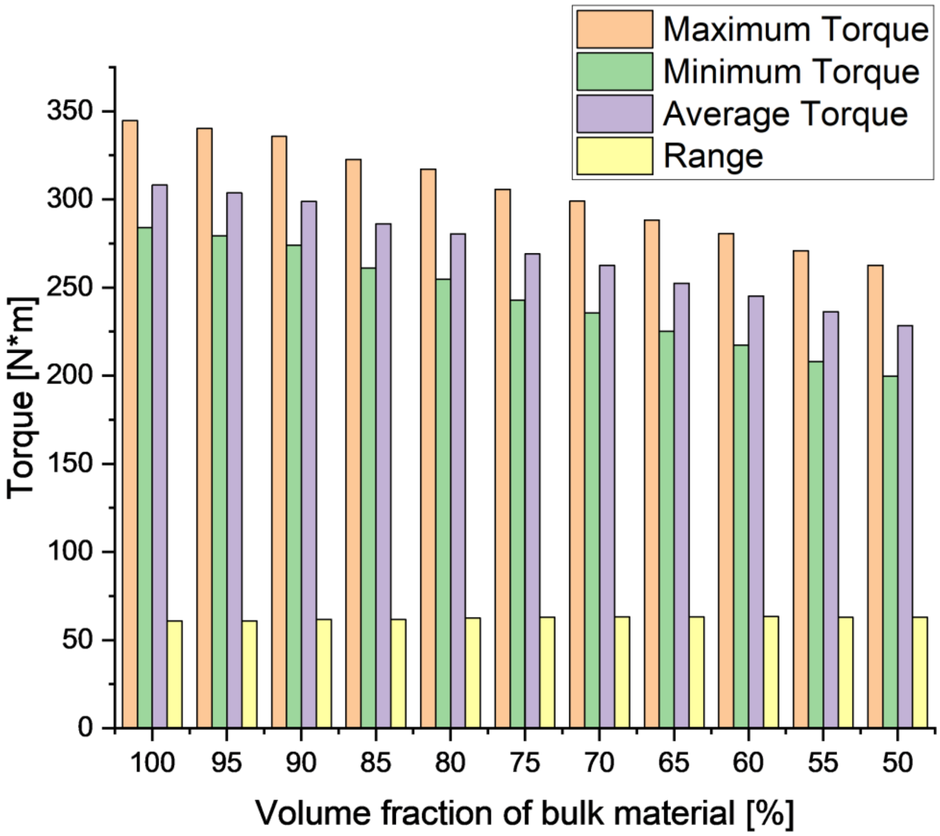

Figure 7. 17 Showing the torque values obtained when varying the volume fraction in the x-axis of the bulk and film material.

Shown in Figure 7. 17, all values from the torque show a decrease with a smaller volume fraction of bulk material, the first study predicted this, but the percentage change in Figure 7. 18 shows a better representation of the performance loss relative to the volume fraction.

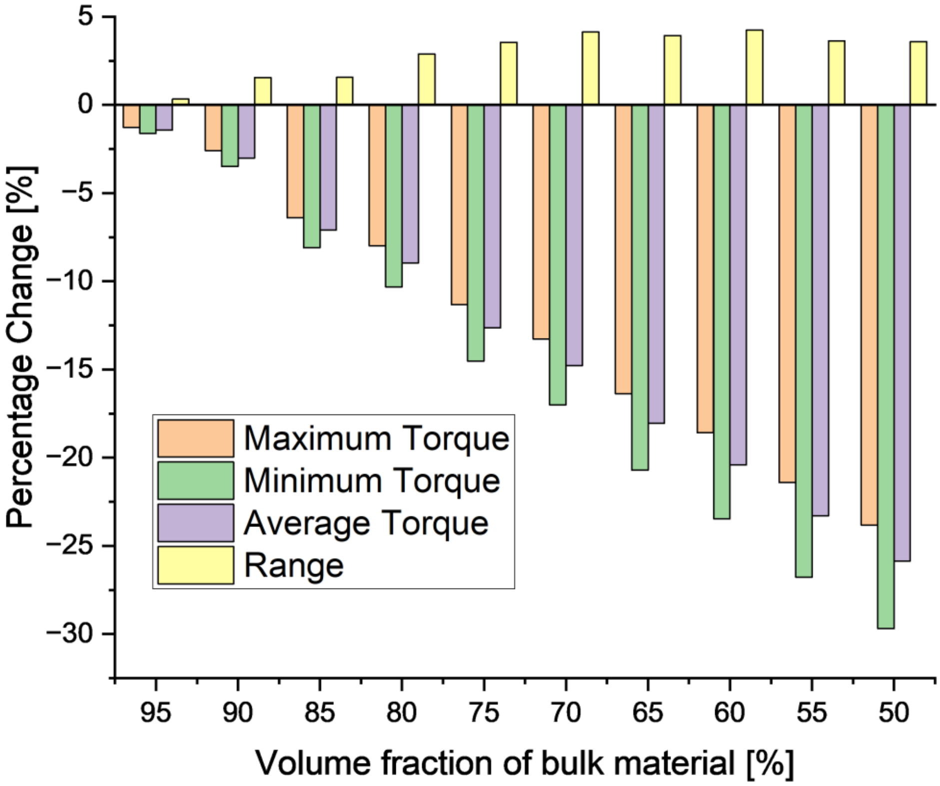

Figure 7. 18 Showing the percentage change of the torque values compared to the 100% volume fraction in the x-axis.

A 50:50 volume fraction reduces the performance of the average torque by 26% as the largest reduction. A 95:05 volume fraction which resembles a film more than the other volume fractions, reduced the average torque by 1.4%. This demonstrates that a magnet could be optimised by reducing the volume fraction and replacing the bulk material with a lower magnetisation and potentially cheaper magnetic material in order to maximise cost saving over performance. This can range from a full replacement shown in the 50:50 or resembling a film in the 95:05.

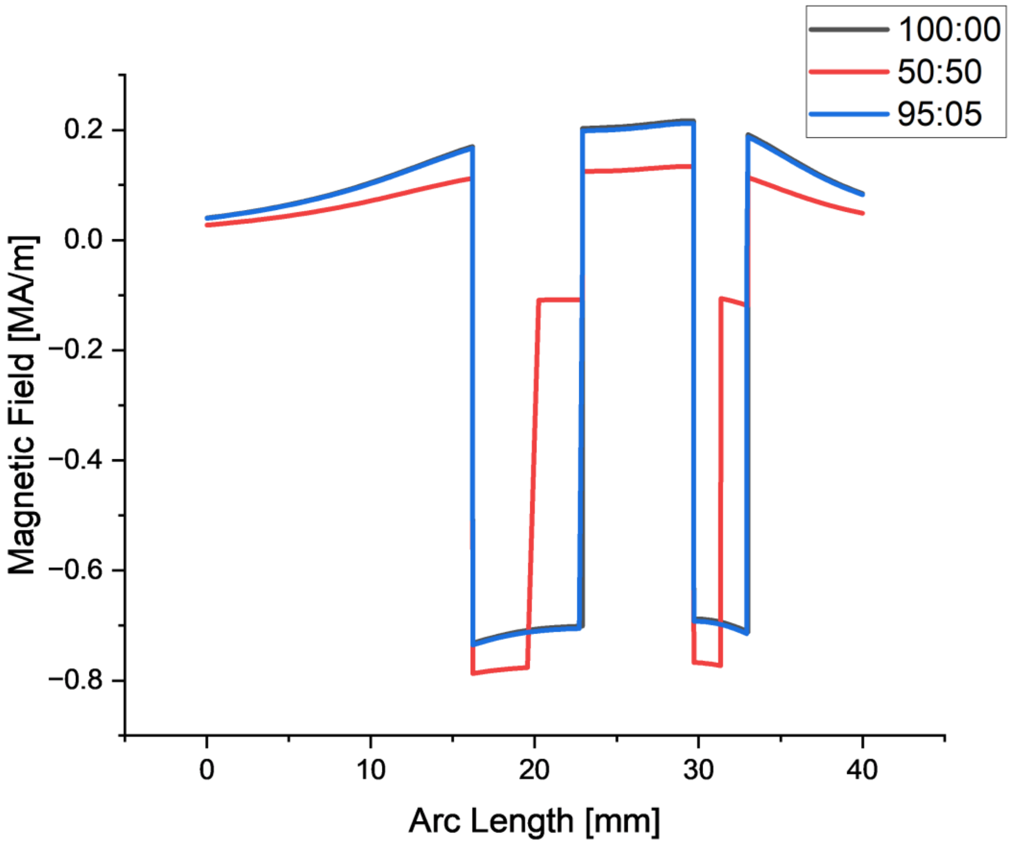

Figure 7. 19 Showing the magnetic field line scans of different volume fractions in the x-axis.

The performance of the motor reduces with reducing the volume fraction of the bulk material. But shown in Figure 7. 19, a 50:50 ratio creates a region of high stability from the lower magnetisation, a transition of -0.79 MA/m for the bulk region to -0.11 MA/m of the large magnet. The external field produced by 50:50 is reduced by 43% compared to the 100:00. The 95:05 which resembles a film, has a demagnetisation transition of -0.71 MA/m to -0.048 MA/m and reduced the external field by 2.5%

7.3.2 Y-axis volume fraction

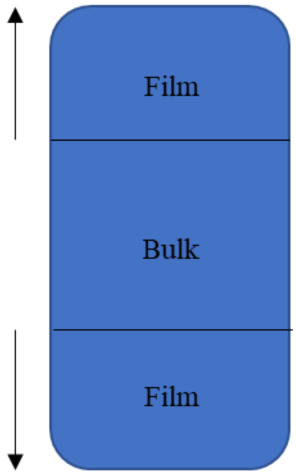

Figure 7. 20 Showing a 33:33:33 volume fraction in the y-axis of the bulk and film with the direction of the moving volume fraction shown.

Figure 7. 20 shows a different method for the addition of films to the bulk material to ensure they are covered on the corners facing the applied field, unlike the x-axis method this also covers all of the corners of the magnet. The simulated torque values are shown below for a variable volume fraction in Figure 7. 21.

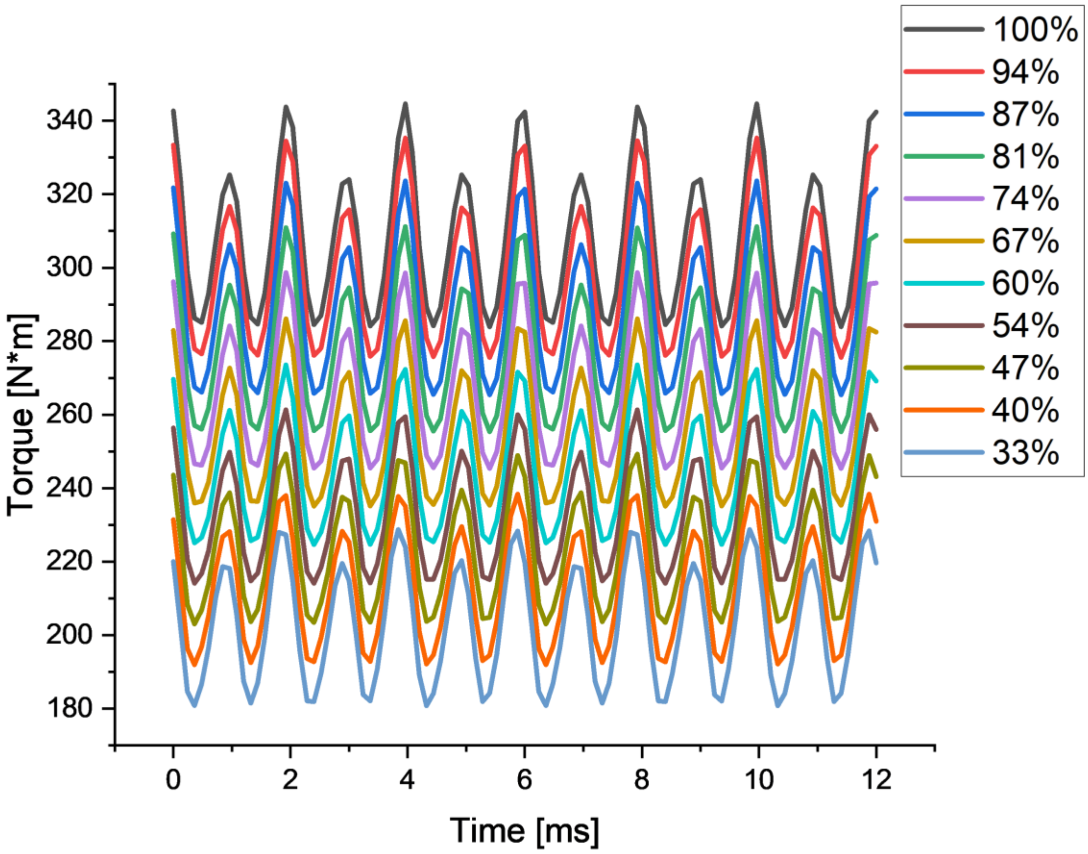

Figure 7. 21 Showing the simulated motor torque values for a variable volume fraction in the y-axis.

The torque results obtained in Figure 7. 21 reiterate the results of Figure 7. 16, where reducing the volume of the bulk material reduces the torque. A more detailed view of the torque values is shown in Figure 7. 22.

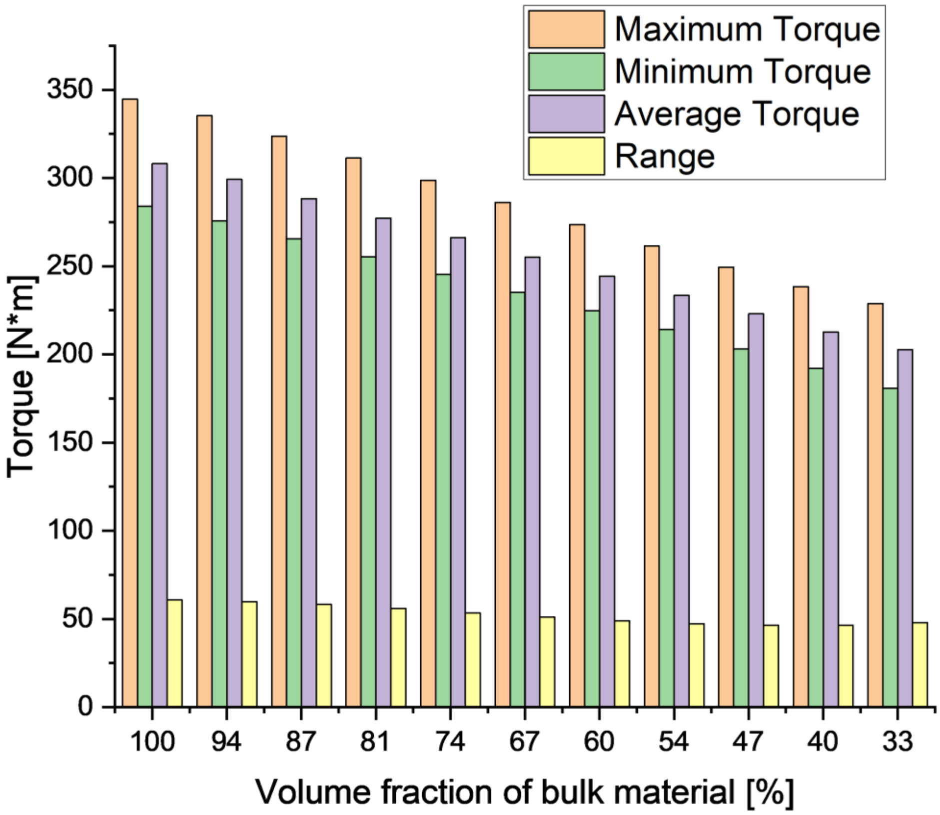

Figure 7. 22 Showing the torque values obtained when varying the volume fraction in the y-axis of the bulk and film material.

As shown by the torque plots of Figure 7. 21, the derived values in Figure 7. 22 show a more detailed decline of performance from the bulk material of 33%. The percentage changes shown in Figure 7. 23 show that the maximum percentage loss of the average torque is 34% from the 33% bulk magnet. The 94% bulk magnet induced an average torque loss of 2.9%, for the bulk magnets and film divided in the y-axis, the average torque loss is a few percent away from being half of the volume fraction of the film region. This suggest that there is some linearity between the volume fraction of the film and the torque percentage loss.

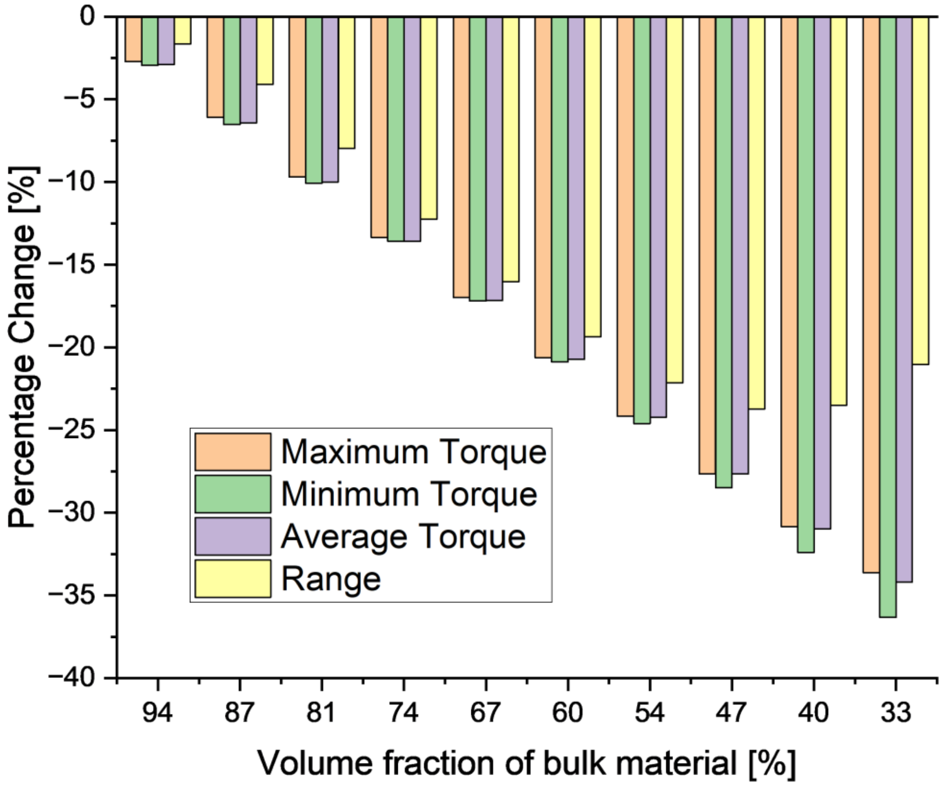

Figure 7. 23 Showing the percentage change of the torque values compared to the 100% volume fraction in the y-axis.

A comparison between the average torque loss of Figure 7. 18 and Figure 7. 23 shown in Figure 7. 24, demonstrates the strong correlation between a reduced volume fraction of bulk material and the result of reduced torque. This suggests that there is no benefit to dividing the volume fraction in either the x or y-axis.

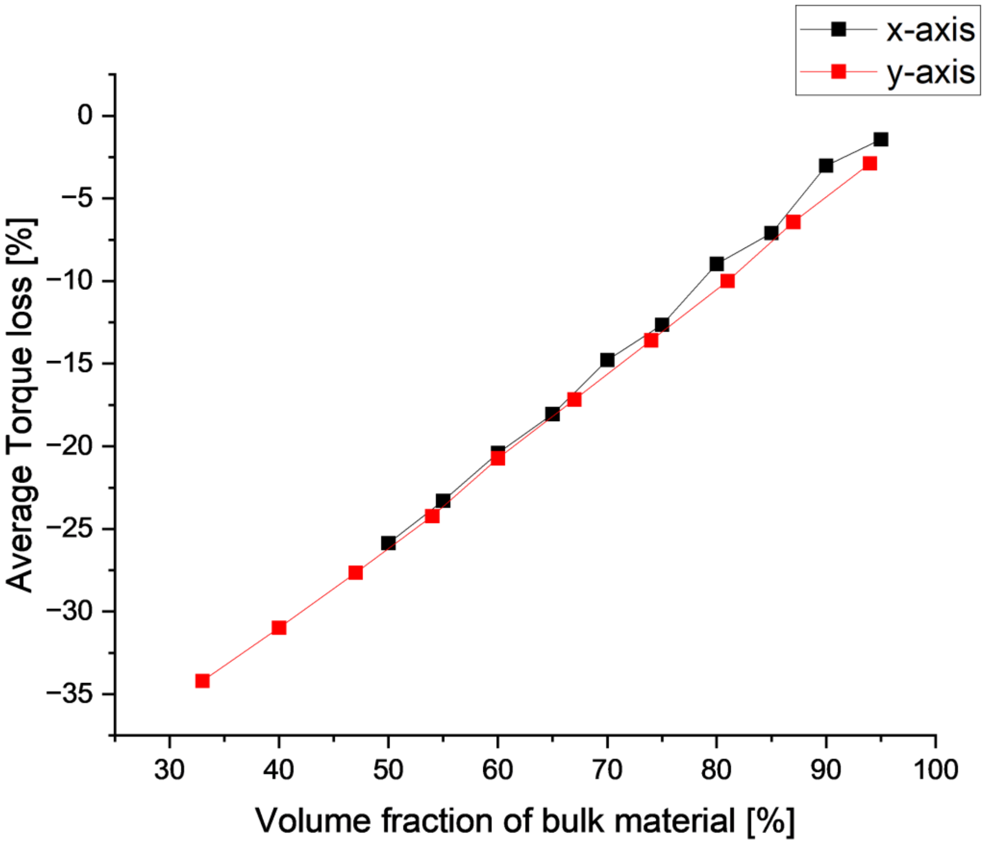

Figure 7. 24 Showing a comparison of the average torque loss for different volume fractions of bulk material when divided in the x and y-axis.

Although the motor shows a loss of performance with a reduced volume fraction, the magnets, the magnets demagnetisation reduced by 0.7% and the external field by 1.5% for the 94% bulk volume fraction in Figure 7. 25. The line scan follows the path through the centre of both magnets as shown previously in Figure 7. 7, which suggests that having a film on the edges of the magnet does have a reduction to the larger bulk material in terms of demagnetisation field. But the gain of demagnetisation field at the corners is not measured in the line scan.

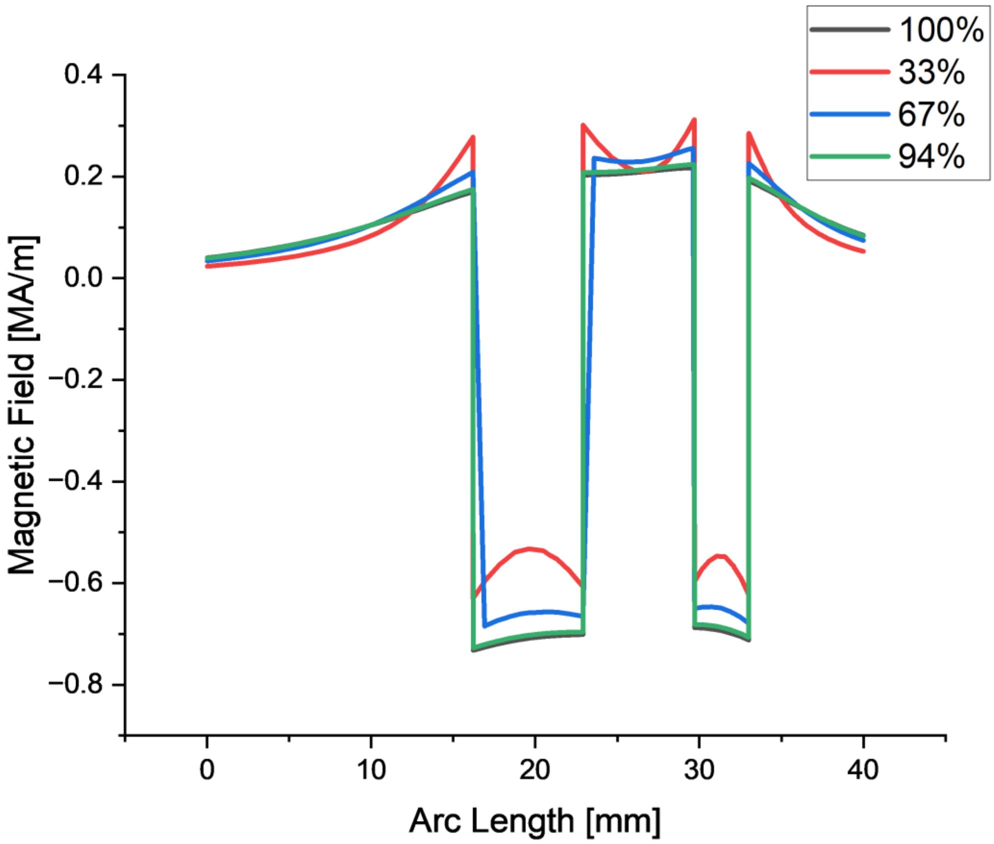

Figure 7. 25 Showing the magnetic field line scans of different volume fractions in the y-axis.

The 94% bulk volume fraction had a corner demagnetisation field of -0.24 MA/m which is a 20% reduction compared to the 100% bulk material. This implies that although the performance of the magnet is improved with respect to its demagnetisation field and external field, this does not directly translate into motor performance.

The reduction of the volume fraction of bulk material is designed to mimic an eventual concept which can be translated into real-world applications, where the bulk material is a RE magnet, such as NdFeB and the film is a much lower and cheaper magnetic material such as MnAl, Sr/Ba-Ferrite.

7.4 Ellipsoidal core-based magnets

The next investigation focused on creating a core region of bulk material which is surrounded by another weaker magnetic material "film", shown in Figure 7. 26.

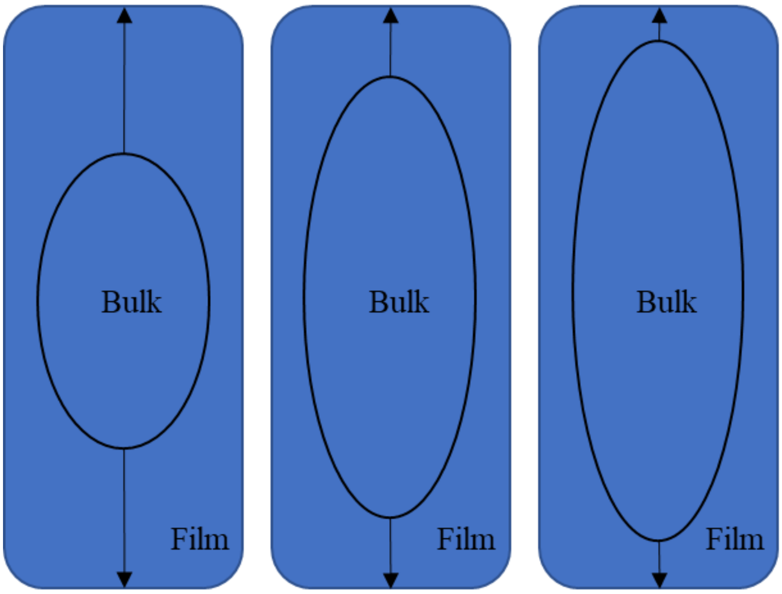

Figure 7. 26 Showing how the volume fraction in the ellipsoidal-core bulk and film changes, with the direction of the volume fraction division will be moving is shown.

The torque for a varying volume fraction with an ellipsoidal-core and film are shown in Figure 7. 27, with a 70% volume fraction being the maximum achievable due to the dimensions of the ellipse.

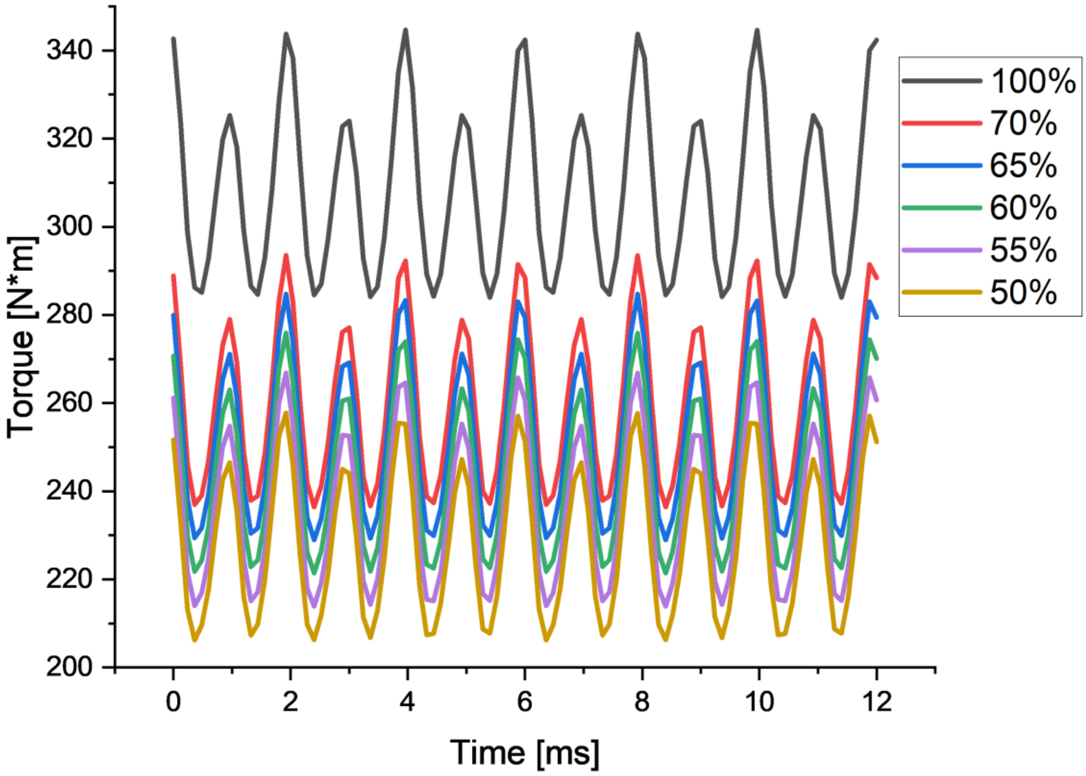

Figure 7. 27 Showing the torque plots for a varying volume fraction with the magnet having a bulk ellipsoidal core.

As the results in Figure 7. 16 and Figure 7. 21, Figure 7. 27 shows that with a reduction of the bulk material the torque is reduced. As 70% is the maximum volume fraction achievable the torque plots cannot converge towards 100%, hence the gap observed in Figure 7. 27. The different torque values are shown in Figure 7. 28.

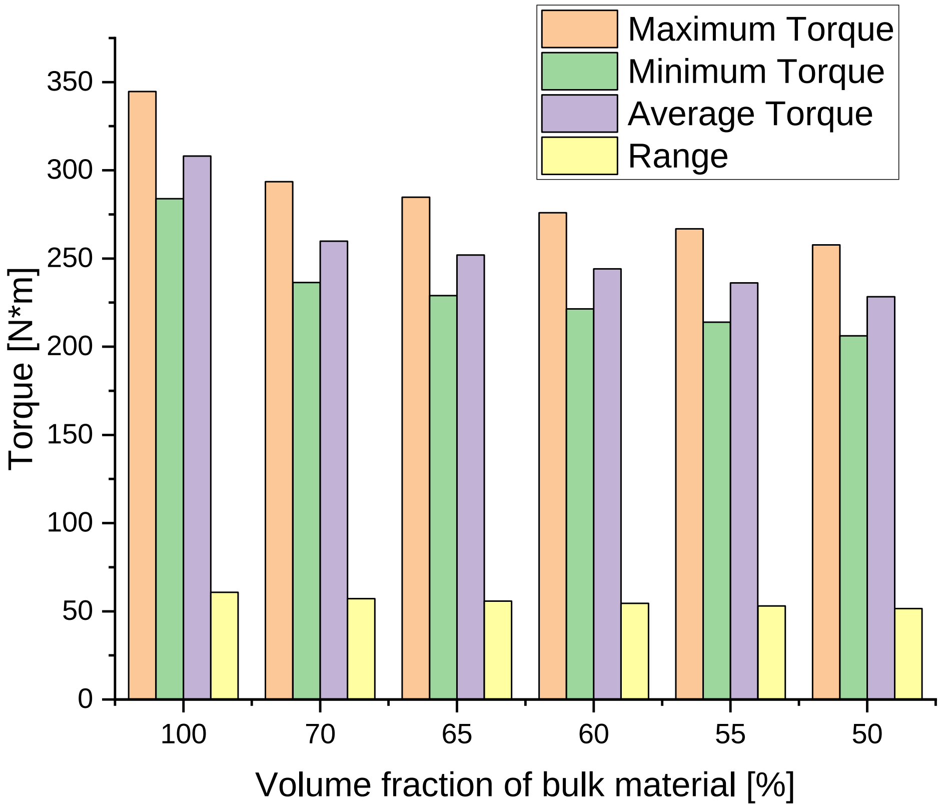

Figure 7. 28 Showing the torque values obtained when varying the volume fraction in the ellipsoidal-core bulk and film magnet.

The torque values reduced with a smaller volume of bulk material as shown by all other model iterations. The percentage change of the average torque is shown in more detail in Figure 7. 29.

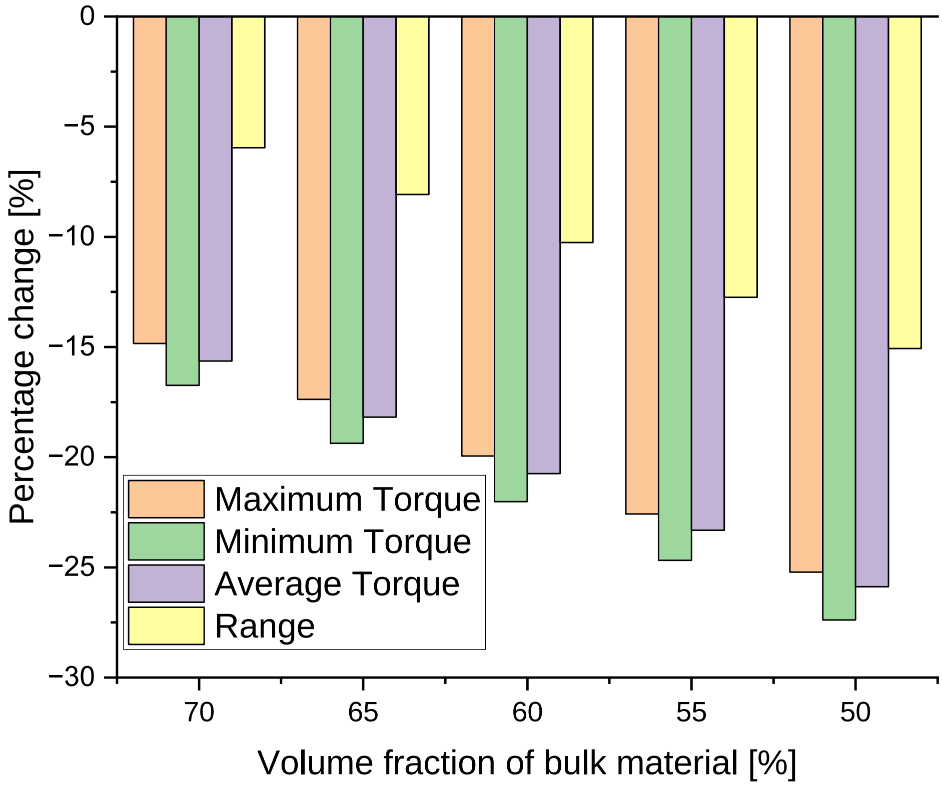

Figure 7. 29 Showing the percentage change of the torque values compared to the 100% volume fraction in the ellipsoidal-core magnet.

The percentage loss of the average torque for the 50:50 iteration is 26%, which is the same as when the magnet is divided into a film in the x-axis (Figure 7. 18). As previously discussed, how the material is divided appears to have very little deviation (Figure 7. 24) as to the torque calculated and remains dependent on the volume fraction of the bulk material. However, the magnets independent performance has a reduction of 16% for the 70:30 volume fraction, and a demagnetisation field reduction of 98% through the centre axis line scan, as shown in Figure 7. 30.

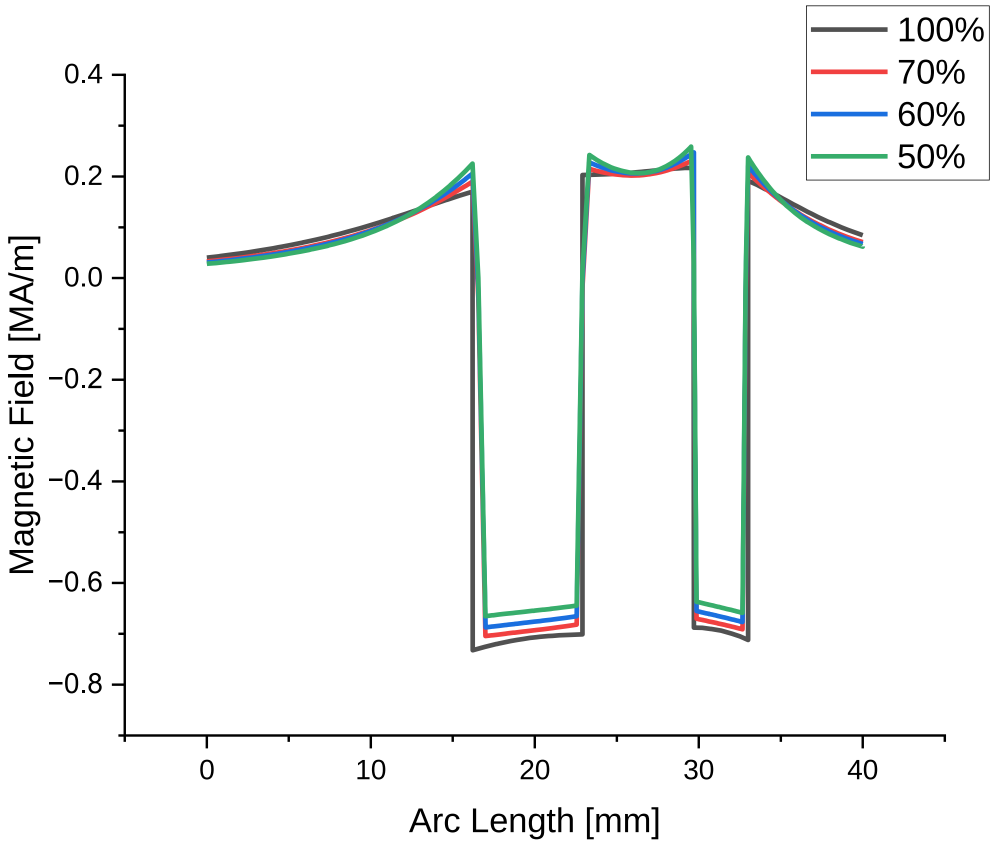

Figure 7. 30 Showing the magnetic field line scans of different volume fractions in the ellipsoidal-core magnet.

Creating the ellipsoid-core increased the magnets performance and creates an increase in external field of 24% for the 50:50 volume fraction 34 µm from the small magnet surface, slowly declining until at 2.4 mm where it drops below the external field delivered by the 100:00 bulk magnet and reduced to a loss of 26% at the edge of the line scan.

7.4.1 Bulk and semi-circle core

The ellipsoidal core magnets give a performance increase at certain external distances and has an improved demagnetisation but still results in a lower torque performance of the motor. All other models have demonstrated that a higher volume fraction of the bulk material results in more torque and the closer to 100% the closer to the standard case of results are obtained.

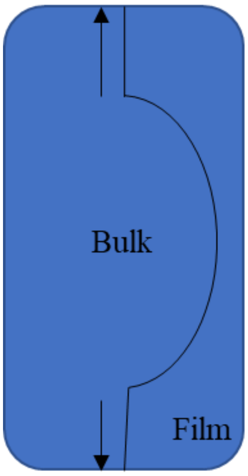

Figure 7. 31 Showing a 75:25 volume fraction in the bulk with semi-circle core and film, with the direction of the volume fraction division will be moving is shown.

Figure 7. 31 shows an adaptation to the ellipsoidal core magnet, where the volume fraction of the bulk material is increased whilst still having a film region of lower magnetisation that is over the corners to provide the lower demagnetisation field. Due to the semi-circle the maximum volume fraction achievable is 85%, shown in Figure 7. 32.

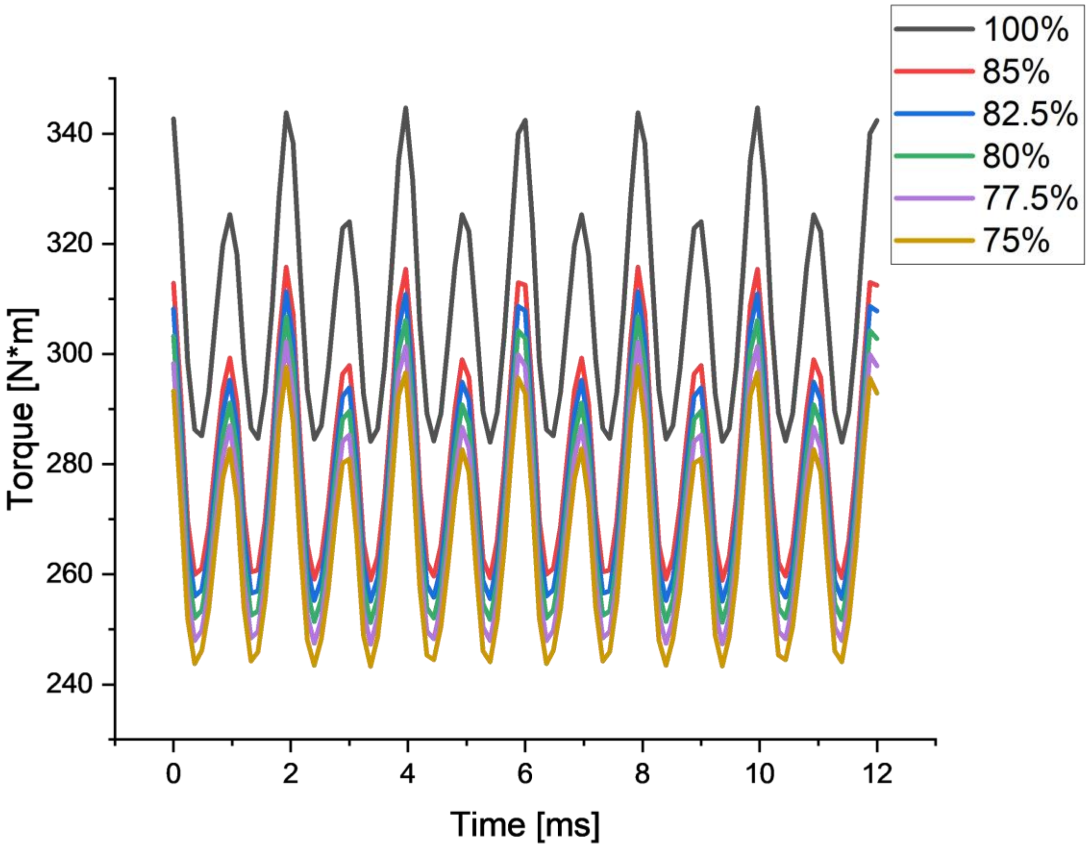

Figure 7. 32 Showing the torque plots for a varying volume fraction with the magnet having a bulk and semi-circle core.

Setting up the magnets with a bulk and semi-circle core with an 85:15 volume fraction had a reduction in the average torque of 8.5% and reducing to 14% for a 75:25 volume fraction as shown in Figure 7. 33.

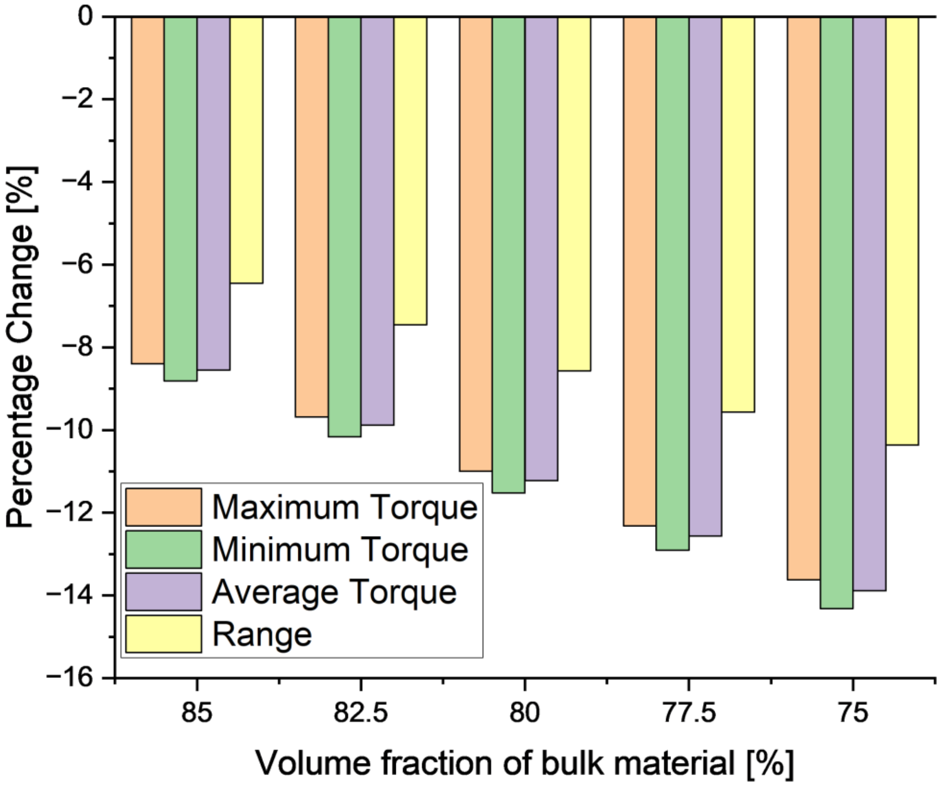

Figure 7. 33 Showing the percentage change of the torque values compared to the 100% volume fraction in the bulk semi-circle core magnet.

The trend of reduction of torque with the volume fraction of bulk material, shown in Figure 7. 33 and Figure 7. 29 correlates with the data obtained in Figure 7.24. A comparison of all the data is shown in Figure 7. 34.

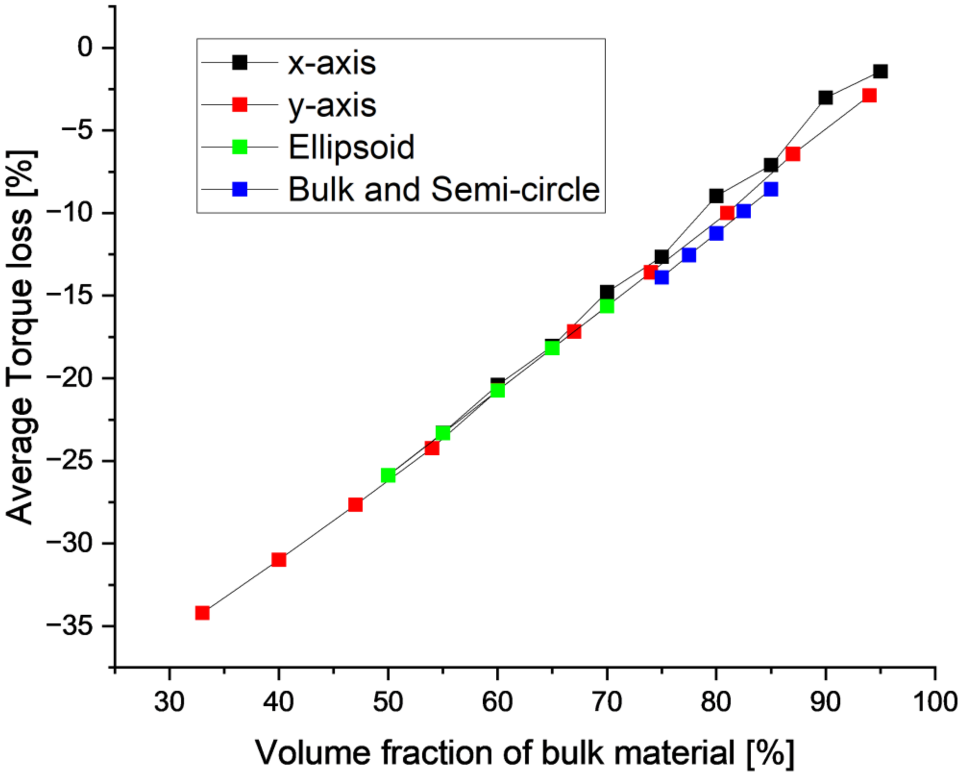

Figure 7. 34 Showing a comparison of the average torque loss for different volume fractions of bulk material when divided in the x, y-axis, ellipsoidal and bulk with semi-circle.

All results for the volume fraction for bulk to film magnetic material show a correlation between the ratio of bulk material and the simulated average torque loss. This highlights the compromise required, between motor performance and potential coercivity improvement of the magnets using a film with lower magnetisation than the bulk material.

A deeper investigation into the use of the bulk with semi-circle core with different film magnetisations was carried out to show that rather than changing the magnet into two separate materials, the film material could have a magnetisation closer to that of the bulk material which could be achievable by the current practise method of grain-boundary diffusion. The percentage loss of torque is shown in Figure 7. 35.

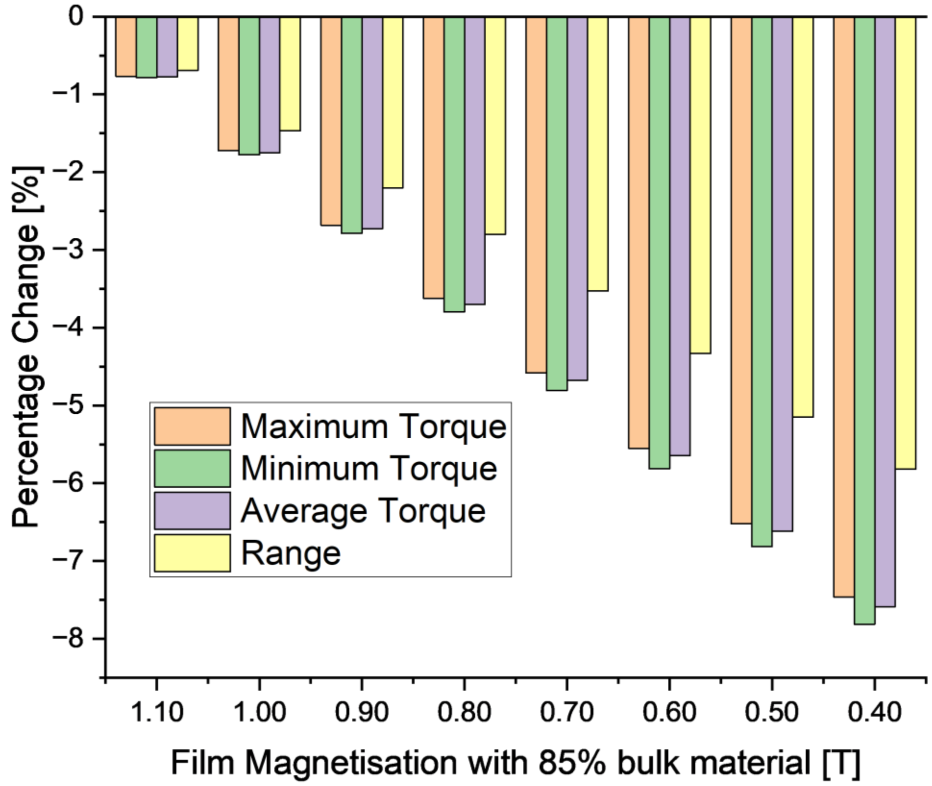

Figure 7. 35 Showing the percentage change of the torque values compared to the 100% volume fraction in the bulk semi-circle core magnet with varying film magnetisation.

The film possessing a magnetisation of 1.1T reduced the torque performance by 0.7% and the external field by 0.8% but had an increase of the coercive field of 8%.

7.5 Graded magnetisation

In chapter 5 and 6, the use of a graded magnetisation was shown to significantly improve the FoM to above 2 for some cases. The resulting decrease of the demagnetisation field should increase the coercivity and therefore its performance within a motor application. However, as discussed in this chapter, the increased volume of lower magnetisation material results in a lower operational torque. Using this knowledge and that gathered in previous chapters 5 and 6, the magnets architecture was changed to that similar of Figure 7. 15, where the film is now replaced with a graded magnetisation region, in 1 or 2 axis by equation 4.17 and equation 4.18, shown in Figure 7. 36.

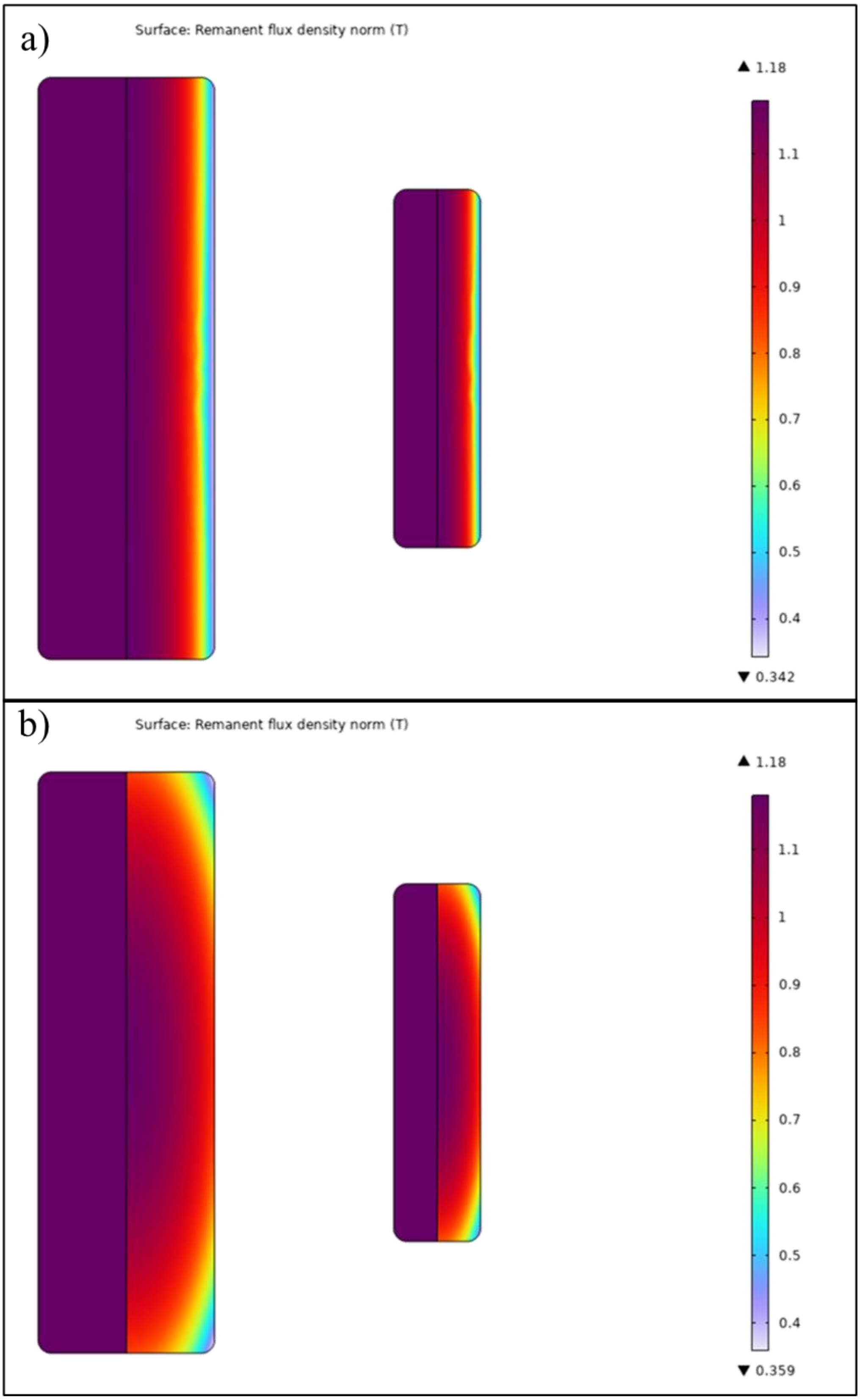

Figure 7. 36 Showing the magnetisation profile for the graded magnets, with a) single x-axis grading and b) double xy-axis (right) grading.

The length of the graded magnets remained the same, but the gradient of the magnetisation reduction was changed in order to give a higher minimum magnetisation, the effect this had on torque is shown in Figure 7. 37.

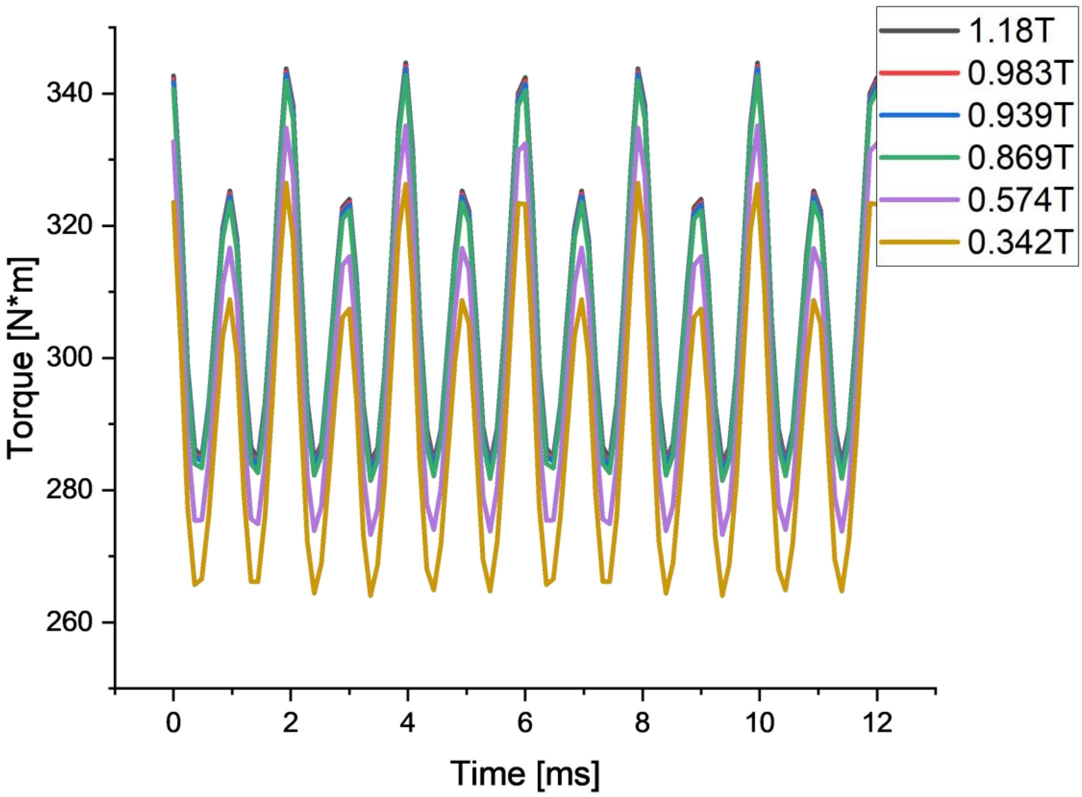

Figure 7. 37 Showing the torque plots for a minimum magnetisation value for x-axis grading.

As expected, grading the magnetisation to a lower value of 0.359 T reduced the average torque by 5.9%, and a slight reduction to 0.985 T to a 0.15% reduction. The aim of changing the magnetic profile of the magnets was to reduce their magnetisation field, the magnetic field line sans shown in Figure 7. 38 demonstrate this.

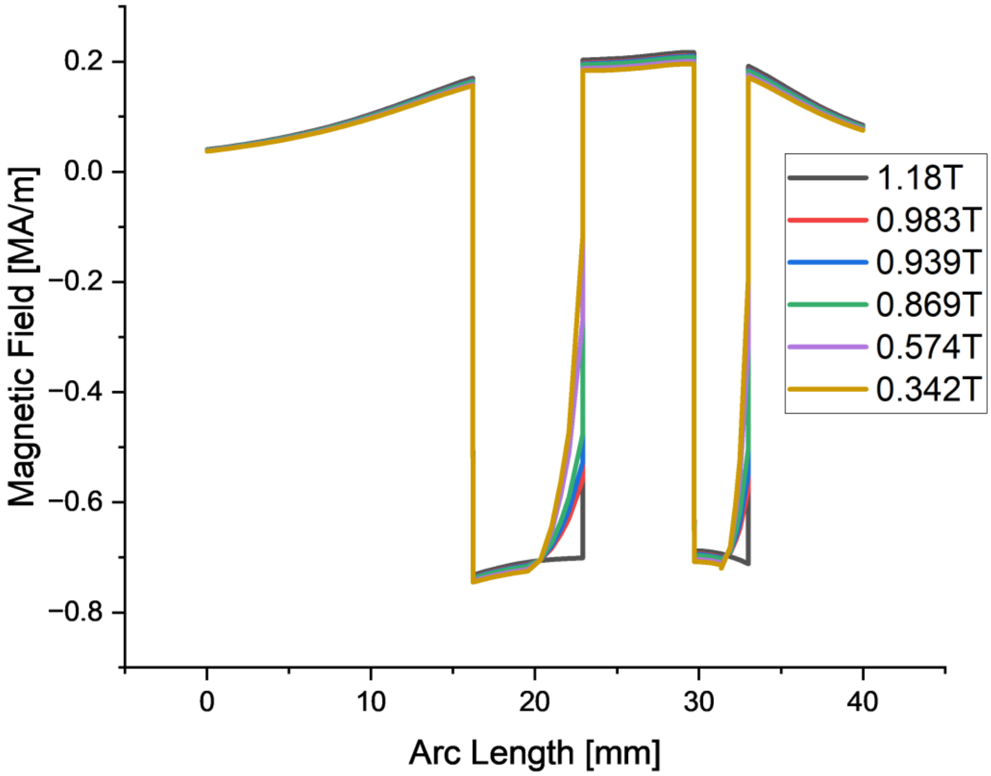

Figure 7. 38 Showing the magnetic field line scans of different minimum magnetisations for an x-axis grading.

The line scans show a smooth curve reduction of the demagnetisation field for all cases, with a reduction of 44% the 0.342 T and 10% for 0.983 T, the expected reduction of the external field was calculated to be 8% and 2.5% respectively. This demonstrates the trade-off between a magnets coercivity and external field performance, considering the magnets application within a motor there becomes another factor to consider when designing a magnet this way.

As the motor simulation is in 2D, the magnetisation is capable of being graded in another axis, this should create more region of high magnetisation whilst still concentrating the region of lower magnetisation and therefore lower demagnetisation to the corners of the magnet. The torque results are shown in Figure 7. 39.

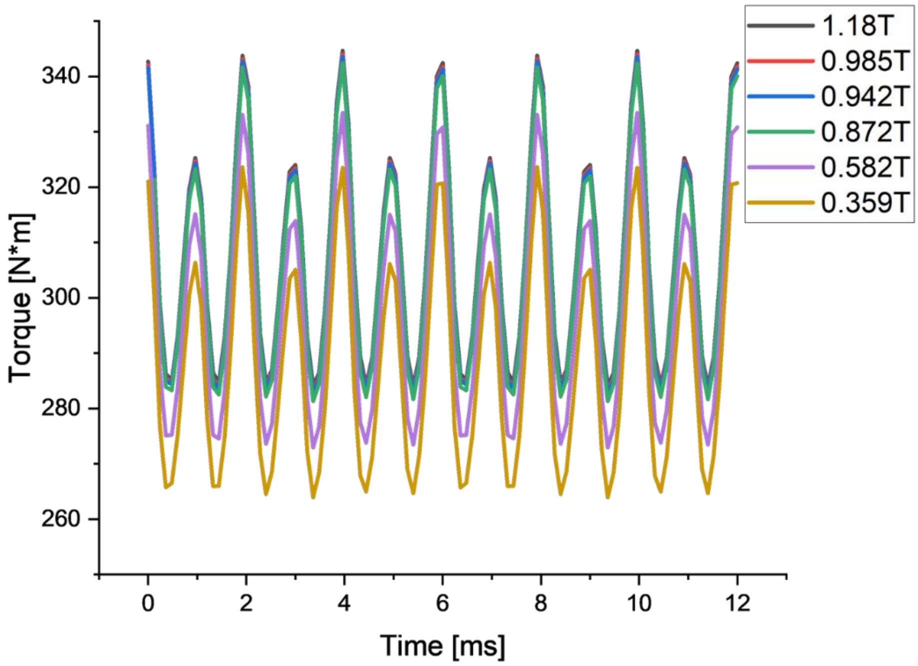

Figure 7. 39 Showing the torque plots for a minimum magnetisation value for an xy-axis grading.

The torque results for a xy-axis grading do not vary much compared to the x-axis graded magnets, with an average torque loss of 6.4% for 0.359 T and 0.18% for 0.983 T minimum magnetisation. As the grading is occurring in two axes, the grading is spread out resulting in a smaller region with higher magnetisation and an increase in the lower magnetisation region, this would explain why the loss of performance is increased for this magnetic profile compared to the x-axis grading.

Grading in the xy-axis is designed to increase the reduction of the demagnetisation field with emphasis on the corners of the magnet and not hamper the external field produced as much, shown in Figure 7. 40.

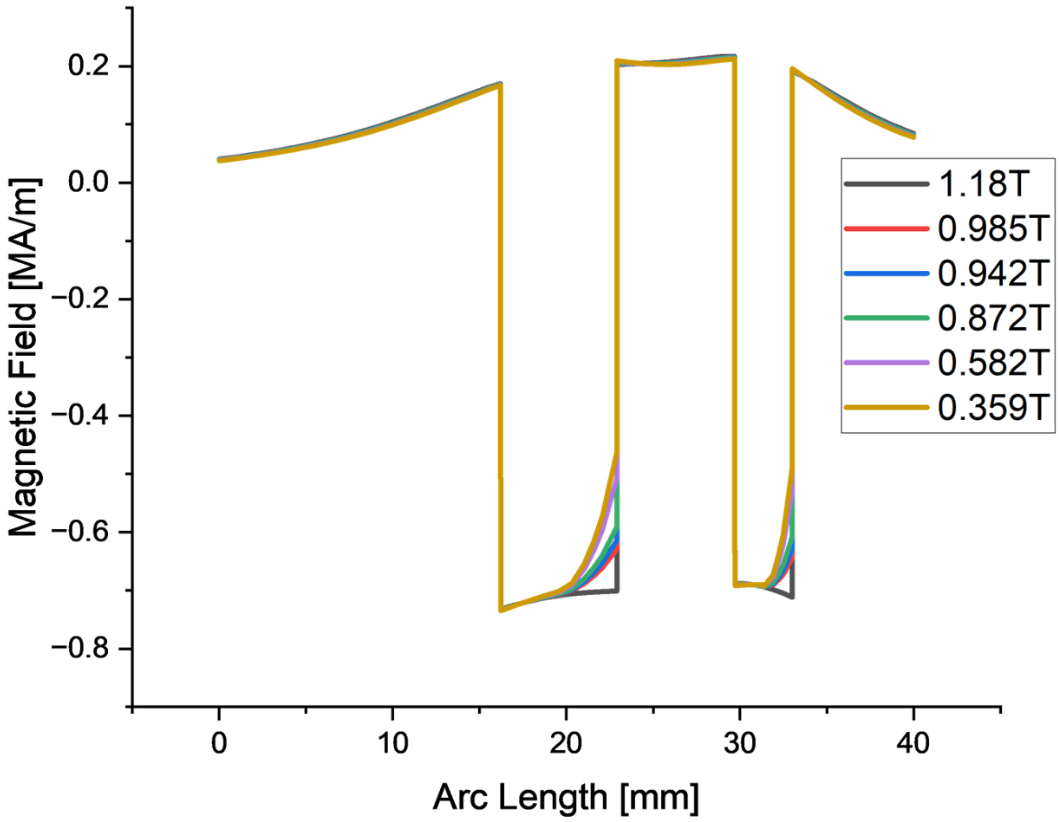

Figure 7. 40 Showing the magnetic field line scans of different minimum magnetisations for an xy-axis grading.

When comparing the results of Figure 7.39 to Figure 7.37, the gradient of the curve for the demagnetisation field of the magnets appears to reduce, results in a demagnetisation field reduction of 83.2% for a minimum magnetisation of 0.359 T and 20.3% for 0.985 T, this is around double the reduction for comparable minimum magnetisations for the x-axis grading. The external field is also only reduced by 11.1% and 3.2% respectively, this is larger than the x-axis grading by around one and half times, but is still only a few percent difference.

The grading of the magnetisation in an xy-axis has dramatically improved the performance of the magnet, as suggested by previous work in chapter 5 and 6, without significantly reducing the external field produced and the resulting torque performance of the motor.

7.6 Summary

This chapter has investigated the effects different magnetic architectures have on the performance of the motor when the initial aim was to improve the performance of the independent magnet such as in chapter 5 and 6. It was found that a lower magnetisation material has a negative impact on the torque due to the reduction in external field produced. A hybrid magnet with a combination of two different magnetic materials in different orientations was found to improve the performance of the magnet, but the reduction of high magnetisation material inevitably results in lower torque produced by the motor. This highlighted the trade-off decision required, essentially, reducing the volume of high magnetisation material in the aim of higher magnet stability and lower potential costs, resulting in lower performance from the motor. But the compromise can be swung to either sides benefit, a torque performance loss could be made up for in other parts of motor design to compensate for the gained performance of the magnets. The study also found a linear trend between the volume reduction of bulk material and the torque performance loss, which shows that performance in this case is very dependent on the volume of bulk material. The most realistic architecture that could be created and implemented, involve the x and y axis division with a maximum volume fraction of bulk material, to focus the reduction of demagnetisation field to the corners of the magnet and keep as much bulk material as possible. This could be achieved by a thick film of magnetic material in these key regions. As grading the magnetisation was the most promising model in all other previous work, it was modelled in the motor to produce a minimum 20% reduction of demagnetisation through the centre, which resulted in a 3.2% reduction in average torque when the minimum magnetisation was 0.985 T. This could potentially be achieved experimentally by GBD of non or anit-ferromagnetic material to reduce the magnetisation in the key area.

8. Summary and Future Recommendations

8.1 Summary

Commercially available Nd-Fe-B based magnets are commonly used within electric motor applications. Current methods to improve their coercivity involve the GBD of anti-ferromagnetic rare-earth Dy. The mining of rare-earth is extremely hazardous to the environment and is expensive. The use of such materials should be kept to a minimum but as the world strives towards an increased renewable energy and transport system the use of these materials is necessary. The aim of the research was to investigate new magnetic architectures with an increased performance with the goal of not using any rare-earth materials.

To model new architectures a 1D model was created to calculate demagnetisation and external field. The idea behind the use of a low magnetic film is that a lower magnetisation results in a lower demagnetisation field, which could be used as an anchor point on the poles and corners of the bulk material to lower its demagnetisation field more than the loss of external field. For the use of a uniformly magnetised film, the highest FoM came from the 1.1 MA/m due to the magnetisation being the closest one tested to the bulk material. This result became the foundation of the multilayer and eventually graded films. Multilayer films with the smallest gradient had the best FoM, which was again found in the graded films with the longer graded distance and a minimum magnetisation value. Optimisation of the graded film had a FoM of 2.80, which in essence is a 180% improvement.

A 3D model confirmed the results obtained in the 1D model, the model was developed further to study the effect of cubic magnets, as all other iterations had been based on the cylindrical magnets. The results for the use of a magnetic film with a cubic magnet showed the same trend as with the cylinders, a thinner film with magnetisation closer to that of the bulk material had the highest FoM. Grading the cubic magnets gave much more control over having a lower magnetisation at the corners whilst maintaining the high magnetisation region for the bulk material. Grading in various combinations of the X, Y, and Z axis gave a variety of FoM's, which could be essential when designing a magnet for different industrial applications. Grading the magnet in the XYZ combination resulted in a high FoM of 1.25, but not the highest, and exhibited a flat demagnetisation field. A flat demagnetisation field was the original aim when using a graded magnetisation in the 1D model, but it was not found to occur as planned. This flat demagnetisation field implies that there are no points of weakness or regions of high demagnetisation field and therefore an improved coercivity.

The transfer of the principles to improve performance of magnets into a motor proved to lower the motor torque. Any such reduction of magnetisation translates into a reduction of torque. However, the use of films to create a hybrid magnet did show that a 5% replacement of volume fraction would only reduce the torque by 1.5% for a 0.3 T film. A higher magnetisation film would result in the torque loss reducing. Grading half of the magnet to 0.983 T only reduced the torque by 0.18% and theoretically there is a larger region which can be modified.

Therefore, the work presented in this thesis shows that the use of a variable magnetisation architecture can be beneficial to an isolated magnet, whether it be using films or a graded magnetisation. The use of such magnets in an electric motor application is feasible and could be beneficial depending on the desired outcome.

8.2 Future Recommendations

The future work that could directly follow on the work in this thesis:

Using additive manufacturing to replicate the principle of graded magnetic materials and then test with a motor. Nd-Fe-B is notoriously hard to use in additive manufacturing and the performance of the magnets is far below that of the sintered Nd-Fe-B. A cheaper and more realistic alternative could be AlNiCo or ferrite and adding Cr to lower the magnetisation could initially prove the principle. The transition will have to be made to try and produce this with RE permanent magnets to attempt to show it is possible. Improvements to the additive manufacturing process will be required as it is notoriously difficult to produce Nd-Fe-B magnets this way that are comparable to traditionally sintered magnets.

Analysing graded magnet materials with X-ray, SEM techniques to see the physical impact such changes would have. As it is expected that such recommended changes to the magnet will have an impact on the microstructure of the grains and certainly the grain boundaries. This will also require investigation and comparison of the different methods to produce these types of magnets; AM, hybrid, GBD, sintered.

Micromagnetic models to investigate the effect of a graded magnetisation would have on the coercivity. And consider magnetocrystalline anisotropy for different materials using the results from the investigation into the effect a varying magnetisation will have on the microstructure. This would also aid in the investigation into the possible manufacturing techniques.

Optimisation of the motor to investigate changing the location, size and shape of the hybrid magnets to see if a reduction in the Nd-Fe-B volume can maintain motor performance with the use of other magnetic materials. As an ellipsoidal magnet is optimal for demagnetisation but has difficulties with sintering and implementation into the motor due to its shape. Regarding motor design, a motor which consisted of surface mounted magnets should also be modelled, as this would reduce the impact of a weakened external field of the magnet and require less design changes to compensate for the loss of performance.

9. References

[1] S. Sugimoto, “Current status and recent topics of rare-earth permanent magnets,” *J Phys D Appl Phys*, vol. 44, no. 6, p. 064001, Feb. 2011, doi: 10.1088/0022-3727/44/6/064001.

[2] S. Kozawa, “Trends and Problems in Research of Permanent Magnets for Motors-Addressing Scarcity Problem of Rare Earth Elements,” 2011.

[3] G. Bailey, N. Mancheri, and K. Van Acker, “Sustainability of Permanent Rare Earth Magnet Motors in (H)EV Industry,” *Journal of Sustainable Metallurgy*, vol. 3, no. 3, pp. 611–626, Sep. 2017, doi: 10.1007/s40831-017-0118-4.

[4] Y. Yang *et al.*, “REE Recovery from End-of-Life NdFeB Permanent Magnet Scrap: A Critical Review,” *Journal of Sustainable Metallurgy*, vol. 3, no. 1, pp. 122–149, Mar. 2017, doi: 10.1007/s40831-016-0090-4.

[5] J. W. Darcy, H. M. Dhammika Bandara, B. Mishra, B. Blanplain, D. Apelian, and M. H. Emmert, “Challenges in Recycling End-of-Life Rare Earth Magnets,” *JOM.*, vol. 65, no. 11, pp. 1381–1382, 2013, doi: 10.1007/s11837-013-0783-0.

[6] L. Omodara, S. Pitkäaho, E. M. Turpeinen, P. Saavalainen, K. Oravisjärvi, and R. L. Keiski, “Recycling and substitution of light rare earth elements, cerium, lanthanum, neodymium, and praseodymium from end-of-life applications - A review,” *J Clean Prod*, vol. 236, no. 236, pp. 1–13, Nov. 2019, doi: 10.1016/j.jclepro.2019.07.048.

[7] S. H. Ali, “Social and environmental impact of the rare earth industries,” *Resources.*, vol. 3, no. 1, pp. 123–134, Mar. 2014, doi: 10.3390/resources3010123.

[8] N. A. Mancheri, B. Sprecher, G. Bailey, J. Ge, and A. Tukker, “Effect of Chinese policies on rare earth supply chain resilience,” *Resour Conserv Recycl*, vol. 142, pp. 101–112, Mar. 2019, doi: 10.1016/j.resconrec.2018.11.017.

[9] V. Balaram, “Rare earth elements: A review of applications, occurrence, exploration, analysis, recycling, and environmental impact,” *Geoscience Frontiers*, vol. 10, no. 4, pp. 1285–1303, Jul. 2019, doi: 10.1016/j.gsf.2018.12.005.

[10] Reality Team Check and BBC Monitoring, “Are rare earth minerals China’s trump card in its trade war with US? - BBC News,” *BBC NEWS*, 2019.

https://www.bbc.co.uk/news/world-asia-48366074#:~:targetText=The one rare earth mine,import tariff imposed by China. (accessed Dec. 05, 2019).

[11] T. May, "PM speech on science and modern Industrial Strategy: 21 May 2018 - GOV.UK," *UK Government*, 2018. https://www.gov.uk/government/speeches/pm-speech-on-science-and-modern-industrial-strategy-21-may-2018 (accessed Jan. 08, 2020).

[12] L. Butcher, S. Hinson, and D. Hirst, "Electric vehicles and infrastructure," *House of Commons Library*, vol. 0, no. February, pp. 295–314, 2018, doi: 10.1007/978-3-540-33037-0_13.

[13] J. Cui *et al.*, "Current progress and future challenges in rare-earth-free permanent magnets," *Acta Mater*, vol. 158, pp. 118–137, Oct. 2018, doi: 10.1016/j.actamat.2018.07.049.

[14] P. Friedrichs, "Geological Survey of Finland Comparison of EV motors GTK Open File Work Report Commission by Title of report Comparison of EV motors, the EV sector's demand of commodities and the Chinese market influence-A brief review," *GTK Open File Work Report*, Accessed: Aug. 23, 2023. [Online]. Available: https://tupa.gtk.fi/raportti/arkisto/18_2023.pdf

[15] N. A. Spaldin, *Magnetic Materials: Fundamentals and Applications*, Second. Cambridge University Press, 2011. Accessed: Jan. 09, 2020. [Online]. Available: https://books.google.co.uk/books?hl=en&lr=&id=vnrOE8pQUgIC&oi=fnd&pg=PR7&dq=magnetic+materials+fundamentals+and+applications+by+nicola+a.+spaldin&ots=JVCf_X7Bzr&sig=me5ZcHAClm8GJp1ksKAqli27_6I#v=onepage&q=magnetic materials fundamentals and applications b

[16] A. Arora, "Optical and electric field control magnetism," 2018.

[17] B. D. Cullity and C. D. Graham, *Introduction to Magnetic Materials*. Hoboken, NJ, USA: John Wiley & Sons, Inc., 2008. doi: 10.1002/9780470386323.

[18] S. Chikazumi and C. D. Graham, *Physics of Ferromagnetism*. Oxford University Press, 1997.

[19] G. Y. Dayanıklı, "Design and Implementation of Wideband Stripline Circulators," 2012.

[20] “Curie-Weiss law.” https://www.doitpoms.ac.uk/tlplib/ferromagnetic/curie-weiss.php (accessed Aug. 31, 2023).

[21] G. S. Abo, Y. K. Hong, J. Park, J. Lee, W. Lee, and B. C. Choi, “Definition of magnetic exchange length,” *IEEE Trans Magn*, vol. 49, no. 8, pp. 4937–4939, 2013, doi: 10.1109/TMAG.2013.2258028.

[22] G. Hrkac *et al.*, “The role of local anisotropy profiles at grain boundaries on the coercivity of Nd2Fe14B magnets,” *Appl Phys Lett*, vol. 97, no. 23, p. 232511, Dec. 2010, doi: 10.1063/1.3519906.

[23] “Magnetic Hysteresis Loop including the B-H Curve.” https://www.electronics-tutorials.ws/electromagnetism/magnetic-hysteresis.html (accessed Nov. 17, 2022).

[24] R. Skomski, “Permanent magnets: History, current research, and outlook,” *Springer Series in Materials Science*, vol. 231, pp. 359–395, Mar. 2016, doi: 10.1007/978-3-319-26106-5_9/COVER.

[25] C. Tannous and J. Gieraltowski, “The Stoner–Wohlfarth model of ferromagnetism,” *Eur J Phys*, vol. 29, pp. 475–487, 2008, Accessed: Jan. 15, 2020. [Online].

[26] E. C. Stoner and E. P. Wohlfarth, “A mechanism of magnetic hysteresis in heterogeneous alloys,” *Philosophical Transactions of the Royal Society of London. Series A, Mathematical and Physical Sciences*, vol. 240, no. 826, pp. 599–642, May 1948, doi: 10.1098/RSTA.1948.0007.

[27] G. Zhao, X. Zhang, and F. Morvan, “Theory for the Coercivity and Its Mechanisms in Nanostructured Permanent Magnetic Materials,” *Reviews in Nanoscience and Nanotechnology*, vol. 4, no. 1, pp. 1–25, May 2015, doi: 10.1166/rnn.2015.1063.

[28] J. M. D. Coey, *Rare-earth Iron Permanent Magnets*. United Kingdom: Oxford Science Publications, 1996. Accessed: Aug. 26, 2021. [Online]. Available: https://books.google.co.uk/books?hl=en&lr=&id=bR4b4qLh1aIC&oi=fnd&pg=PR17&dq=J.+M.+D.+Coey,+Rare-Earth+Iron+Permanent+Magnets,+Oxford+Science+so-called+single+phased+permanent+magnets+where+defects+Publications,+United+Kingdom+(1996),+pp.+1–56.&ots=D9Dmax

[29] A. Aharoni and A. Arrott, “Introduction to the Theory of Ferromagnetism,” *Phys Today*, vol. 50, no. 9, p. 66, Jan. 2008, doi: 10.1063/1.881916.

[30] D. Givord and M. F. Rossignol, *Rare-earth Iron Permanent Magnets*. United Kingdom: Oxford Science Publications, 1996.

[31] G. C. Hadjipanayis and W. Gong, “Magnetic hysteresis in melt-spun Nd-Fe-Al-B-Si alloys with high remanence,” *J Appl Phys*, vol. 64, no. 10, pp. 5559–5561, 1988, doi: 10.1063/1.342307.

[32] W. F. Brown, “Virtues and Weaknesses of the Domain Concept,” *Rev Mod Phys*, vol. 17, no. 1, p. 15, Jan. 1945, doi: 10.1103/RevModPhys.17.15.

[33] E. H. Frei, S. Shtrikman, and D. Treves, “Critical Size and Nucleation Field of Ideal Ferromagnetic Particles,” *Physical Review*, vol. 106, no. 3, p. 446, May 1957, doi: 10.1103/PhysRev.106.446.

[34] E. P. Wohlfarth and K. H. J. Buschow, *Handbook of Magnetic Materials*, vol. 3. Elsevier Science, 1982. Accessed: Aug. 27, 2021. [Online]. Available: https://www.google.co.uk/books/edition/Handbook_of_Magnetic_Materials/-AC0MQEACAAJ?hl=en&sa=X&ved=2ahUKEwi2vrj4vNHyAhUYQEEAHXzQCbQQiqUDMBl6BAgDEAI

[35] S. Moaveni, *Finite element analysis : theory and application with ANSYS*, 4th ed. Pearson, 2014.

[36] V. Girault and P.-A. Raviart, “Finite Element Approximation of the Navier-Stokes Equations,” vol. 749, 1979, doi: 10.1007/BFB0063447.

[37] S. C. Brenner and L. R. Scott, *The Mathematical Theory of Finite Element Methods*, vol. 15. in Texts in Applied Mathematics, vol. 15. New York, NY: Springer New York, 2008. doi: 10.1007/978-0-387-75934-0.

[38] J. E. Akin, *Finite Element Analysis with Error Estimators: An Introduction to the FEM and Adaptive Error Analysis for Engineering Students*. Elsevier, 2005. doi: 10.1016/B978-0-7506-6722-7.X5030-9.

[39] S. H. D. Lo, *Finite Element Mesh Generation*. 2014. Accessed: Apr. 27, 2023. [Online]. Available: https://books.google.co.uk/books?hl=en&lr=&id=IJfSBQAAQBAJ&oi=fnd&pg=PP1&dq=Introduction+to+Finite+Element+Mesh+Generation&ots=WpA2MpUPwD&sig

=Oksmf3J78HRJI38AacIuvu6ZT_8&redir_esc=y#v=onepage&q=Introduction%20to%20Finite%20Element%20Mesh%20Generation&f=false

[40] S. Moaveni, *Global edition Finite element analysis Theory and Application with ANSYS*, 4th ed. 2011. Accessed: Apr. 27, 2023. [Online]. Available: www.FreeEngineeringbooksPdf.com

[41] "What Are Boundary Conditions? Numerics Background | SimScale." https://www.simscale.com/docs/simwiki/numerics-background/what-are-boundary-conditions/ (accessed Sep. 15, 2023).

[42] H. Petter Langtangen and A. Logg, *Solving PDEs in Python-The FEniCS Tutorial Volume I*. 2017.

[43] D. J. Griffiths, *Introduction to Electrodynamics*. Cambridge University Press, 2017. doi: 10.1017/9781108333511.

[44] G. Bhag Singh and R. H. Hüseyin, *Electromagnetic Field Theory Fundamentals*, 2nd ed. Cambridge University Press, 2009.

[45] J. L. Meriam, L. G. Kraige, and J. N. Bolton, *Engineering Mechanics: Dynamics*, 9th ed. 2018. Accessed: May 02, 2023. [Online]. Available: https://www.wiley.com/en-gb/Engineering+Mechanics%3A+Dynamics%2C+9th+Edition-p-9781119390985

[46] R. Krishnan, *Electric Motor Drives Modeling, Analysis, and Control*. Prentice Hall, 2001. Accessed: May 02, 2023. [Online]. Available: https://www.academia.edu/26714897/R_Krishnan_Electric_Motor_Drives_Modeling_Analysis_and_Control_2001_

[47] S. J. Chapman, *Electric Machinery Fundamentals*, 4th ed. 2005. Accessed: May 02, 2023. [Online]. Available: http://powerunit-ju.com/wp-content/uploads/2016/11/Book-Fundamentals-of-Electric-Machinery-by-Chapman-4ed.pdf

[48] K. J. Strnat and R. M. W. Strnat, "Rare earth-cobalt permanent magnets," *J Magn Magn Mater*, vol. 100, no. 1–3, pp. 38–56, 1991, doi: 10.1016/0304-8853(91)90811-N.

[49] K. Strnat, G. Hoffer, J. Olson, W. Ostertag, and J. J. Becker, "A Family of New Cobalt-Base Permanent Magnet Materials," *J Appl Phys*, vol. 38, p. 1001, 1967, doi: 10.1063/1.1709459.

[50] O. Gutfleisch, "Controlling the properties of high energy density permanent magnetic materials by different processing routes," *J Phys D Appl Phys*, vol. 33, no. 17, pp. R157–R172, Sep. 2000, doi: 10.1088/0022-3727/33/17/201.

[51] S. Miyake, *Novel Materials Processing by Advanced Electromagnetic Energy Sources*. Elsevier, 2005. doi: 10.1016/B978-0-08-044504-5.X5000-4.

[52] J. Fischbacher *et al.*, "Micromagnetics of rare-earth efficient permanent magnets," *J Phys D Appl Phys*, vol. 51, no. 19, p. 193002, May 2018, doi: 10.1088/1361-6463/aab7d1.

[53] J. M. D. Coey, "Perspective and Prospects for Rare Earth Permanent Magnets," Elsevier, Jun. 2019. doi: 10.1016/J.ENG.2018.11.034.

[54] G. H. Yan, R. J. Chen, Y. Ding, S. Guo, D. Lee, and A. Yan, "The preparation of sintered NdFeB magnet with high-coercivity and high temperature-stability," *J Phys Conf Ser*, vol. 266, p. 012052, 2011, Accessed: Jun. 24, 2020. [Online]. Available: https://iopscience.iop.org/article/10.1088/1742-6596/266/1/012052

[55] K. Hono and H. Sepehri-Amin, "Strategy for high-coercivity Nd–Fe–B magnets," *Scr Mater*, vol. 67, no. 6, pp. 530–535, Sep. 2012, doi: 10.1016/J.SCRIPTAMAT.2012.06.038.

[56] W. B. Cui, Y. K. Takahashi, and K. Hono, "Microstructure optimization to achieve high coercivity in anisotropic Nd–Fe–B thin films," *Acta Mater*, vol. 59, no. 20, pp. 7768–7775, Dec. 2011, doi: 10.1016/J.ACTAMAT.2011.09.006.

[57] W. Chen *et al.*, "Microstructure and improved properties of sintered Nd-Fe-B magnets by grain boundary diffusion of non-rare earth," *J Magn Magn Mater*, vol. 476, pp. 134–141, Apr. 2019, doi: 10.1016/j.jmmm.2018.12.048.

[58] D. Brown, B. M. Ma, and Z. Chen, "Developments in the processing and properties of NdFeb-type permanent magnets," *Journal of Magnetism and Magnetic Materials*, vol. 248, no. 3. Elsevier, pp. 432–440, 2002. doi: 10.1016/S0304-8853(02)00334-7.

[59] T. G. Woodcock *et al.*, "Understanding the microstructure and coercivity of high performance NdFeB-based magnets," *Scr Mater*, vol. 67, no. 6, pp. 536–541, 2012, doi: 10.1016/j.scriptamat.2012.05.038.

[60] H. Gleiter, “Nanocrystalline materials,” *Prog Mater Sci*, vol. 33, no. 4, pp. 223–315, 1989, doi: 10.1016/0079-6425(89)90001-7.

[61] R. Birringer, “Nanocrystalline materials,” *Materials Science and Engineering A*, vol. 117, no. C, pp. 33–43, Sep. 1989, doi: 10.1016/0921-5093(89)90083-X.

[62] G. Herzer, “Soft magnetic nanocrystalline materials,” *Scripta Metallurgica et Materiala*, vol. 33, no. 10–11, pp. 1741–1756, Dec. 1995, doi: 10.1016/0956-716X(95)00397-E.

[63] G. C. Hadjipanayis, “Nanophase hard magnets,” *J Magn Magn Mater*, vol. 200, no. 1–3, pp. 373–391, Oct. 1999, doi: 10.1016/S0304-8853(99)00430-8.

[64] T. Li *et al.*, “Bulk SmCo3 nanocrystalline magnets with magnetic anisotropy,” *J Magn Magn Mater*, vol. 502, p. 166552, May 2020, doi: 10.1016/j.jmmm.2020.166552.

[65] X. Li *et al.*, “Novel Bimorphological Anisotropic Bulk Nanocomposite Materials with High Energy Products,” *Advanced Materials*, vol. 29, no. 16, p. 1606430, Apr. 2017, doi: 10.1002/adma.201606430.

[66] M. Yue, X. Zhang, and J. P. Liu, “Fabrication of bulk nanostructured permanent magnets with high energy density: Challenges and approaches,” *Nanoscale*, vol. 9, no. 11. Royal Society of Chemistry, pp. 3674–3697, Mar. 21, 2017. doi: 10.1039/c6nr09464c.

[67] X. Y. Zhang, J. W. Zhang, W. K. Wang, W. Yu, J. H. Zhao, and Y. F. Xu, “Microstructure and magnetic properties of Sm2(Fe,Si)17Cx/α-Fe nanocomposite magnets prepared under high pressure,” *Appl Phys Lett*, vol. 74, no. 4, pp. 597–599, Jan. 1999, doi: 10.1063/1.123157.

[68] N. Lu, X. Song, and J. Zhang, “Crystal structure and magnetic properties of ultrafine nanocrystalline SmCo3 compound,” *Nanotechnology*, vol. 21, no. 11, 2010, Accessed: Jun. 11, 2020. [Online]. Available: https://iopscience.iop.org/article/10.1088/0957-4484/21/11/115708

[69] J. M. D. Coey, “Permanent magnets: Plugging the gap,” *Scr Mater*, vol. 67, pp. 524–529, 2012, doi: 10.1016/j.scriptamat.2012.04.036.

[70] J. M. D. Coey, “Hard magnetic materials: A perspective,” *IEEE Trans Magn*, vol. 47, no. 12, pp. 4671–4681, Dec. 2011, doi: 10.1109/TMAG.2011.2166975.

[71] J. Fischbacher *et al.*, "Searching the weakest link: Demagnetizing fields and magnetization reversal in permanent magnets," *Scr Mater*, vol. 154, pp. 253–258, Sep. 2018, doi: 10.1016/j.scriptamat.2017.11.020.

[72] M. Soderznik *et al.*, "Magnetization reversal of exchange-coupled and exchange-decoupled Nd-Fe-B magnets observed by magneto-optical Kerr effect microscopy," *Acta Mater*, vol. 135, pp. 68–76, 2017, Accessed: Jun. 12, 2020. [Online].

[73] S. Hirosawa, Y. Matsuura, H. Yamamoto, S. Fujimura, M. Sagawa, and H. Yamauchi, "Magnetization and magnetic anisotropy of $R_2Fe_{14}B$ measured on single crystals," *J Appl Phys*, vol. 59, no. 3, pp. 873–879, Feb. 1986, doi: 10.1063/1.336611.

[74] J. Bauer, M. Seeger, A. Zern, and H. Kronmüller, "Nanocrystalline FeNdB permanent magnets with enhanced remanence," *J Appl Phys*, vol. 80, no. 3, pp. 1667–1673, Aug. 1996, doi: 10.1063/1.362965.

[75] M. J. Kramer, R. W. McCallum, I. A. Anderson, and S. Constantinides, "Prospects for non-rare earth permanent magnets for traction motors and generators," *JOM.*, vol. 64, no. 7, pp. 752–763, Jul. 2012, doi: 10.1007/s11837-012-0351-z.

[76] "Chemical elements by market price," *Leonland*, 2019. http://www.leonland.de/elements_by_price/en/list (accessed Dec. 02, 2019).

[77] "First4magnets," 2020. https://www.first4magnets.com/ (accessed Jan. 17, 2020).

[78] L. Q. Yu, Y. H. Wen, and M. Yan, "Effects of Dy and Nb on the magnetic properties and corrosion resistance of sintered NdFeB," *J Magn Magn Mater*, vol. 283, no. 2–3, pp. 353–356, Dec. 2004, doi: 10.1016/j.jmmm.2004.06.006.

[79] J. Li *et al.*, "Effects of diffusing DyZn film on magnetic properties and thermal stability of sintered NdFeB magnets," *J Magn Magn Mater*, vol. 454, pp. 215–220, May 2018, doi: 10.1016/J.JMMM.2018.01.070.

[80] H. Ucar, D. S. Parker, I. C. Nlebedim, R. W. McCallum, S. K. McCall, and M. Parans Paranthaman, "Strategic coating of NdFeB magnets with Dy to improve the coercivity of permanent magnets," *Advances in materials Research*, vol. 4, no. 4, pp. 227–233, Dec. 2015, doi: 10.12989/amr.2015.4.4.227.

[81] J. Liu *et al.*, "Grain size dependence of coercivity of hot-deformed Nd-Fe-B anisotropic magnets," *Acta Mater*, vol. 82, pp. 336–343, Jan. 2015, doi: 10.1016/j.actamat.2014.09.021.

[82] W. F. Li, T. Ohkubo, K. Hono, and M. Sagawa, "The origin of coercivity decrease in fine grained Nd–Fe–B sintered magnets," *J Magn Magn Mater*, vol. 321, no. 8, pp. 1100–1105, 2009, Accessed: Jan. 08, 2020. [Online]. Available: https://kopernio.com/viewer?doi=10.1016/j.jmmm.2008.10.032&token=WzE1NjUyNjksIjEwLjEwMTYvai5qbW1tLjIwMDguMTAuMDMyIl0.dmFZDE8QH1PaajOn_OnwuJluM-o

[83] H. Sepehri-Amin, T. Ohkubo, and K. Hono, "Grain boundary structure and chemistry of Dy-diffusion processed Nd–Fe–B sintered magnets," *J Appl Phys*, vol. 107, no. 9, p. 09A745, May 2010, doi: 10.1063/1.3351247.

[84] W. Rave, K. Ramstöck, and A. Hubert, "Corners and nucleation in micromagnetics," *J Magn Magn Mater*, vol. 183, no. 3, pp. 329–333, Mar. 1998, doi: 10.1016/S0304-8853(97)01086-X.

[85] J. Fidler and T. Schrefl, "Overview of Nd-Fe-B magnets and coercivity," *J Appl Phys*, vol. 79, p. 5029, 1996, doi: 10.1063/1.361565.

[86] H. Sepehri-Amin, S. Hirosawa, and K. Hono, "Advances in Nd-Fe-B Based Permanent Magnets," *Handbook of Magnetic Materials*, vol. 27, pp. 269–372, Jan. 2018, doi: 10.1016/BS.HMM.2018.08.003.

[87] M. V. Riesgo García, A. Krzemień, M. Á. Manzanedo del Campo, C. Escanciano García-Miranda, and F. Sánchez Lasheras, "Rare earth elements price forecasting by means of transgenic time series developed with ARIMA models," *Resources Policy.*, vol. 59, pp. 95–102, Dec. 2018, doi: 10.1016/j.resourpol.2018.06.003.

[88] S. Constandinides, "The Important Role of Dysprosium in Modern Permanent Magnets Introduction," 2017.

[89] S. Fu, M. Yan, J. Jin, H. Nagata, and J. Xie, "Further enhancing the coercivity of Nd-Tb-Fe-B sintered magnets by Dy grain boundary diffusion," *Mater Lett*, vol. 283, p. 128718, Jan. 2021, doi: 10.1016/J.MATLET.2020.128718.

[90] J. Jin *et al.*, “Grain boundary engineering towards high-figure-of-merit Nd-Ce-Fe-B sintered magnets: Synergetic effects of (Nd, Pr)Hx and Cu co-dopants,” *Acta Mater*, vol. 204, p. 116529, Feb. 2021, doi: 10.1016/J.ACTAMAT.2020.116529.

[91] M. Zhu *et al.*, “Influence of Ce content on the rectangularity of demagnetization curves and magnetic properties of Re-Fe-B magnets sintered by double main phase alloy method,” *IEEE Trans Magn*, vol. 50, no. 1, p. 1000104, 2014, doi: 10.1109/TMAG.2013.2278018.

[92] I. Poenaru *et al.*, “Ce and La as substitutes for Nd in Nd 2 Fe 14 B-based melt-spun alloys and hot-deformed magnets: a comparison of structural and magnetic properties,” *J Magn Magn Mater*, vol. 478, pp. 198–205, May 2019, doi: 10.1016/j.jmmm.2019.01.095.

[93] H. Kara, A. Chapman, T. Crichton, P. Willis, N. Morley, and K. Deegan, “Lanthanide Resources and Alternatives,” 2010. Accessed: Dec. 09, 2019. [Online]. Available: www.oakdenehollins.co.uk

[94] K. Loewe, D. Benke, C. Kübel, T. Lienig, K. P. Skokov, and O. Gutfleisch, “Grain boundary diffusion of different rare earth elements in Nd-Fe-B sintered magnets by experiment and FEM simulation,” *Acta Mater*, vol. 124, pp. 421–429, Feb. 2017, doi: 10.1016/j.actamat.2016.11.034.

[95] S. Zhong, Y. Munan, S. U. Rehman, L. Yaojun, L. Jiajie, and B. Yang, “Microstructure, magnetic properties and diffusion mechanism of DyMg co-deposited sintered Nd-Fe-B magnets,” *J Alloys Compd*, vol. 819, p. 153002, Apr. 2020, doi: 10.1016/j.jallcom.2019.153002.

[96] F. E. Camp and A. S. Kim, “Effect of microstructure on the corrosion behavior of NdFeB and NdFeCoAlB magnets,” *J Appl Phys*, vol. 70, no. 10, pp. 6348–6350, Nov. 1991, doi: 10.1063/1.349938.

[97] W. Mo, L. Zhang, A. Shan, L. Cao, J. Wu, and M. Komuro, “Improvement of magnetic properties and corrosion resistance of NdFeB magnets by intergranular addition of MgO,” *J Alloys Compd*, vol. 461, no. 1–2, pp. 351–354, Aug. 2008, doi: 10.1016/j.jallcom.2007.06.093.

[98] T. Schrefl, J. Fidler, and H. Kronmüller, “Remanence and coercivity in isotropic nanocrystalline permanent magnets,” *Phys Rev B*, vol. 49, no. 9, pp. 6100–6110, 1994, doi: 10.1103/PhysRevB.49.6100.

[99] M. Sagawa, S. Fujimura, N. Togawa, H. Yamamoto, and Y. Matsuura, “New material for permanent magnets on a base of Nd and Fe (invited),” *J Appl Phys*, vol. 55, no. 6, pp. 2083–2087, 1984, doi: 10.1063/1.333572.

[100] Y. Shen *et al.*, “Hybrid nanograin rare earth magnets with improved thermal stability,” *J Appl Phys*, vol. 99, no. 8, p. 08B520, 2006, doi: 10.1063/1.2172582.

[101] D. Wang, N. Poudyal, C. Rong, Y. Zhang, M. J. Kramer, and J. Ping Liu, “Exchange-coupled nanoscale SmCo/NdFeB hybrid magnets,” *J Magn Magn Mater*, vol. 324, no. 18, pp. 2836–2839, Sep. 2012, doi: 10.1016/j.jmmm.2012.04.018.

[102] M. Pan, P. Zhang, H. Ge, N. Yu, and Q. Wu, “First-order-reversal-curve analysis of exchange-coupled SmCo/NdFeB nanocomposite alloys,” *J Magn Magn Mater*, vol. 361, pp. 219–223, 2014, doi: 10.1016/j.jmmm.2014.02.044.

[103] B. Z. Cui and M. J. O’Shea, “Hard magnetic properties of rapidly annealed NdFeB/Co films and intergrain interactions,” *J Magn Magn Mater*, vol. 279, pp. 27–35, 2004, Accessed: Jan. 20, 2020. [Online].

[104] M. Shindo and M. Ishizone, “Magnetic properties of exchange-coupled α-Fe/Nd–Fe–B multilayer thin-film magnets,” *J Appl Phys*, vol. 81, no. 8, p. 4444, 1997, Accessed: Jan. 20, 2020. [Online].

[105] C. J. Yang and S. Won Kim, “Observations of exchange coupling in Nd2Fe14B/Fe/Nd2Fe14B sandwich structures and their magnetic properties,” *J Magn Magn Mater*, vol. 202, no. 2–3, pp. 311–320, 1999, Accessed: Jan. 20, 2020. [Online].

[106] H. Jiang and M. J. O’Shea, “The influence of anneal time on exchange-coupling in Nd/sub 2/Fe/sub 14/B/α-Fe films,” *IEEE Trans Magn*, vol. 37, no. 4, pp. 2579–2581, 2001, Accessed: Jan. 20, 2020. [Online].

[107] H. Jiang and M. J. O’Shea, “Structure and magnetic properties of NdFeB thin films with Cr, Mo, Nb, Ta, Ti, and V buffer layers,” *J Magn Magn Mater*, vol. 212, no. 1–2, pp. 59–68, 2000, Accessed: Jan. 20, 2020. [Online].

[108] X. Xu *et al.*, “Bulk defects induced coercivity modulation of Co thin film based on a Ta/Bi double buffer layer,” *J Magn Magn Mater*, vol. 500, p. 166388, Apr. 2020, doi: 10.1016/j.jmmm.2020.166388.

[109] J. Yang *et al.*, “Structural and Magnetic Properties of Nanocomposite Nd–Fe–B Prepared by Rapid Thermal Processing,” *Engineering*, vol. 6, no. 2. Elsevier Ltd, pp. 132–140, Feb. 01, 2020. doi: 10.1016/j.eng.2019.12.008.

[110] Q. Ao, W. Zhang, and W. Jiansheng, “Exchange coupling and remanence enhancement in nanocomposite Nd–Fe–B/FeCo multilayer films,” *J Magn Magn Mater*, vol. 299, pp. 440–444, 2006, Accessed: Jan. 22, 2020. [Online].

[111] R. Coehoorn, B. Mooij, D, and D. Waard, C, “Rare-Earth Permanent Magnets,” *J Magn Magn Mater*, vol. 80, pp. 101–104, 1989, Accessed: Jan. 22, 2020. [Online]. Available: https://books.google.co.uk/books?hl=en&lr=&id=HZ47AAAAQBAJ&oi=fnd&pg=PA101&dq=Coehoorn+R,+De+Mooij+D+B+and+De+Waard+C+1989b+J.+Magn.+Magn.+Mater.+80+101-4&ots=siuAsnuu-n&sig=h1QIFJOYnz0yNxCzA1y3FcwQatc&redir_esc=y#v=onepage&q&f=false

[112] W. B. Cui *et al.*, “Anisotropic behavior of exchange coupling in textured Nd2Fe 14B/α-Fe multilayer films,” *J Appl Phys*, vol. 104, no. 5, p. 053903, 2008, doi: 10.1063/1.2973688.

[113] V. Neu, S. Sawatzki, M. Kopte, C. Mickel, and L. Schultz, “Fully epitaxial, exchange coupled SmCo 5/Fe multilayers with energy densities above 400 kJ/m 3,” *IEEE Trans Magn*, vol. 48, no. 11, pp. 3599–3602, 2012, doi: 10.1109/TMAG.2012.2195646.

[114] E. E. Fullerton, J. S. Jiang, and S. D. Bader, “Hard/soft magnetic heterostructures: model exchange-spring magnets,” *J Magn Magn Mater*, vol. 200, pp. 392–404, 1999, Accessed: Jan. 24, 2020. [Online].

[115] E. E. Fullerton, J. S. Jiang, M. Grimsditch, C. H. Sowers, and S. D. Bader, “Exchange-spring behavior in epitaxial hard/soft magnetic bilayers,” *Phys Rev B*, vol. 58, no. 18, pp. 12193–12200, Nov. 1998, doi: 10.1103/PhysRevB.58.12193.

[116] M. Faraday, “VI. Experimental researches in electricity.-Seventh Series,” *Philos Trans R Soc Lond*, vol. 124, pp. 77–122, Dec. 1834, doi: 10.1098/RSTL.1834.0008.

[117] H. Thiemer, "Influence of automotive 42 v powernet on small PM DC motors," *IEMDC 2001 - IEEE International Electric Machines and Drives Conference*, pp. 591–593, 2001, doi: 10.1109/IEMDC.2001.939373.

[118] J. De Santiago *et al.*, "Electrical motor drivelines in commercial all-electric vehicles: A review," *IEEE Trans Veh Technol*, vol. 61, no. 2, pp. 475–484, Feb. 2012, doi: 10.1109/TVT.2011.2177873.

[119] "Are brushed motors suitable for industrial applications?" https://www.linearmotiontips.com/are-brushed-motors-suitable-for-industrial-applications/ (accessed Jun. 15, 2023).

[120] John. Fenton and Ron. Hodkinson, *Lightweight Electric/Hybrid Vehicle Design*, 1st ed. Elsevier Science, 2001.

[121] W. Cai, X. Wu, M. Zhou, Y. Liang, and Y. Wang, "Review and Development of Electric Motor Systems and Electric Powertrains for New Energy Vehicles," *Automotive Innovation*, vol. 4, no. 1, pp. 3–22, Feb. 2021, doi: 10.1007/S42154-021-00139-Z/TABLES/10.

[122] "Induction Motor Working Principle- Single Phase and Three Phase Induction Motor." https://circuitdigest.com/tutorial/induction-motor-working-principle-single-phase-and-three-phase-induction-motor (accessed Jun. 15, 2023).

[123] "What is a Permanent Magnet DC Motor (PMDC Motor)?" https://www.movematic.in/post/what-is-pmdc-motor (accessed Jun. 15, 2023).

[124] C. C. Chan and K. T. Chau, "An overview of power electronics in electric vehicles," *IEEE Transactions on Industrial Electronics*, vol. 44, no. 1, pp. 3–13, 1997, doi: 10.1109/41.557493.

[125] F. Márquez-Fernández, A. Reinap, and M. Alaküla, "Design, optimization and construction of an electric motor for an electric rear wheel drive unit application for a hybrid passenger car," *19th International Conference on Electrical Machines, ICEM 2010*, 2010, doi: 10.1109/ICELMACH.2010.5608184.

[126] Y. Takano *et al.*, "Design and analysis of a switched reluctance motor for next generation hybrid vehicle without PM materials," *2010 International Power*

Electronics Conference - ECCE Asia -, IPEC 2010, pp. 1801–1806, 2010, doi: 10.1109/IPEC.2010.5543565.

[127] "Switched Reluctance Motor (SRM) Construction, Working, Types, Advantages | Electrical4u." https://www.electrical4u.net/induction-motor/switched-reluctance-motor-srm-construction-working-types-advantages/?utm_content=cmp-true (accessed Jun. 15, 2023).

[128] "DC Motor Optimization | NMB Technologies." https://nmbtc.com/resources/dc-motor-optimization/ (accessed Jun. 15, 2023).

[129] G. Friedrich, "Comparative study of three control strategies for the synchronous salient poles and wound rotor machine in automotive applications with on board energy," *Fifth International Conference on Power Electronics and Variable-Speed Drives*, 1994, Accessed: May 24, 2023. [Online]. Available: https://ieeexplore.ieee.org/document/341623

[130] C. Rossi, D. Casadei, A. Pilati, and M. Marano, "Wound rotor salient pole synchronous machine drive for electric traction," *Conference Record - IAS Annual Meeting (IEEE Industry Applications Society)*, vol. 3, pp. 1235–1241, 2006, doi: 10.1109/IAS.2006.256689.

[131] J. de Santiago and H. Bernhoff, "Comparison between axial and radial flux PM coreless machines for flywheel energy storage," *Journal of Electrical Systems*, vol. 6, no. 2, 2010, Accessed: May 24, 2023. [Online]. Available: https://www.researchgate.net/publication/289883202_Comparison_between_axial_and_radial_flux_PM_coreless_machines_for_flywheel_energy_storage

[132] X. Wang, J. Chen, and Y. Guo, "The analysis and simulation of the armature magnetic field in coreless permanent magnet synchronous motor," *Proceedings - The 12th International Conference on Electrical Machines and Systems, ICEMS 2009*, 2009, doi: 10.1109/ICEMS.2009.5382907.

[133] L. I. Farfan-Cabrera, "Tribology of electric vehicles: A review of critical components, current state and future improvement trends," *Tribol Int*, vol. 138, pp. 473–486, Oct. 2019, doi: 10.1016/J.TRIBOINT.2019.06.029.

[134] Ó. Lopez, J. Álvarez, J. Doval-Gandoy, and F. D. Freijedo, "Multilevel multiphase space vector PWM algorithm with switching state redundancy," *IEEE Transactions on Industrial Electronics*, vol. 56, no. 3, pp. 792–804, 2009, doi: 10.1109/TIE.2008.2004390.

[135] E. Levi, "Multiphase electric machines for variable-speed applications," *IEEE Transactions on Industrial Electronics*, vol. 55, no. 5, pp. 1893–1909, May 2008, doi: 10.1109/TIE.2008.918488.

[136] E. Levi, R. Bojoi, F. Profumo, H. A. Toliyat, and S. Williamson, "Multiphase induction motor drives - A technology status review," *IET Electr Power Appl*, vol. 1, no. 4, pp. 489–516, 2007, doi: 10.1049/IET-EPA:20060342.

[137] M. Simoes, "A high-torque low-speed multiphase brushless machine-a perspective application for electric vehicles," *IEEE Transactions on Industrial Electronics*, Jan. 2002, Accessed: May 24, 2023. [Online]. Available: https://www.academia.edu/es/22700993/A_high_torque_low_speed_multiphase_brushless_machine_a_perspective_application_for_electric_vehicles

[138] K. K. Young, W. L. Jin, K. L. Yong, Y. C. You, and S. M. Hyung, "Drive system of 25kW in wheel type IPMSM for electric vehicle," *Electrical Machines and Systems (ICEMS)*, 2010, Accessed: May 24, 2023. [Online]. Available: https://www.researchgate.net/publication/251971304_Drive_system_of_25kW_in_wheel_type_IPMSM_for_electric_vehicle

[139] K. Cakir and A. Sabanovic, "In-wheel motor design for electric vehicles," *9th IEEE International Workshop on Advanced Motion Control, 2006.*, vol. 2006, pp. 613–618, 2006, doi: 10.1109/AMC.2006.1631730.

[140] L. Chang, "Comparison of AC Drives for Electric Vehicles—A Report on Experts' Opinion Survey," *IEEE Aerospace and Electronic Systems Magazine*, vol. 9, no. 8, pp. 7–11, 1994, doi: 10.1109/62.311235.

[141] S. Zhang *et al.*, "Permanent magnet technology for electric motors in automotive applications," *2012 2nd International Electric Drives Production Conference, EDPC 2012 - Proceedings*, 2012, doi: 10.1109/EDPC.2012.6425118.

[142] S. E. Oti and C. C. Awah, “Influence of Magnetic Remanence and Coercive Force on the Electromagnetic Output of Permanent Magnet Machine,” *Progress In Electromagnetics Research M*, vol. 109, pp. 75–88, 2022, doi: 10.2528/PIERM22012711.

[143] Y. Chen, T. Cai, X. Zhu, D. Fan, and Q. Wang, “Analysis and Design of a New Type of Less-Rare-Earth Hybrid-Magnet Motor with Different Rotor Topologies,” *IEEE Transactions on Applied Superconductivity*, vol. 30, no. 4, Jun. 2020, doi: 10.1109/TASC.2020.2965879.

[144] C. Yunyun, C. Tongle, Z. Xiaoyong, and D. Yu, “Optimization of a New Asymmetric-Hybrid-PM Machine with High Torque Density and Low Torque Ripple Considering the Difference of Magnetic Materials,” *IEEE Trans Magn*, vol. 58, no. 2, Feb. 2022, doi: 10.1109/TMAG.2021.3086859.

[145] K. Liu, L. Shi, Z. Liu, W. Wang, and H. Ding, “Analysis and Optimization of Asymmetric Hybrid Permanent Magnet Motor for Electric Vehicle,” *Journal of Electrical Engineering and Technology*, pp. 1–13, Feb. 2023, doi: 10.1007/S42835-023-01418-X/FIGURES/22.

[146] T. H. Boyer, “The force on a magnetic dipole,” *Am J Phys*, vol. 56, p. 688, 1988, doi: 10.1119/1.15501.

[147] H. Semat and R. Katz, “The Magnetic Field,” *Physics (College Park Md)*, vol. 29, pp. 538–556, 1958.

[148] “COMSOL Multiphysics Reference Manual,” 1998, Accessed: Sep. 15, 2023. [Online]. Available: www.comsol.com/blogs

[149] P. Nieves *et al.*, “Database of novel magnetic materials for high-performance permanent magnet development,” *Comput Mater Sci*, vol. 168, pp. 188–202, Oct. 2019, doi: 10.1016/j.commatsci.2019.06.007.

10. Appendix A

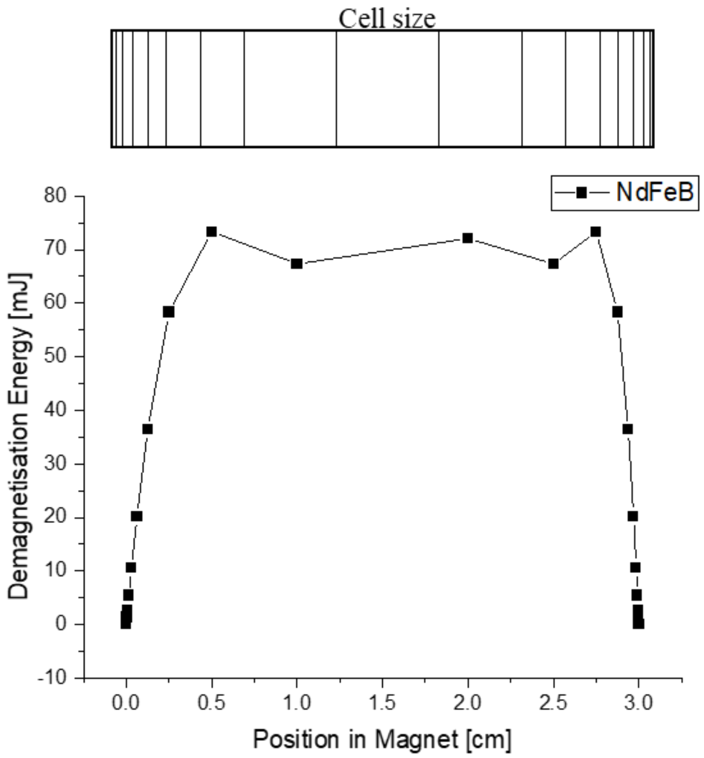

Figure A1 Showing the first line scan of demagnetisation energy with smaller cell size in the edge region, also described visually by the schematic (top) which is not to scale.

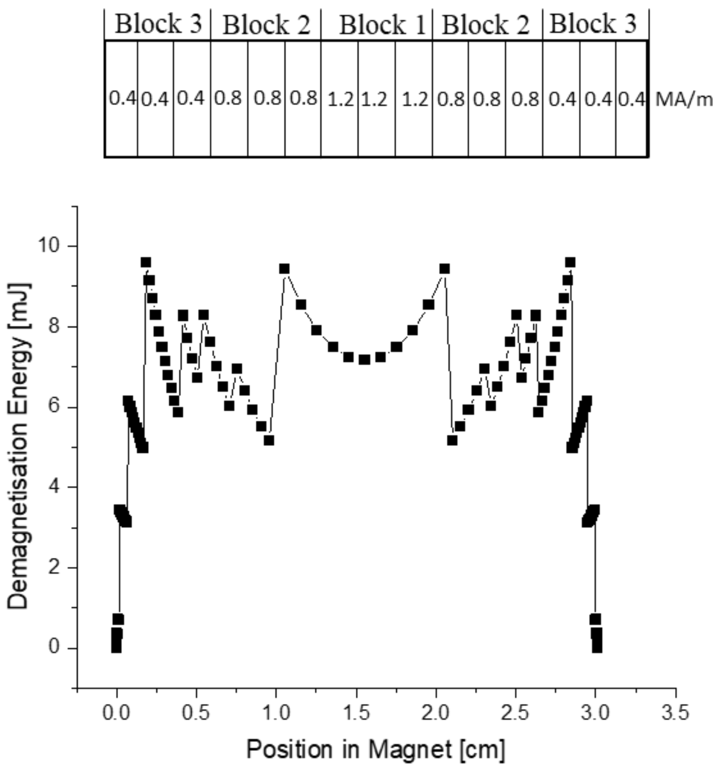

Figure A2 Showing a line scan of demagnetisation energy when the cell size is largest at the centre and reduces in blocks towards the edge of the magnet, with a visual schematic example of the how "blocks" are assigned with uniform cell size but each block having a descending magnetisation.

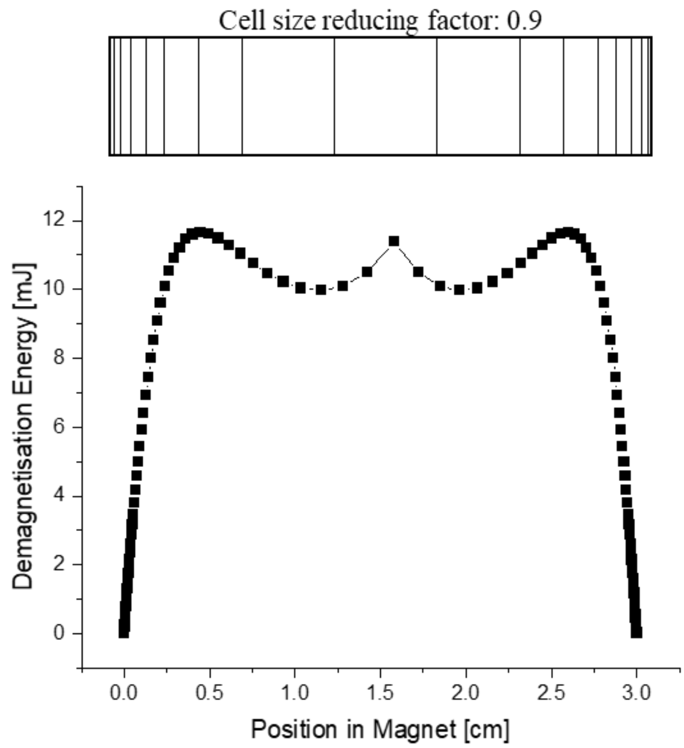

Figure A3 Showing a line scan of demagnetisation energy when each cell is reduced by a factor of 0.9 from the previous cell originating from the centre.

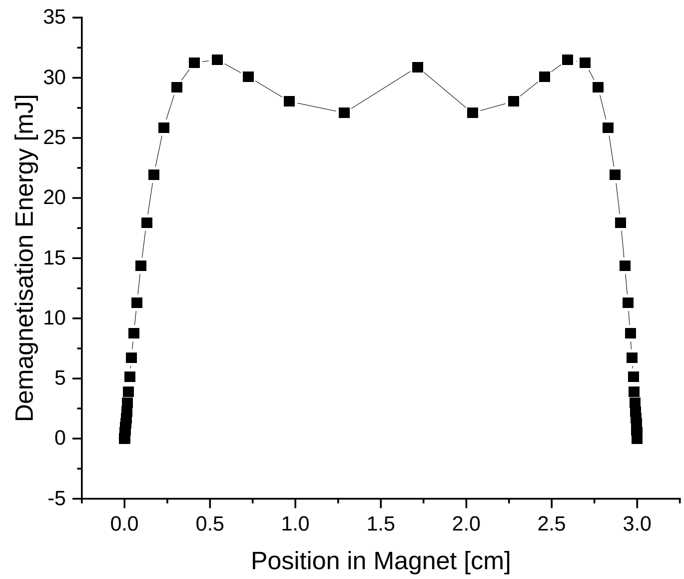

Figure A4 Showing a line scan of demagnetisation energy when each cell is reduced by a factor of 0.75 from the previous cell originating from the centre.

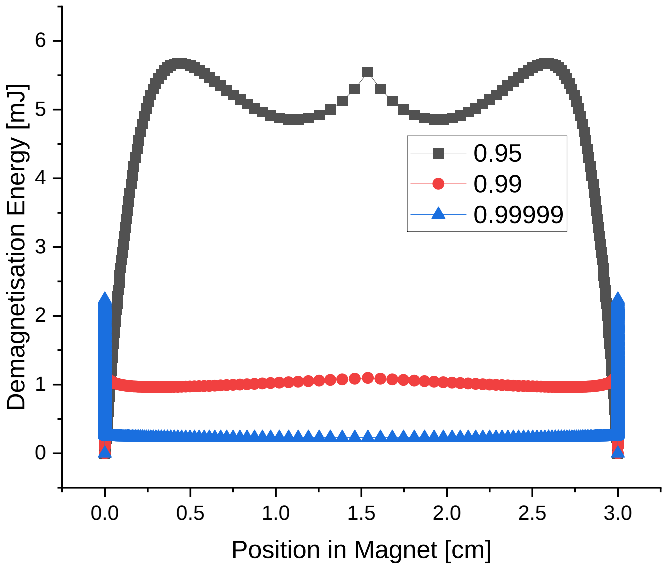

Figure A5 Showing a line scan of demagnetisation energy when each cell is reduced by a different factor from the previous cell originating from the centre.